

Towards Stable Polymer Solar Cells through Crosslinking and Sidechain Cleavage

by

Chi Zhang

B.Sc., Beihang University, 2009

Thesis Submitted in Partial Fulfillment of the
Requirements for the Degree of
Doctor of Philosophy

in the

Department of Chemistry
Faculty of Science

© **Chi Zhang 2017**

SIMON FRASER UNIVERSITY

Summer 2017

All rights reserved.

However, in accordance with the *Copyright Act of Canada*, this work may be reproduced, without authorization, under the conditions for Fair Dealing. Therefore, limited reproduction of this work for the purposes of private study, research, education, satire, parody, criticism, review and news reporting is likely to be in accordance with the law, particularly if cited appropriately.

Approval

Name: Chi Zhang
Degree: Doctor of Philosophy
Title: *Towards Stable Polymer Solar Cells through Crosslinking and Sidechain Cleavage*
Examining Committee: **Chair:** George Agnes
Professor

Steven Holdcroft
Senior Supervisor
Professor

Tim Storr
Supervisor
Associate Professor

Zuo-Guang Ye
Supervisor
Professor

Loren Kaake
Internal Examiner
Assistant Professor
Department of Chemistry

Gregory Welch
External Examiner
Assistant Professor
Department of Chemistry
University of Calgary

Date Defended/Approved:

August 22, 2017

Abstract

This thesis focuses on the investigation of two strategies for stabilizing the photovoltaic performance of polymer solar cells. Polymer solar cells (PSC) fabricated using solution processable conjugated polymers offer the potential for high-speed production of solar cell modules at low cost. However, achieving high power conversion efficiency (PCE) and long lifetime remains a challenge for PSCs. Photoexcitation of a conjugated polymer generates tightly bound electron-hole pairs (i.e., excitons) that require an electron acceptor (e.g., fullerene) for the dissociation of excitons into free charges. An interpenetrating network of conjugated polymer and fullerene (i.e., bulk heterojunction) is ideal for efficient charge generation due to the existence of a high interfacial area. However, such a morphology is not thermodynamically stable and is subject to large phase segregation in the form of fullerene aggregation provoked by the build-up of excessive heat during the operation of PSCs. Consequently, the PCE of PSCs degrades over time. In this thesis, two strategies for morphological stabilization are investigated using derivatives of poly(benzo[1,2-b:4,5-b']dithiophene-thieno[3,4-b]thiophene) (PTB). In one strategy, a derivative of PTB having thermally-cleavable tetrahydropyran (THP) sidechains (PTB(THP)) is synthesized. Removal of the THP sidechains by thermal annealing reduces the mobility of PTB, thus retarding the diffusion of fullerene through the polymer matrix to form large aggregates. Photovoltaic (PV) devices made from PTB(THP) after thermal-cleavage of the sidechains exhibited stable PCE over prolonged thermal annealing, which is attributed to the thermally-stable morphology observed by microscopic studies. In the second strategy, a series of PTB derivatives bearing photocrosslinkable chlorooctyl sidechains (PTB-Cl) are synthesized. Photocrosslinking initiated by deep UV is able to insolubilize thin films of PTB-Cl. PV devices having stable PCE over prolonged thermal annealing were demonstrated using photocrosslinked PTB-Cl. However, high-number of photocrosslinkable sidechains and prolonged UV irradiation pose negative effects on the PCE and stability of PV devices made from PTB-Cl. In addition, accurate PCE measurement is of importance for the research of PSC. In Chapter 4, measurement errors of PCE using a simple xenon arc lamp are discussed. Improvements of measurement accuracy are demonstrated following simple modifications of the instruments and the measurement procedure.

Keywords: Polymer solar cells; morphological stability; PTB; thermal-cleavage; photocrosslinking; accurate measurement

*To my wife, Ping Li,
and my parents,
Dr. Qiwei Zhang and Mrs. Wenzhi Liu*

Acknowledgements

I would like to thank:

Dr. Steven Holdcroft for offering me the opportunity to study at SFU, and conduct research in his laboratory; for his patience, guidance, and instruction throughout my research at SFU.

My committee members, Dr. Tim Storr, and Dr. Zuo-guang Ye, for their insightful comments and suggestions to my research.

Dr. Ning Li for graciously answering my technical questions about device fabrication and characterization.

Pierayeh Vahdani for performing microscopic studies in Chapter 2.

My colleagues for providing help and support in the laboratory.

National Science and Engineering Research Council for providing research funding.

PV innovation network for financially supporting me to attend PV conferences nationwide and overseas.

My wife Ping Li for her invaluable care and support during my thesis writing.

Table of Contents

Approval.....	ii
Abstract.....	iii
Dedication.....	v
Acknowledgements.....	vi
Table of Contents.....	vii
List of Tables.....	x
List of Figures.....	xi
List of Schemes.....	xvii
List of Acronyms.....	xviii
Chapter 1. Introduction.....	1
1.1. Polymer Solar Cells.....	4
1.1.1. Device configuration and principle of operation.....	5
1.1.2. Device characterization.....	7
1.1.3. Materials.....	9
Conjugated polymers.....	9
Fullerenes.....	13
Buffer layer and electrode materials.....	14
1.2. Design and Synthesis of Conjugated Polymers.....	16
1.2.1. Traditional polymers.....	16
1.2.2. Strategies for reduction of the bandgap.....	18
1.2.3. Effects of substituents attached to the polymer backbone.....	21
1.2.4. Synthesis of conjugated polymers.....	25
1.3. Morphologies of the Active Layer.....	29
1.4. Stability of the Polymer Solar Cells.....	32
1.4.1. Degradation of the metal electrode.....	32
Diffusion of oxygen and water.....	32
Chemical degradation of the metal electrode.....	33
1.4.2. Degradation of the buffer layers and the TCO.....	34
Degradation of the buffer layers.....	34
Degradation of the TCO.....	35
1.4.3. Degradation of the active layer.....	35
Chemical degradation of the conjugated polymer.....	35
Chemical degradation of fullerene.....	41
Stabilizing and destabilizing effects of fullerene.....	42
Thermally-induced morphological degradation of the active layer.....	43
1.4.4. Accelerated lifetime test.....	45
1.5. Strategies for Morphological Stabilization of the Active Layer.....	46
1.5.1. Block/graft copolymers.....	47
1.5.2. Crosslinking.....	49
1.5.3. Thermally-cleavable sidechains.....	51
1.6. Summary and Thesis Scope.....	53

Chapter 2. A Low-bandgap, High-efficiency Conjugated Polymer Bearing Thermally-Cleavable Sidechains for Stable Photovoltaic Devices	55
2.1. Introduction	55
2.2. Experimental Section	56
2.2.1. Materials and synthesis	56
2.2.2. Characterization	58
2.3. Results and Discussion	60
2.3.1. Synthesis and thermal-cleavage of THP	60
2.3.2. Optical and electronic properties	63
2.3.3. Photovoltaic properties and thermal stability	64
2.3.4. Morphological stability of the active layer	67
2.4. Conclusion	69
Chapter 3. Thermal Stability of Polymer Solar Cells Using Low-bandgap, High-efficiency, Photocrosslinkable Polymers	70
3.1. Introduction	70
3.2. Experimental Section	71
3.2.1. Materials	71
3.2.2. Synthesis	72
3.2.3. General characterization	74
3.2.4. Crosslinking	74
3.2.5. PV device fabrication, characterization, and stability	75
3.3. Results and Discussion	76
3.3.1. Synthesis and characterization	76
3.3.2. Opto-electronic properties	80
3.3.3. Crosslinking studies	81
3.3.4. Photovoltaic properties	88
3.3.5. Stability of PV devices	91
3.4. Conclusion	99
Chapter 4. Accurate Characterization of Polymer Solar Cells Using a Simple Xenon Arc Lamp in an All-in-one Apparatus	101
4.1. Introduction	101
4.2. Experimental Section	102
4.2.1. Materials and device fabrication	102
4.2.2. Photovoltaic measurements	103
4.3. Results and Discussion	103
4.3.1. Instrument setup	103
4.3.2. Device layout and test fixture	104
4.3.3. Sources of error	105
4.3.4. Area determination and mask design	106
4.3.5. Spectral mismatch	107
4.3.6. Spatial uniformity	108
4.3.7. Mismatch factor and intensity calibration	112
4.3.8. Sample measurements	115
4.4. Conclusion	118

Chapter 5. General Conclusion and Future Work..... 119

References 127

List of Tables

Table 1.1	Donor-acceptor polymers with high photo conversion efficiencies	20
Table 1.2	Photovoltaic parameters of polymer solar cells made from PTB2, PTB3, PTB7, and PTB9.....	23
Table 2.1	Photovoltaic parameters of devices made from PTB4, PTB(THP), and deprotected PTB(THP) (PTB(OH)) before and after each hour of thermal annealing at 120 °C	65
Table 3.1	Structural characterization and opto-electronic properties of PTB7 and PTB-CIs	80
Table 3.2	Visual appearance of polymer thin films that were UV-irradiated for various times and subsequently immersed in chlorobenzene	82
Table 3.3	Photovoltaic characteristics of devices made from PTB7 and various PTB-CIs.....	90
Table 4.1	Photovoltaics parameters of P3HT/PCBM devices measured with and without a mask.....	106
Table 4.2	Sizes of illuminated areas with A, B, or C spatial uniformity ratings using different homogenizing optics (unit: mm ²).....	111
Table 4.3	Photovoltaic parameters of P3HT/PCBM devices measured at SFU and NREL.....	117

List of Figures

Figure 1.1	Conventional (a) and inverted (b) configurations of polymer solar cells	6
Figure 1.2	The photovoltaic process in a polymer solar cell: exciton generation (a); exciton diffusion (b); charge transfer (CT) state formation (c); charge separation (d); charge transportation (e); charge collection (f)	7
Figure 1.3	Current density–voltage (J-V) curve and key values extracted from a current–voltage (I-V) measurement. The black dot represents the point of maximum power density (P_{\max}). J_{\max} and V_{\max} are the current density and applied voltage at P_{\max} , respectively	8
Figure 1.4	Development of the band structure from calculated energy levels of thiophene oligomers ($n = 1-6$), where E_g is the electron bandgap. The general chemical structure of polythiophene is depicted above. Adapted from ref. [77]	10
Figure 1.5	Schematic representation of the Coulomb wells and electron wavefunctions of an exciton generated in an inorganic semiconductor (Si) and an organic semiconductor (P3HT), with the positive charge carrier (i.e., hole) positioned at 0 nm. The ovals are schematic representations of the electron's wavefunction. r_C is the radius of the Coulomb well at room temperature ($T = 300$ K), r_B is the Bohr radius of the electron wavefunction, and $k_B T$ represents the thermal energy at room temperature ($T = 300$ K). The values of r_B and the dielectric constants (ϵ) were extracted from refs. [82], [84], and [85]	11
Figure 1.6	Schematic representation of charge transport through thin films of conjugated polymers. Charges travel along an individual polymer chain and transfer onto another chain at ordered regions (polymer crystallites). High conductivity is realized if there is a high population of ordered regions that are effectively connected by high-molecular-weight polymer chains. Adapted from ref. [107]	13
Figure 1.7	Chemical structures of various fullerenes.....	14
Figure 1.8	Chemical structures of PEDOT:PSS, polyethylenimine (PEI), polyethylenimine ethoxylated (PEIE), and poly [(9,9-bis(3'-(N, N-dimethylamino)propyl)-2,7-fluorene)-alt-2,7-(9,9-dioctylfluorene)] (PFN)	15
Figure 1.9	Chemical structures of MDMO-PPV and P3HT	17
Figure 1.10	Three different isomers of a 3-hexylthiophene dimer	17
Figure 1.11	Resonance structures of polyacetylene (a), polythiophene (b), and poly(isothianaphthene) (c)	18

Figure 1.12	The hybridization of energy levels of a donor-acceptor polymer (a) and the intramolecular photoexcitation of poly[2-(thiophene-2-yl)pyridine] (b)	19
Figure 1.13	The chemical structures of PTB2, PTB3, PTB7, and PTB9 (top); the energy levels of PTB2, PTB3, PTB7, PTB9, PC ₆₁ BM, and PC ₇₁ BM (bottom). Data extracted from ref. [188], [174], [189], and [190].....	22
Figure 1.14	The chemical structures of P3HT and P3EHT (a); PffBT4T-1ON, PffBT4T-2OD, PffBT4T-3OT, PTBzT ² -C12 α , PTBzT ² -C12 β , and PTh ₄ FBT (b). Schematic representation of the docking of PC ₆₁ BM with PBDTTPD(EH/C8), and PBDTTPD(C14/EH) (c). Redrawn from refs. [194], [89], [196], [195], and [197]	25
Figure 1.15	Three types of morphologies of the active layer used in polymer solar cells: (a) bilayer, (b) bulk heterojunction (BHJ), and (c) ordered BHJ	29
Figure 1.16	TEM images of PTB7/PC ₇₁ BM films spin-coated from a chlorobenzene solution without (a) and with (b) diiodooctane (DIO); dark areas are PCBM-rich phases, scale bar: 200 nm. Schematic representation of the spin-coating processes without (c) and with (d) DIO. DIO reduces the PCBM aggregation in solution, preventing the formation of large PCBM phases in the film. Reprinted from ref. [174] and [257]	31
Figure 1.17	Common degradations in a polymer solar cell: diffusion of oxygen and water through the metal electrode (a); oxidation of the metal electrode (b); ingress of water through the PEDOT:PSS layer (c); diffusion of indium from degraded ITO (d); oxygen attack of polymer and fullerene (e); photochemical degradation of polymer and fullerene (f); thermally induced large phase segregation (g)	32
Figure 1.18	Energy diagram showing the formation mechanism of singlet oxygen (¹ O ₂) in a PTB7/PCBM blend. A polymer triplet (³ P*) is formed by direct intersystem crossing from a polymer singlet (¹ P*), or through bi-molecular recombination of dissociated charges. Quenching of ³ P* by ground state oxygen (³ O ₂) gives rise to the formation of ¹ O ₂ , which consequently degrades PTB7. Adapted from ref. [298]	38
Figure 1.19	TEM images of MDMO-PPV/PCBM (1:4 w/w) films before (a) and after (b) 20 min of thermal annealing at 130 °C. The inset shows the selected area electron diffraction (SAED) pattern of PCBM crystals (dark objects surrounded by white halos). Reprinted from ref. [356]	44
Figure 1.20	Schematics of strategies for morphological stabilization using block copolymers (a), graft copolymers (b), crosslinking (c), and thermally-cleavable sidechains (d). The legend is presented in (e)	47

Figure 1.21	Two synthetic methods for block copolymers: the “graft-from” method (top) where the polymerization of the second block is initiated by the end-functionalized first block, and the “graft-onto” method (bottom) where two pre-synthesized blocks couple with each other to form the block copolymer	47
Figure 1.22	Examples of rod-coil, rod-rod, and coil-coil block copolymers, redrawn from refs. [385], [386], and [387]	48
Figure 1.23	Chemical structures of crosslinkable materials used in polymer solar cells with the crosslinkable functions highlighted in red: crosslinkable conjugated polymers bearing bromine, azide, vinyl, and oxetane groups, respectively (a)–(d), a crosslinkable fullerene bearing an azide group (e), a difunctionalized crosslinker bearing hydroxyl groups (f). Redrawn from refs. [402], [403], [404], [405], [406], and [407].....	50
Figure 2.1	Chemical structures of PTB(THP), PTB4, and the thermally induced sidechain cleavage process of PTB(THP).	56
Figure 2.2	TGA results of neat PTB(THP) (green), and PTB(THP) with 5 mol% camphorsulfonic acid (blue).....	62
Figure 2.3	FTIR spectra of PTB(THP) before (green), and after (blue) thermal-cleavage (i.e., deprotection) of THP groups. The inset highlights the region from 1140 to 1110 cm^{-1}	62
Figure 2.4	DSC results of PTB(THP) showing the first scan (a) and the second scan (b). The scan rate was 10 $^{\circ}\text{C}/\text{min}$ for both scans	63
Figure 2.5	Absorption spectra of PTB(THP) (solid lines) and PTB(THP)/PC ₆₁ BM (dashed lines) before (green lines) and after (blue lines) thermal-cleavage of THP (i.e., deprotection)	64
Figure 2.6	Cyclic voltammogram of PTB(THP). The dashed lines provide guidance for determining the HOMO and LUMO levels	64
Figure 2.7	Current density–voltage (J-V) curves of PTB4 (a), PTB(THP) (b), and deprotected PTB(THP) (c) after each hour of thermal annealing at 120 $^{\circ}\text{C}$. The degradation profile of PCE as a function of annealing time is shown in (d)	66
Figure 2.8	External quantum efficiency (EQE) curves of PTB4 (a), PTB(THP) (b), and deprotected PTB(THP) (c) after each hour of thermal annealing at 120 $^{\circ}\text{C}$	67
Figure 2.9	Optical microscopic images of the PTB4/PCBM film (a)–(d), PTB(THP)/PCBM film (e)–(h), and deprotected PTB(THP)/PCBM film (i)–(l) at different stages of thermal annealing at 130 $^{\circ}\text{C}$: as-cast (a), (e), (i), 1 h (b), (f), (j), 3 h (c), (g), (k), and 6 h (d), (h), (l)	68
Figure 3.1	Chemical structures of PTB7 and PTB-CIs	71

Figure 3.2	Chemical structures of PTB-CIs and TTBDDTTT-CI with the protons on $-\text{O}-\text{CH}_2-$ and $-\text{CH}_2-\text{Cl}$ highlighted in red and blue, respectively, NMR spectra of PTB-CIs at room temperature (a), NMR spectra of PTB-CIs at 120 °C (b), heteronuclear single quantum coherence spectroscopy (HSQC) of PTB- Cl_{100} at room temperature (c), and dynamic NMR spectra of TTBDDTTT-CI (d).....	78
Figure 3.3	DSC results of PTB7 (a) and PTB- Cl_{100} (b). Scan rate: 10 °C/min	79
Figure 3.4	Absorption spectra of PTB7 and PTB-CIs in dilute CHCl_3 solutions (a), and in ~120 nm thin films (b).....	81
Figure 3.5	Visual appearances of the peeled-off films made from PTB- Cl_{25} (a), (b), and PTB- $\text{Cl}_{12.5}$ (c), (d) in CB after UV irradiation for 10 min (a), (c), and 20 min (b), (d)	83
Figure 3.6	Quantitative evaluation of the photocrosslinking using UV-vis spectroscopy (a) and profilometry (b). Absorption spectra of PTB7 (c), PTB- Cl_{100} (d), PTB- Cl_{50} (e), PTB- Cl_{25} (f), and PTB- $\text{Cl}_{12.5}$ (g) before and after 20 min of UV irradiation followed by CB immersion.....	85
Figure 3.7	Demonstration of photolithography with PTB-CIs: a positive mask was applied across three polymer films (a), PTB- Cl_{100} , PTB- Cl_{50} , and PTB- Cl_{25} ; positive and negative patterning of PTB- Cl_{100} (b).....	86
Figure 3.8	XPS spectra of PTB- Cl_{100} before and after UV irradiation	88
Figure 3.9	Current density–voltage (J-V) curves (a) and external quantum efficiency (EQE) curves (b) of PTB7 and PTB-CI devices cast from dichlorobenzene (DCB); J-V curves (c) and EQE curves (d) of PTB- Cl_{100} devices made from DCB (dotted) and (solid) CB/DIO (97:3 v/v).....	90
Figure 3.10	J-V curves of PTB- Cl_{50} (a) and PTB7 devices (b): as-cast (solid), after 10-min UV exposure (dotted), and thermally annealed following UV treatment (dashed)	91
Figure 3.11	PCEs of PTB- $\text{Cl}_{100}/\text{PC}_{71}\text{BM}$ (a), PTB- $\text{Cl}_{50}/\text{PC}_{71}\text{BM}$ (b), PTB- $\text{Cl}_{25}/\text{PC}_{71}\text{BM}$ (c), and PTB- $\text{Cl}_{12.5}/\text{PC}_{71}\text{BM}$ (d) devices with various UV exposure times as a function of annealing time at 120 °C, compared with PTB7/ PC_{71}BM device.....	92
Figure 3.12	J_{sc} of PTB- $\text{Cl}_{100}/\text{PC}_{71}\text{BM}$ (a), PTB- $\text{Cl}_{50}/\text{PC}_{71}\text{BM}$ (b), PTB- $\text{Cl}_{25}/\text{PC}_{71}\text{BM}$ (c), and PTB- $\text{Cl}_{12.5}/\text{PC}_{71}\text{BM}$ (d) devices with various UV exposure times as a function of annealing time at 120 °C, compared with PTB7/ PC_{71}BM device.....	93
Figure 3.13	V_{oc} of PTB- $\text{Cl}_{100}/\text{PC}_{71}\text{BM}$ (a), PTB- $\text{Cl}_{50}/\text{PC}_{71}\text{BM}$ (b), PTB- $\text{Cl}_{25}/\text{PC}_{71}\text{BM}$ (c), and PTB- $\text{Cl}_{12.5}/\text{PC}_{71}\text{BM}$ (d) devices with various UV exposure times as a function of annealing time at 120 °C, compared with PTB7/ PC_{71}BM device.....	94

Figure 3.14	FF of PTB-Cl ₁₀₀ /PC ₇₁ BM (a), PTB-Cl ₅₀ /PC ₇₁ BM (b), PTB-Cl ₂₅ /PC ₇₁ BM (c), and PTB-Cl _{12.5} /PC ₇₁ BM (d) devices with various UV exposure times as a function of annealing time at 120 °C, compared with PTB7/PC ₇₁ BM device.....	95
Figure 3.15	Optical microscopic images of PTB-Cl ₁₀₀ /PC ₇₁ BM films UV treated for different times after 0, 6, 10, 20 h of thermal annealing at 150 °C, compared with PTB7/PC ₇₁ BM films. Scale bar: 20 μm.....	95
Figure 3.16	Optical microscopic images of PTB-Cl ₅₀ /PC ₇₁ BM films UV treated for different times after 0, 6, 10, and 20 h of thermal annealing at 150 °C, compared with PTB7/PC ₇₁ BM films. Scale bar: 20 μm.....	96
Figure 3.17	Optical microscopic images of PTB-Cl ₂₅ /PC ₇₁ BM films UV treated for different times after 0, 6, 10, and 20 h of thermal annealing at 150 °C, compared with PTB7/PC ₇₁ BM films. Scale bar: 20 μm.....	97
Figure 3.18	Optical microscopic images of PTB-Cl _{12.5} /PC ₇₁ BM films UV treated for different times after 0, 6, 10, 20 hours of thermal annealing at 150 °C, compared with PTB7/PC ₇₁ BM films. Scale bar: 20 μm.....	98
Figure 3.19	The visual appearance of a PTB-Cl ₁₀₀ /PC ₇₁ BM device without UV treatment (a), and the optical microscopic image of pinhole formation at the edge of the Ca/Al electrode (scale bar: 20 μm) (b), after 20 h of thermal annealing at 150 °C	99
Figure 4.1	The layout of the instrument used in this study. A beam splitter diverts a portion of the light to the side as the source of light for I-V measurement.....	104
Figure 4.2	PV device layout showing all the layers (a); front view of the device holder (b). The device fixed on the back cover of the vacuum chamber is viewed through the quartz window	105
Figure 4.3	A solar cell device viewed from the glass substrate (left), and the configuration of the mask (right). The red rectangle and blue arrows indicate the effective device area and the photocurrent contributed from outside this area, respectively	106
Figure 4.4	I-V curves of P3HT/PCBM solar cells measured with and without a mask.....	107
Figure 4.5	The spectral match of the xenon arc lamp source. The orange dashed lines represent ±25% deviation from the AM 1.5 G spectrum (A rating limits). The blue dotted lines represent ±40% deviation from the AM 1.5 G spectrum (B rating limits). The black dots represent the spectrum of the xenon arc lamp corrected by an AM 1.5G filter.....	108
Figure 4.6	I-V curves of a P3HT/PCBM device measured with the test fixture turned at four different angles (a). PCE vs. angle of the test fixture with the orientation of the test fixture illustrated (b)	109

Figure 4.7	Light intensity distribution of the xenon arc lamp using various optics at the test plane, with no optics (a)-(c), with an optical diffuser (d)-(f), with an imaging multi-aperture beam integrator (g)-(i). (a), (d), (g) are heat maps of the test plane, each square in the grids is 2 mm × 2 mm. (b), (e), (h) are topographic maps of the test plane. (c), (f), (i) are the light spot images at the test plane 110
Figure 4.8	Working principle of the imaging multi-aperture beam integrator. object array (a); field array (b); primary condensing lens (c); overlapped image of the sub-aperture at the illumination plane (d) 112
Figure 4.9	J-V curves of P3HT/PCBM devices measured at SFU and NREL: (□) fast scan at SFU under erroneous conditions, (■) fast scan at SFU under improved conditions, (○) fast scan at NREL, (●) slow asymptotic scan at NREL 117
Figure 5.1	Chemical structures of PTB2F, PTB7, and PTB4..... 122
Figure 5.2	Chemical structures of PTB7-Th, PTB-Th-Br, PTB-Th-THP, and PTB-Th-ester 124

List of Schemes

Scheme 1.1	Suzuki coupling (a), Suzuki polycondensation (b), and the catalytic cycle of Suzuki coupling (c)	27
Scheme 1.2	Stille coupling (a), Stille polycondensation (b), and the catalytic cycle of the Stille coupling (c)	28
Scheme 1.3	Radical mechanism of photooxidation of polymers. Adapted from ref. [286]	36
Scheme 1.4	Photodegradation of poly(3-alkylthiophene) through the formation of peroxy radicals: photodegradation of the sidechain (a), chain scission (b), and ring-opening (c). Adapted from refs. [287], [288], and [290].....	37
Scheme 1.5	Proposed mechanism of charge transfer complex (CTC) formation of P3HT and oxygen. Adapted from ref. [307]	40
Scheme 1.6	Photodegradation mechanism of MDMO-PPV in the absence of oxygen. Adapted from ref. [316]	40
Scheme 1.7	Photoinduced dimerization of fullerene and heat-initiated dimer dissociation. Reprinted from ref. [263].....	41
Scheme 1.8	Thermal-cleavage of ester (top) and THP (bottom) sidechains. Redrawn from [433] and [444]	52
Scheme 2.1	Synthetic route of the monomer BDT(THP) (3) and PTB(THP).....	61
Scheme 3.1	Synthetic procedures of the monomer BDT-Cl (3) and the polymers, PTB-Cl _s , with different contents of chlorooctyl sidechain	76
Scheme 3.2	Proposed mechanism of photocrosslinking for PTB-Cl: homolytic photolysis of the C–Cl bond (a); hydrogen abstraction (b); termination of two radical species (c) and (d).....	87
Scheme 5.1	Proposed synthetic route for PTB-Brs	121
Scheme 5.2	Proposed synthetic routes for PTB-Th-Br (a), PTB-Th-THP (b), and PTB-Th-ester (c)	126

List of Acronyms

$^1\text{O}_2$	Singlet oxygen
$^3\text{O}_2$	Triplet oxygen
AF	Acceleration factor
AM 1.5D	Air Mass 1.5 Direct
AM 1.5G	Air Mass 1.5 Global
a-Si	Amorphous silicon
BDT	Benzo[1,2-b:4,5-b']dithiophene
BHJ	Bulk heterojunction
BT	2,1,3-Benzothiadiazole
CB	Chlorobenzene
CdTe	Cadmium telluride
CFC	Chlorofluorocarbon
CIGS	Copper indium gallium selenide
CSA	Camphorsulfonic acid
c-Si	Crystalline silicon
CT	Charge transfer state
CTC	Charge transfer complex
CV	Cyclic voltammetry
D-A polymer	Donor-acceptor polymer
DCB	<i>o</i> -Dichlorobenzene
DCM	Dichloromethane
DIO	1,8-diiodooctane
DMF	N,N-dimethyl formamide
DPP	Diketopyrrolopyrrole
DSC	Differential scanning calorimetry
E_a	Activation energy
E_g	Bandgap
EQE	External quantum efficiency
ESR	Electron spin resonance spectroscopy

ETL	Electron transporting layer
FF	Fill factor
FTIR	Fourier transform infrared spectroscopy
FTO	Fluorine doped tin oxide
GPC	Gel permeation chromatography
HOMO	Highest occupied molecular orbital
HSQC	Heteronuclear single quantum coherence spectroscopy
HTL	Hole transporting layer
ICBA	Indene-C ₆₀ bisadduct
ISOS	International Summit on OPV Stability
ITO	Indium tin oxide
I-V	Current – voltage
J _{sc}	Short circuit current
J-V	Current density – voltage
KG5 filter	KG5 colored glass bandpass filter, 330 - 665 nm
LDA	Lithium diisopropylamide
LiF	Lithium fluoride
LUMO	Lowest unoccupied molecular orbital
MDMO-PPV	Poly([2-methoxy-5-(3,7-dimethyloctyloxy)]-1,4-phenylene-vinylene)
MoO ₃	Molybdenum oxide
NMR	Nuclear magnetic resonance (spectroscopy)
NREL	National Renewable Energy Laboratory
O ₂ ^{•-}	Superoxide anion
OPV	Organic photovoltaics
P3HT	Poly(3-hexylthiophene)
PBDT	Polybenzodithiophene
PBDTPD	Poly(benzo[1,2-b:4,5-b']dithiophene-thieno[3,4-c]pyrrole-4,6-dione)
PC ₆₁ BM	Phenyl-C ₆₁ -butyric acid methyl ester
PC ₇₁ BM	Phenyl-C ₇₁ -butyric acid methyl ester
PCBM	PC ₆₁ BM and PC ₇₁ BM in general
PCE	Power conversion efficiency
PEDOT:PSS	Poly(3,4-ethylenedioxythiophene) doped with poly(styrene-4-sulfonate)
PEI	Polyethylenimine

PEIE	Polyethylenimine ethoxylated
PffBT4T	Poly(difluoro-2,1,3-benzothiadiazole-quarterthiophene)
PFN	Poly [(9,9-bis(3'-(N, N-dimethylamino)propyl)-2,7-fluorene)-alt-2,7-(9,9–dioctylfluorene)]
P_{in}	Incident power
PITN	Poly(isothianaphthene)
P_{max}	Maximum power
PPP	Poly(<i>p</i> -phenylene)
PPV	Poly(phenylenevinylene)
PSC	Polymer solar cells
PT	Polythiophene
PTB	Poly(benzo[1,2-b:4,5-b']dithiophene-thieno[3,4-b]thiophene)
PTFE	Polytetrafluoroethylene
PTP	Poly[2-(thiophene-2-yl)pyridine]
PV	Photovoltaic
RR-P3HT	Regioregular poly(3-hexylthiophene)
SAED	Selected area electron diffraction
SFU	Simon Fraser University
TCO	Transparent conducting oxide
TEM	Transmission electron microscope
T_g	Glass transition temperature
TGA	Thermogravimetric analysis
THF	Tetrahydrofuran
THP	Tetrahydropyran
TOF-SIMS	Time-of-flight secondary ion mass spectrometry
TPD	Thieno[3,4-c]pyrrole-4,6-dione
TT	Thieno[3,4-b]thiophene
UV-vis	Ultraviolet–visible spectroscopy
V_{oc}	Open circuit voltage
W_f	Work function
WO ₃	Tungsten oxide
XPS	X-ray photoelectron spectroscopy
ZnO	Zinc oxide

Chapter 1.

Introduction

Presently, the world produces 23,815 TWh of electricity in a year, of which 66.7% comes from power plants that burn fossil fuels. In contrast, renewable energies, such as solar, wind, tide, and geothermal, only contribute 4.2% to the overall electricity production.¹ In the context of global energy production, renewable energies account for a mere 1%.² Despite the low global output, renewable energies have undergone rapid growth since the 1970s, largely because of increasing awareness of the limited sources of fossil fuels and the imminent threat of global warming. Without any efforts to reduce greenhouse gas emissions, the increasing energy demands under the current structure of energy production are estimated to increase the global temperature to ~5 °C above pre-industrial values by the end of the 21st century.³ The goal of the 2015 United Nations Climate Change Conference is to keep the increase to < 2 °C,⁴ which would require extensive replacement of fossil fuel combustion with renewable energies.⁵ In addition, coal burning and fuel combustion used in the transportation sector generate large amounts of sulfur oxides, nitrogen oxides, and fine particulates that adversely affect human health.⁶ The growing concern of air pollution, especially in densely populated countries and cities, also calls for expedited development of clean, renewable energies.

The sun delivers 4.3×10^{20} J of energy to the surface of the earth every hour.⁷ If only a small fraction of the total solar irradiation is harvested by humans, the current world energy needs could be completely met. Unlike other types of renewable energy, solar energy is ubiquitous, free of charge, and easily accessible throughout the world. Therefore, solar power is unlikely to be affected by price volatility, import/export restrictions, and can contribute to energy self-sustainability in countries that lack natural resources. Photovoltaic (PV) devices provide direct conversion of light into electricity. When paired with appropriate energy storage technologies, PV devices provide

sustainable clean energy. In large metropolises, solar PV devices can be used to charge electric vehicles during the daytime, lowering grid burdens and reducing pollution.⁸ Once installed, solar PV devices do not generate greenhouse gases and do not emit pollutants. Large solar PV plants require minimal water consumption, which is a key benefit for countries and regions where fresh water is limited. Small-size solar cells combined with rechargeable batteries can serve as self-sustained, off-grid electricity sources. This combination can be utilized in remote areas where grid connection is not economically feasible. A successful example is the Lighting Africa program, which has been providing lighting in various African countries using batteries connected to solar cells.⁹

Despite the advantages and benefits, solar PV only contribute a marginal 0.6% of the world's electricity¹⁰ and only 14% of the electricity produced by renewable sources.¹ One major issue associated with solar PV is the cost of electricity production. Although the cost of PV electricity has been reduced to 80–100 USD/MWh, it is still more expensive than wind and traditional fossil-fuel-based power generation.¹¹ The PV market is currently dominated by crystalline silicon (c-Si) because it is a mature technology and has been successfully commercialized.¹⁰ Manufacturing crystalline silicon solar cells usually involves three major processes: casting a silicon crystalline ingot, slicing the ingot into wafers, and fabricating the wafer into solar cells.¹² Approximately 50% of the cost of c-Si cells comes from the silicon wafer¹² because the manufacturing process of silicon ingot is highly energy demanding and the tolerance for defects is extremely low.¹³ Therefore, reducing the thickness of the wafer is imperative in the development of c-Si solar cells. However, following a rapid decline in wafer thicknesses from the late 1970s, this trend has slowed down in recent years. Further thinning of the wafer would require extensive development of processing technologies.¹² Alternatively, several thin film PV technologies have emerged in an effort to lower material usage in PV modules. Examples of thin-film PV technologies are amorphous silicon (a-Si),¹⁴ cadmium telluride (CdTe),¹⁵ and copper indium gallium selenide (CIGS).¹⁶ Instead of slicing from bulk crystalline materials, PV thin films are grown directly from precursors onto conducting substrates. The thickness of thin-film PV devices vary from a few hundred nanometers to tens of micrometers, which is much thinner than c-Si PV devices (typically one to two hundred micrometers).¹⁷ Also, thin film PV manufacturing processes consume far less energy than c-Si PV devices because bulk crystal growth is avoided.¹³ When deposited onto flexible substrates, such as metal

foil or plastic sheets, thin-film PV devices become flexible and can be stored in rolls and more easily installed.^{18,19} Roll-to-roll production of thin-film PV modules based on flexible substrates have a higher throughput and lower cost than traditional wafer-by-wafer manufacturing in clean rooms.²⁰

Like its predecessor, thin-film PV technologies have their own shortcomings. The major impediment of a-Si PV devices is light-induced degradation during operation.²¹ While CIGS do not undergo light-induced degradation,²² the scarcity of indium makes them essentially non-sustainable for mass-production. CdTe suffers from an extremely low abundance of tellurium, and it is also challenged by wide-spread concerns related to the toxicity of cadmium.²³ Only a finite number of elements are present in inorganic PV materials; thus, the variation largely relies on advanced engineering. In contrast, the electronic and opto-electronic properties of organic semiconductors can be finely tuned by synthetically altering the chemical structures. Thus, organic PV (OPV) devices are more likely to achieve high-performance, low-cost solar cells in the future. Additionally, experiments and calculations have shown that manufacturing OPV devices requires minimal energy consumption and low material cost such that the energy pay back time (time required to produce the same amount of energy that is consumed during its production) is projected to be as low as one day.²⁴ This feature is largely attributed to the high solubility of organic semiconductors in common organic solvents, and it enables large-scale, high-speed production using printing techniques at room temperature.^{25,26} The abundance of carbon, which forms the skeleton of organic molecules, contributes to the low cost of the raw material. OPV devices are flexible, transparent, and light-weight; therefore, they can be used in niche applications, such as portable power sources for personal electronic devices, window-mounted PV devices, and wearable solar cells.²⁷ However, when viewed as a PV technology that will play a serious role in mass power generation, OPV devices are far from meeting industrial standards and requirements for commercialization.²⁸

The power conversion efficiency (PCE), lifetime, and cost are the three key properties that determine the commercial viability of a certain type of PV technology.²⁹ Failure in one of these three categories will limit a PV technology to a niche market. Commercial c-Si modules have an average of 16% PCE, and lifetimes of ~ 20–30 years.¹⁰

In comparison, OPV devices show lower performances in both areas. Over the years, with enormous amount of effort devoted to the field, the PCE of OPV has surpassed 10%.^{30–38} However, these record numbers are based on lab-scale devices (tens of square millimetres in size), and manufacturing high-PCE large-scale modules remains a challenge.³⁹ Nonetheless, a module PCE as low as 5% is considered acceptable²⁹ and can still make OPV devices competitive as long as the cost of manufacturing lies well below that of other technologies. The major obstacle is the short lifetime. Although the reported life expectancy of OPV devices has been improved from several minutes to a few years over the past two decades,^{40,41} the research field remains disorganized—reliable outdoor evaluations are deficient and standard indoor accelerated test protocols are not consistently followed.⁴² Compared to the steady improvement of PCE, the subject of performance stability is generally less studied because of its complex mechanism and overlooked importance. Thus, more research must be devoted to the field of OPV for OPV devices to become serious contenders in the PV industry and ultimately contribute to the transformation of energy structure towards clean, renewable energies.

1.1. Polymer Solar Cells

Anthracene was the first organic compound whose photoconductivity was discovered and investigated in the early 20th century.^{43–45} Around the same time, Albert Einstein received the Nobel Prize in Physics for his discovery of the photoelectric effect, which laid the foundation for the development of photovoltaics in the late 20th century.⁴⁶ After the invention of the first silicon photovoltaic cell at Bell Laboratory in 1954,⁴⁷ investigation of photovoltaic properties in organic materials focused mostly on organometallic complexes.^{48–51} These so-called “dyes” were sandwiched between two metal electrodes, and achieved a PCE up to 0.01% by 1975.⁵² Two years later, high conductivities were observed in certain conjugated polymers after doping,⁵³ which earned Allan J. Heeger, Alan G. MacDiarmid, and Hideki Shirakawa the Nobel Prize in Chemistry in 2000.^{54–56} In the following years, semiconducting conjugated polymers became a niche subject of PV cells, where similar sandwiched electrode-polymer-electrode architectures were used, yielding low PCEs.^{57,58} A major breakthrough in the field came in 1986 when Tang reported the first bi-layer organic solar cell using two different dyes and achieved a

PCE of 1%.⁵⁹ This heterojunction concept forms the basis of all types of subsequent organic solar cells where two materials with different electron affinities were brought into contact to facilitate charge separation and charge transportation. Hiramoto et al. added a third layer consisting of two co-sublimated dyes within the bi-layer architecture and achieved a photocurrent that was two times greater than that of a bi-layer cell.⁶⁰ The dispersed heterojunction, later called a bulk heterojunction (BHJ), likely increases the heterojunction interface, facilitating charge separation. After the low solubility issue of C₆₀ (a widely-used electron acceptor) was solved by the invention of a soluble fullerene, it became possible to fabricate bulk heterojunctions of conjugated polymer/fullerene via solution processing.⁶¹ Taking this advantage, another breakthrough in the field was made by Yu et al. In their seminal paper published in 1995, solar cells with a spin-coated bulk heterojunction of polymer/fullerene achieved a then record-high PCE of 2.9%.⁶² Since then, polymer solar cells (PSCs) have gained significant interest and become one of the most studied systems within the realm of organic solar cells.

1.1.1. Device configuration and principle of operation

As a thin-film PV technology, a complete polymer solar cell comprises multiple layers of thin films. The conventional and inverted configurations are shown in Figure 1.1. Both configurations are built on a transparent substrate coated with a layer of transparent conducting oxide (TCO) as the bottom electrode. The active layer, which is essentially the bulk heterojunction of a conjugated polymer and fullerene, serves as the core of the entire device where the photovoltaic effect occurs. The active layer is sandwiched by two buffer layers: the electron transport layer (ETL) and the hole transport layer (HTL). The main function of the buffer layers is to selectively conduct one type of charge carrier while blocking the other, such that charge carrier recombination at the active layer/electrode interface is prevented during device operation.⁶³ The device is finished with a metallic top electrode, which is usually deposited by thermal evaporation. The polarities of the top and bottom electrodes, as well as the locations of the ETL and HTL, are opposite in these two configurations.

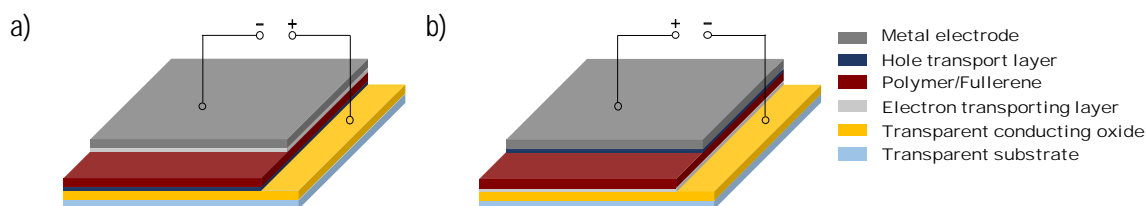
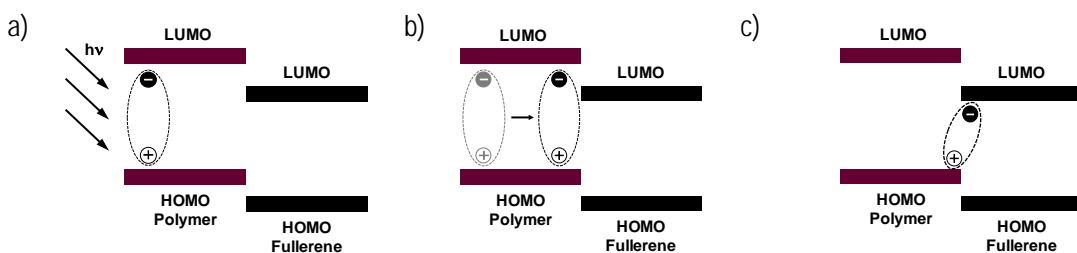


Figure 1.1 Conventional (a) and inverted (b) configurations of polymer solar cells

Unlike inorganic semiconductors, an electrically bound electron-hole pair (exciton) is formed in conjugated polymers upon photoexcitation. An electron accepting material with a band energy offset greater than the exciton binding energy is needed for efficient generation of mobile charges (see Section 1.1.3). Fullerenes enable ultrafast electron transfer from conjugated polymers and are generally used as the electron acceptor in PSCs.⁶⁴ Figure 1.2 illustrates the key steps in a full photovoltaic process in a PSC using an energy diagram. The highest occupied molecular orbitals (HOMOs) and lowest unoccupied molecular orbitals (LUMOs) are analogous to the valence band and conduction band, respectively, of an inorganic semiconductor (see Section 1.1.3). When a photon with an energy greater than the bandgap (i.e., the energy difference between the HOMO and LUMO) is absorbed by the polymer, an exciton is formed. Within its lifetime, the exciton may diffuse to the polymer/fullerene interface, where a charge transfer (CT) state is formed.⁶⁵ After that, the CT exciton dissociates into separate charges (i.e., an electron and a hole), which are transported through the polymer and fullerene, before being collected at the electrodes. The mechanism of charge dissociation after CT formation remains debated among researchers. Several pathways involving hot exciton formation and infrared (IR) absorption have been proposed.^{66–68} Alternatively, an exciton can be generated when the fullerene absorbs a photon. These excitons are separated at the polymer/fullerene interface driven by the energy difference of the HOMOs.



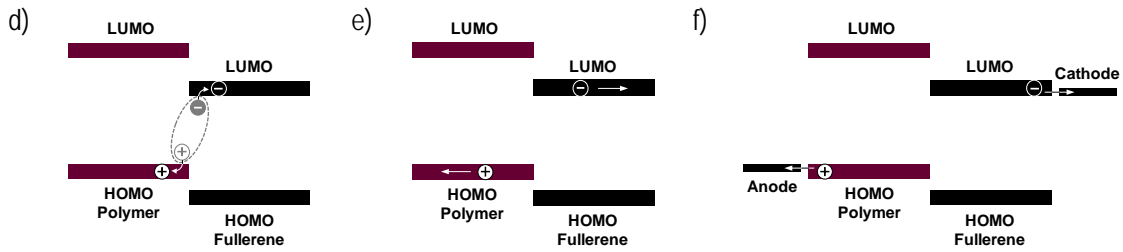


Figure 1.2 The photovoltaic process in a polymer solar cell: exciton generation (a); exciton diffusion (b); charge transfer (CT) state formation (c); charge separation (d); charge transportation (e); charge collection (f)

1.1.2. Device characterization

The key values obtained in a typical current-voltage (I-V) characterization are illustrated in Figure 1.3. A typical characterization of a photovoltaic device is called an I-V test. During the test, the device is placed under the illumination of a pre-calibrated solar simulator. A voltage sweep is applied to the solar cell device, and the current response is recorded. The current is converted to current density (J) (with respect to the device area (A)) and plotted against the applied voltage (V), yielding the well-known current density-voltage (J-V) curve. The device area is the area where all layers of the device overlap. If a mask is used, the aperture of the mask is used to define the device area. From the J-V curve, the point of maximum power density (P_{max}) is located where the product of $J \times V$ reaches a maximum, and the PCE can be calculated from:

$$PCE = \frac{P_{max}}{P_{in}} \quad (1.1)$$

where P_{max} is the maximum output power density and P_{in} is the power density of the incident light. The intercepts on the J-axis and V-axis are the short circuit current density (J_{sc}) and the open circuit voltage (V_{oc}), respectively. The fill factor (FF) is the ratio of P_{max} to the product of $J_{sc} \times V_{oc}$ (Equation 1.2a). Graphically, FF describes the “squareness” of the J-V curve.⁶⁹ The FF and PCE can be expressed as:

$$FF = \frac{P_{max}}{J_{sc} \cdot V_{oc}} \quad (1.2a)$$

$$PCE = \frac{J_{sc} \cdot V_{oc} \cdot FF}{P_{in} \cdot A} \quad (1.2b)$$

where I_{sc} is the short circuit current and A is the effective area of the solar cell. The ratio of I_{sc} to A is the short circuit current density (J_{sc}). In practice, a few tens to a few hundreds of samples of one particular device are usually fabricated and characterized for publications with an emphasis on reporting PCE breakthroughs.^{70–74} The deviations of PCE in these experiments are typically around 0.2%. However, experimental errors in PCE are subjected to the reliability of instruments; 15-25% deviation in PCE is not uncommon for a single batch of devices.

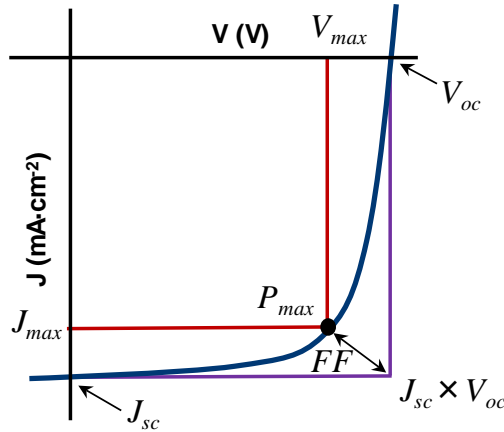


Figure 1.3 Current density–voltage (J-V) curve and key values extracted from a current–voltage (I-V) measurement. The black dot represents the point of maximum power density (P_{max}). J_{max} and V_{max} are the current density and applied voltage at P_{max} , respectively

Aside from I-V measurements, external quantum efficiency (EQE) measurements provide additional information about the device performance. The EQE is a dimensionless parameter that measures the number of electrons extracted at the electrode per incident photon. During an EQE test, the device is placed under a short circuit condition (i.e., zero applied voltage), and illuminated by monochromatic light across a certain wavelength range. The current response at each wavelength is recorded, and the EQE is calculated by:

$$EQE = \frac{1.24 \cdot I_{sc}}{\lambda \cdot P_{in}} \quad (1.3)$$

where I_{sc} is the short circuit current (mA), λ is the wavelength (nm), P_{in} is the power of the incident photon (W), and 1.24 is the product of the Planck constant and the speed of light

divided by the elementary charge (i.e., $h \cdot c/e$) including unit conversion factors.⁷⁵ Plotting the EQE against the wavelength generates an EQE curve.

1.1.3. Materials

Conjugated polymers

Polymers are linear macromolecules composed of many repeating units of the same chemical structure. Conjugated polymers have alternating single and double bonds along the backbone. The carbon atoms in a conjugated polymer adopt sp^2 hybridization. The remaining p orbitals form molecular π orbitals that are delocalized across the entire molecule. These π orbitals include bonding π orbitals that are filled with electrons in the ground state and anti-bonding π^* orbitals that are vacant at ground state. Figure 1.4 shows how energy levels develop as thiophene oligomers grow in length.⁷⁶ As more thiophene rings are added, the π orbitals are more hybridized. At infinity, the π orbitals form continuous energy states rather than discrete energy levels. The highest state formed by bonding π orbitals is called the HOMO, and the lowest state formed by anti-bonding π^* orbitals is called the LUMO. The gap between the two bands is called the bandgap (E_g).

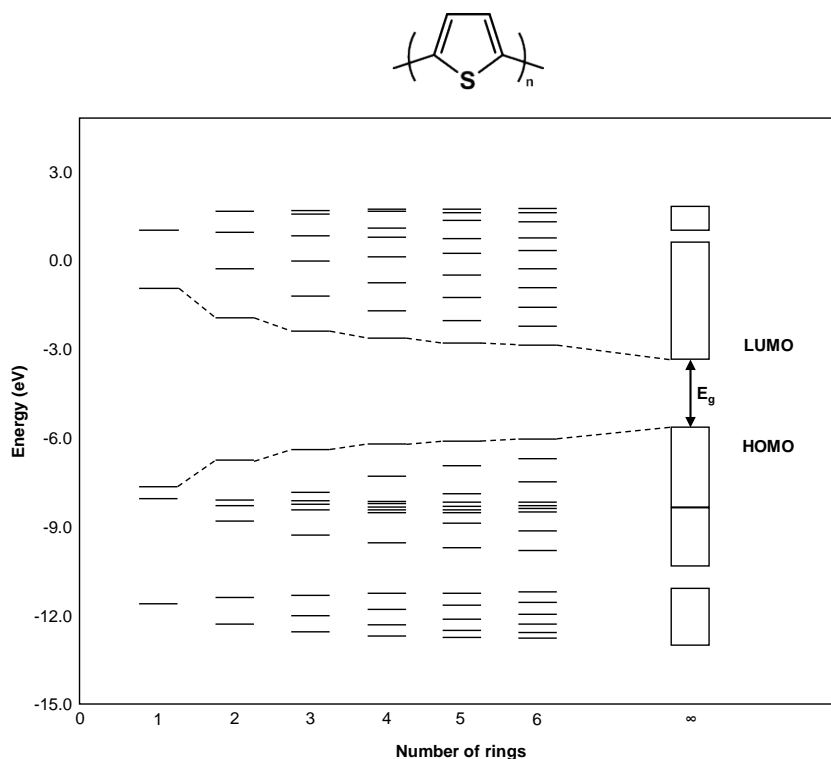


Figure 1.4 Development of the band structure from calculated energy levels of thiophene oligomers ($n = 1-6$), where E_g is the electron bandgap. The general chemical structure of polythiophene is depicted above. Adapted from ref. [77]

In general, when a photon with an energy greater than the bandgap of a semiconductor is absorbed, an electron-hole pair bonded by Coulomb attractions (i.e., an exciton) is generated. Organic semiconductors have weak intermolecular interactions and low dielectric constants, which result in tightly bonded electron-hole pairs. On the other hand, inorganic semiconductors exhibit much greater intermolecular interactions with much higher dielectric constants, producing weakly bonded electron-hole pairs upon excitation.^{78,79} This is illustrated by Figure 1.5, which compares the Coulomb wells of poly(3-hexylthiophene) (P3HT) and silicon. The high dielectric constant of silicon ($\epsilon = 11.7$) produces a narrow Coulomb well whose radius (r_C) at room temperature (i.e., $T = 300$ K) is smaller than the radius (r_B) of the exciton. Therefore, the thermal energy (i.e., $E = k_B T$, where k_B is the Boltzmann constant) at room temperature is enough to overcome the Coulomb attraction; hence, free charges are generated in silicon upon excitation. In contrast, r_C is much greater than r_B for P3HT at room temperature, which means that the thermal energy is less than the exciton binding energy. Hence, the electron-hole pair

remains bonded. The lifetime of a photogenerated exciton within a conjugated polymer is on the order of several hundreds of picoseconds.⁶⁵ Accordingly, the excitons have a diffusion length of ~ 10 nm.^{80–82} Therefore, unlike inorganic semiconductors, organic semiconductors need another material to form an interface with an energy difference to assist exciton dissociation.⁸³ Otherwise, photoexcitation will be compensated by charge recombination, rendering organic semiconductors useless for photovoltaic applications.

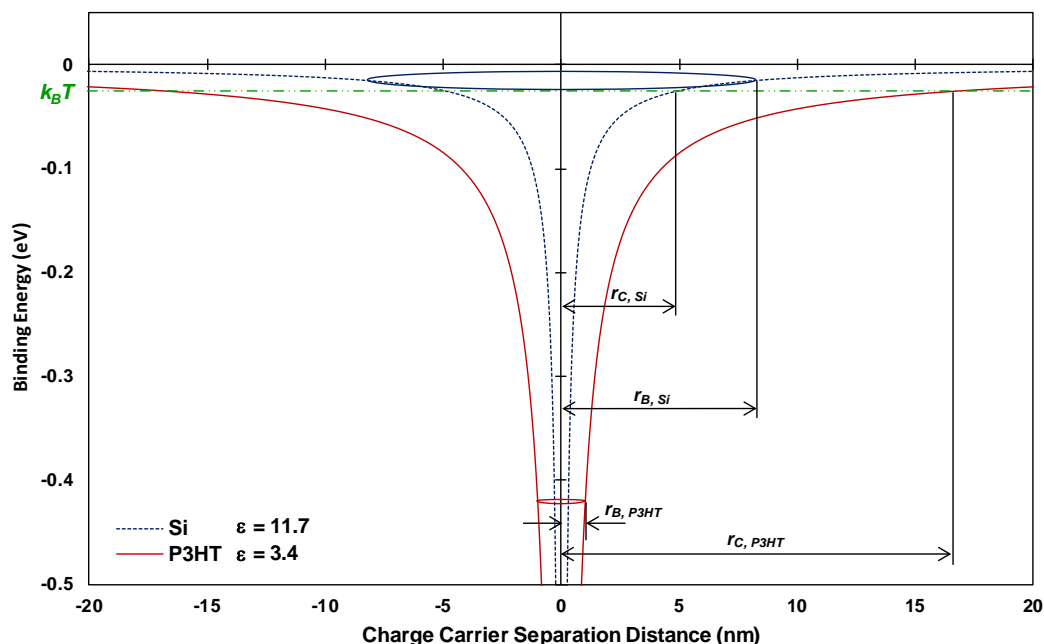


Figure 1.5 Schematic representation of the Coulomb wells and electron wavefunctions of an exciton generated in an inorganic semiconductor (Si) and an organic semiconductor (P3HT), with the positive charge carrier (i.e., hole) positioned at 0 nm. The ovals are schematic representations of the electron's wavefunction. r_C is the radius of the Coulomb well at room temperature ($T = 300$ K), r_B is the Bohr radius of the electron wavefunction, and $k_B T$ represents the thermal energy at room temperature ($T = 300$ K). The values of r_B and the dielectric constants (ϵ) were extracted from refs. [82], [84], and [85]

Conjugated polymers are efficient light absorbers. The absorption coefficients of most conjugated polymers at their absorption maxima are above 10^5 cm^{-1} ;^{86–89} thus, film thicknesses of a few hundred nanometers are adequate for light harvesting.⁹⁰ In comparison, intrinsic silicon has an absorption coefficient on the order of 10^2 – 10^4 cm^{-1} .⁹¹

Correspondingly, the thickness required for 90% absorption of photons with energies above the bandgap is 125 μm for silicon.⁹²

Furthermore, conjugated polymers are intrinsic semiconductors. Introducing charges by p-doping and n-doping with small redox species can enhance the conductivity of conjugated polymers,^{93,94} such as the widely used hole transporting material—poly(3,4-ethylenedioxythiophene) doped with poly(styrene-4-sulfonate) (PEDOT:PSS).⁹⁵ However, for most applications, conjugated polymers are used as synthesized. Most conjugated polymers used in photovoltaic applications preferably conduct holes; hence, they are conventionally called “p-type” polymers.^{96–99} However, this should not be confused with traditional p-type inorganic semiconductors because these polymers are not doped. In fact, it is possible for “p-type” polymers to conduct electrons or exhibit ambipolar conductivities under certain conditions (e.g., inert atmosphere, suitable electrodes).¹⁰⁰ Conduction in conjugated polymers mainly proceeds through a hopping mechanism, in which thermally activated charges hop from one localized state to another across highly disordered regions.¹⁰¹ Thanks to the rapid advancement of molecular design and processing techniques, conjugated polymers with carrier mobilities on the order of 10 $\text{cm}^2\cdot\text{V}^{-1}\cdot\text{s}^{-1}$ have been reported; this value is comparable to that of amorphous silicon.^{102–105} On a molecular scale, charges are conducted through overlapped π orbitals. High conductivity along the polymer backbone (intramolecular conductivity) and moderate conductivity through π – π stacking (intermolecular conductivity) have been observed in polymer crystallites.¹⁰⁶ In a recent model proposed by Noriega et al., charge conduction through the bulk is accomplished by two processes: 1) along single polymer chains that connect polymer crystallites through disordered regions; 2) through π – π stacking within polymer crystallites that serve as “transfer stations” because individual chains rarely extend across an entire device (Figure 1.6).¹⁰⁷ The latter is the rate-limiting process. This model successfully accounted for the high mobility observed in several new types of conjugated polymers that form interconnected short-range ordering distributed in a seemingly amorphous polymer matrix.^{108,109}

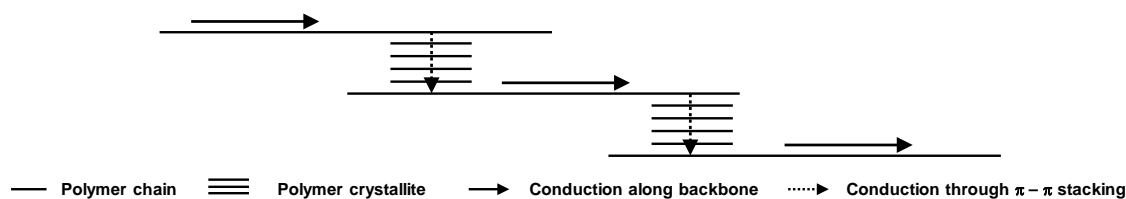


Figure 1.6 Schematic representation of charge transport through thin films of conjugated polymers. Charges travel along an individual polymer chain and transfer onto another chain at ordered regions (polymer crystallites). High conductivity is realized if there is a high population of ordered regions that are effectively connected by high-molecular-weight polymer chains. Adapted from ref. [107]

Fullerenes

Fullerenes are excellent electron acceptors. C_{60} and C_{70} can accept up to 6 electrons upon reduction.¹¹⁰ The high electron mobility of fullerenes enables fast electron transport.^{111–113} Additionally, fullerenes show absorption maxima in the UV region, which can promote exciton formation and contribute to photocurrent generation in PSCs.¹¹⁴ Fullerenes based on C_{60} and C_{70} with solubilizing sidechains have been synthesized for their applications in solution-processed PSCs (Figure 1.7). Phenyl- C_{61} -butyric acid methyl ester ($PC_{61}BM$) was the first of its kind reported and is one of the most widely used fullerenes.⁶¹ $PC_{71}BM$ is the C_{70} equivalent of $PC_{61}BM$.¹¹⁵ $PC_{71}BM$ is frequently paired with low-bandgap polymers to create high efficiency PSCs because of its broader and stronger absorption that encroaches into the visible region. Fullerenes with multiple substitutions show higher LUMO levels.¹¹⁶ Since V_{oc} is roughly the difference between the fullerene LUMO and the polymer HOMO, fullerene multiadducts provide a higher V_{oc} in PSCs.¹¹⁷ Bis- $PCBM$ increases the V_{oc} of the P3HT/ $PCBM$ device by 0.15 V, increasing the PCE by 20%.¹¹⁸ The indene- C_{60} bisadduct (ICBA), developed by He et al., can raise the V_{oc} of P3HT/ $PCBM$ devices by 0.25 V while maintaining the photocurrent, nearly doubling the PCE.^{119,120} Replacing fullerenes with polymer-based or small molecule-based acceptors remains an active topic in the research field because of their high cost and limited modification pathways. Recently, this direction has started to increase in popularity.^{121–125}

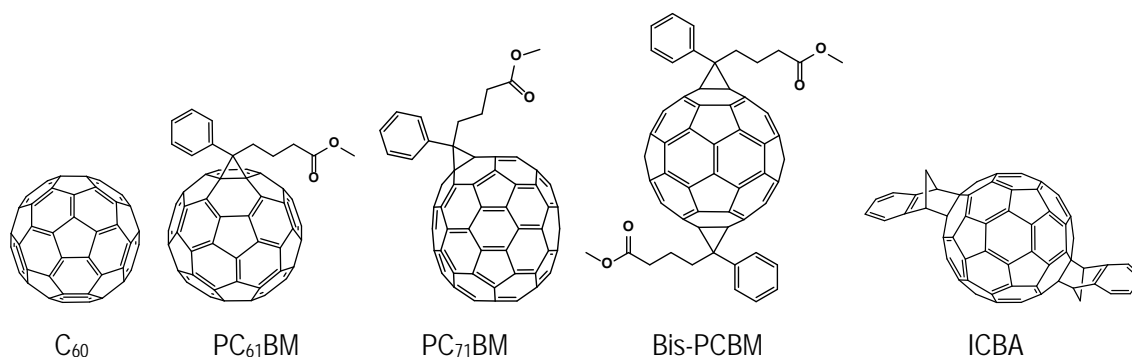


Figure 1.7 Chemical structures of various fullerenes

Buffer layer and electrode materials

A buffer layer ensures an ohmic contact between the active layer materials and the electrode at their interface with a selective conductivity of one of the carriers. Additionally, buffer layers modify surface properties at the active layer/electrode interfaces, prevent diffusion of metal ions, and serve as optical spacers such that the optical field is strongest in the active layer.¹²⁶ Poly(3,4-ethylenedioxythiophene):poly(styrene sulfonic acid) (PEDOT:PSS) is the by far the most frequently applied HTL in conventional devices. PEDOT is an insoluble, semiconductive polymer. PSS serves as a polyelectrolyte during the oxidative polymerization of EDOT, and remains as a counter ion to the positively doped PEDOT in the product (Figure 1.8).⁹⁵ This ionic polymer blend is water-soluble and resistive to common organic solvents, which enables direct solution deposition of polymer/fullerene solutions. PEDOT:PSS generally shows a conductivity of 1~10 S·cm⁻¹ and has a good thermal stability.^{95,127} The conductivity of PEDOT:PSS can be further increased to > 1000 S·cm⁻¹ via solvent treatment, making it possible to fabricate TCO-free devices.¹²⁸ Other than the hole transporting function, a thin layer of PEDOT:PSS also reduces the roughness of the TCO/active layer interface, which improves the FF of the device.¹²⁹ In addition, the organic nature of PEDOT:PSS improves the surface wettability of organic solvents as compared to TCO alone, facilitating active layer casting and preventing delamination of the layers.¹³⁰

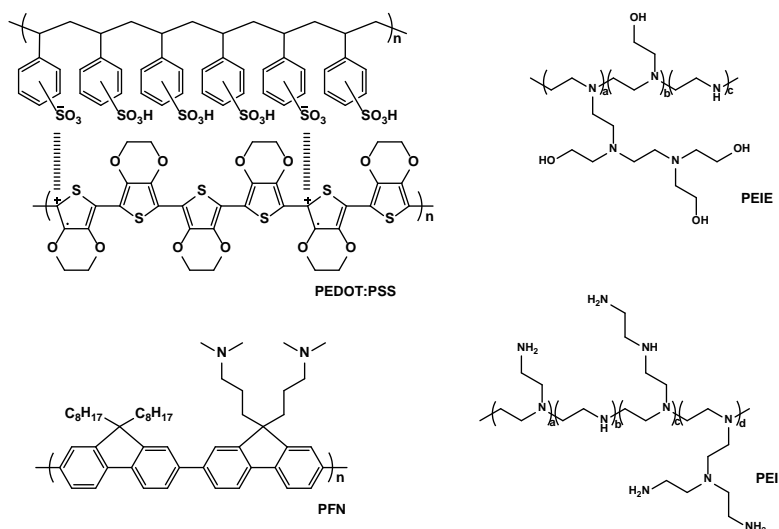


Figure 1.8 Chemical structures of PEDOT:PSS, polyethylenimine (PEI), polyethylenimine ethoxylated (PEIE), and poly [(9,9-bis(3-(N, N-dimethylamino)propyl)-2,7-fluorene)-alt-2,7-(9,9-dioctylfluorene)] (PFN)

Transition metal oxides with a wide range of work functions (W_f), good stabilities, and wide bandgaps are widely used as buffer layers in PSCs.¹³¹ ZnO has a W_f that closely matches the LUMO of PCBM and is transparent in the visible region.¹³² As a result, ZnO is commonly inserted between the active layer and the TCO, serving as the ETL. ZnO is mainly deposited onto TCO as spin-coated nanoparticles or through a sol-gel process.^{132,133} Metal oxides with high W_f , such as MoO₃ and WO₃, have been used as the HTLs in inverted devices.^{134–136} They are usually thermally evaporated before evaporating the metal electrode.

Lithium fluoride (LiF) used to be a common ETL in the early development of PSCs.¹³⁷ Adding a thin layer of LiF improves the performance of the solar cell and the device stability.^{138,139} The improvement is believed to be caused by the introduction of molecular dipole moments at the active layer/metal electrode interface that facilitates charge extraction.⁶³ Based on similar dipole effects, thin polymer electron transport layers have been reported (Figure 1.8). Branched polyethylenimine (PEI) and polyethylenimine ethoxylated (PEIE) can effectively lower the W_f of TCOs, enabling efficient electron extractions.^{72,140} Thin layer poly [(9,9-bis(3-(N, N-dimethylamino)propyl)-2,7-fluorene)-alt-2,7-(9,9-dioctylfluorene)] (PFN), a derivative of polyfluorene, also uses tertiary amine

to impart dipole moments.⁷⁰ It has been employed as an effective ETL in devices with record-high PCEs.^{36,71}

In a conventional configuration, low W_f metals, such as Ca and Al, are usually deposited as the top electrode for efficient electron extraction, because the metals' work function is pinned at the work function of PCBM, forming an Ohmic contact.¹⁴¹ However, using inverted structures allows the use of high W_f metals like Ag and Au, which improves device stability.^{142,143} TCOs are heavily doped metal oxides that are highly conductive and transparent. Indium tin oxide (ITO) is the most commonly used TCO.^{144,145} Fluorine-doped tin oxide (FTO) without the expensive element of indium is also used.¹⁴⁶ However, TCO thin films are naturally brittle and not suitable for flexible substrates. In roll-to-roll production of flexible PSCs the transparent electrode is made of screen printed silver nanoparticles, which allow passage of 80% of visible light.²⁵

1.2. Design and Synthesis of Conjugated Polymers

1.2.1. Traditional polymers

In the early stage of polymer solar cell research, two types of conjugated polymers with simple chemical structures predominated the field: poly(alkoxy-phenylenevinylene) and poly(3-alkylthiophene). Poly([2-methoxy-5-(3,7-dimethyloctyloxy)]-1,4-phenylenevinylene) (MDMO-PPV) and poly(3-hexylthiophene) were among the most studied derivatives of the two, respectively (Figure 1.9). The bulky sidechains introduced to the PPV backbone imparted high solubility and good processability. Shaheen et al. first reported bulk heterojunction solar cells made from solutions of MDMO-PPV and PC₆₁BM, which achieved 2.5% PCE.¹⁴⁷ Later, the efficiency was improved to 3.0% using PC₇₁BM, which can absorb more light.¹¹⁵ However, morphological control of MDMO-PPV/PCBM polymers has been difficult since its first report, and has remained an issue for this polymer throughout its development.¹⁴⁸

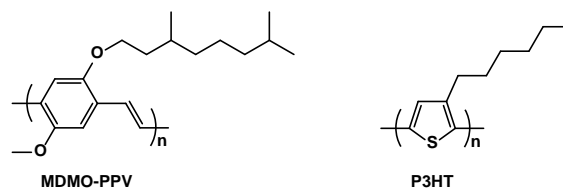


Figure 1.9 Chemical structures of MDMO-PPV and P3HT

Research interests quickly shifted to P3HT/PCBM solar cells, due to the many superior features of P3HT. Unsubstituted polythiophenes have excellent electrical and optical properties; however, they are not soluble.¹⁴⁹ Adding only one alkyl sidechain at the 3-position of the thiophene ring sufficiently improves the solubility of polythiophenes without undermining their conjugation.¹⁵⁰ Three different couplings, namely head-to-tail, head-to-head, and tail-to-tail, can occur during the polymerization of 3-hexylthiophene based on the asymmetry of its chemical structure (Figure 1.10). However, McCullough and coworkers developed a facile Grignard metathesis to obtain P3HT with > 99% head-to-tail regioregularity and a high molecular weight.¹⁵¹ Unlike MDMO-PPV, regioregular P3HT (RR-P3HT) shows a strong tendency to crystalize into lamellar stacks in the solid state.¹⁰⁶ The charge carrier mobility of P3HT ranges from 0.1 to 0.3 $\text{cm}^2 \cdot \text{V}^{-1} \cdot \text{s}^{-1}$, and it is dependant on the degree of regioregularity.^{152–154} The PCE of P3HT/PCBM solar cell devices could reach as high as 5% after post-deposition thermal annealing (see Section 1.3).^{155,156} Moreover, P3HT is more stable against photooxidation than MDMO-PPV (See degradation).¹⁵⁷ To date, P3HT remains the benchmark for solar cells based on conjugated polymers and fullerenes.^{158,159} However, the performance of P3HT/PCBM devices is limited because of the high bandgap and high HOMO level of P3HT.¹⁶⁰ Recent studies have used fullerene derivatives with lower electron affinities (e.g., ICBA) than PCBM for P3HT, which increased the V_{oc} value and provided a PCE of 6.5%.¹²⁰

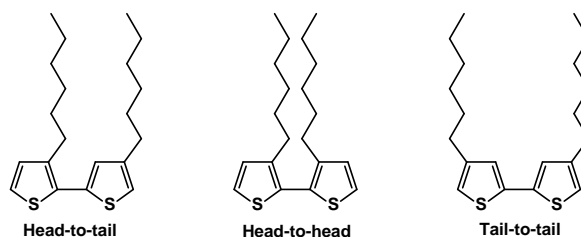


Figure 1.10 Three different isomers of a 3-hexylthiophene dimer

1.2.2. Strategies for reduction of the bandgap

The photocurrent produced by a solar cell is directly proportional to the number of absorbed photons.¹⁶¹ The highest photon flux occurs at ~700 nm of the AM 1.5G solar spectrum.¹⁶² Therefore, it is rational to design conjugated polymers with absorptions that extend into the near-infrared region. The bandgap of a polymer can be lowered using two strategies: stabilizing the quinoid structure and using an alternating donor-acceptor structure on the mainchain.

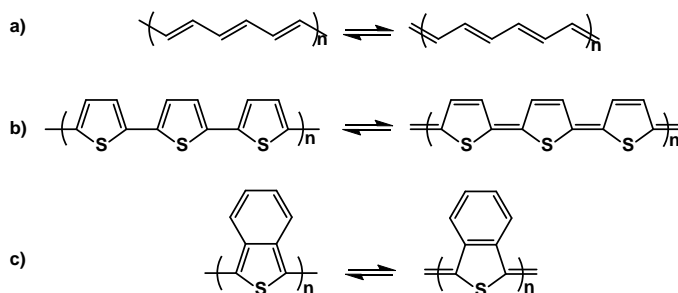


Figure 1.11 Resonance structures of polyacetylene (a), polythiophene (b), and poly(isothianaphthene) (c)

In the ground state, polyacetylene has two alternating resonance structures of the same energy (Figure 1.11).^{163,164} In contrast, the ground state of a conjugated polymer consisting of aromatic rings is not degenerate. The quinoid form has a higher energy and a smaller bandgap because of the decreased bond length alternation that is restricted by the aromatic rings.¹⁶⁵ Stabilizing the quinoid form can increase the contribution of the quinoid form at the ground state of the polymer and hence reduce the bandgap. Using a fused ring system is an effective method of securing the quinoid structure. For example, the tendency of the fused benzene ring to remain aromatic stabilizes the quinoid form of poly(isothianaphthene) (PITN) (Figure 1.6). Consequently, the bandgap of PITN is ~1 eV, which is approximately half the bandgap of polythiophene (2 eV).¹⁶⁶

Another way to lower the bandgap involves incorporating alternating electron donating units (donor) and electron withdrawing units (acceptor) on the polymer mainchain (D-A polymer). The hybridization of the energy levels of the donor and acceptor simultaneously increase the HOMO level and decrease the LUMO level (Figure 1.12a).¹⁶⁷ The bandgap of the D-A polymer is lower than those of the donor and acceptor homogeneous polymers, as demonstrated for poly[2-(thiophene-2-yl)pyridine] (PTP).¹⁶⁸

When a photon is absorbed by a D-A polymer, an intramolecular excitation is induced, where the positive charge resides at the donor unit while the negative charge resides at the acceptor unit (Figure 1.12b).¹⁶⁸ The different electron affinities of the alternating units help to stabilize the exciton.

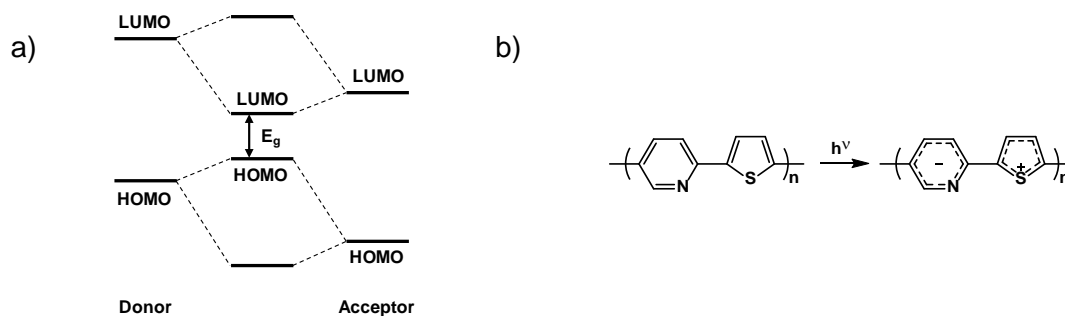
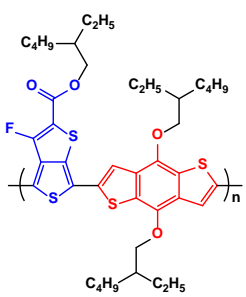
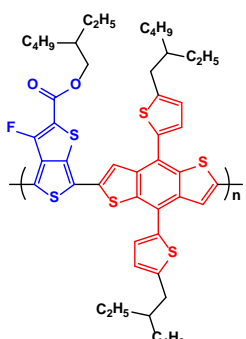
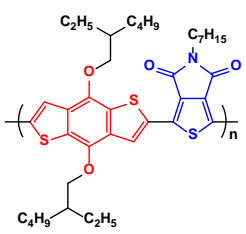
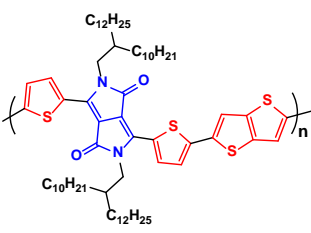
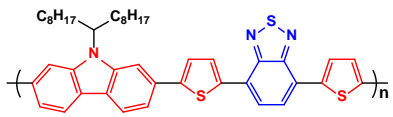
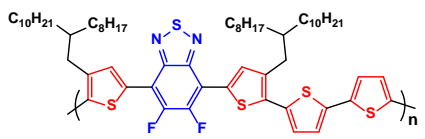
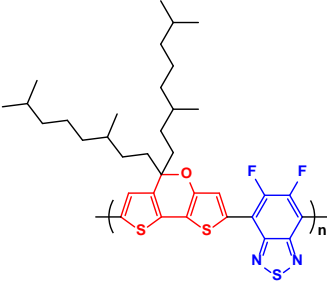


Figure 1.12 The hybridization of energy levels of a donor-acceptor polymer (a) and the intramolecular photoexcitation of poly[2-(thiophene-2-yl)pyridine] (b)

The abundant choices of donor and acceptor building blocks enable researchers to rationally design conjugated polymers for high-efficiency photovoltaic devices.^{169,170} The building blocks can be chemically modified (e.g., by adding different sidechains and heteroatom substituents) to finely tune the energy levels, solubility, and morphology of the polymer.^{171,172} The polymers with high molecular weights can be easily synthesized from two monomers through Stille or Suzuki polycondensation.¹⁷³ Table 1.1 lists several modern D-A polymers that have provided high device performances. The donor units are red, and the acceptor units are blue. Among them are some popular donor blocks, such as benzodithiophene (BDT, Entry 1, 2, 3), and thiophene (T, Entry 4, 5, 6), and several popular acceptor blocks, such as thienothiophene (TT, Entry 1, 2), benzothiadiazole (BT, Entry 5, 6, 7), and diketopyrrolopyrrole (DPP, Entry 4).

Table 1.1 Donor-acceptor polymers with high photo conversion efficiencies

Entry	Polymer Structure ^a	Name	E _g (eV) ^b	PCE ^c
1		PTB7	1.8 ¹⁷⁴	9.2% ⁷¹
2		PTB7-Th	1.6 ¹⁷⁵	10.6% ³⁶
3		PBDTTPD	1.7 ¹⁷⁶	8.5% ¹⁷⁷
4		DT-PDPP2T-TT	1.4 ¹⁷⁸	9.0% ¹⁷⁹
5		PCDTBT	1.9 ¹⁸⁰	7.9% ¹⁸¹
6		PffBT4T-2OD	1.7 ⁸⁹	10.8% ⁸⁹

Entry	Polymer Structure ^a	Name	E _g (eV) ^b	PCE ^c
7		PDTP-DFBT	1.6 ¹⁸²	8.0% ¹⁸²

^a Donor units and acceptor units are colored in red and blue, respectively;

^b Electrochemical bandgap;

^c Obtained with optimized solar cell devices.

1.2.3. Effects of substituents attached to the polymer backbone

Substituents attached to the polymer backbone are of paramount importance in conjugated polymers. Flexible alkyl sidechains are indispensable for solution processability, while electron donating and withdrawing functional groups are useful tools for fine tuning energy levels. Since V_{oc} is essentially the difference between the fullerene LUMO level and the polymer HOMO level, lowering the HOMO level of the conjugated polymers can increase the V_{oc} , which improves the PCE.¹¹⁷ The minimum difference between the LUMO levels of the conjugated polymer and fullerene is 0.3 eV for efficient exciton dissociation.^{117,183} Therefore, lowering the HOMO level of the polymer while maintaining at least a 0.3 eV LUMO difference is a sound strategy to boost the PCE beyond bandgap engineering. Indeed, attaching an electron withdrawing substituent can lower the HOMO level, while an electron donating substituent can raise it.¹⁸⁴ This is best exemplified by the PTB series polymers (Table 1.1 Entry 1). Poly(thieno[3,4-b]thiophene-benzo[1,2-b:4,5-b']dithiophene) (PTB) is a series of D-A polymers developed by Yu and coworkers.¹⁸⁵ The design concept is that the three fused rings of the BDT donor unit would provide certain degrees of π - π stacking, which ensures good hole mobility, and two positions for alkyl sidechain attachment, which provide high solubility. Meanwhile, the fused thiophenes on the TT acceptor unit stabilize the quinoid structure.¹⁸⁶ PTB polymers have optical bandgaps of ~1.6 eV and absorption maxima at 600–700 nm.¹⁸⁷ When paired with PC₇₁BM, the absorption of the blended film almost covers the entire UV to near infrared region. The most successful derivative, PTB7, once held the world record for PCE of polymer solar cells (9.2%).⁷¹ Further modification by adding two thiophene rings on the

sidechains of the BDT unit (PTB7-Th, Table 1.1 Entry 2) incorporated the π electrons from the sidechain-thiophenes to the conjugation of the mainchain, further lowering the bandgap and providing an even higher PCE > 10%.³⁶

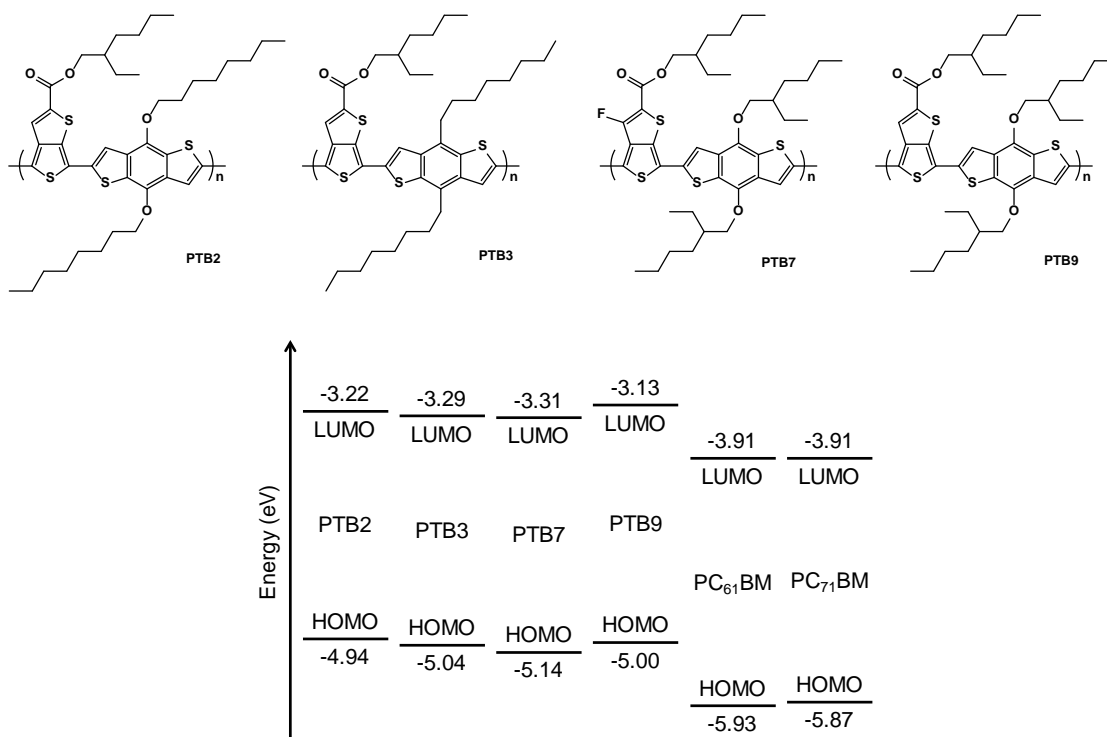


Figure 1.13 The chemical structures of PTB2, PTB3, PTB7, and PTB9 (top); the energy levels of PTB2, PTB3, PTB7, PTB9, PC₆₁BM, and PC₇₁BM (bottom). Data extracted from ref. [188], [174], [189], and [190]

Systematic studies of polymers based on the PTB backbone have revealed how substituents may influence the opto-electrical properties of the polymers.^{185,191,192} Figure 1.13 shows four PTB polymers and their respective energy levels. PTB2 and PTB3 differ only by the sidechains on the BDT unit. The less electron donating alkyl sidechains on PTB3 lower the polymer energy levels compared to PTB2, which has alkoxy side chains instead.¹⁸⁸ Consequently, the PTB3:PC₆₁BM device shows a V_{oc} that is ~1 eV higher than that of the PTB2:PC₆₁BM device (Table 1.2). Similarly, the energy levels of PTB7 are ~1.5 eV lower than those of PTB9, which is attributed to the electron withdrawal effect of the fluorine atom on the TT unit.^{174,189} Solar cell devices based on PTB7:PC₇₁BM, and PTB9:PC₇₁BM exhibit similar J_{sc} and FF values (Table 1.2). The vast difference in PCE (7.4% vs. 5.7%) is a direct result of the increased V_{oc} of the PTB7:PC₇₁BM device.

Table 1.2 Photovoltaic parameters of polymer solar cells made from PTB2, PTB3, PTB7, and PTB9

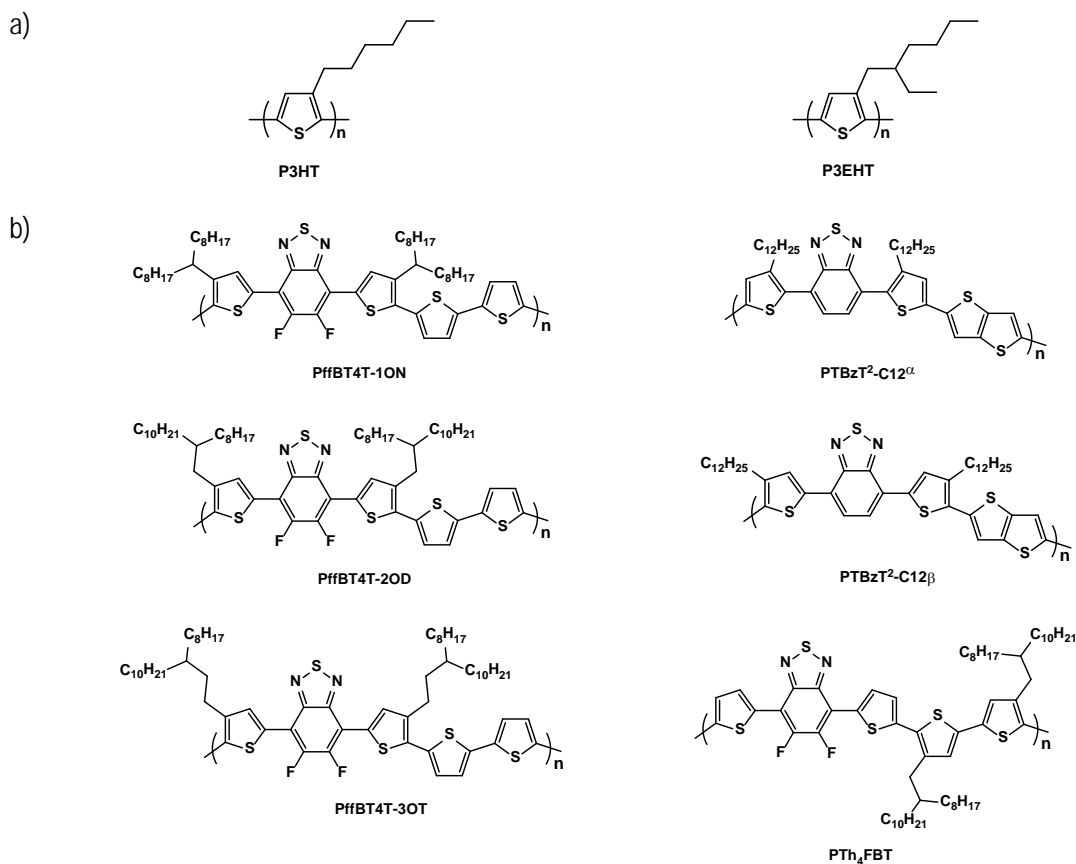
	V_{oc} (V)	J_{sc} (mA·cm ⁻²)	FF	PCE (%)
PTB2:PC ₆₁ BM	0.60	12.8	0.66	5.1
PTB3:PC ₆₁ BM	0.74	13.1	0.57	5.5
PTB7:PC ₇₁ BM	0.74	14.5	0.69	7.4
PTB9:PC ₇₁ BM	0.60	14.3	0.66	5.7

The position, quantity, and chemical structure of the alkyl sidechain significantly influence the solubility and intermolecular interactions of the conjugated polymer. As previously mentioned, two alkyl sidechains on polythiophene disrupt the conjugation, while unsubstituted polythiophenes are not soluble.¹⁴⁹ In general, polymers with branched sidechains are more soluble in solution but form weaker π - π stacking in the solid state, compared to those with linear sidechains.¹⁹³ A recent study revealed that poly[3-(2-ethylhexyl)thiophene] (P3EHT, Figure 1.14a) exhibits longer π - π stacking distances and lower degrees of aggregation than P3HT.¹⁹⁴ As a result, P3EHT has an optical bandgap that is ~0.1 eV wider than that of P3HT. A similar trend is observed for PTB polymers.¹⁹¹ PTB polymers with linear sidechains on the BDT unit exhibit closer π - π stackings than those with branched sidechains.

The fine balance of solubility and polymer aggregation is best demonstrated by poly(difluorobenzothiadiazole-quarterthiophene) (PffBT4T, Figure 1.14b). Liu et al. studied three derivatives of this polymer with sidechain branching points on the first, second, and third carbon from the attaching thiophene ring.⁸⁹ The PffBT4T with a 1-octylnonyl sidechain whose branching point is on the first carbon from the polymer backbone (PffBT4T-1ON) exhibited poor aggregation and crystallinity, which caused a low PCE. In contrast, PffBT4T-3OT (with the octyl chain branching from the third carbon of the tridecyl sidechain) showed a strong aggregation and the polymer solution formed a gel before spin coating; thus, the polymer was no longer solution processable. PffBT4T-2OD lies in the “sweet point” between solubility and molecular aggregation, and thus exhibited the best performance among the three polymers.

Furthermore, the attaching point of the sidechains also plays a key role in the final performance of the polymer. Prior to the development of PffBT4T-2OD, Jheng et al.

reported a similar polymer isomeric to PffBT4T-2OD.¹⁹⁵ Instead of having sidechains on the two thiophene rings next to the benzothiadiazole, the sidechains were attached to the middle two thiophene rings (PTh₄FBT, Figure 1.14b). The resulting polymer failed to show strong aggregation, and performed poorly in solar cell devices. A possible reason is that the middle two thiophenes determine the solid-state ordering of the polymer and should be left unsubstituted. In addition, Biniek et al. studied a series of polymers with similar structures and found that placing the sidechains on the α position of the thiophenes next to the benzothiadiazole induced a strong twist on the polymer backbone (PTBzT²-C12 α , Figure 1.14b).¹⁹⁶ Consequently PTBzT²-C12 α has a significantly higher (0.32 eV) bandgap than PTBzT²-C12 β .



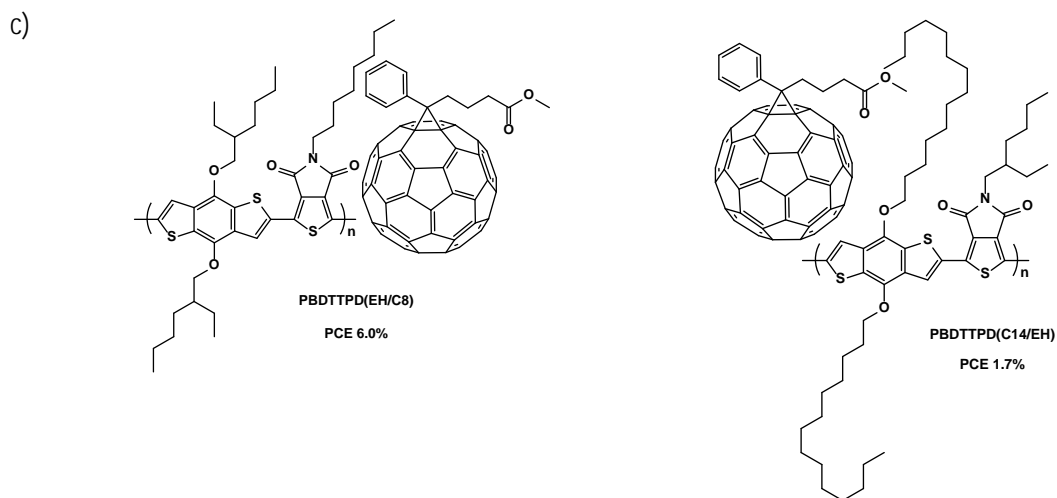


Figure 1.14 The chemical structures of P3HT and P3EHT (a); PffBT4T-1ON, PffBT4T-2OD, PffBT4T-3OT, PTBzT²-C12 α , PTBzT²-C12 β , and PTh₄FBT (b). Schematic representation of the docking of PC₆₁BM with PBDTTPD(EH/C8), and PBDTTPD(C14/EH) (c). Redrawn from refs. [194], [89], [196], [195], and [197]

Finally, the sidechain pattern of the conjugated polymer impacts the polymer:PCBM interaction. Graham et al. recently discovered that the polymer:PCBM interaction of PBDTTPD-type polymers is sterically controlled.¹⁹⁷ PCBM tend to rest near the donor or acceptor unit that has linear sidechains (Figure 1.14 c). However, electron transfer between the polymer and the PCBM is more efficient when PCBM docks at the acceptor unit (TPD) because the negative charge (i.e., electron) is localized at the acceptor unit of a D-A polymer (Section 1.2.2). As a result, devices using PBDTTPD having 2-ethylhexyl sidechains on the BDT units and n-octyl sidechains on the TPD units PBDTTPD(EH/C8) exhibited a PCE of 6.0%, while those made from PBDTTPD having n-tetradecyl sidechains on the BDT units and 2-ethylhexyl sidechains on the TPD units PBDTTPD(C14/EH) only exhibited a PCE of 1.7%. Examining various reports of 14 other D-A polymers, the authors confirmed that the PCBM docking mechanism is generally applicable to polymers consisting of alternating donor and acceptor backbones.

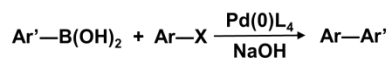
1.2.4. Synthesis of conjugated polymers

The synthesis of conjugated polymers relies on C-C bond formation between sp² carbons. In chemistry, this is realized by transition-metal-catalyzed cross-coupling

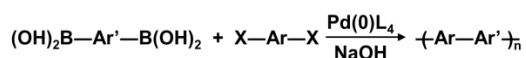
reactions.¹⁹⁸ Such cross-couplings occur between an aryl-halide species and another functionalized organic species. Depending on the functionality of the other species, these cross-coupling reactions are classified by the names of their developers as Heck reactions (alkene),¹⁹⁹ Kumada coupling (Grignard reagent),²⁰⁰ Negishi coupling (organozinc),²⁰¹ Stille coupling (organostannane),²⁰² Sonogashira coupling (alkyne),²⁰³ and Suzuki coupling (organoboron),²⁰⁴ etc. The 2010 Nobel Prize in Chemistry was awarded to Richard F. Heck, Ei-ichi Negishi, and Akira Suzuki for their contributions to palladium-catalyzed cross-coupling reactions in organic synthesis.^{205,206} For modern D-A-type polymers, the donor units and acceptor units are bi-functionalized into coupling partners. Cross-coupling of equal amounts of the two monomers leads to the formation of a donor-acceptor alternating polymer, and the process is called polycondensation. Among those cross-coupling reactions, Suzuki and Stille reactions are the most common in synthesizing conjugated polymers for OPV applications, probably because of the high functional group tolerance of the reactions, as well as the ease in preparing the organoboron and organostannane species.

Although Suzuki coupling ranks highest among all cross-coupling reactions in the number of research papers and patents published, it has found limited use in synthesizing conjugated polymers for high-performance polymer solar cells.¹⁹⁸ Instead, Stille coupling is the most widely used synthetic method in this field. Six out of the seven high performance polymers listed in Table 1.1 were synthesized by Stille polycondensation (entries 1, 2, 3, 4, 6, and 7), while the remaining PCDTBT (entry 5) was synthesized via Suzuki polycondensation. This is because of the high content of thiophene or thiophene derivatives in the backbones of modern D-A polymers. Thiophenylboronic acid and thiophenylboronic esters are unstable during Suzuki coupling.^{207,208} In addition, boronic ester/acid functionalized complex thiophene derivatives are more difficult to synthesize and purify than the organostannane versions.^{209,210}

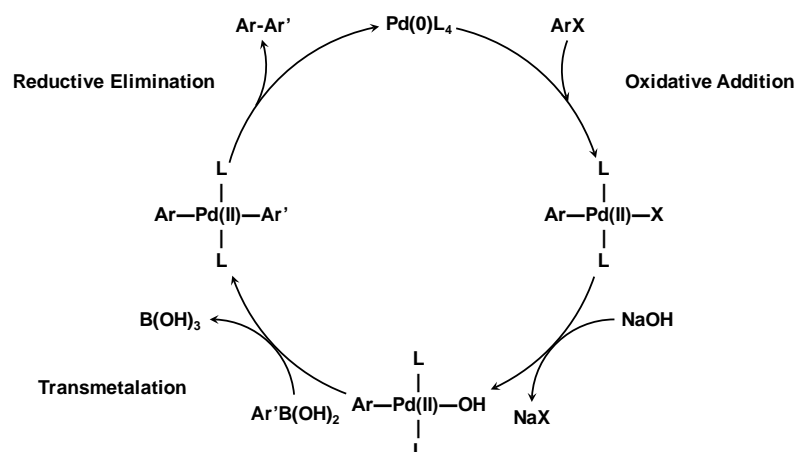
a)



b)



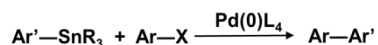
c)



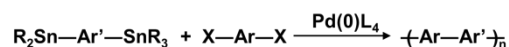
Scheme 1.1 Suzuki coupling (a), Suzuki polycondensation (b), and the catalytic cycle of Suzuki coupling (c)

Suzuki coupling, developed by Suzuki and Miyaura in the late 1970s, is a palladium-catalyzed cross-coupling between an arylhalide and an arylboronic acid/ester in the presence of a base.²¹¹ The general chemical equations of Suzuki coupling and Suzuki polycondensation are shown in Scheme 1.1. The catalytic cycle of the reaction includes oxidative addition, transmetalation, and reductive elimination (Scheme 1.1); transmetalation is the rate-determining step.²⁰⁴ It is unique for Suzuki coupling to have an additional step in the usual three-step catalytic cycle of a transition-metal-catalyzed cross-coupling. A base is required to convert the product of the oxidative addition step into reactive [ArPd(II)OH(L₂)] species for transmetalation with the organoboron species.²¹² The boronic acid species have been gradually phased out in favor of boronic esters because of their susceptibility to deboronation during the reaction and the inevitable trace water content.^{207,213} Bulky boronic esters, such as pinacol boronic esters, are more stable than boronic acids; thus, monomers bearing boronic esters are almost exclusively used to for Suzuki polycondensations.^{208,214,215}

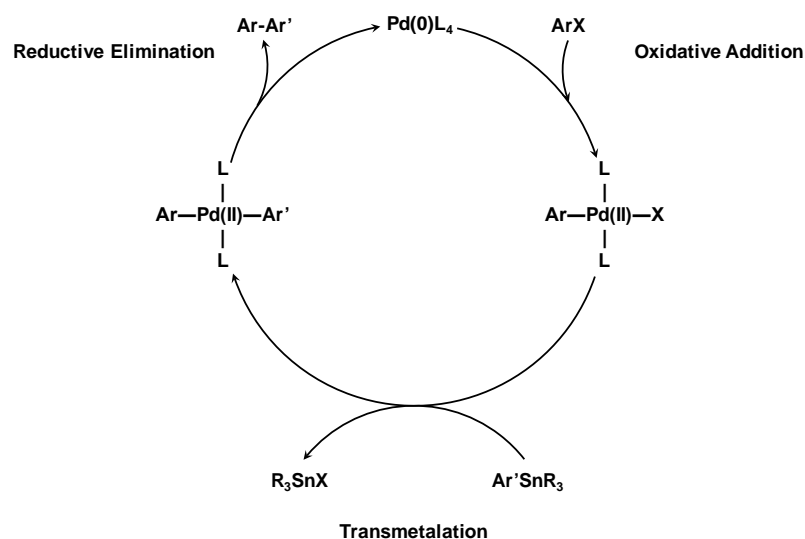
a)



b)



c)



Scheme 1.2 Stille coupling (a), Stille polycondensation (b), and the catalytic cycle of the Stille coupling (c)

The cross-coupling reactions between an aryl or vinyl halide and an organostannane species were explored by John K. Stille and others in the 1970s and 1980s, which later became known as Stille couplings.^{202,216–218} Stille coupling remains one of the most useful palladium-catalyzed cross-couplings.¹⁹⁸ Had Dr. Stille's life not been cut short by a tragic accident, he could have been nominated for the 2010 Nobel Prize in Chemistry.²¹⁹ The catalytic cycle of Stille coupling consists of three steps: oxidative addition, transmetalation, and reductive elimination (Scheme 1.2). The transmetalation is the rate-determining step.²⁰² Tetrakis(triphenylphosphine)-palladium(0) ($\text{Pd}(\text{PPh}_3)_4$) is the most widely used catalyst for Stille couplings, although more stable ligands, such as triphenylarsine (AsPh_3) and tri(*o*-tolyl)phosphine ($\text{P}(\text{o-tol})_3$), have been explored.^{220,221} *N,N*-dimethylformamide (DMF) accelerates the reaction by stabilizing the catalyst, but polymers dissolve poorly in DMF.²²² Therefore, a solvent mixture of DMF and toluene was developed for Stille polycondensation.²²⁰

The biggest disadvantage of Stille coupling is the toxicity of the organostannanes. The most common organostannanes used in Stille couplings are trimethyltin chloride and tributyltin chloride. Trimethyltin chloride is a neurotoxin that negatively affects specific sub-regions of the brain and spinal cord,²²³ while tributyltin chloride induces apoptosis in human T-cells.²²⁴ Some studies show that organostannanes disrupt oxidative

phosphorylation in mitochondria.²²⁵ While organostannanes have not been proven to be carcinogenic, there are studies showing that organotin compounds can significantly reduce lytic functions of human natural killer cells, and thus, promote cancer development and viral infections.²²⁶ Although trimethyltin is more toxic than tributyltin, trimethyltin is fairly water soluble and can be removed in the extraction step.²²⁷ Using trimethyltin also simplifies the purification process of the organostannane monomer because of the ease of recrystallization compared to its tributyltin counterparts.²²⁸ However, when column chromatography is required for monomer purification, tributyltin is preferred because of its higher stability in silica columns.¹⁸²

1.3. Morphologies of the Active Layer

The active layer is the core of polymer solar cells—it is where photons are absorbed and electrical charges are generated. Generally, three types of morphologies have been used for the active layer of polymer solar cells: bilayer, bulk heterojunction (BHJ), and ordered BHJ (Figure 1.15).



Figure 1.15 Three types of morphologies of the active layer used in polymer solar cells: (a) bilayer, (b) bulk heterojunction (BHJ), and (c) ordered BHJ

In a bilayer device, photogenerated excitons can only dissociate at the interface of the two layers. Excitons formed in the bulk of the polymer or C₆₀ layers cannot diffuse to the interface within their lifetime. Thus, a high percentage of photoexcitation is wasted, and the bilayer devices are not efficient.⁵⁹ A bulk heterojunction is formed during fast drying of the common solution of the polymer and the fullerene.⁶² The bulk heterojunction is essentially a “solid mixture” of the two components. The polymer and fullerene form an interpenetrating network that significantly increases their interfacial area, facilitating exciton dissociation. However, the morphology of the bulk heterojunction relies on the self-organization of the polymer and fullerene and can only be controlled by the component ratio, concentration, and choice of solvent before casting.^{159,229–233} Ideally, an ordered BHJ

should maximize the exciton dissociation and charge transportation. In an ordered BHJ, the polymer and fullerene form interdigitating pillars with widths on the scale of the exciton diffusion length and perpendicular to the electrodes. The fabrication of ordered BHJ is mainly realized by patterning the conjugated polymers.²³⁴ However, this process is highly complicated and time consuming, and it has not achieved a significantly higher efficiency than that of ordinary solution-processed bulk heterojunction devices.^{235,236}

Solution processed bulk heterojunctions are still the most commonly adopted active layer morphologies in modern polymer solar cells.²³⁷ Studies of the BHJ morphology revealed that highly efficient polymer solar cells have domain sizes of approximately 10~20 nm, which is similar to the exciton diffusion length.^{232,238,239} Efficient charge generation and charge transportation are desired to maximize cell efficiency. For semi-crystalline conjugated polymers, such as regioregular P3HT, thermal annealing has been proven as an effective way to improve morphology and provide a higher efficiency.^{156,238} Heating the devices at an elevated temperature enhances P3HT crystallization, which is beneficial for charge generation (because it increases the conjugation) and charge transportation (because it improves the connectivity of respective domains).^{238,240} The driving force for thermal annealing is the crystallization of P3HT, the process of which will keep expelling PCBM into the intermixed P3HT-PCBM amorphous region.²⁴¹ Therefore, there is an optimal temperature for thermal annealing (e.g., 170 °C), after which the annealing will trigger PCBM crystallization, which rapidly degrades the solar cell performance.²⁴²

When it comes to high-performance D-A-type polymers, thermal annealing generally degrades the performance of solar cell devices rather than improving it.^{243–246} The reason is that thermal annealing causes unfavorable PCBM aggregation, which leads to the loss of PCBM percolation within the film.²⁴⁵ However, high boiling-point solvent additives can be used to improve the efficiencies of the D-A-type polymers.²⁴⁷ Two general criteria have been proposed for selecting the solvent additives: (1) a boiling point higher than the main solvent used for polymer-fullerene solution and (2) a selective solubility for either the polymer or the fullerene.^{248,249} The different treatments used for P3HT and D-A-type polymers can be attributed to the different crystallinities. D-A type polymers are not generally crystalline, unlike regioregular P3HT, whose crystallinity ranges from 40% to

60% in neat or PCBM blend films.^{250,251} As a result, the morphology that forms during typical processing is driven by liquid-liquid separation rather than polymer crystallization, which manifests as large PCBM droplets distributed over an amorphous polymer phase (Figure 1.16a).^{174,252,253} The addition of a solvent additive can either induce polymer crystallization in the solution before casting^{254–256} or reduce PCBM aggregates,²⁵⁷ depending on the polymer-fullerene system. For example, adding diiodooctane (DIO) to a chlorobenzene (CB) solution of PTB7 and PC₇₁BM reduces aggregates of PC₇₁BM in the solution, which in turn reduces the size of PC₇₁BM domains in the film (Figure 1.16d).^{257,258} The morphology is improved to provide a larger interface between domains and better percolation of PCBM. Adding DIO enhances the charge separation and charge transportation, which boost the PCE from 3.9% to 7.4%.¹⁷⁴

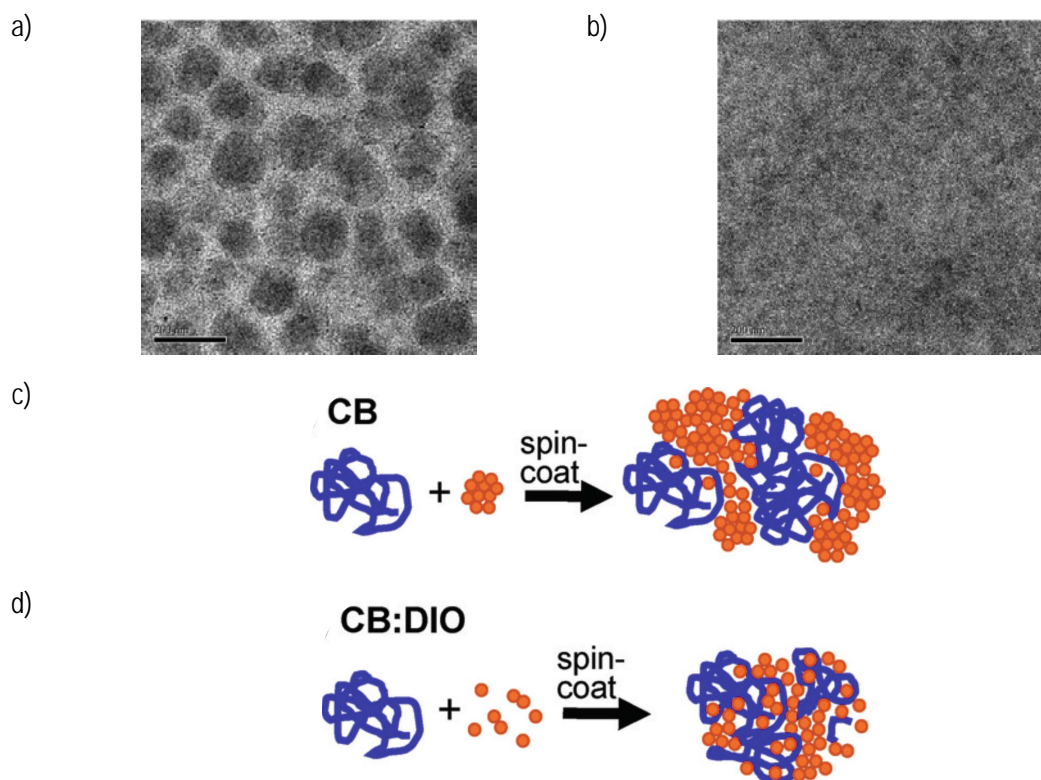


Figure 1.16 TEM images of PTB7/PC₇₁BM films spin-coated from a chlorobenzene solution without (a) and with (b) diiodooctane (DIO); dark areas are PCBM-rich phases, scale bar: 200 nm. Schematic representation of the spin-coating processes without (c) and with (d) DIO. DIO reduces the PCBM aggregation in solution, preventing the formation of large PCBM phases in the film. Reprinted from ref. [174] and [257]

1.4. Stability of the Polymer Solar Cells

Polymer solar cells undergo various types of degradation, which generally manifest themselves as the loss of PCE. Water vapor, oxygen, illumination, and heat are the main stimuli responsible for the degradation.²⁵⁹ These factors can act alone but usually the degradation is the result of a combined effect. From the nature of the changes, degradation can be categorized into chemical processes and physical processes.^{260,261} Various degradations occur in all layers of the polymer solar cell and at the interfaces.²⁶² From the perspective of the elementary photovoltaic processes contributing to the performance loss, the degradations can be attributed to absorption loss, charge generation loss, and charge extraction loss.²⁶³ Figure 1.17 summarizes the common degradation processes present in polymer solar cells. In this section, polymer solar cell degradation will be discussed and organized by the location of the processes. Within each location, chemical and physical processes will be discussed separately.

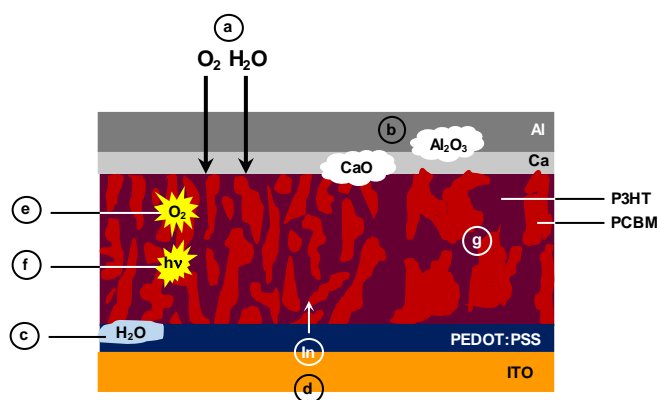


Figure 1.17 Common degradations in a polymer solar cell: diffusion of oxygen and water through the metal electrode (a); oxidation of the metal electrode (b); ingress of water through the PEDOT:PSS layer (c); diffusion of indium from degraded ITO (d); oxygen attack of polymer and fullerene (e); photochemical degradation of polymer and fullerene (f); thermally induced large phase segregation (g)

1.4.1. Degradation of the metal electrode

Diffusion of oxygen and water

Polymer solar cells are vulnerable to water and oxygen attacks when exposed to the air. Water and oxygen can corrode the metal electrode and participate in the

degradation processes in other layers. Oxygen and water mainly diffuse through the grain boundaries and defect pinholes on the aluminum electrode rather than through the edge.^{142,264–268} However, it is also reported that water ingress can occur at the edge.²⁶⁹ Once inside, oxygen and water can diffuse laterally and vertically across the entire active layer and eventually reach the counter electrode.^{265–267} Using time-of-flight secondary ion mass spectrometry (TOF-SIMS), Norrman et al. found that water effectively and homogeneously diffuses through the grain boundaries of the aluminum electrode while oxygen preferably diffuses through the defect pinholes on the electrode.²⁶⁷ Conversely, when silver is used as the metal electrode, oxygen mainly diffuses through the edge because of the lack of pinholes on the silver electrode.¹⁴²

Chemical degradation of the metal electrode

Conventional configuration PSCs use low work function metals, such as aluminum and calcium, as the cathode, which are susceptible to oxidation by atmospheric water and oxygen. The main degradation path for these metals is the formation of metal oxides at the interface, which act as insulating patches and hinder charge transport.^{142,270,271} These insulating patches cause a charge-transport imbalance in the devices, which is responsible for the S-shaped I-V curves observed in PV measurements.^{272,273} Under high humidities, the metal oxide patches could expand and cause delamination between the metal electrode and the organic layer.²⁷¹ Hermenau et al. showed that water causes more degradation than oxygen, as the degradation profile agrees well with the water ingress.^{268,270} Interestingly, although calcium has a low work function, it does not react with oxygen at room temperature. Rather, calcium is highly sensitive to water and is oxidized by water to form calcium oxide and calcium hydroxide.²⁷⁴ Lloyd et al. found that the shelf life (i.e., ambient dark storage) of polymer solar cells is determined by the decay behavior of the metal contact and metal/organic interface.¹⁴² In the case of a conventional PSC with sequentially deposited Al/Ca electrode (Al on top of Ca), small voids at the Al/Ca interface expand with time and protrude into the calcium layer. Calcium oxide is also evident at the Al/Ca interface. In contrast, the formation of silver oxide raises the work function of the silver anode in an inverted PSC, which is beneficial for charge collection.

Aside from reactions with water and oxygen, chemical reactions between metal electrodes and organic materials (i.e., polymers or fullerenes) have also been

documented. PPV can react with aluminum to form Al-C bonds.²⁷⁵ Krebs et al. attributed the formation of Al₂O₃ at the Al/organic interface to the oxidation of initially formed organoaluminum species by diffused oxygen.²⁶⁶ They also found in an earlier report that the aluminum may react with photo-induced radicals in the PPV/C₆₀ devices in the absence of oxygen and water.²⁷⁶ Indeed, Ag₂S and AgS have been detected in a P3HT BHJ device, which the author attributed to reactions between silver and P3HT.¹⁴²

1.4.2. Degradation of the buffer layers and the TCO

Degradation of the buffer layers

Degradation of the hole transporting layer

PEDOT:PSS is the most commonly used HTL for conventional PSCs, and its degradation has been widely studied. PEDOT:PSS is hydroscopic in nature, which may promote water ingress through the PEDOT:PSS layer. Kawano et al. studied the stability of ITO/PEDOT:PSS/MDMO-PPV:PCBM/Al devices and found that water absorption by PEDOT:PSS is the dominant factor of degradation.²⁷⁷ Insulating patches formed at the PEDOT:PSS/active layer interface can deteriorate the conductivity. Similar findings were made by Voroshazi et al., who reported that diffused water could make its way to the cathode and cause cathode oxidation.²⁷⁸ In a study where devices with three different HTLs are subjected to light soaking in ambient up to 7 h, Ecker et al. found that devices with water-based HTLs, including PEDOT:PSS, degrade much faster than their non-water-based counterparts, and stated that the water ingress is the main cause for efficiency loss.²⁷⁹ Aside from water invasion, PEDOT:PSS has been found to chemically degrade and form PSS:HBA (polystyrene:hydroxybenzoic acid) particles, which might have been catalyzed by the polymer donor.²⁶⁴ Manceau et al. also claimed that PEDOT:PSS introduces degradation to the active layer after prolonged illumination in the absence of oxygen and water, which resulted in absorption loss and formation of PSS-related aggregates.²⁸⁰ Further, in a study applying PEDOT:PSS as the HTL in an inverted device, the major degradation pathway was identified as the phase segregation between PEDOT and PSS, which then led to selective oxidation of PEDOT near the PEDOT/active layer interface.²⁸¹

Degradation of the electron transporting layer

ZnO is naturally resistant to moisture and oxygen in air because of the water insolubility and the high oxidation state of zinc. However, increased series resistance was observed at the ZnO contact when inverted polymer solar cell devices were exposed in air for a prolonged period. The authors attribute this phenomenon to chemisorption of molecular oxygen at the ZnO layer, which can be reversed by UV soaking in an inert atmosphere through a photodesorption process.²⁸² Devices with only PEIE as the ETL have a much shorter shelf life than those with ZnO. Those with only PEIE lost 81% of their initial efficiency after 50 days of ambient storage.²⁸³

Degradation of the TCO

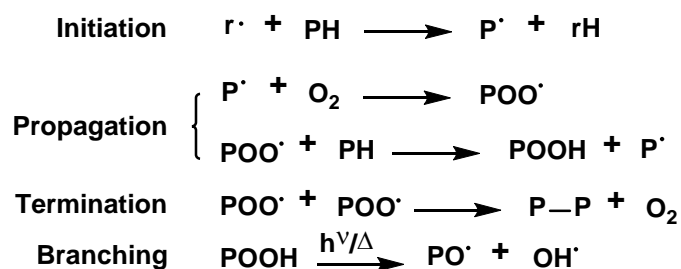
Degradation of the ITO is mostly associated with PEDOT:PSS. de Jong et al. used Rutherford backscattering to probe the PEDOT:PSS/ITO interface and revealed that the indium content in PEDOT:PSS increased by a factor of 10 after 2500 h of thermal annealing in a N₂ atmosphere. The process is accelerated at room temperature when devices are exposed to an ambient atmosphere.²⁸⁴ The author attributed the findings to acid etching of the ITO by sulfonic groups on the PSS, which can be promoted in humid air. Bulle-Lieuwma et al. also found increased indium content in the PEDOT:PSS layer of a bilayer device using TOF:SIMS profiling. The signal stopped at the interface with the active layer, which was attributed to the apolar nature of PCBM.²⁸⁵ Conversely, Krebs et al. detected an indium signal throughout the entire active layer of the device.²⁸⁶

1.4.3. Degradation of the active layer

Chemical degradation of the conjugated polymer

Three mechanisms have been proposed for the photooxidation of conjugated polymers: oxidation through the formation of peroxy radicals, oxidation through the generation of singlet oxygen, and oxidation through the formation of superoxide anions. For traditional conjugated polymers, the peroxy radical route is usually the predominant process. The process starts with a radical attack at the C–H bond on the sidechain closest to the aromatic backbone by a photogenerated radical species, resulting in hydrogen abstraction and formation of a macroradical. The macroradical can then react with a

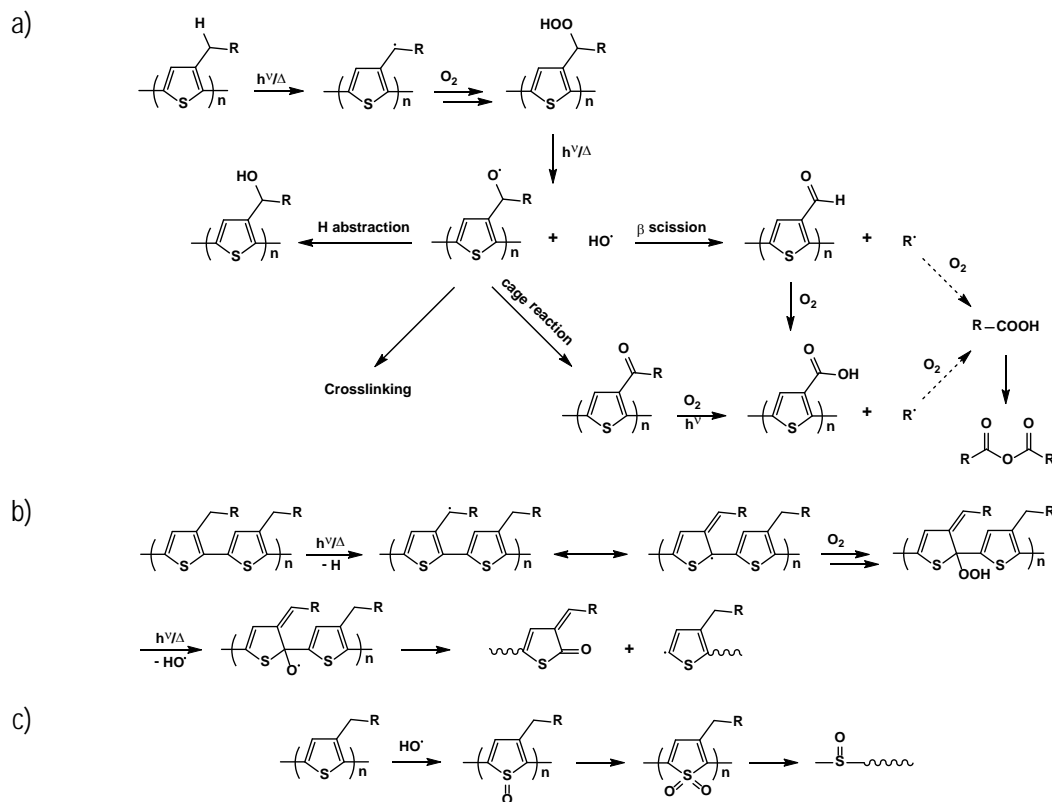
molecular oxygen to generate a peroxy radical, which can further abstract another hydrogen from the polymer and undergo homolysis, forming an alkoxy macroradical and a highly reactive hydroxy radical (Scheme 1.3).²⁸⁶ The alkoxy radical can then undergo a series of radical reactions, leading to various alterations of the sidechain, while the hydroxy radical may attack the polymer backbone, destroying the aromaticity or cleaving the backbone. Alternatively, the polymeric macroradical can undergo rearrangements to form an alkoxy radical with the unpaired electron on the mainchain and ultimately causes scission of the polymer backbone.^{287,288}



Scheme 1.3 Radical mechanism of photooxidation of polymers. Adapted from ref. [286]

Chambon et al. studied the photooxidation products of MDMO-PPV using a combination of IR spectroscopy and UV-vis spectroscopy.²⁸⁹ They proposed that the degradation begins with a radical attack at the ether sidechain and the generated hydroxy radical causes oxidation of the exocyclic double bond, leading to a loss of conjugation, and chain scission, which are responsible for the observed decrease of absorption. In the photodegradation of P3HT, hydrogen abstraction of the CH₂ group on the α -position of the hexyl sidechain leads to the formation of hydroperoxide species either on the sidechain or on the mainchain (Scheme 1.4).^{287,290} Cleavage of the sidechain hydroperoxide by light generates a hydroxyl radical and an alkoxy macroradical that can subsequently form a variety of functional groups on the α -position of the sidechain, including alcohol, aldehyde, ketone, and carboxylic acid (Scheme 1.4a).^{287,290} Alternatively, the alkoxy macroradical can promote crosslinking of P3HT films.²⁸⁸ Rearrangement following homolysis of the mainchain hydroperoxide causes chain scission of the polymer (Scheme 1.4b).²⁸⁷ The hydroxyl radical can oxidize the sulfur atoms on the polythiophene backbone, eventually causing ring opening and the loss of conjugation (Scheme 1.4c).^{290,291} Unlike O₂, O₃ attacks P3HT by direct addition to the double bonds on the backbone, as discovered by

Hintz et al., this process is at least one order of magnitude slower than O₂ attack under ambient conditions.²⁹²



Scheme 1.4 Photodegradation of poly(3-alkylthiophene) through the formation of peroxy radicals: photodegradation of the sidechain (a), chain scission (b), and ring-opening (c). Adapted from refs. [287], [288], and [290]

When it comes to the modern D-A-type low bandgap polymers, photooxidation is also observed through a radical route. For example, the first step of PCDTBT photodegradation is photoinduced homolysis of the C–N bond at the sidechain of the carbazole unit.²⁹³ The formed radical species then abstract hydrogens on the tertiary carbon on the sidechain causing oxidation on the sidechains and the formation of harmful hydroxy radicals. In the second phase of degradation, the thiophene atoms are attacked, resulting in chain scission. Similarly, the vulnerability of the C–N bond had been reported previously in a study of photostability of poly(*N*-vinylcarbazole). The mainchain scission

mechanism concluded from the study coincides with the sidechain photooxidation mechanism of PCDTBT.²⁹⁴

Singlet oxygen ($^1\text{O}_2$) may be formed via sensitization of ground state oxygen by photoexcited conjugated polymer.^{295,296} $^1\text{O}_2$ is high in energy, and once formed, can readily oxidize organic materials.²⁹⁷ Photobleaching of P3HT in solution by $^1\text{O}_2$ was reported by Holdcroft et al. and was attributed to the Diels-Alder addition of $^1\text{O}_2$ that disrupted thiophene rings on the polymer backbone.^{287,296} Soon et al. discovered that photobleaching of PTB7:PC₇₁BM in the presence of oxygen can be explained by a singlet oxygen mechanism.²⁹⁸ Evidence of polymer triplet states with high energy was observed in PTB7 under illumination, and a high volume of $^1\text{O}_2$ was detected for films of neat PTB7 and PTB7:PCBM. They propose that the energy transfer from the polymer triplet state to the oxygen ground state can be assisted by intersystem crossing from the excited polymer singlet state and non-geminate recombination of separated charges (Figure 1.18), which explains the higher $^1\text{O}_2$ yield in the blend film than that in the neat PTB7 film. Their findings corroborated observations by Alem et al.,²⁹⁹ who attributed the photobleaching of PTB to $^1\text{O}_2$ oxidation and proposed the product to be an endoperoxide species at the BDT unit analogous to the oxidation product of anthracene.³⁰⁰ Interestingly, in the same study, Alem et al. also found that alkoxy sidechains retard the degradation process compared to alkyl sidechains, which agrees with an earlier report by Dam et al., where they concluded that electron withdrawing substituents decrease the reaction rate between $^1\text{O}_2$ and PPV oligomers.³⁰¹

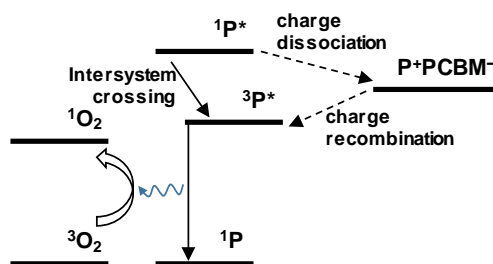


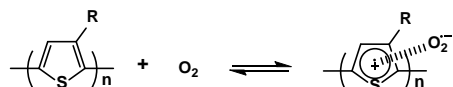
Figure 1.18 Energy diagram showing the formation mechanism of singlet oxygen ($^1\text{O}_2$) in a PTB7/PCBM blend. A polymer triplet ($^3\text{P}^*$) is formed by direct intersystem crossing from a polymer singlet ($^1\text{P}^*$), or through bi-molecular recombination of dissociated charges. Quenching of $^3\text{P}^*$ by ground state oxygen ($^3\text{O}_2$) gives rise to the formation of $^1\text{O}_2$, which consequently degrades PTB7. Adapted from ref. [298]

Unlike the formation of singlet oxygen via energy transfer, some researchers propose that charges may transfer from excited states of polymer or fullerene to ground state oxygen ($^3\text{O}_2$).^{302,303} The result is the generation of superoxide anions (O_2^-), which are responsible for the oxidation of conjugated polymers.

Systematic studies aiming at providing a more general understanding of photooxidative stability of conjugated polymers have been reported. Silva et al. performed DFT calculations on oligomers of poly(*p*-phenylene) (PPP), polythiophene (PT), polybenzodithiophene (PBDT), and PTB with alkyl and alkoxy sidechains against photooxidation.³⁰⁴ They found that the insertion of an oxygen atom between the aliphatic sidechains and the aromatic backbone rendered the polymers more resistant to photooxidation by radical attack. Mateker et al. probed the correlation between photooxidative stability and molecular packing by studying 12 conjugated polymers and small molecules and found that planar materials that form dense, crystalline film morphologies are the most stable towards photooxidation.³⁰⁵ In a comprehensive study by Manceau et al., 12 building blocks were made into conjugated polymers and their photostabilities were ranked.³⁰⁶ The authors suggested that exocyclic double bonds, quaternary sites, and readily cleavable bonds, such as C–N, are the weak points susceptible to photooxidation, while aromatic polycyclic units exhibit good photochemical stabilities. Further, sidechain cleavage can dramatically improve the photostability of polymers (see Section 1.5.3), and substituting the quaternary carbon for silicon for attachment increases the stability by a large margin.

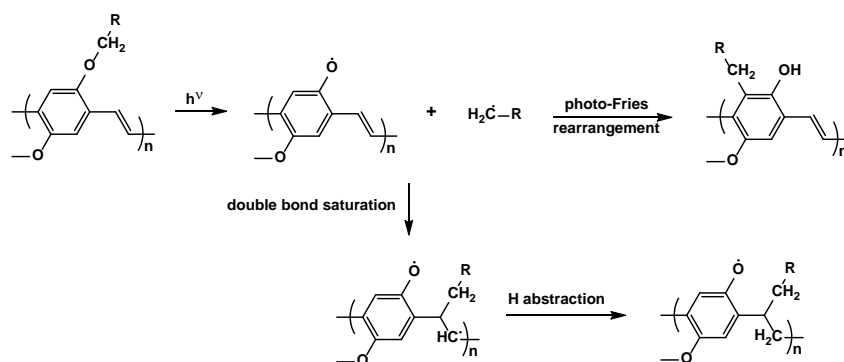
Besides irreversible chemical degradation, conjugated polymers have been well-known to undergo a reversible p-type doping by oxygen under illumination. In a pioneering work published by Abdou et al., P3HT thin film formed a charge transfer complex (CTC) with oxygen in the form of $\text{P3HT}^+\cdot\text{O}_2^-$ with a binding energy of -10.6 kJ/mol, which is similar to that for moderate hydrogen bonding.^{307,308} The authors observed a decreased charge carrier mobility and effective fluorescence quenching. The calculated spacing between these CTCs is ~12 nm, which is similar to the exciton diffusion distance and explains the observed quenching. A proposed structure is also given (Scheme 1.5). In a polymer solar cell device, this photo-induced doping results in increased trapping sites and a loss of J_{sc} .^{309,310} Additionally, p-doping lowers the Fermi energy of the polymer/fullerene blend and

causes a misalignment of the energy levels.³¹¹ This process is accelerated dramatically by illumination, and is fully or partially reversible upon removal of oxygen.^{307,310,312–315} The reverse process is slow but can be accelerated by thermal annealing at ~100 °C.³¹² Similar p-doping is also found on PCDTBT-based polymer solar cells.³¹⁵



Scheme 1.5 Proposed mechanism of charge transfer complex (CTC) formation of P3HT and oxygen. Adapted from ref. [307]

In the absence of oxygen, conjugated polymers photodegrade because of photoinduced radical formation at a much slower rate than that of photooxidation.²⁸⁶ In an early study of the photochemical stability of MDMO-PPV under solely prolonged illumination, homolysis of the C–O bond on the alkoxy sidechain was observed. Of the generated alkyl radicals, 60% attacked the adjacent proton, while the other 40% saturated the exocyclic double bond, accounting for the reduced conjugation (Scheme 1.6).³¹⁶ Other research published by the same group attributed the decreased absorption in the visible region of P3HT to the disruption of conjugation caused by alkyl radical attack following photolysis of the sidechain.³¹⁷ In a more recent study, Frolova et al. investigated the radical accumulation in polymer thin films after continuous illumination in a helium atmosphere using electron spin resonance spectroscopy (ESR).³¹⁸ A large volume of radical species were detected in the polymer films belonging to the PTB families. In contrast, P3HT and PCDTBT demonstrated superior stabilities in the context of photolytic radical formation. Among the three PTB polymers studied, the ones with fluorine substitution on the TT unit displayed higher stabilities.

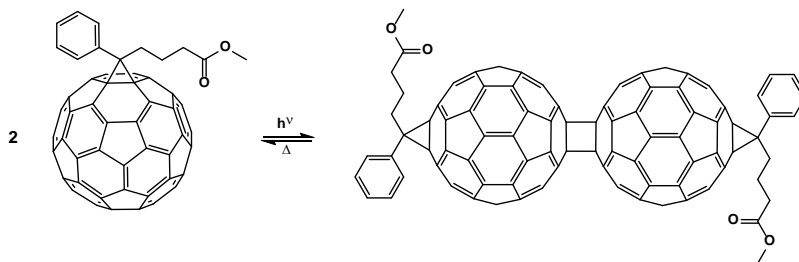


Scheme 1.6 Photodegradation mechanism of MDMO-PPV in the absence of oxygen. Adapted from ref. [316]

Chemical degradation of fullerene

Fullerenes are quite stable against oxidation when thermally heated to 100 °C.³¹⁹ However, under exposure to oxygen and illumination, C₆₀ can lead to formation of CO and CO₂ carbonyl-like structures.³²⁰ Indeed, the photooxidation method has been applied in the past to produce fullerene epoxide species (i.e., addition of an oxygen atom to the C=C bond) from C₆₀ and C₇₀.³²¹ Additionally, oxygen can induce trap states in fullerenes that are able to hinder charge transportation and quench excitons which account for reduced charge conductivity and J_{sc} loss in organic solar cell devices.^{322,323} Similar to the oxygen induced p-doping of conjugated polymers, this process can be reversible upon thermal annealing under vacuum.³²⁴

Fullerenes can polymerize to a certain extent under illumination in the absence of oxygen.^{325,326} The most abundant product is the fullerene dimer. Hence, this photochemical process is usually referred to as fullerene dimerization.³²⁷ This reaction proceeds through a [2+2] cycloaddition between two adjacent fullerene molecules, forming a four-membered ring (Scheme 1.7).^{328–330} The reaction requires the alignment of two 6-6 double bonds (double bonds shared by two hexagons) from the two monomers.³²⁹ The reaction mechanism is still under debate. The fact that the presence of oxygen retards the process has led many researchers to propose a mechanism involving the fullerene triplet state.^{328,331–333} Interestingly, the photoinduced dimerization is reversible upon thermal annealing in the dark.^{332,334,335} Therefore, the competing processes of dimer formation and dimer dissociation have been observed in polymer solar cell devices annealed under illumination.^{336,337}



Scheme 1.7 Photoinduced dimerization of fullerene and heat-initiated dimer dissociation. Reprinted from ref. [263]

Fullerene dimerization is linked to the “burn-in” phase of polymer solar cell operation, which is the initial drop of performance under continuous illumination even if the cell is encapsulated.^{335,338} This cause of performance degradation has been proposed to be shallow trap formation associated with fullerene dimerization, which affects the charge mobility.³³⁵ However, devices using C₇₀ based or multisubstituted fullerenes, such as PC₇₁BM and bis-PC₆₁BM, show improved stabilities against fullerene dimerization.^{335,338} This is due to the fact that these fullerenes have fewer reactive double bonds compared to C₆₀ and monosubstituted fullerenes.^{326,332} Other than the fullerene types, crystallinity and polymer/fullerene blend properties also affect fullerene dimerization. Heumueller et al. found that thermally annealed neat PC₆₁BM films show less dimerization than freshly cast films, which they attribute to the geometric restrictions imposed by more ordered molecular packing in the annealed films.³³⁸ The authors also found the more well-mixed films formed between the amorphous polymer, such as PCDTBT, and PC₆₁BM have a smaller tendency to undergo dimerization. The low purity of fullerene domains in such films likely prevent PC₆₁BM molecules from reacting with each other. Besides, dimerization also imparts insolubility to the fullerenes.³³² The switch from soluble to insoluble after light-induced dimerization has led to the success of patterning PCBM films using UV or visible lasers.^{339,340}

Stabilizing and destabilizing effects of fullerene

Conjugated polymers usually exhibit a slower rate of photobleaching in blend films with fullerene.^{280,317,341–344} This is mainly attributed to the excellent radical scavenging ability of fullerenes.³⁴⁵ Indeed, the highly conjugated system of fullerene provides great stabilization effects for unpaired electrons.³⁴⁶ Alkyl, alkoxy, and multi-adduct fullerene radical species have been reported in the past.^{346–348} However, the overall stability of polymer solar cells is not always improved. Instead, fullerene may undergo photooxidation, forming trap states that hinder charge extraction.^{342–344} On the other hand, fullerenes may accelerate the photooxidation of polymer in a blend via a different mechanism. This destabilizing effect is associated with enhanced singlet oxygen or superoxide anion formation assisted by fullerenes. In fact, photoexcited fullerenes alone are capable of generating ¹O₂ through its triplet state.³⁴⁹ As exemplified above, PTB7:PCBM blend film shows a higher rate of photodegradation due to the additional energy transfer pathway of charge recombination from PCBM (Figure 1.18).²⁹⁸ Similarly,

Distler et al. reported increased photooxidation of PCPDTBT after adding PCBM.³⁵⁰ They attributed this result to the high lying charge transfer state of PCPDTBT/PCBM compared to the PCPDTBT triplet state, which provided 50% more triplet states than neat PCPDTBT films. In a study conducted by Hoke et al., fullerenes with high electron affinities (high LUMO levels), such as ICBA, promote polymer oxidation.³⁰³ The authors propose that fullerenes with high electron affinities can donate an electron received from photoexcited polymer to ground state oxygen, forming O_2^- , which can further oxidize the polymers.

Thermally-induced morphological degradation of the active layer

The bulk heterojunction composed of an interpenetrating network of polymers and fullerenes that formed after spin-coating is not at thermodynamic equilibrium.³⁵¹ In fact, the active layer morphology may degrade under thermal stress. This degradation is generally manifested as the formation of micrometer-sized PCBM crystals within the active layer (Figure 1.19).^{148,352} Such large-scale phase segregation reduces the polymer/fullerene interface, which hinders effective exciton dissociation. Further, the aggregation of fullerene causes a loss of percolation pathways for electron conduction. Both of these effects lead to a deteriorated photocurrent and overall PV performance. Studies conducted on a MDMO-PPV/PCBM blend revealed that the process starts with nucleation of PCBM and then follows an Ostwald ripening type of crystal growth.^{353,354} PCBM molecules originally dispersed in the polymer matrix are drawn towards growing crystals, a process that is driven by lowering the surface energy of the system. Nucleation is governed by the diffusion rate of PCBM and the surface free energy of the nuclei. These two factors act in opposite ways, such that nucleation is favored at a high temperature because of the fast diffusion but also hindered because of the increased surface free energy. Therefore, the rate of nucleation reaches its highest value at an intermediate temperature.^{143,355} The rate of crystal growth, however, increases monotonically with temperature, and is only limited by PCBM diffusion.^{143,353,355–357} The micrometer-sized PCBM crystals can grow to several hundreds of nanometers thicker than the rest of the blend film, and are usually surrounded by a white “halo” observed under TEM or optical microscopy (Figure 1.19b).^{353,356,358} The white “halo” has been identified as the PCBM depleted area formed by collapsing of the polymer, filling the voids left by PCBM that have diffused away and integrated onto the crystal.^{353,358}

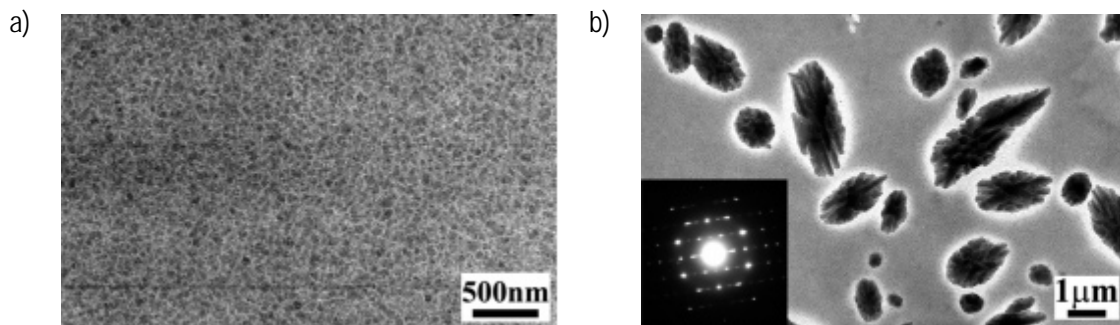


Figure 1.19 TEM images of MDMO-PPV/PCBM (1:4 w/w) films before (a) and after (b) 20 min of thermal annealing at 130 °C. The inset shows the selected area electron diffraction (SAED) pattern of PCBM crystals (dark objects surrounded by white halos). Reprinted from ref. [356]

The morphological degradation is related to the glass transition temperature of the polymer (T_g).³⁵⁹ Polymer mainchain movement becomes significant above T_g , allowing faster PCBM diffusion. Therefore, devices made from polymers with higher values of T_g are more resistant towards thermally induced morphological degradations.^{355,360} For crystalline polymers like P3HT, brief (~10 min) thermal annealing increases polymer crystallinity, which improves device performance.^{238,240} However, prolonged annealing times and excessively high temperatures cause formation of large PCBM crystals, which deteriorate the morphology.^{361,362} At temperatures below T_g , PCBM diffusion and crystallization still occur and proceed at a much slower rate.^{148,363,364} However, a glass transition is not a thermodynamic phase transition. Chain relaxation below T_g is suppressed but not prohibited.³⁶⁵ Conings et al. found the morphological degradation rate of MDMO-PPV/PCBM solar cells follows an Arrhenius-type relationship with temperature, and an activation energy (E_a) of 0.85 eV was identified.³⁵⁴ Based on this model, the authors could estimate a one-year shelf life for MDMO-PPV/PCBM solar cells (90% I_{sc} retained after one year of room-temperature storage in the dark and under an inert atmosphere). Additionally, the substrate and top electrode can retard PCBM diffusion and crystallization upon thermal annealing.^{356,357} The onset of crystallization is delayed, and the size and prominence of the PCBM crystals are reduced in the active layer sandwiched between the ITO and metal electrode.³⁵⁶ Finally, PCBM dimerization is conducive to morphological stability. A modest light soaking (e.g., 1/10 suns) before or during thermal annealing of polymer/PCBM devices can introduce small amounts of fullerene dimers, which inhibit the nucleation of PCBM crystals.^{336,337,366} However, if the annealing temperature becomes too

high, the stabilization effect is lost because of the high rate of de-oligomerization of the dimers.^{336,337}

1.4.4. Accelerated lifetime test

As polymer solar cells are becoming more and more stable with lifetimes extending over several years, accelerated lifetime tests become necessary for evaluating the long-term stabilities within a reasonable time frame.^{367–369} Testing protocols set forth during the third international summit on OPV stability (ISOS-3) provide standard laboratory ageing procedures, in which the thermal stress temperature is set to 65 or 85 °C.³⁷⁰ Nevertheless, ageing temperatures in the range of 100–200 °C are not uncommon in publications.^{143,148,337,355,363} The accelerated lifetime test at elevated temperatures is based on the assumption that the degradation of polymer solar cells follows a simple Arrhenius behavior, where the rate constant of degradation increases exponentially with increasing temperature. This relationship is represented by

$$k_{deg} = Ae^{-\frac{E_a}{k_B T}} \quad (1.4)$$

where k_{deg} is the degradation rate constant, E_a is the degradation activation energy, k_B is the Boltzmann constant, T is the absolute temperature, and A is a pre-exponential constant. The acceleration factor (AF) can be derived from equation (1.4) as

$$\ln AF = \ln \left(\frac{k_{deg2}}{k_{deg1}} \right) = \frac{E_a}{k_B} \left(\frac{1}{T_1} - \frac{1}{T_2} \right) \quad (1.5)$$

where k_{deg2} is the degradation rate constant at T_2 and k_{deg1} is the degradation rate constant at T_1 . Using equation (1.5), one can deduce the rate of degradation at a certain temperature from experimental data once the activation energy (E_a) is known. The rate of degradation is commonly represented by the rate of I_{sc} degradation.^{139,354,371,372} By plotting $\ln(k_{deg})$ against $1/T$, E_a can be extrapolated from the slope. However, only a handful of E_a have been reported so far. Schuller et al. calculated an E_a of 0.35 eV for MDMO-PPV/PCBM cells thermally aged in encapsulation.³⁷¹ Gevorgyan et al. reported E_a values of ~0.1 eV and ~0.06 eV for P3HT/PCBM devices aged in an ambient and an inert atmosphere, respectively.³⁷² The thermal morphological degradation of MDMO-

PPV/PCBM solar cells has an E_a of 0.85 eV.³⁵⁴ In the real world, solar cell modules are subjected to weathering from oxygen and moisture, as well as temperature cycling between day and night, although the average surface temperature of a panel in an Arizona desert only reaches ~ 40 °C.^{373,374} Taking these conditions into account, and using E_a values ranging from 0.3–0.6 eV, Haillant et al. were able to estimate an acceleration factor of ~ 7 – 11 between the laboratory accelerated lifetime and real outdoor lifetime, which translates to ~ 1000 h in the laboratory to 1 year in real life.³⁷⁴

1.5. Strategies for Morphological Stabilization of the Active Layer

Encapsulation with transparent inorganic or polymeric films is effective in protecting polymer solar cells from oxygen and moisture attack when exposed to air.³⁷⁵ Additionally, polymer solar cells based on inverted structures are generally more stable under ambient conditions than normal-structured ones.^{142,143,376} However, thermally induced morphological degradation is a physical process that originates from the thermodynamically disfavored morphology formed during film casting, and should be controlled by modifying the intrinsic properties of the materials within the active layer. Generally, the strategies for morphological stabilization strategies aim to stop fullerene diffusion within the active layer. These strategies include utilizing block/graft copolymers, crosslinking, and thermally-cleavable sidechains (Figure 1.20).

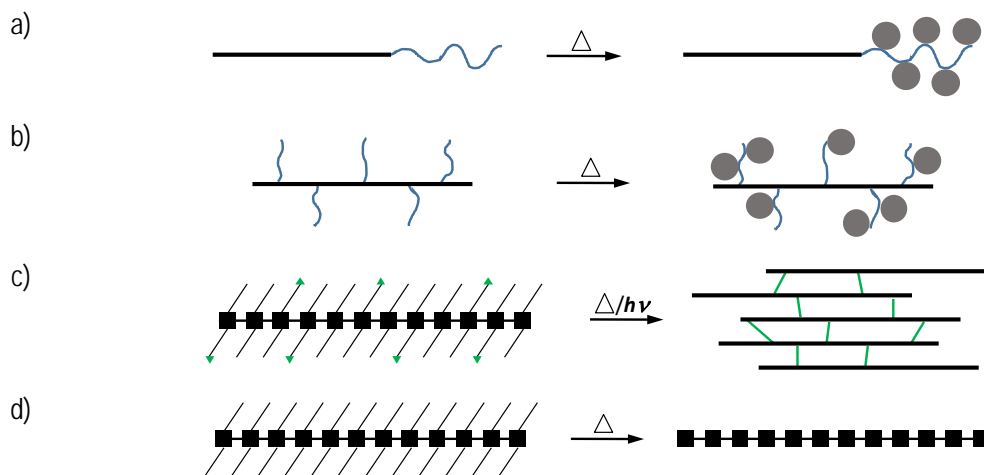




Figure 1.20 Schematics of strategies for morphological stabilization using block copolymers (a), graft copolymers (b), crosslinking (c), and thermally-cleavable sidechains (d). The legend is presented in (e)

1.5.1. Block/graft copolymers

Block copolymers are linear polymers that contain two or more blocks of homogeneous polymers linked by chemical bonds.³⁷⁷ Due to the thermodynamic incompatibility between different blocks, block copolymers tend to self-organize into separate phases that consist of homogeneous blocks in the solid state.^{378,379} However, the phase separation of block copolymers is limited by the chemical linkages between the blocks, and is rather small compared to polymer blends. Block copolymers designed for polymer solar cell applications usually contain a block of conjugated polymer, and another block of polymer capable of chemically coupling fullerenes.^{380,381} This strategy is based on the idea that the microscale phase separation is favorable for exciton dissociation while the chemical linkages prevent macroscale phase separation. The graft copolymers are similar but with the second blocks attached as “sidechains” to the main block (Figure 1.20b).

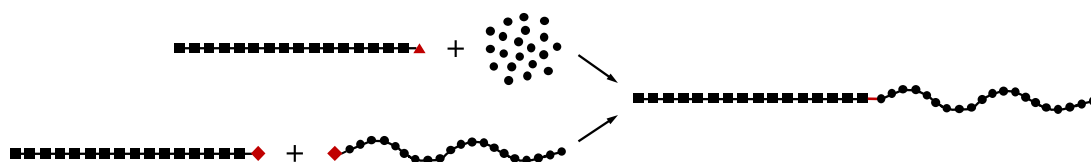


Figure 1.21 Two synthetic methods for block copolymers: the “graft-from” method (top) where the polymerization of the second block is initiated by the end-functionalized first block, and the “graft-onto” method (bottom) where two pre-synthesized blocks couple with each other to form the block copolymer

There are generally two ways of synthesizing a block copolymer, namely the “graft-from” and the “graft-onto” methods (Figure 1.21).³⁸² In the “graft-from” method, the first polymer block is synthesized and then converted into a “macroinitiator” via end-group functionalization.³⁸³ Then, the radical polymerization of the second block is initiated by the first block, forming the desired block copolymer. In the “graft-onto” method, two

homogenous polymer blocks are first individually synthesized. Their chain ends are capped with functionalities that are capable of coupling onto each other. The block copolymer is formed in the final step by coupling the two blocks, or simply by using one functionalized block to quench the chain growth of the other block.³⁸⁴

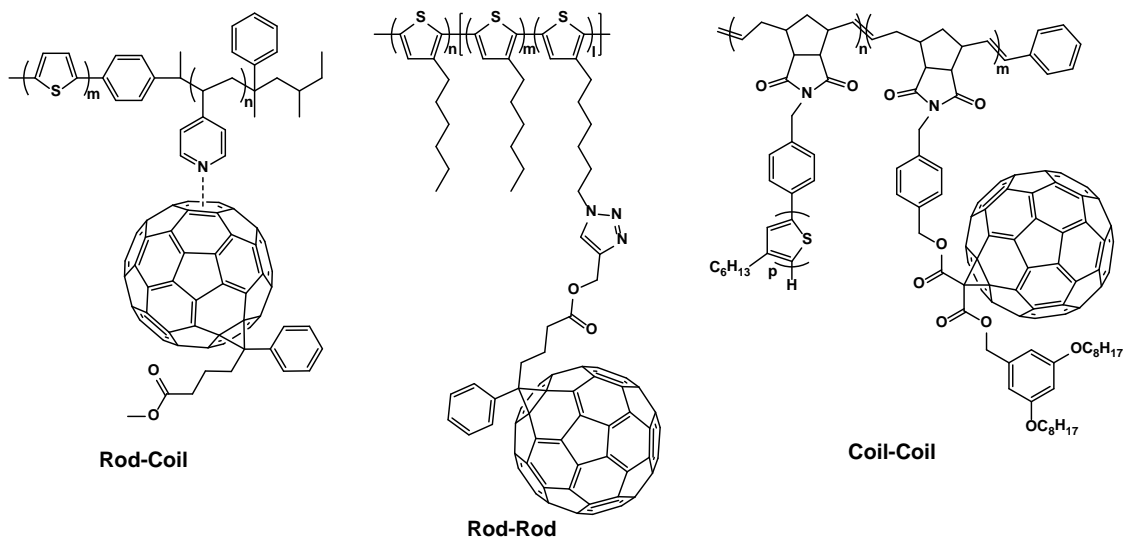


Figure 1.22 Examples of rod-coil, rod-rod, and coil-coil block copolymers, redrawn from refs. [385], [386], and [387]

Based on the stiffness of the individual block, the block copolymers can be divided into three types: rod-coil, rod-rod, and coil-coil. A rod block is essentially a conjugated polymer block where the π conjugation limits the mainchain conformation. A coil block lacks conjugation and the mainchain is flexible because of the free rotation of the σ bonds. All three types of block copolymers have found applications in polymer solar cells. An example of each type is shown in Figure 1.22. Rod-coil block copolymers are the most common. The incompatibility of the two blocks, plus the semi-crystallinity of the conjugated block grants these copolymers a variety of thin film morphologies, which can be meticulously tuned via chemical means.^{388,389}

Generally, block copolymers made for polymer solar cells show poor efficiencies when used alone as the donor.^{386,387,390–393} This is partially due to the photo-inactive and insulating nature of the coil blocks.^{387,390,391} However, block copolymers incorporating fullerenes do impart morphological stability, as evidenced by the absence of macroscale fullerene crystallization after thermal ageing.^{386,387,392–394} An efficient way of incorporating

block copolymers into polymer solar cells is to use them as compatibilizers (e.g., 10–20%). The nature of block copolymers and the fact that they contain both the donor and acceptor facilitate morphology development in the active layer, which ensures comparable or slightly superior efficiencies compared to homopolymer/fullerene blends.^{387,394–399} In some cases, the small amount of block copolymer added is sufficient to improve the long-term stability of solar cells.^{393,394,398}

1.5.2. Crosslinking

The crosslinking strategy utilizes crosslinkable groups that are capable of forming covalent bonds in solid-state films initiated by various stimuli, such as heat and UV irradiation.^{400,401} The crosslinkable groups can be attached to the conjugated polymer, fullerene, or onto a free-standing crosslinker as an additive (Figure 1.23). The crosslinking can form linkages between conjugated polymers, between fullerenes, or between conjugated polymers and fullerenes.⁴⁰⁰ In any case, fullerene diffusion is greatly hindered and morphological stability is ensured.

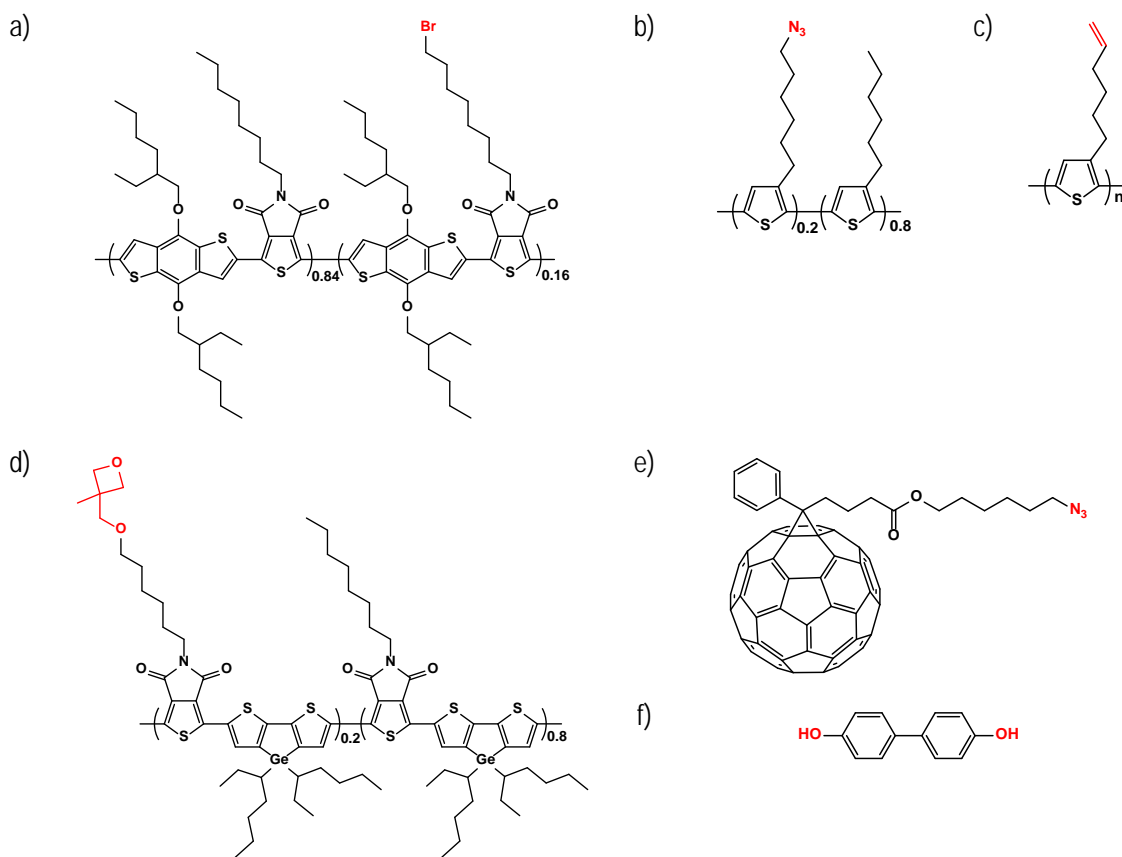


Figure 1.23 Chemical structures of crosslinkable materials used in polymer solar cells with the crosslinkable functions highlighted in red: crosslinkable conjugated polymers bearing bromine, azide, vinyl, and oxetane groups, respectively (a)–(d), a crosslinkable fullerene bearing an azide group (e), a difunctionalized crosslinker bearing hydroxyl groups (f). Redrawn from refs. [402], [403], [404], [405], [406], and [407]

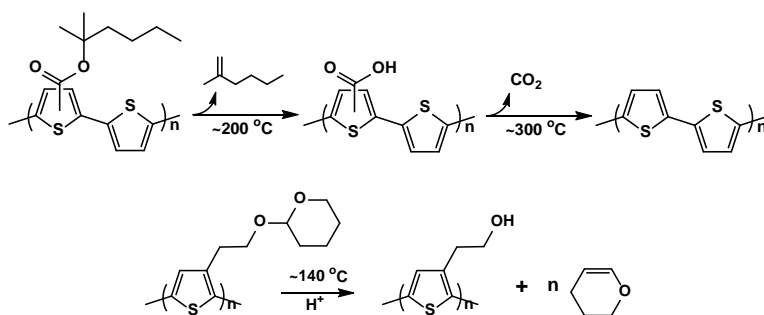
Among various reports, bromine, azide, vinyl, and oxetane are the most frequently used crosslinking groups. Crosslinking with alkyl bromide sidechains is initiated by UV irradiation.^{402,405,408–411} The C–Br bond undergoes photo-induced homolysis, generating bromine radicals.^{412–414} The bromine radical can abstract a hydrogen from another alkyl sidechain, forming a polymeric radical species. The crosslinking occurs when two sidechains bearing unpaired electrons terminate.^{405,415} Both heat and UV can trigger crosslinking by alkyl azides.^{403,406,409,411,416–419} Highly reactive alkyl nitrene species can form when alkyl azides are subjected to heat or UV.^{420,421} These species preferably attack adjacent alkyl sidechains under UV,⁴²² or the double bonds on fullerenes under heat, forming the crosslinking network.⁴²³ Crosslinking through terminal vinyl groups can be

activated by both heat and UV, and is believed to be similar to free radical polymerizations.^{404,424} Oxetanes crosslink via cationic ring opening polymerization, and trace amounts of a photoactivated acid must be used to initiate the reaction.⁴²⁵ Additionally, the high fluorine content of recently developed high-performance D-A-type polymers inspired the design of a hydroxyl functionalized crosslinker (Figure 1.23f).⁴⁰⁷ The crosslinking is based on hydrogen bond formations between the crosslinker and polymer backbones.

Crosslinking between polymers usually renders the polymer thin film insoluble.^{402–405,408,410,411,416} Utilizing this feature, multi-layer solution deposition can be realized.^{408,426} Polymer solar cells adopting the crosslinking strategy generally display a long-term performance stability because of the suppressed morphological degradation.^{403,404,406,408,410,411,417,427} However, the heat and UV required to initiate crosslinking can negatively affect the initial efficiency of the polymer solar cells.^{402,405,419} In such cases, a compromise between performance and stability must be reached or alternative materials and strategies must be considered.⁴⁰⁵

1.5.3. Thermally-cleavable sidechains

Polymers with longer sidechains have higher T_g values than those with shorter or no sidechains.³⁵⁹ This is because polymers with shorter sidechains pack close to each other in the solid state, which hinders mainchain movement. This reduced mobility in turn hampers the diffusion of fullerenes, prohibiting morphological degradation.⁴²⁸ However, conjugated polymers with short or no sidechains are not solution processable. To fabricate polymer solar cells using these polymers from solution, thermally-cleavable sidechains are attached to the polymers. These sidechains can be removed or shortened by heat in the solid state after the polymer/fullerene blend films are cast. The majority of thermally-cleavable sidechains are based on ester groups^{429–443} and tetrahydropyran (THP) groups.^{236,444–451} Alternative approaches include the use of carbonate,^{452,453} silyl,^{454,455} *o*-nitrobenzyl,^{456–459} and ketone groups.⁴⁶⁰



Scheme 1.8 Thermal-cleavage of ester (top) and THP (bottom) sidechains. Redrawn from [433] and [444]

Thermal-cleavage of an ester group proceeds through two steps: first, the ester group undergoes thermolysis cleaving the sidechain and leaving behind a carboxylic acid; at a higher temperature, decarboxylation occurs, leaving the polymer without any functionality (Scheme 1.8).⁴³³ This process is essentially a well-known ester pyrolysis reaction.^{461,462} The mechanism is believed to be a unimolecular process involving a β -hydrogen on the alcohol. The temperature onset of thermal-cleavage increases dramatically as the α -carbon of the alcohol becomes less branched, and the annealing temperature can be reduced by as much as 150 °C using a catalytic amount of trifluoromethylsulfonic acid.⁴⁴⁰

THP is an excellent protecting group for alcohols.⁴⁶³ The thermal-cleavage of THP only removes a part of the sidechain, exposing the hydroxyl group after thermal annealing (Scheme 1.8).⁴⁴⁴ Hydrogen bonding is likely present in the deprotected films, which consist of polymers with shortened sidechains bearing hydroxyl end groups, which can cause the insolubility of such films in common organic solvents.^{445,464,465} Holdcroft et al. took advantage of the solubility “switch-off” by THP deprotection and applied these conjugated polymers in chemically amplified lithography,^{444,446} laser induced thermal patterning,^{447,449,450} and PMMA assisted nanostructuring.^{236,448} THP can be cleaved from the polymer films at ~ 140 °C in the presence of a catalytic amount of organic acid or ~ 250 °C with no additives.^{445,446,450}

Apart from introducing insolubility, cleaving the thermally labile sidechains enhances crystallinity in P3HT and DPP-type polymers, which in turn improve the charge mobility.^{429,442,466} Moreover, sidechain cleavage enables the fabrication of bulk

heterojunctions with non-substituted polythiophene,⁴³⁴ as well as all-solution processed tandem solar cells.⁴⁶⁷ However, due to the unfavorable high temperature required to remove the sidechains, polymer solar cells consisting of polymers with thermally-cleavable sidechains generally show poor efficiencies.^{430,434–438,442,451,468} In contrast, these polymer solar cells exhibit long-term stability in air under thermal stress and continuous illumination because of the lack of sidechains after thermal-cleavage.^{430,431,436}

1.6. Summary and Thesis Scope

In this chapter, an in-depth review of polymer solar cells and their degradation mechanism is provided. Polymer solar cells are built on a blend of a solution-processable conjugated polymer and fullerene. Due to the small dielectric constant, excitation of conjugated polymers generates excitons that require an acceptor, such as fullerene, for charge generation. The optimal morphology of a polymer/fullerene blend is an interpenetrating network called a bulk heterojunction, which can be optimized by thermal annealing and the addition of solvent additives. Broader coverage of the solar spectrum can be achieved by lowering the bandgap of conjugated polymers by securing the quinoid structure and adopting a donor-acceptor chemical structure. Efficient conjugated polymers require careful design of the substituents, which affect the solubility, molecular packing, and polymer-fullerene interactions. The synthesis of conjugated polymers is usually performed by palladium catalyzed polycondensation. Various degradation pathways exist in polymer solar cells. Oxygen and water can diffuse through the top electrode and degrade all layers of a polymer solar cell device. The polymers are mainly degraded through photooxidation, which involves three mechanisms: radical attack, formation of singlet oxygen, and generation of superoxide anions. Reversible p-doping by oxygen and photolysis in the absence of air are also observed. A major degradation pathway of fullerenes is the photoinduced dimerization, which accounts for the burn-in loss of polymer solar cells. Stabilizing and destabilizing effects are both present for fullerenes. Further, the bulk heterojunction morphology is degraded by excessive heat. Fullerene crystals are commonly found in the active layer of thermally degraded polymer solar cells. To evaluate the stability of PSC in a timely manner, accelerated lifetime tests are generally performed at high temperatures and the degradation is assumed to follow an Arrhenius behaviour.

Lastly, there are generally three strategies of stabilizing a polymer solar cell against morphological degradation, using block copolymers, crosslinking, and thermally-cleavable sidechains.

The rest of the thesis is organized as follows: in Chapter 2, a PTB-based polymer with thermally-cleavable sidechains is presented. The thermal removal of the sidechain is studied and confirmed by thermogravimetric analysis (TGA), Fourier transform infrared spectroscopy (FTIR), and differential scanning calorimetry (DSC). PV devices made with this polymer after sidechain cleavage show stable performances, consistent with the microscopic study of the morphology. In Chapter 3, a series of PTB-based polymers with photocrosslinkable sidechains are introduced. The photocrosslinking can insolubilize the polymer films and stabilize the PV performance. Two negative effects of photocrosslinking are identified and discussed. In Chapter 4, an accurate PV measurement is demonstrated using a simple, all-in-one setup. The measurement results are verified by the National Renewable Energy Lab (NREL) and compared with non-calibrated conditions to reveal that large errors can be mitigated by simple instrument adjustments and by following standard measurement procedures. Finally, Chapter 5 provides a comprehensive conclusion and compares the two stabilizing strategies. It also includes a plan for future work.

Chapter 2.

A Low-bandgap, High-efficiency Conjugated Polymer Bearing Thermally-Cleavable Sidechains for Stable Photovoltaic Devices

2.1. Introduction

In Chapter 1, the degradation mechanisms of polymer solar cells and the stabilizing strategies towards stable active layer morphologies have been thoroughly reviewed. In this chapter, a low bandgap conjugated polymer with thermally-cleavable sidechains based on poly(thieno[3,4-b]thiophene-benzo[1,2-b:4,5-b']dithiophene) (PTB) is presented. PTB polymers are a family of low bandgap, donor-acceptor-type conjugated polymers used in polymer solar cells with exceptionally high PCEs (see Section 1.2.3).^{71,192} However, due to the low degree of crystallization of PTB, large-scale phase segregation readily occurs upon thermal annealing of PTB/PCBM bulk heterojunction films.^{243,469} In this study, two tetrahydropyran (THP) terminated sidechains are attached to the benzodithiophene (BDT) unit of PTB; upon thermal annealing, the sidechains are cleaved, leaving shortened, hydroxyl-terminated sidechains (Figure 2.1). Conjugated polymers with thermally-cleavable THP sidechains were demonstrated by Holdcroft and coworkers (see Section 1.5.3).^{236,444–451} THP cleavage renders these conjugated polymers insoluble after casting from solution, thus enabling thermal patterning and multi-layer solution deposition. However, low efficiencies (e.g., PCE < 1 %) were reported for PSCs based on THP-bearing polythiophenes.^{236,451} Moreover, the device lifetime and morphological stability of a BHJ composed of THP-bearing conjugated polymers have not yet been reported. In this study, the synthesis and characterization of the new polymer, PTB(THP), are presented. The thermal-cleavage process and its influence on polymer properties is investigated. Additionally, PSC devices made from PTB(THP)/PCBM are fabricated and tested. The stabilities of these devices and their morphological changes after thermal annealing are studied. For comparison, a model polymer, PTB4 (Figure 2.1), which is structurally similar to PTB(THP), is also investigated.

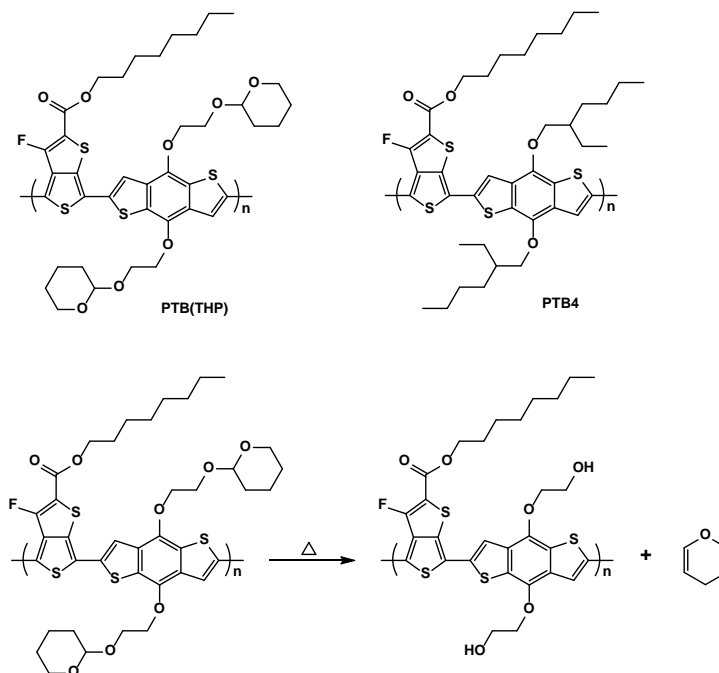


Figure 2.1 Chemical structures of PTB(THP), PTB4, and the thermally induced sidechain cleavage process of PTB(THP).

2.2. Experimental Section

2.2.1. Materials and synthesis

General information

Benzo[1,2-b:4,5-b']dithiophene-4,8-dione (**1**), octyl 4,6-dibromo-3-fluorothieno[3,4-b]thiophene-2-carboxylate (**4**), and (4,8-bis((2-ethylhexyl)oxy)benzo[1,2-b:4,5-b']dithiophene-2,6-diyl)bis(trimethylstannane) (**5**) were purchased from SunaTech Inc. All other chemicals used in the synthesis were purchased from Sigma-Aldrich, Alfa Aesar, or TCI America. Zinc powder was activated by stirring with diluted hydrochloric acid, and washed with deionized water, ethanol, and anhydrous diethyl ether before being dried in a vacuum oven. Tetrahydropyran (THF) was refluxed with sodium and distilled before the reaction. Other chemicals and solvents were used without further purification. PTB4 was synthesized following a procedure published in the literature.¹⁸⁸

Synthetic procedures

2-(2-bromoethoxy)tetrahydro-2H-pyran. 2-Bromoethan-1-ol (25.41 g, 203 mmol) and 4-methylbenzenesulfonic acid (3.87 g, 20 mmol) were added to 80 mL of methylene chloride in a 250-mL round-bottom flask. The mixture was stirred and kept cool with an ice bath, while 3,4-dihydro-2H-pyran (20.53 g, 244 mmol) was added through a drop funnel. The reaction was allowed to warm up to room temperature and stirred overnight; then, it was washed with distilled water. The organic phase was concentrated and subjected to vacuum distillation, which yielded the titled compound as a colorless oil (31 g, 73%). ¹H NMR (400 MHz, CDCl₃): δ 4.67 (t, 1H), 4.01 (m, 1H), 3.88 (m, 1H), 3.76 (m, 1H), 3.51 (m, 3H), 1.84 (m, 1H), 1.72 (m, 1H), 1.66–1.48 (m, 4H).

4,8-bis(2-((tetrahydro-2H-pyran-2-yl)oxy)ethoxy)benzo[1,2-b:4,5-b']dithiophene (2). **1** (19.30 g, 88 mmol), activated zinc powder (12.64 g, 193 mmol), sodium hydroxide (52.6 g, 1.32 mol), and 263 mL of distilled water were added to a 500-mL round-bottom flask and refluxed for 2 h. Then, to the mixture, 2-(2-bromoethoxy)tetrahydro-2H-pyran (55.03 g, 263 mmol) and tetrahydroammonium hydrogen sulfate (2.98 g, 8.8 mmol) were added, and the reaction was refluxed overnight. The reaction mixture was extracted several times with diethyl ether, and the organic phase was filtered and dried over anhydrous sodium sulfate. Recrystallization in hexanes yielded the titled compound as white crystals (28.42 g, 68%). ¹H NMR (400 MHz, CDCl₃): δ 7.60 (d, 2H), 7.39 (d, 2H), 4.78 (t, 2H), 4.47 (t, 4H), 4.10 (m, 2H), 3.90 (m, 4H), 3.56 (m, 2H), 1.91 (m, 2H), 1.74 (m, 4H), 1.58 (m, 6H).

(4,8-bis(2-((tetrahydro-2H-pyran-2-yl)oxy)ethoxy)benzo[1,2-b:4,5-b']dithiophene-2,6-diyl)bis(trimethylstannane) (3). **2** (10 g, 20.9 mmol) and 200 mL of anhydrous tetrahydrofuran were added to a 500-mL round-bottom flask RBF under argon and then cooled to -78 °C. n-Butyllithium solution (20.9 mL, 2.5 M in hexanes) was added dropwise into the flask, and the reaction was stirred at -78 °C for 2 h. Then, trimethyltin chloride solution (62.68 mL, 1.0 M in THF) was added dropwise using a syringe. The reaction mixture was allowed to warm to room temperature and stirred overnight. The reaction was quenched using distilled water, extracted with diethyl ether, and dried over anhydrous sodium sulfate. The crude product was recrystallized twice in hexanes, yielding the titled compound as white crystals (5.10 g, 30%). ¹H NMR (400 MHz, CD₂Cl₂): δ 7.63

(s, 2H), 4.79 (t, 2H), 4.49 (t, 4H), 4.09 (m, 2H), 3.90 (m, 4H), 3.55 (m, 2H), 1.95 (m, 2H), 1.77 (m, 4H), 1.61 (m, 6H), 0.45 (s, 18H).

PTB(THP). 4 (0.1363 g, 0.289 mmol), **3** (0.2321 g, 0.289mmol), and Pd(PPh₃)₄ (13 mg, 4 mol%) were weighed into a 25-mL round-bottom flask. The flask was subjected to three successive cycles of vacuum/argon-refill. Then, anhydrous *N,N*-dimethylformamide (DMF, 1 mL) and anhydrous toluene (5 mL) were added using a syringe. The polymerization was carried out at 120 °C for 20 h under argon protection. The raw product was precipitated into methanol and collected by filtration. The precipitate was extracted with methanol, acetone, and hexanes consecutively on a Soxhlet extractor. Finally, the product was collected by extraction with chloroform, and then precipitated into methanol to afford 0.18 g (79.3% yield) of a dark purple solid. ¹H NMR (500 MHz, CD₂Cl₂): δ 7.70-7.00 (2H, br), 5.00-3.00 (16H, br), 2.50-0.70 (27H, br). GPC: M_n (10.5 × 10³ g/mol), PDI (2.82).

2.2.2. Characterization

General characterizations

NMR spectroscopy was performed on a Bruker AVANCE III 400 MHz and a Bruker AVANCE III 500 MHz spectrometer, and referenced to tetramethylsilane. The molecular weight was obtained by gel permeation chromatography (GPC), with THF as the eluent. The GPC setup was composed of a Waters 1515 HPLC pump, a 2487 dual absorbance detector, and three Styragel columns, and was calibrated against polystyrene standards. TGA analysis was performed at 10 °C/min with 5 - 8 mg of polymer sample under N₂ using a HiRes TGA 2950 thermogravimetric analyzer (TA Instruments). The onset temperature was estimated from the point of intersection of the two lines: one was extrapolated from the slope of the curve just prior to the loss of the THP group and the second from the steepest part of the curve. FTIR spectra were recorded using a Bomem Michelson FTIR spectrometer (120 series). PTB(THP) and its mixture with 5 mol% of camphorsulfonic acid (CSA) in chloroform were drop-cast separately onto sodium chloride disks. The PTB(THP) film with CSA was heated at 150 °C for 5 min and rinsed with acetonitrile to remove the

residual CSA. UV-vis absorption spectra were measured using a Cary 300 Bio (Varian) spectrophotometer. Film thicknesses were measured by an Alpha-Step IQ surface profiler.

Cyclic voltammetry measurements were carried out in 0.1 M acetonitrile solution of tetrabutylammonium tetrafluoroborate (Bu_4NBF_4) under an inert N_2 atmosphere. PTB(THP) was drop cast onto glassy carbon, serving as the working electrode. A platinum wire acted as the counter electrode, and a saturated calomel electrode was used as the reference electrode. Scan rate was set to $50 \text{ mV}\cdot\text{s}^{-1}$. The potential of ferrocene/ferrocenium (Fc/Fc^+) was used as a calibration, and was found at 0.4 V under the same experimental condition. The reported absolute potential of Fc/Fc^+ is 4.80 eV.⁴⁷⁰ Therefore, the HOMO and LUMO levels of the polymer are calculated by

$$E = (-4.4 - \varphi) \text{ eV} \quad (2.1)$$

where E is either the HOMO or LUMO, φ is the corresponding potential measured with CV. Differential scanning calorimetry (DSC) was performed on a TA Instruments Q2000 model. The polymer sample (~3 mg) was sealed in a standard aluminum pan. An empty sealed pan was used as the reference. Optical microscopic images were taken with a Zeiss Axio microscope equipped with an AxioCam MRc 5 camera. The optical microscopy samples were prepared and thermally annealed following the same procedure as that for device fabrication, except silicon wafers were used as the substrates.

PV Device fabrication and characterization

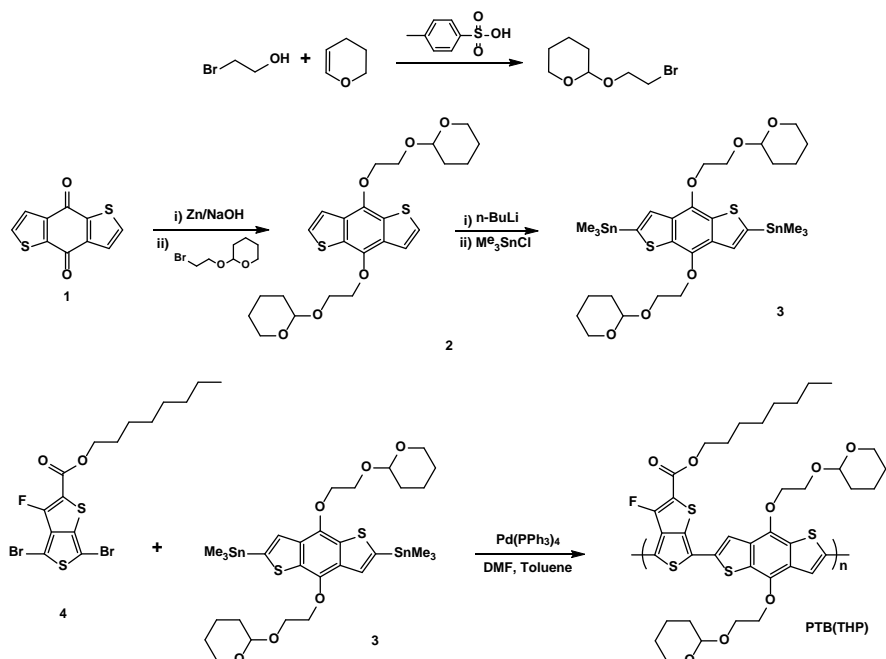
ITO-coated glass slides ($2.0 \times 1.0 \text{ cm}^2$) were ultrasonically cleaned in isopropyl alcohol, acetone, deionized $\text{H}_2\text{O}:\text{H}_2\text{O}_2:\text{NH}_4\text{OH}$ (5:1:1 vol. ratio), deionized H_2O , and acetone, consecutively. PEDOT:PSS (~35 nm; Clevios P VP Al 4083, Heraeus GmbH) was spin-coated onto the ITOs and annealed at $140 \text{ }^\circ\text{C}$ in air for 10 min in a pre-heated oven and then immediately transferred into a nitrogen-filled glove box. Subsequently, the active layer of polymer: PC_{61}BM at a weight ratio of 1:1 with or without 5 mol% of CSA was spin-coated from chloroform/dichlorobenzene (1:1 v/v). To cleave THP groups, the active films with CSA were heated to $150 \text{ }^\circ\text{C}$ for 5-10 min on top of a hotplate in the glovebox. Ca (~20 nm) and then Al (~80 nm) were thermally evaporated at $\sim 1 \times 10^{-8}$ torr through a shadow mask. The active area of the devices was around 0.30 cm^2 , and the active layer

thickness was ~80 nm. PV devices were placed under an AM 1.5D spectrum delivered by a xenon arc lamp source (Newport model 66983) with a power density of 100 mW·cm⁻², calibrated with a power meter. The J-V curves were measured using a Keithley 2400 source meter. Monochromatic light for the EQE measurement was provided by a Newport CS-260 monochromator (Model 74100).

2.3. Results and Discussion

2.3.1. Synthesis and thermal-cleavage of THP

Specifically, PTB(THP) is based on PTB4, one of the highest performing polymers in the PTB family. PTB4 has a linear octyl sidechain on the TT unit and two branched 2-ethylhexyl sidechains on the BDT unit to provide solubility (Figure 2.1). A fluorine substituent is attached to the TT unit, effectively lowering the HOMO level of the polymer, resulting in a higher V_{oc} than PSCs made from PTB derivatives with a hydrogen on the same site.¹⁸⁸ PTB(THP) replaces the 2-ethylhexyl sidechains on the BDT unit with thermally-cleavable, THP-terminated sidechains. The main reason the THP sidechains are attached to the BDT unit is the synthetic simplicity. The sidechain on the TT unit must be attached to the molecule before the bithiophene structure is fully formed.¹⁸⁸ Subsequent synthetic procedures involve harsh and acidic conditions that can potentially destroy the THP sidechain. Synthetic routes for the BDT(THP) monomer (**3**), PTB(THP), and PTB4 are outlined in Scheme 2.1. The chemical structures of all the synthesized compounds and polymers were confirmed by NMR spectroscopy, and GPC analysis was used to determine the molecular weight of the polymers. The polymer was not end-capped, because the concentration of the end groups is extremely low in high-molecular-weight polymers and the effect of end-capping is out of the scope of this study. PTB(THP) is highly soluble in common solvents, such as THF, chloroform, dichloromethane, toluene, chlorobenzene, and dichlorobenzene. However, after removal of THP by heating, the resulting film is no longer soluble in common solvents, except in THF and DMF.



Scheme 2.1 Synthetic route of the monomer BDT(THP) (3) and PTB(THP)

THP is a protecting group for alcohols, which deprotects under acidic conditions.⁴⁶³ Along the same line, a small amount of acid can catalyze the deprotection of THP-bearing polymers.^{445,446,450} Thermogravimetric analyses of neat PTB(THP) and PTB(THP) containing CSA (5 mol% based on the THP unit) are shown in Figure 2.2. The observed mass loss is ~20 wt% for both neat PTB(THP) and PTB(THP) with CSA. The THP functionality is calculated to be 21.3 wt% of PTB(THP), which confirms that the mass loss is indeed due to thermal cleavage of the THP group and elimination of dihydropyran. The onset temperature of thermal cleavage decreased from 210 °C to 140 °C in the presence of a catalytic amount of CSA, consistent with previous findings.^{445,446} However, the rate of deprotection decreased with the addition of CSA. The diffusion of acid may limit the rate of reaction, as a previous study has found that increasing the CSA loading increases the rate of deprotection.⁴⁴⁵ Figure 2.3 shows FTIR spectra of PTB(THP) films before and after the thermal treatment at 150 °C with 5 mol% CSA. The asymmetric C-O-C stretching band assigned to THP groups (located at around 1120 cm⁻¹) disappears, and a strong, broad band emerges at 3450 cm⁻¹ due to the O-H stretch of the alcohol.

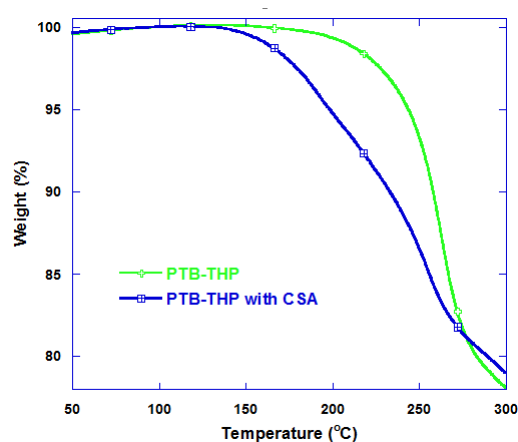


Figure 2.2 TGA results of neat PTB(THP) (green), and PTB(THP) with 5 mol% camphorsulfonic acid (blue)

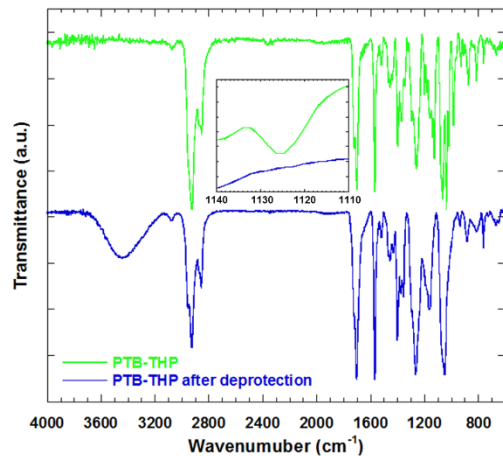


Figure 2.3 FTIR spectra of PTB(THP) before (green), and after (blue) thermal-cleavage (i.e., deprotection) of THP groups. The inset highlights the region from 1140 to 1110 cm^{-1}

The thermal-cleavage process is further studied with DSC (Figure 2.4). The PTB(THP) sample was sealed in an aluminum pan and subjected to two cycles of heating and cooling with a scan rate of 10 $^{\circ}\text{C}/\text{min}$. The thermal transitions at ~ 185 $^{\circ}\text{C}$ are attributed to the glass transition of polymers. The prominent endothermic peak at 270 $^{\circ}\text{C}$ in the first scan corresponds to the thermal-cleavage of the THP. This peak is not observed in the second scan, indicating the completeness of the process. There is no obvious change in T_g after thermal-cleavage of the sidechains. In theory, T_g increases with shorter sidechain lengths; however, bulky pendant groups also hinder the main-chain movement and raise T_g .³⁵⁹ Therefore, the effect of shortening the sidechain might be balanced by the loss of

the bulky tetrahydropyran group, resulting in a T_g that is indistinguishable from that before thermal annealing. However, the DSC results only showcase the thermal process of bulk materials. The T_g of polymer thin films and polymer/fullerene BHJ films may differ greatly from that determined by DSC, and this will require future investigations.³⁵⁹

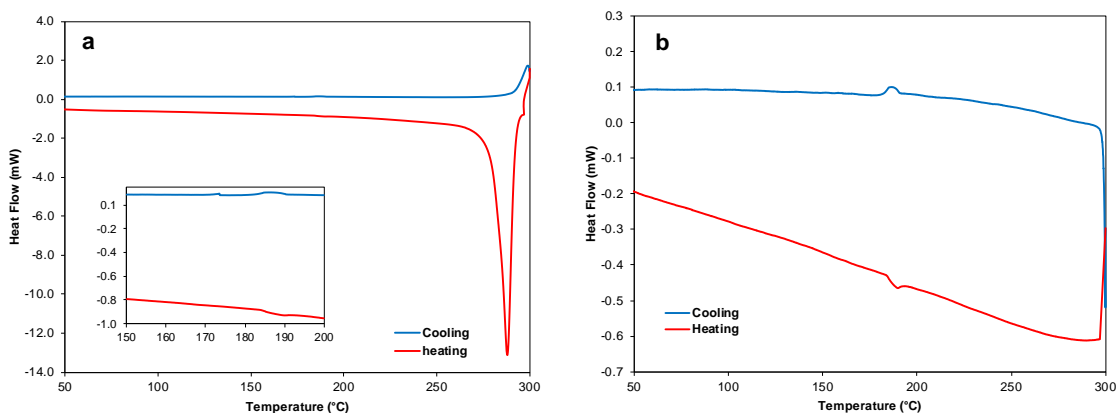


Figure 2.4 DSC results of PTB(THP) showing the first scan (a) and the second scan (b). The scan rate was 10 °C/min for both scans

2.3.2. Optical and electronic properties

The UV-Vis absorption spectra of the PTB(THP) polymer films before and after deprotection are shown in Figure 2.5. The absorption spectra of the blends of PTB(THP) and PC₆₁BM (1:1, w/w) before and after deprotection are also shown. The films of PTB(THP) before and after deprotection exhibit no absorption differences, except for a slight decrease in the absorption intensity after deprotection. The same trend is observed in the spectra of the blend film in the long wavelength range of 500-730 nm. The results indicate that the thermal-cleavage of THP does not alter the optical properties of the polymer or the blend film to a great extent. A cyclic voltammogram of PTB(THP) is shown in Figure 2.6. From the onset of the oxidation and reduction peaks, the HOMO and LUMO levels are determined to be -5.2 eV and -3.4 eV, respectively. Their difference yields an electrochemical bandgap of 1.8 eV. These findings are in good agreement with the published values of PTB4, showing the minimal impact of the THP sidechains.¹⁸⁸

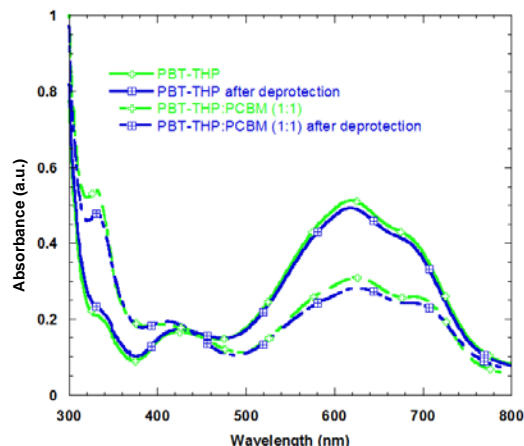


Figure 2.5 Absorption spectra of PTB(THP) (solid lines) and PTB(THP)/PC₆₁BM (dashed lines) before (green lines) and after (blue lines) thermal-cleavage of THP (i.e., deprotection)

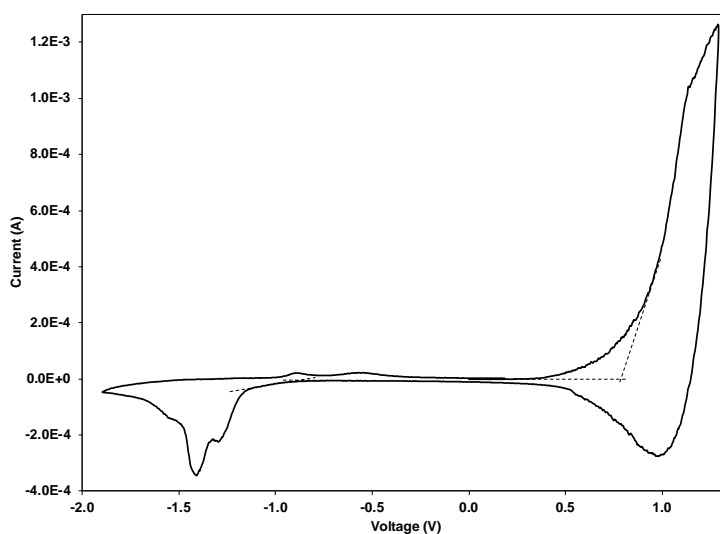


Figure 2.6 Cyclic voltammogram of PTB(THP). The dashed lines provide guidance for determining the HOMO and LUMO levels

2.3.3. Photovoltaic properties and thermal stability

Photovoltaic devices were fabricated based on the conventional configuration of ITO/PEDOT:PSS/Polymer:PC₆₁BM/Ca/Al with a PTB(THP):PC₆₁BM weight ratio of 1:1. For comparison, reference devices based on PTB4:PC₆₁BM (1:1 w/w) were also fabricated. To investigate their thermal stabilities, all the devices were annealed in a nitrogen-filled glovebox at 120 °C for up to 6 h and characterized every hour. The J–V curves of the PTB4, PTB(THP), and deprotected PTB(THP) devices are shown in

Figure 2.7. Their photovoltaic properties are summarized in Table 2.1. The PCE degradations as functions of annealing time at 120 °C are plotted in Figure 2.7d. The performance of the PTB4 and PTB(THP):PCBM devices decreases as the annealing time increases. The PCEs degraded dramatically from 3.2% to 0.2% for the PTB4 device and from 3.4% to 0.6% for the PTB(THP):PCBM device after 6 h of annealing. It is worth mentioning that the dark J-V curves of the devices based on PTB4 after thermal annealing for 3 h starts to deteriorate and the leakage current starts to increase (Figure 2.7a), which verifies that the photovoltaic devices have started to show defects. As shown in Table 2.1, the decrease in efficiency is mainly caused by the decrease in both J_{sc} and V_{oc} values. In sharp contrast, the PTB(THP):PCBM device exhibit stable device characteristics after deprotection. After the first hour of annealing, the photovoltaic performance increased slightly to a PCE value of 2.5%. After 2 h of annealing, the device performance started to stabilize with a V_{oc} of ~ 0.62 V, a J_{sc} of ~ 7.6 mA \cdot cm $^{-2}$, a FF of $\sim 34\%$, and a PCE of 1.6%. The EQE curves shown in Figure 2.8 also confirm the different stabilities of the photovoltaic devices. For PTB4, the EQE curves started to deteriorate after annealing the devices for 3 h. Although the EQE is stable for PTB(THP) after annealing for 2 h, the maximum EQE is lower than 30%. Conversely, the EQE of PTB(THP) after deprotection stays relatively stable at around 40% throughout the annealing process. The improved stability is associated with the thermal-cleavage of THP sidechains. Not only does the reduction of effective sidechain length hinder polymer movements, but the exposed hydroxyl groups may also form intermolecular hydrogen bonds that can lock-in the morphology. Therefore, the large-scale phase segregation in the active layer because of PCBM aggregation is greatly suppressed.

Table 2.1 Photovoltaic parameters of devices made from PTB4, PTB(THP), and deprotected PTB(THP) (PTB(OH)) before and after each hour of thermal annealing at 120 °C

Ann. Time (h)	J_{sc} (mA \cdot cm $^{-2}$)			V_{oc} (V)			FF (%)			PCE (%)		
	PTB4	PTB (THP)	PTB (OH)	PTB4	PTB (THP)	PTB (OH)	PTB4	PTB (THP)	PTB (OH)	PTB4	PTB (THP)	PTB (OH)
0	7.98	14.6	6.37	0.73	0.62	0.57	54.5	37.5	41.5	3.2	3.4	1.5
1	5.84	9.74	10.22	0.73	0.62	0.64	46.3	37.1	38.5	2.0	2.2	2.5
2	4.87	3.97	8.34	0.71	0.56	0.62	44.7	31.3	34.3	1.6	0.7	1.8
3	3.82	3.67	7.84	0.37	0.56	0.62	26.6	30.8	33.9	0.4	0.6	1.6
4	4.00	3.33	7.65	0.52	0.56	0.62	29.0	30.5	33.9	0.6	0.6	1.6

Ann. Time (h)	J_{sc} (mA·cm ⁻²)			V_{oc} (V)			FF (%)			PCE (%)		
	PTB4	PTB (THP)	PTB (OH)	PTB4	PTB (THP)	PTB (OH)	PTB4	PTB (THP)	PTB (OH)	PTB4	PTB (THP)	PTB (OH)
5	2.07	3.33	7.22	0.37	0.56	0.62	25.7	30.5	34.1	0.2	0.6	1.5
6	2.01	3.39	7.59	0.44	0.55	0.62	27.1	30.7	33.6	0.2	0.6	1.6

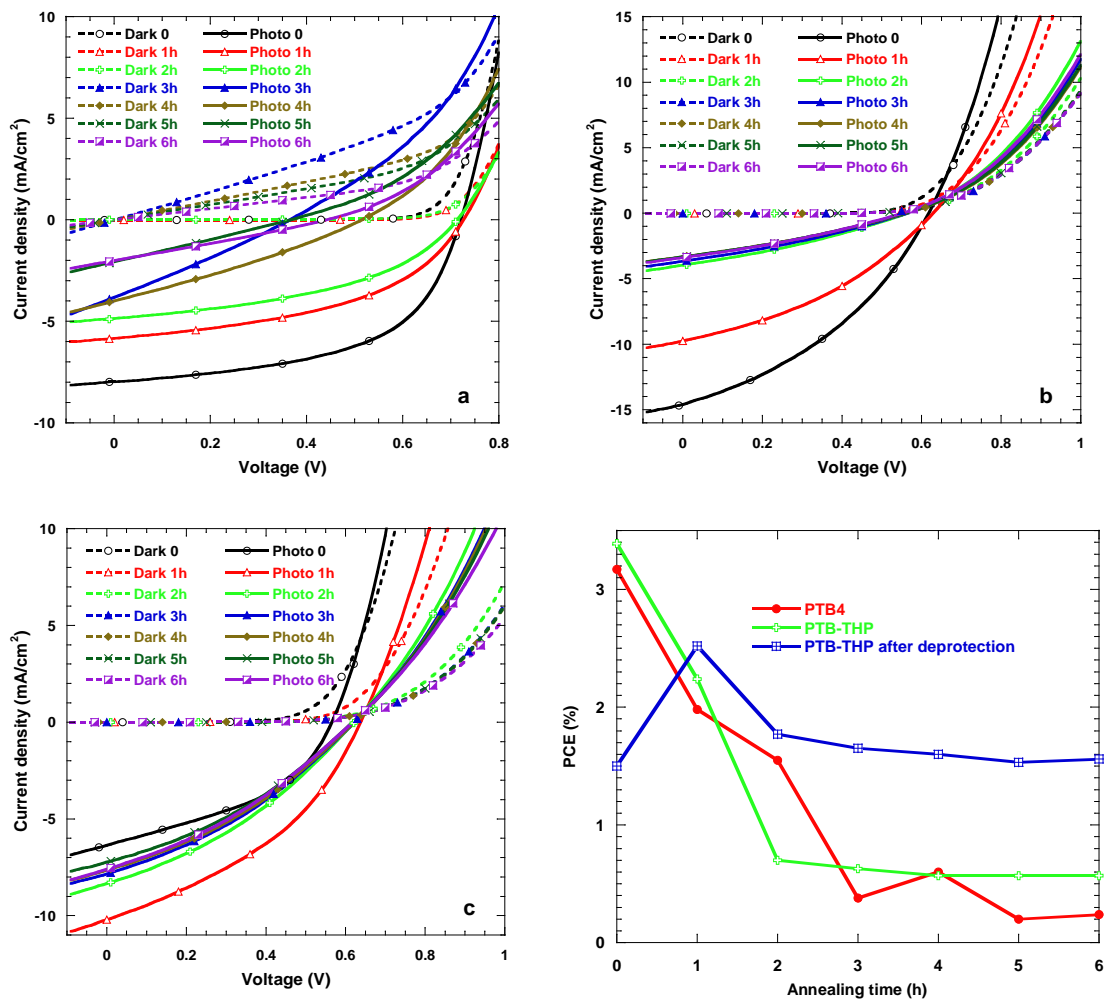


Figure 2.7 Current density–voltage (J-V) curves of PTB4 (a), PTB(THP) (b), and deprotected PTB(THP) (c) after each hour of thermal annealing at 120 °C. The degradation profile of PCE as a function of annealing time is shown in (d)

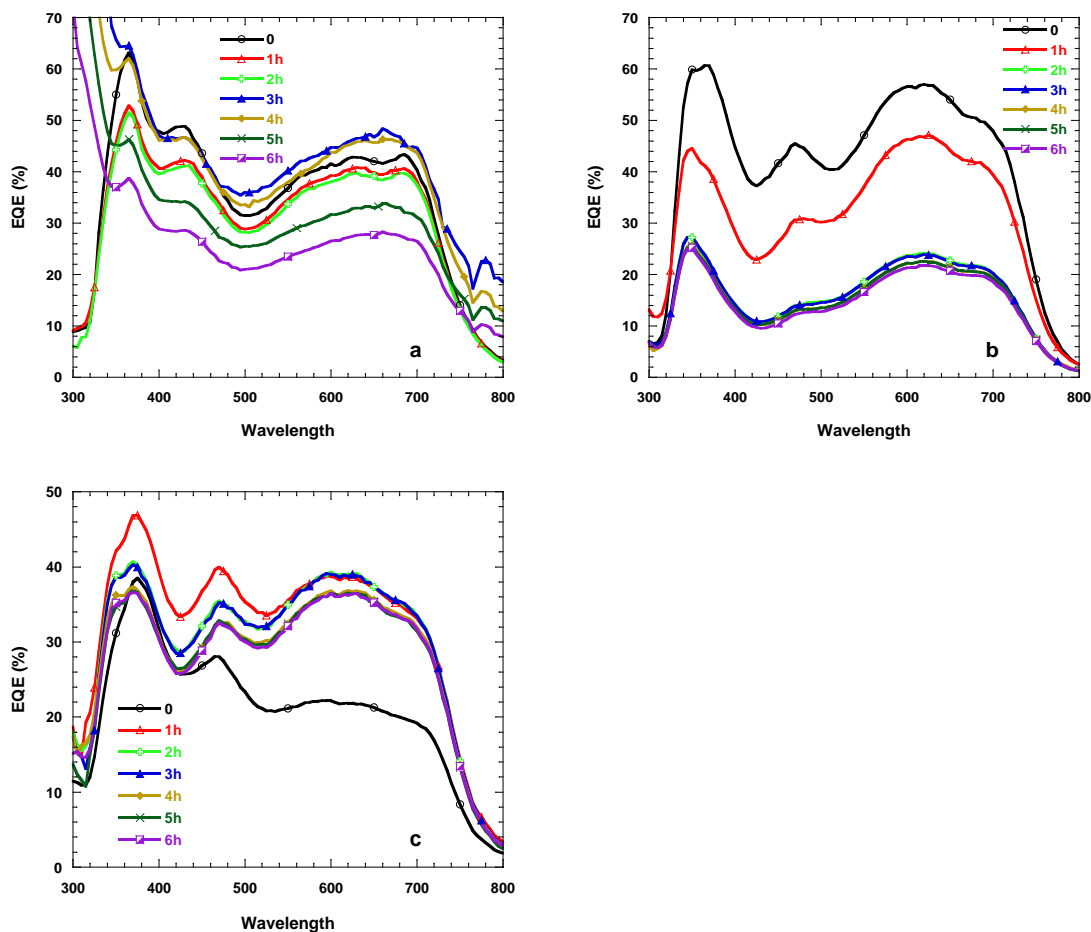


Figure 2.8 External quantum efficiency (EQE) curves of PTB4 (a), PTB(THP) (b), and deprotected PTB(THP) (c) after each hour of thermal annealing at 120 °C

2.3.4. Morphological stability of the active layer

The active layer morphology evolution of PTB4/PCBM, PTB(THP)/PCBM, and deprotected PTB(THP)/PCBM devices are presented in Figure 2.9. The as-cast films of all samples show smooth morphologies under the optical microscope. Upon thermal annealing, PCBM aggregates started to appear in the PTB4 and PTB(THP) films, which grew in size and population by the end of the 6-h annealing. On the other hand, no observable phase change is found in the deprotected PTB(THP) film throughout the annealing, indicating a thermally stable morphology. The microscopic results are in line with the degradation profiles of the corresponding solar cell devices (Figure 2.7d). These findings imply that the unstable active layer morphologies of PTB4 and PTB(THP) films

are highly responsible for the thermal degradation of their PV performances. The hampered mainchain movement, as well as the potential hydrogen bonding network, likely contribute to the stable morphology, and hence the stable PV parameters of deprotected PTB(THP). In addition, the PCBM crystal formation proceeds under different kinetics for PTB4 and PTB(THP). PTB(THP)/PCBM forms many small PCBM crystals, while PTB4/PCBM forms fewer but larger crystals. The appearance of PCBM crystals is also delayed in PTB4/PCBM. This phenomenon points to the different rates of PCBM nucleation. The PCBM nucleation rate is slower in the PTB4 film than in the PTB(THP) film, but the crystal growth rates are similar. The cause might be that the PTB(THP) with shorter, linear THP sidechains adopts a closer molecular packing, while the highly soluble, branched 2-ethylhexyl sidechains on PTB4 provide better mixing of PTB4 with PCBM in the as-cast film.¹⁹¹ Hence, the energy barrier for PCBM to transition from a mixed phase to a pure crystal phase is lower in the PTB(THP) films, providing a higher rate of nucleation.

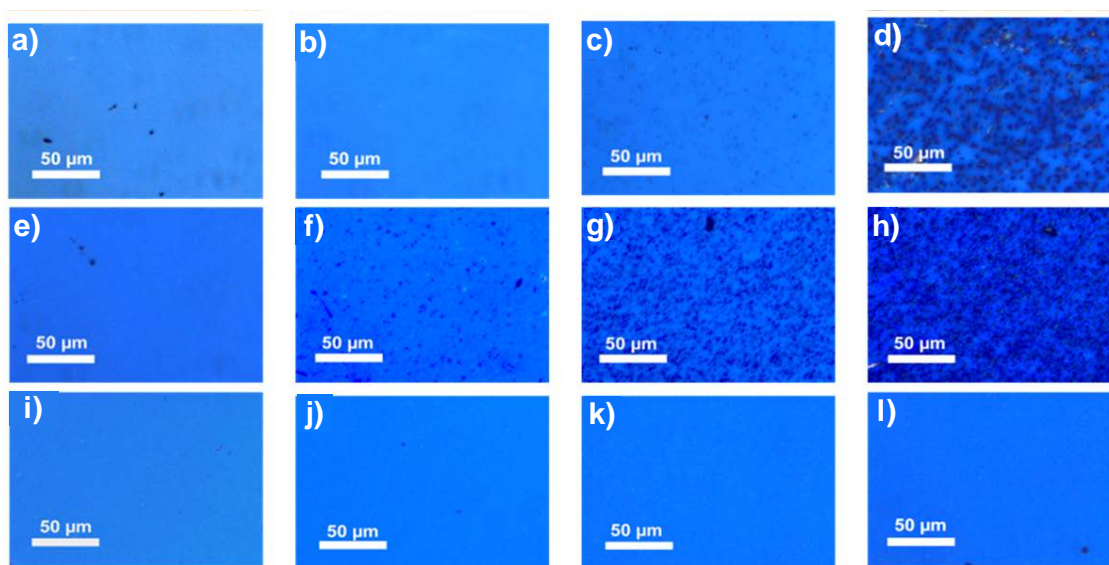


Figure 2.9 Optical microscopic images of the PTB4/PCBM film (a)–(d), PTB(THP)/PCBM film (e)–(h), and deprotected PTB(THP)/PCBM film (i)–(l) at different stages of thermal annealing at 130 °C: as-cast (a), (e), (i), 1 h (b), (f), (j), 3 h (c), (g), (k), and 6 h (d), (h), (l)

2.4. Conclusion

In conclusion, a low bandgap conjugated polymer based on PTB bearing thermally-cleavable THP sidechains is synthesized and characterized. Thermal cleavage of the THP group shortens the sidechains on the polymer and renders the polymer insoluble in the solid state. The deprotection (i.e., thermal-cleavage) process proceeds under a mild condition in the presence of a small amount of a solid acid catalyst. The onset temperature is effectively lowered from 210 °C to 140 °C with 5 mol% of CSA. PTB(THP) has a similar absorption profile and bandgap as the reference polymer PTB4. Further, solar cell devices based on PTB(THP)/PCBM bulk heterojunctions exhibit comparable PV performances to those made of PTB4/PCBM. Deprotection of PTB(THP) greatly improves the thermal stability of the device, albeit with a slight compromise of the initial efficiency. Finally, optical microscopy reveals that the large phase segregation caused by PCBM aggregation is effectively suppressed in the deprotected PTB(THP)/PCBM films after prolonged thermal annealing. Thus, the stable PV characteristics are likely the result of the stable active layer morphology caused by the thermal-cleavage of sidechains.

Chapter 3.

Thermal Stability of Polymer Solar Cells Using Low-bandgap, High-efficiency, Photocrosslinkable Polymers

3.1. Introduction

In the previous chapter, a PTB polymer bearing thermally-cleavable sidechains was presented, and the thermal stabilities of its solar cell devices were examined. In this chapter, a series of photocrosslinkable polymers based on PTB is reported. Crosslinkable conjugated polymers for photovoltaic applications were reviewed in Section 1.5.3. Bromide, azide, oxetane, and vinyl groups are the most widely used crosslinking functionalities, and thermal energy and photo energy are the two main sources to initiate crosslinking.⁴⁰⁰ Photocrosslinking has the advantage of avoiding initial thermal annealing, which may negatively affect the device performance before crosslinking can stabilize it.^{392,419} D-A-type, low bandgap photocrosslinkable polymers have been reported in a small number of cases. Griffini et al. synthesized a PBDTPD derivative with bromooctyl chains on the TPD units (Figure 1.23a).⁴⁰² Similarly, Yau et al. reported another TPD based polymer with the same crosslinkable bromooctyl sidechain appended on the TPD unit and studied the film insolubilization kinetics (Figure 1.23c with Br).⁴⁰⁵ There are two reports on photocrosslinkable PTB derivatives, both using a bromooctyl sidechain on the TT unit.^{410,411} Film insolubilization and stable PV performances were achieved after photocrosslinking. The insolubilization property was utilized in a later study to spin-coat a thin layer of the neat polymer before deposition of the active layer, which resulted in a higher PCE.⁴²⁶ The drawback of having the crosslinkable sidechain on the TT unit is the lack of the fluorination. To fabricate the fluorinated TT monomer, the sidechain has to be attached before the fused thienothiophene ring is formed.¹⁸⁸ The bromooctyl sidechain used for the photocrosslinkable PTBs may not be able to withstand the harsh reaction conditions in the later synthetic steps. However, fluoride substitution on the TT unit is a key feature of the successful PTB7 because the introduction of an electron withdrawing group lowers the HOMO level of the polymer, leading to an increased V_{oc} and an improved

Coating Inc. with a sheet resistance of $15 \Omega/\square$. PEDOT:PSS (Clevios P VP Al 4083) was purchased from Heraeus GmbH. PC₇₁BM was purchased from American Dye Sources Inc. All materials were used as received without further purification, unless otherwise mentioned.

3.2.2. Synthesis

4,8-Bis((8-chlorooctyl)oxy)benzo[1,2-b:4,5-b']dithiophene (2). **1** (5 g, 22.7 mmol), activated zinc power (3.3 g, 49.9 mmol), sodium hydroxide (13.6 g, 0.34 mol), and 100 mL of distilled water were added to a 250-mL round-bottom flask and refluxed for 2 h. Then 1,8-dichlorooctane (10.35 g, 56.5 mmol) and tetrahydroammonium hydrogen sulfate (0.77 g, 2.27 mmol) were added, and the reaction was refluxed overnight. The reaction mixture was extracted several times with diethyl ether, and the organic phase was filtered and dried over anhydrous sodium sulfate. The organic phase was concentrated and loaded onto a column packed with silica. Gradient elution with hexanes:ethyl acetate (4:1 to 2:1) yielded the titled compound as a white solid (2.99 g, 26%). ¹H NMR (400 MHz, CDCl₃): 7.48 (d, 2H), 7.36 (d, 2H), 4.28 (t, 4H), 3.54 (t, 4H), 1.88 (tt, 4H), 1.79 (tt, 4H), 1.58 (tt, 4H), 1.46 (tt, 4H), 1.40 (m, 8H).

(4,8-Bis((8-chlorooctyl)oxy)benzo[1,2-b:4,5-b']dithiophene-2,6-diyl)bis(trimethylstannane) (BDT-Cl, 3). **2** (2.97 g, 5.76 mmol) was dissolved in 100 mL of THF in a 250-mL round-bottom flask equipped with a magnetic stir bar under an argon atmosphere. The solution was cooled to -78 °C, and 5.76 mL of n-butyl lithium solution (2.5 M in hexanes) was added dropwise. After 2 h of stirring at the same temperature, 17.28 mL of a trimethyltin chloride solution (1.0 M in THF) was added dropwise to the mixture. The reaction was allowed to warm to room temperature and stirred overnight before it was quenched with water and extracted with diethyl ether. The organic phase was dried over anhydrous sodium sulfate and the solvent was evaporated. Recrystallization in hexanes twice afforded the titled product as white needles (4.22 g, 87%). ¹H NMR (400 MHz, CDCl₃): 7.50 (s, 2H), 4.29 (t, 4H), 3.54 (t, 4H), 1.88 (tt, 4H), 1.79 (tt, 4H), 1.60 (tt, 4H), 1.47 (tt, 4H), 1.41 (m, 8H), 0.45 (t, 18H).

PTB-Cl₁₀₀. **4** (138.7 mg, 0.294 mmol), **3** (271.7 mg, 0.323 mmol), 8 mL of toluene, and 2 mL of *N,N*-dimethylformamide (DMF) were added into a 25-mL round-bottom flask equipped with a magnetic stir bar. The mixture was subjected to three freeze-pump-thaw cycles before being refilled with argon. Tetrakis-(triphenylphosphine)-palladium(0) (Pd(PPh₃)₄ 11 mg, 9.5 × 10⁻³ mmol) was added, and the reaction was heated at 120 °C for 8 h. After the reaction cooled, the crude product was precipitated in methanol and then filtered into an extraction thimble. After Soxhlet extraction with methanol, hexanes, and chloroform, the chloroform solution was passed through a column packed with Celite. The final product was obtained by precipitation into methanol, yielding 240.7 mg of a dark blue solid (93%). GPC: M_n = 48 kg/mol, PDI = 3.3. ¹H-NMR (500 MHz, C₂D₂Cl₄): 8.0-7.0 (br, 2H), 4.5 (br, 6H), 3.6 (br, 4H), 2.4-0.9 (br, 39H).

PTB-Cl₅₀. **4** (76.5 mg, 0.162 mmol), **5** (62.6 mg, 0.081 mmol), **3** (68.1 mg, 0.081 mmol), 8 mL of toluene, and 2 mL of DMF were added to a 25-mL round-bottom flask equipped with a magnetic stir bar. The mixture was subjected to three freeze-pump-thaw cycles before being refilled with argon. Pd(PPh₃)₄ (9 mg, 8.1 × 10⁻³ mmol) was added, and the reaction was heated at 120 °C for 8 h. The purification process was the same as that for PTB-Cl₁₀₀. Yield: 110.3 mg, 86%. GPC: M_n = 152 kg/mol, PDI = 2.8; ¹H-NMR (500 MHz, C₂D₂Cl₄): 8.0-7.0 (br, 2H), 4.4 (br, 6H), 3.6 (br, 2H), 2.4-0.9 (br, 42H).

PTB-Cl₂₅. **4** (76.5 mg, 0.162 mmol), **5** (93.8 mg, 0.122 mmol), and **3** (34.1 mg, 0.041 mmol) were used as the reactants. The rest of the procedure was same as that for PTB-Cl₅₀. Yield: 89.5 mg, 71%; GPC: M_n = 208 kg/mol, PDI = 3.4; ¹H-NMR (500 MHz, C₂D₂Cl₄): 8.0-7.0 (br, 2H), 4.4 (br, 6H), 3.6 (br, 1H), 2.4-0.9 (br, 43.5H).

PTB-Cl_{12.5}. **4** (76.5 mg, 0.162 mmol), **5** (109.5 mg, 0.142 mmol), and **3** (17 mg, 0.020 mmol) were used as the reactants. The rest of the procedure was same as that for PTB-Cl₅₀. Yield: 76.5 mg, 62%; GPC: M_n = 208 kg/mol, PDI = 3.2; ¹H-NMR (500 MHz, C₂D₂Cl₄): 7.0-8.0 (br, 2H), 4.4 (br, 6H), 3.6 (br, 0.5H), 2.4-0.9 (br, 44.25H).

TTBDTTT-Cl. A 50-mL, 2-neck round-bottom flask equipped with a magnetic stir bar was charged with **4** (377.8 mg, 0.8 mmol), 20 mL of toluene, and 4 mL of DMF. The flask was evacuated and refilled with argon several times before Pd(PPh₃)₄ (23.1 mg, 0.02 mmol) was added. **3** (168.2 mg, 0.2 mmol) was dissolved in 10 mL of toluene and purged

with argon for 1 h. The reaction mixture was heated to 100 °C, and the solution of **3** was gradually added using a syringe over 2 h. The reaction was monitored by TLC and terminated by adding water when **3** was fully consumed. The crude product was extracted with methylene chloride (DCM) and dried over MgSO₄. The desired trimer TTBDTTT-Cl was separated from the higher oligomer by flash chromatography eluted using hexanes: DCM (2:1) to yield 16.8 mg of a sticky purple solid (6%). ¹H-NMR (400MHz, CD₂Cl₂): 7.56 (s, 2H), 4.29 (m, br, 8H), 3.58 (t, 4H), 1.91 (m, 4H), 1.83 (m, 4H), 1.76 (m, 2H), 1.64 (m, 4H), 1.56-1.35 (m, br, 28H), 1.02 (t, 6H), 0.97 (t, 6H).

3.2.3. General characterization

NMR was performed on Bruker AVANCE III 400 MHz, Bruker AVANCE III 500 MHz, and Bruker AVANCE II 600 MHz spectrometers equipped with a 5-mm TCI cryoprobe. High temperature NMR was performed on the Bruker AVANCE III 500 MHz. The molecular weights of the polymers were measured using gel permeation chromatography (GPC) composed of a Waters 1515 HPLC pump, a 2487 dual absorbance detector, and three Styragel columns with THF as the eluent. The GPC was calibrated against polystyrene standards.

UV-vis spectroscopy, cyclic voltammetry (CV), and differential scanning calorimetry (DSC) measurements were performed in the same manner as that described in Section 2.2.2. X-ray photoelectron spectroscopy (XPS) was performed using a Kratos Analytical Axis ULTRA spectrometer containing a DLD detector. The film thicknesses were measured using an Alpha-Step IQ profilometer (KLA-Tencor). Optical microscopy was performed using a Nikon Eclipse 50i microscope (equipped with a QICAM FAST 1394 camera).

3.2.4. Crosslinking

ITO glasses were cleaned by consecutive sonication in detergent, 2-propanol, acetone, and deionized water for 15 min each, and then treated with UV/ozone for 30 min. The polymer films (~120-nm thick) were spin-coated from chlorobenzene (CB) solutions (25 mg/mL, stirred at 50 °C overnight) onto the ITO glass substrates in a nitrogen-filled

glovebox. A 4-W hand-held UV lamp was used to provide mild 254 nm UV irradiation to initialize crosslinking. After irradiation, all films were immersed in CB for 10 min before rinsing in acetone and drying. The degree of crosslinking was evaluated using a profilometer and UV-vis absorption.

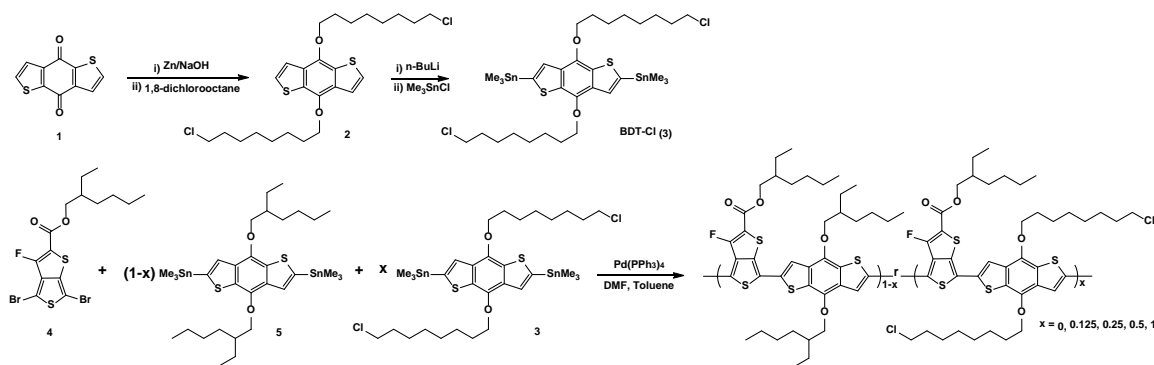
3.2.5. PV device fabrication, characterization, and stability

Patterned ITO glass was cleaned by consecutive sonication in detergent, 2-propanol, acetone, and deionized water for 15 min each, and then treated with UV/ozone for 30 min. PEDOT:PSS was spin-coated onto the ITOs from its stock solution at 5000 rpm for 1 min. The resulting slides were annealed at 140 °C in air for 10 min in a pre-heated oven, and immediately transferred into a nitrogen-filled glove box. Dichlorobenzene (DCB) solutions of polymer/PC₇₁BM (1:1.5 w/w, 25 mg/mL) were stirred overnight at 50 °C in the glove box prior to spin-coating. The solutions were filtered through a 0.45-mm PTFE syringe filter and then applied to the PEDOT:PSS coated substrates (0.2 μL for each slide) and spun at 1000 rpm for 1 min. Photocrosslinking was initiated by exposing the spin-coated films under a 4-W hand-held UV lamp for various periods of time. Subsequently, the devices were transferred into a thermal evaporator, where ~20 nm of Ca and subsequently ~100 nm of Al were evaporated through a shadow mask at ~10⁻⁷ torr. The devices were then mounted onto a test fixture equipped with a mask, and sealed in a homemade vacuum chamber featuring a quartz window. PV measurements were performed under an AM 1.5G spectrum delivered by a xenon arc lamp source (Newport model 66983) with a power density of 100 mW·cm⁻² and calibrated with a NREL calibrated reference diode. The J-V curves were measured using a Keithley 2400 source meter. Monochromatic light for the EQE measurement was provided by a Newport CS-260 monochromator (Model 74100). Evaluation of the device stability was carried out by thermally annealing the devices on top of a hotplate inside the glovebox in the dark at either 120 °C or 150 °C for up to 10 h. PV measurements and optical microscopy of the devices were performed at certain intervals during the thermal annealing.

3.3. Results and Discussion

3.3.1. Synthesis and characterization

The synthesis of the BDT-Cl monomer (**3**) and the general polymerization procedure are illustrated in Scheme 3.1. Compound **2** was synthesized through a one-pot Williamson ether synthesis following a published patent.⁴⁷³ The yield of this reaction is low (25%), probably because of a combined effect of the dual reactivity of dichlorooctane and the E2 elimination of alkyl halide in the presence of base (similar low yields have been observed for dibromooctane).⁴⁰² Although bromine is more widely used in UV sidechain crosslinking, the chlorine-terminated n-octyl chain was chosen as the crosslinkable sidechain in this work. During the development of crosslinkable PTB, the last synthetic step of the bromine version of the BDT-Cl monomer was extremely difficult, possibly because of n-butyl lithium attack on the bromine during the reaction. Indeed, studies have shown that alkyl bromide is more susceptible to lithium-halogen exchange than alkyl chloride.⁴⁷⁴ The choice of a linear octyl sidechain is mainly for synthetic reason because branched alkyl sidechains with halogen substitution on the chain end are difficult to prepare. However, the disadvantage of having the linear sidechain on the BDT unit is the decreased solubility because linear sidechains tend to have poorer solubilizing abilities than branched sidechains.^{89,193}



Scheme 3.1 Synthetic procedures of the monomer BDT-Cl (**3**) and the polymers, PTB-CIs, with different contents of chlorooctyl sidechain

PTB polymers with 100%, 50%, 25%, and 12.5% of BDT-Cl unit were synthesized via Stille polycondensation using toluene/DMF as the solvent.¹⁸⁸ These polymers were not end-capped. The polymerizations yielded molecular weights above 150 kDa, measured

by GPC (Table 3.1). The broad molecular weight distribution may be a result of the polymer aggregation behavior in THF.⁴⁷⁵ Due to the high population of linear sidechains, PTB-Cl₁₀₀ with 1:1 feed ratio of the two monomers exhibited limited solubility in common PV processing solvents, such as chlorobenzene, and *o*-dichlorobenzene. Therefore, the feed ratio of TT:BDT was adjusted to 1:1.1 for PTB-Cl₁₀₀ as a compromise between solution processability and molecular weight. The rest of the polymers with 1:1 TT:BDT ratios are fairly soluble in CB and DCB because of the more solubilizing 2-ethylhexyl groups on the regular BDT unit.

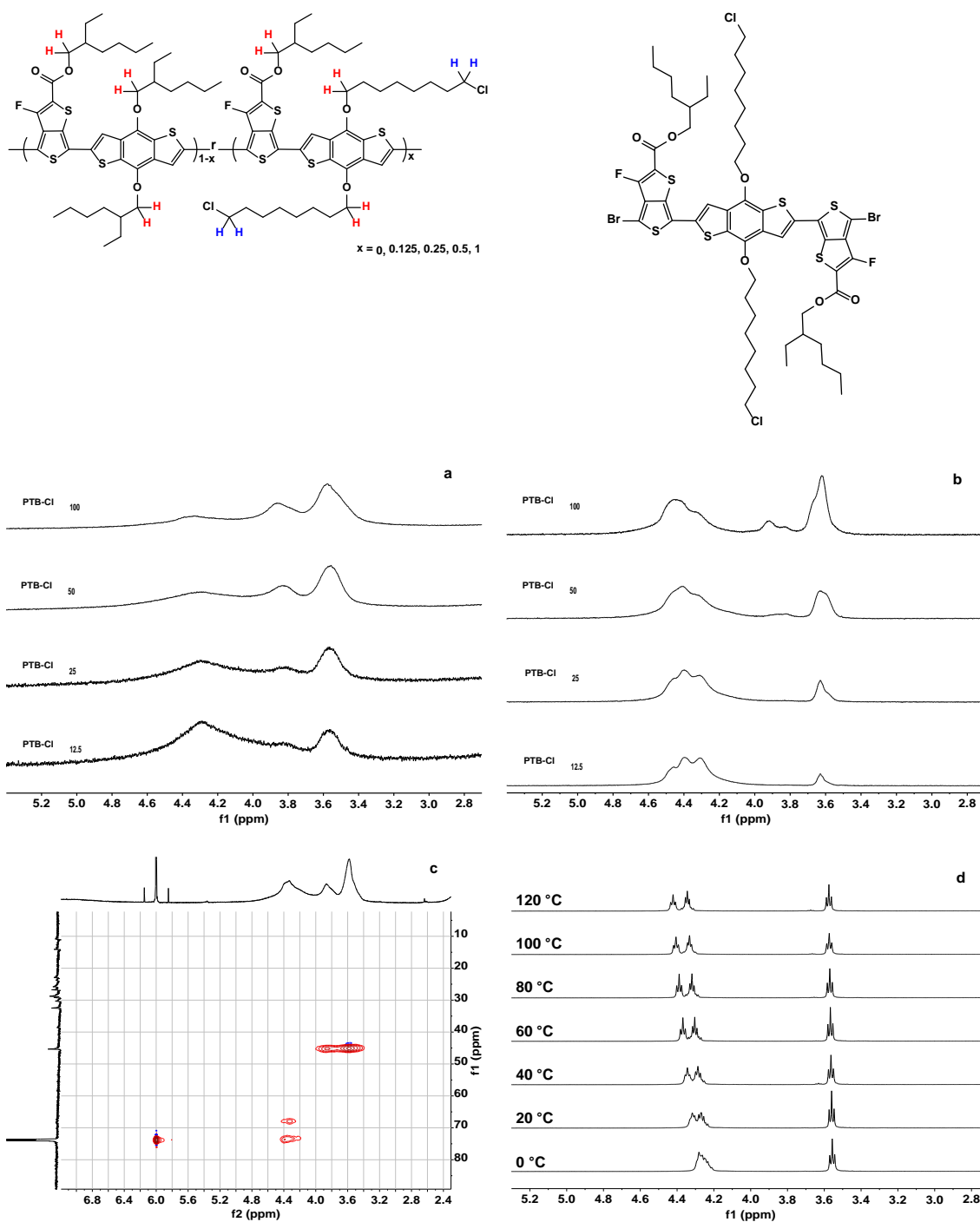


Figure 3.2 Chemical structures of PTB-Cl and TTBDTTT-Cl with the protons on $-O-CH_2-$ and $-CH_2-Cl$ highlighted in red and blue, respectively, NMR spectra of PTB-Cl at room temperature (a), NMR spectra of PTB-Cl at $120\text{ }^\circ\text{C}$ (b), heteronuclear single quantum coherence spectroscopy (HSQC) of PTB-Cl₁₀₀ at room temperature (c), and dynamic NMR spectra of TTBDTTT-Cl (d)

The structures of the polymers were confirmed by NMR spectroscopy. Specifically, the broad peak at ~ 4.4 ppm is assigned to the protons on the $-\text{O}-\text{CH}_2-$ groups, and the one at ~ 3.6 ppm is assigned to the $-\text{CH}_2-\text{Cl}$ group. For every 2-ethylhexyl substituent replaced by *n*-chlorooctyl, two $-\text{CH}_2-\text{Cl}$ protons are introduced and the number of $-\text{O}-\text{CH}_2-$ protons remains the same. Therefore, the ratio between these two peaks grows from 6:0 for PTB7 to 6:4 for PTB-Cl₁₀₀ (Table 3.1). Interestingly, all spectra of PTB-Cl_s acquired at room temperature feature a peak at ~ 3.8 ppm, which shrinks in intensity at 120 °C (Figure 3.2a, b). Counterintuitively, the HSQC result reveals that this peak belongs to the $-\text{CH}_2-\text{Cl}$ proton (Figure 3.2c). The exact origin of this peak is unknown. It has a high intensity at low temperature, a low intensity at high temperature, and is reversible, which suggests that this signal is related to certain polymer conformations in solution at room temperature that become disorganized with increased thermal energy. To gain further insights into the polymer structure, a trimer consisting of one BDT unit sandwiched by two TT units (TTBDTTT-Cl, Figure 3.2) was synthesized. Dynamic NMR spectra ranging from 0 °C to 120 °C show no additional signal between those of $-\text{O}-\text{CH}_2-$ and $-\text{CH}_2-\text{Cl}$, confirming the additional peak is indeed related to behaviours of the polymer (Figure 3.2d). The gradual resolving of the peaks at ~ 4.3 ppm with increasing temperature is likely due to atropisomerism of the trimer.⁴⁷⁶

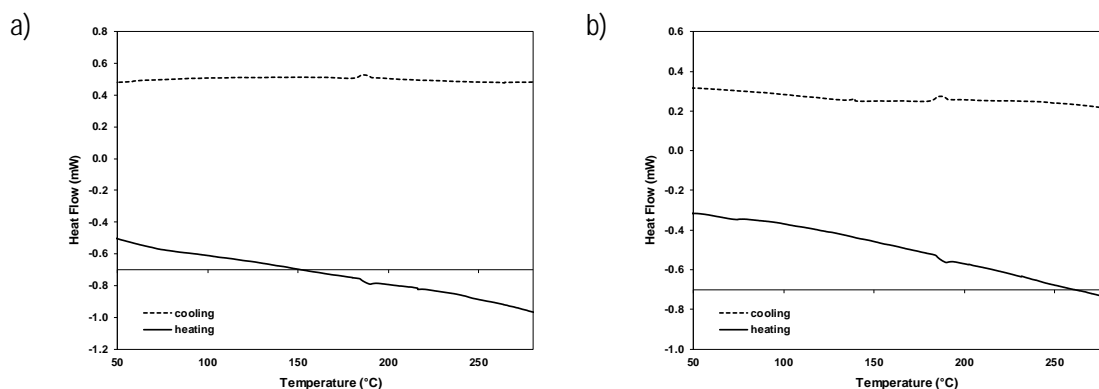


Figure 3.3 DSC results of PTB7 (a) and PTB-Cl₁₀₀ (b). Scan rate: 10 °C/min

Furthermore, DSC was performed on PTB and PTB-Cl₁₀₀ with a scan rate of 10 °C/min from 25 °C to 300 °C and back (Figure 3.3). All polymers exhibited a thermal transition at ~ 185 °C during both the heating and cooling scans; the transition is assigned to the glass transition (Section 2.3.1). No thermal events were detected other than the glass transitions, indicating no thermally activated reactions involving PTB-Cl₁₀₀.

Table 3.1 Structural characterization and opto-electronic properties of PTB7 and PTB-CIs

Polymers	M _n (kDa)	PDI	Int. ratio ^a 4.4 ppm: 3.6 ppm	λ _{max} (film) (nm)	E _g ^{opt} (eV)	HOMO (eV)	LUMO (eV)	E _g ^{CV} (eV)
PTB7	153	2.5	6:0	673, 624	1.70	5.1	3.3	1.8
PTB-CI ₁₀₀	48	3.3	6:4	686, 632	1.65	5.1	3.3	1.8
PTB-CI ₅₀	152	2.8	6:2	680, 630	1.66	5.2	3.4	1.8
PTB-CI ₂₅	208	3.4	6:1	672, 624	1.68	5.2	3.5	1.7
PTB-CI _{12.5}	208	3.2	6:0.5	671, 622	1.69	5.2	3.5	1.7

^a Integration ratio determined by ¹H NMR acquired at 120 °C

3.3.2. Opto-electronic properties

The absorption spectra of PTB7 and PTB-CIs are presented in Figure 3.4. All polymers exhibit similar absorption profiles in solution and in films, with a strong absorbance around 650 nm, which is typical for PTB derivatives.¹⁸⁵ The λ_{max} of PTB-CI₁₀₀ in solution is blue-shifted by ~15 nm compared to the other polymers, which can be ascribed to the effect of low molecular weight. In the solid state, however, the λ_{onset} of PTB-CI₁₀₀ is ~15 nm more than PTB7. In fact, the λ_{onset} is red-shifted as the BDT-CI content increases in PTB-CIs. As a result, the optical bandgap (E_g^{opt}) decreases from 1.70 eV for PTB7 to 1.66 eV for PTB-CI₁₀₀. A similar trend was observed for other groups of PTB polymers.^{185,188} The difference in the sidechain structure is likely the cause of the red shift. Polymers with linear sidechains adopt a closer π-π stacking than those with branched sidechains, allowing intermolecular excitations to be activated with lower energy photons.¹⁹⁴ The sidechains on the BDT unit govern the π-π stacking distance of PTB. Therefore, the introduction of linear sidechains results in closer packing and red-shifted optical absorptions for PTB-CIs. Cyclic voltammetry was performed for all polymers, and electronic bandgaps of 1.7–1.8 eV are found (Table 3.1). These results, together with the HOMO and LUMO levels, are in good agreement with the results for other PTB polymers.^{174,185}

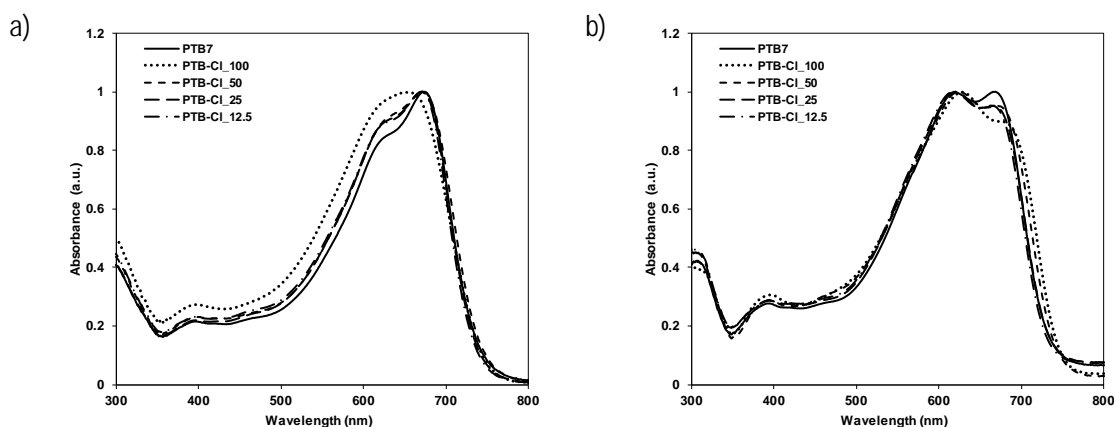






















Figure 3.4 Absorption spectra of PTB7 and PTB-CIs in dilute CHCl_3 solutions (a), and in ~ 120 nm thin films (b)

3.3.3. Crosslinking studies

Photocrosslinking and film insolubilization were evaluated qualitatively by visual observation, and quantitatively by measuring the absorption spectra and film thickness changes. The polymer thin films with a thickness of ~ 120 nm were spin-coated from their neat CB solutions onto UV/ozone-treated ITO substrates. After being illuminated with a low power UV lamp (4W, 254 nm) for 0, 10, 20, and 30 min, the films were immediately immersed in CB, rinsed with acetone, and then dried. The visual appearances of the films after UV irradiation and CB immersion are presented in Table 3.2. Long-term UV exposure clearly insolubilizes the PTB-CI films against CB dissolution, whereas it has no effect on PTB7, which has no photocrosslinkable sidechains. At shorter UV exposure times, the PTB-CI films are crosslinked but tend to peel from the substrate and break into insoluble pieces of various sizes. This observation suggests that the crosslinking starts from the surface of the films and propagates into the bulk of the film with time. The time required to fully insolubilize the PTB-CI films is proportional to the content of the photocrosslinkable sidechains. For PTB-CI₁₀₀ and PTB-CI₅₀, 10 min of UV irradiation is sufficient to insolubilize the film and secure it to the substrate, while for PTB-CI_{12.5}, crosslinking is not sufficient to hold the film together until 30 min of irradiation. UV irradiation through the back of ITO did not produce any crosslinking because of the strong UV absorption of ITO. Interestingly, although both PTB-CI₂₅ and PTB-CI_{12.5} peeled off and disintegrated in CB with 10 min of UV exposure; PTB-CI₂₅ formed large pieces while PTB-CI_{12.5} formed much smaller pieces

(Figure 3.5). After 20 min of UV exposure, PTB-Cl₂₅ became stable in CB while PTB-Cl_{12.5} broke into pieces with sizes similar to that of PTB-Cl₂₅ after 10 min of UV exposure. This observation suggests that the photocrosslinking is homogeneously initiated throughout the film. As the exposure time increases, the crosslinking propagates laterally and vertically until a crosslinked network is formed.

Table 3.2 Visual appearance of polymer thin films that were UV-irradiated for various times and subsequently immersed in chlorobenzene

UV time	PTB7	PTB-Cl ₁₀₀	PTB-Cl ₅₀	PTB-Cl ₂₅	PTB-Cl _{12.5}
0 min					
10 min					
20 min					
30 min					

To further explore the photocrosslinking and insolubilization of PTB-Cl, several other conditions were tested. A more powerful, 15-W UV lamp was used to expedite the crosslinking process. With 5 min of irradiation, all PTB-Cl polymers, except for PTB-Cl_{12.5}, were sufficiently crosslinked and insolubilized on ITO substrates. At 10 min, PTB-Cl_{12.5} was also fully insolubilized. Fast crosslinking is important in roll-to-roll manufacturing of large area devices because a long exposure time may slow the overall production output. Light-induced photo-oxidation has been reported for PTB7.^{298,299,477} To rule out the possibility that photocrosslinking is a combined effect of light and oxygen, photocrosslinking was performed in an oxygen-free and moisture-free glovebox using the low power UV lamp followed by immersing in CB and rinsing with acetone. The photocrosslinking was as effective as tested under ambient conditions, indicating that crosslinking is indeed photoactivated. In addition, the surface temperature of the UV

irradiation platform is measured using a thermal couple. After 30 min of continuous UV irradiation, the temperature reads 26 °C, which is slightly above room temperature. Thus, heat does not contribute to the photocrosslinking process.

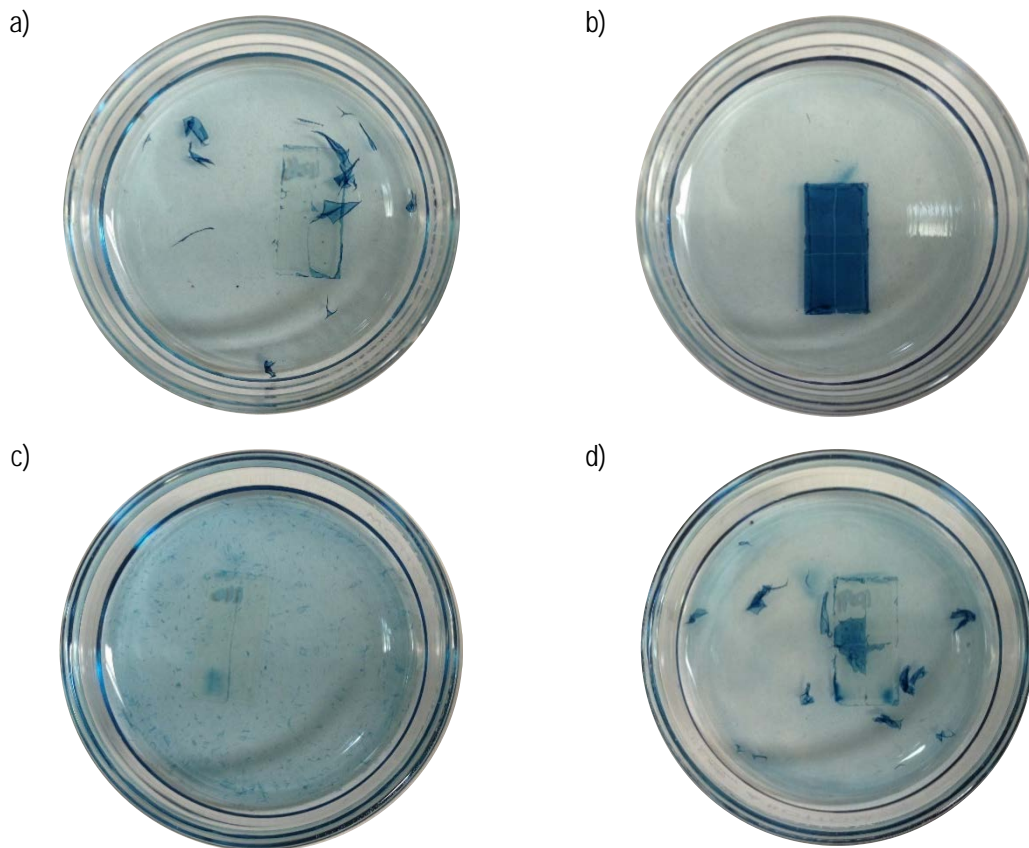
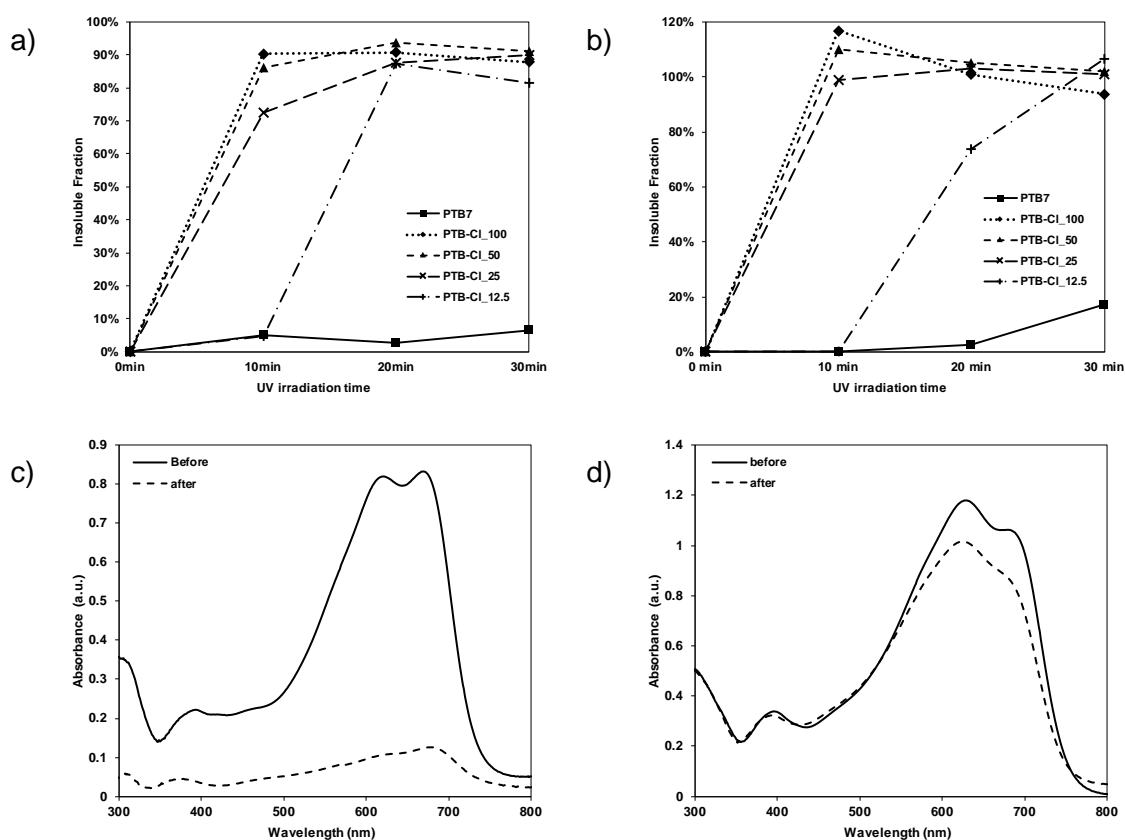


Figure 3.5 Visual appearances of the peeled-off films made from PTB-Cl₂₅ (a), (b), and PTB-Cl_{12.5} (c), (d) in CB after UV irradiation for 10 min (a), (c), and 20 min (b), (d)

Quantitative evaluation of the photocrosslinking was carried out by measuring the change in optical absorbance and film thickness. The percentage of the insoluble fraction was calculated by the ratio of optical absorbance integrations after and before the UV-irradiation/CB-immersion using a UV-vis spectrometer, as well as by the ratio of thickness after and before treatments using a profilometer. The results are presented in Figure 3.6. The quantitative evaluation agrees well with the visual observations of the films. Once the films became insoluble and stable on ITO after CB immersion, the crosslinking is 100%, because it proceeds in a top-down fashion. Some mid-range values could be measured for fractionated film pieces by careful handling of the films (e.g., refraining from agitating

the ITO with a detaching film), as is the case of PTB-CI₂₅ at 10 min in the absorption study and PTB-CI_{12.5} at 20 min in the thickness study. Film swelling was observed after solvent treatment, especially in the less crosslinked films that had been UV irradiated for 10 min. The swelling accounts for the values above 100% in the profilometer studies. The absorption profiles before and after 20 min of UV exposure/CB immersion are also presented in Figure 3.6. Photocrosslinked and insolubilized PTB-CI films retained their absorption characteristics, albeit with a reduction in absorption intensity. In contrast, solvent dissolution resulted in an almost complete disappearance of absorbance for PTB7.



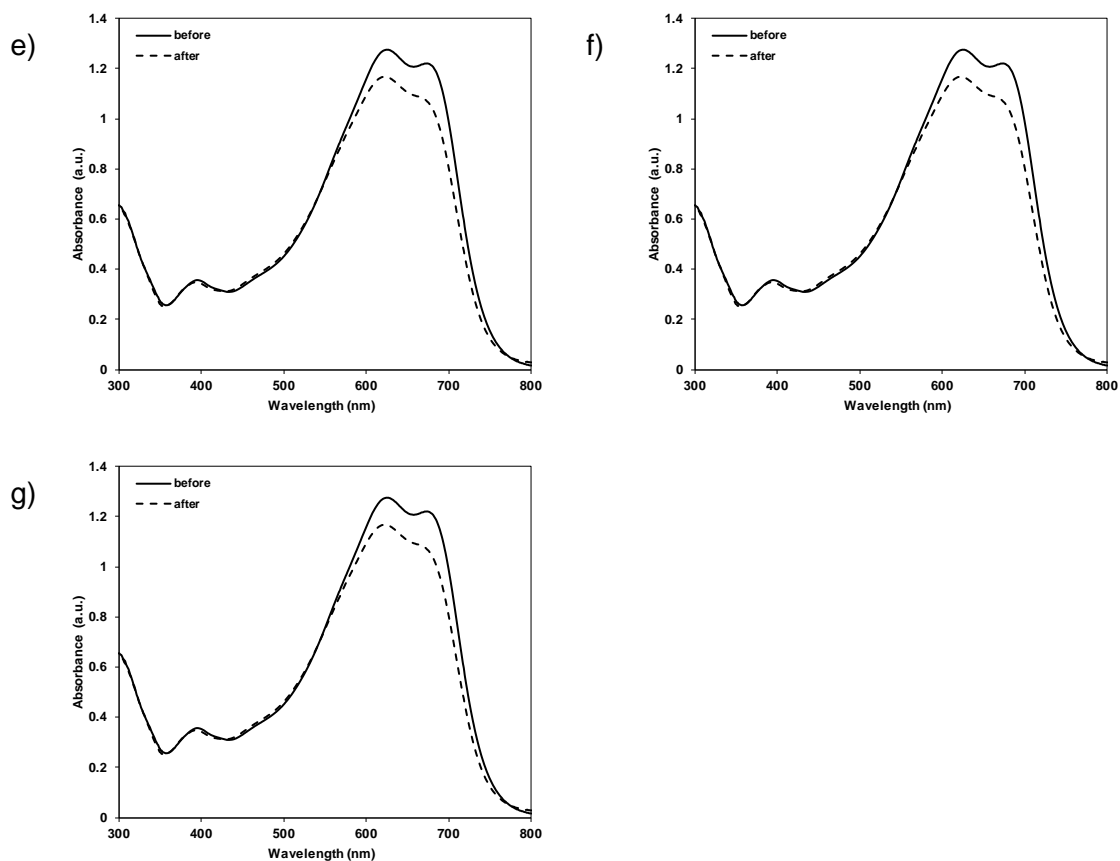


Figure 3.6 Quantitative evaluation of the photocrosslinking using UV-vis spectroscopy (a) and profilometry (b). Absorption spectra of PTB7 (c), PTB-CI₁₀₀ (d), PTB-CI₅₀ (e), PTB-CI₂₅ (f), and PTB-CI_{12.5} (g) before and after 20 min of UV irradiation followed by CB immersion

Next, a preliminary study of the photolithography capability of PTB-CIs was performed. A mask made from paper board with the pattern “SFU” (font width of 1 mm, Figure 3.7) was applied to three side-by-side PTB-CI samples (PTB-CI₁₀₀, PTB-CI₅₀, and PTB-CI₂₅). UV irradiation was delivered inside the glovebox with an exposure time of 30 min. The films were then developed by CB immersion. A clear pattern of the letters with clean edges was obtained across the three films, demonstrating a high selectivity of photocrosslinking (Figure 3.7a). Moreover, both positive and negative patterns were achieved on a single PTB-CI₁₀₀ film (Figure 3.7b). Photolithography of PTB polymers may find applications in the fabrication of high performance microcircuits with polymeric materials.

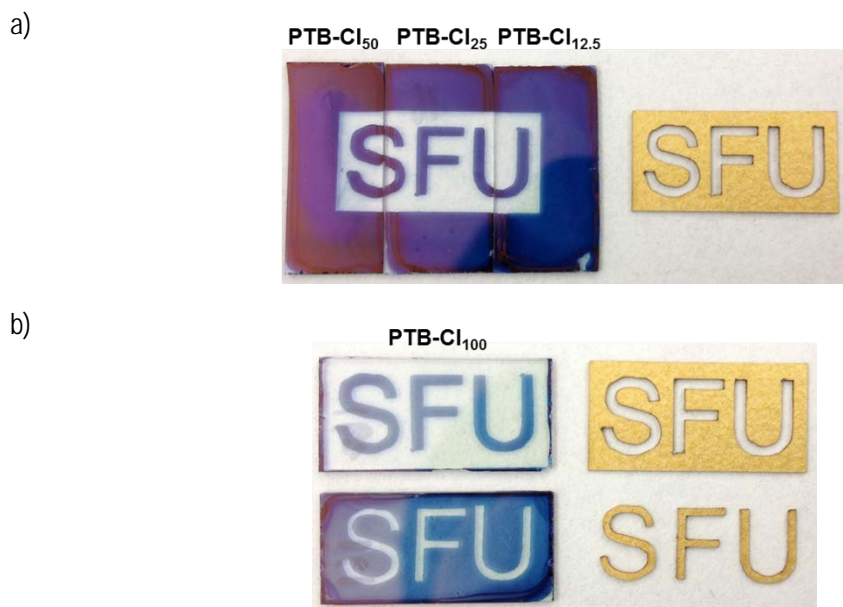
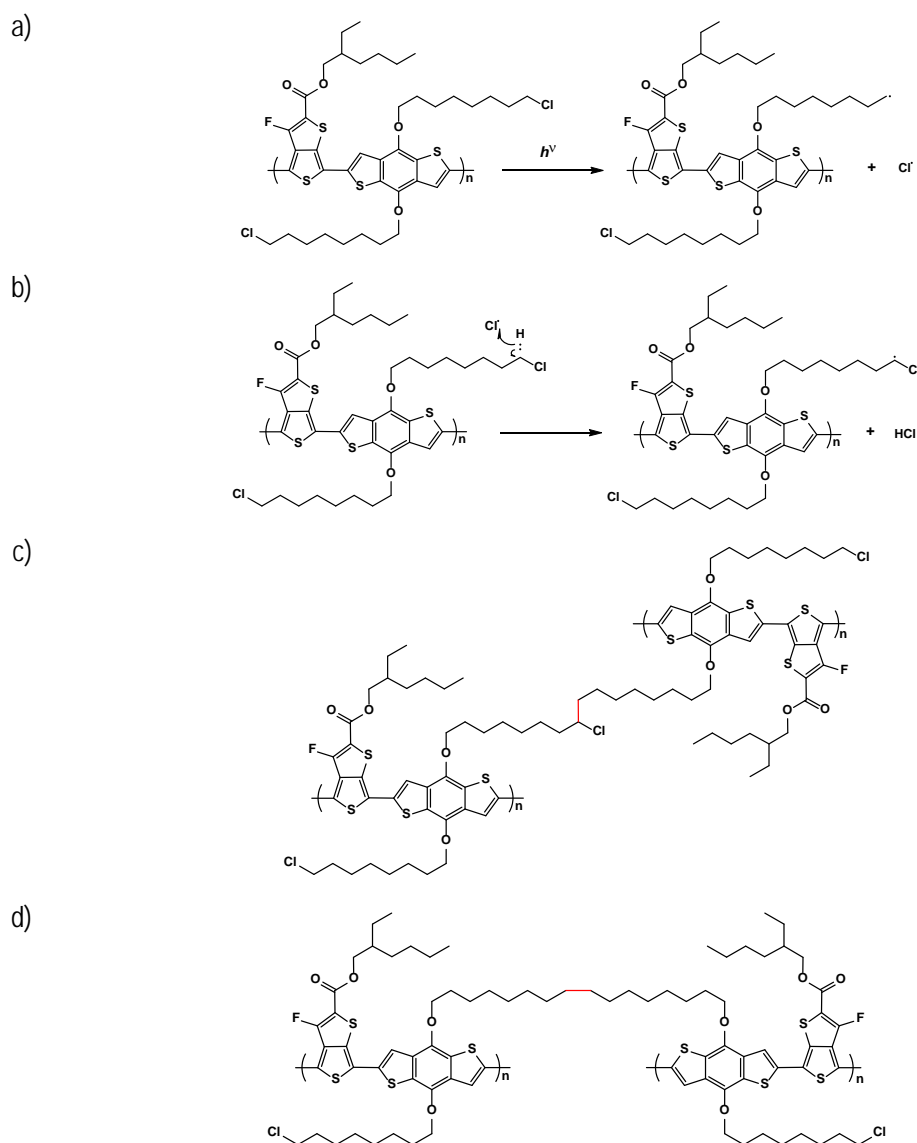


Figure 3.7 Demonstration of photolithography with PTB-Cl_s: a positive mask was applied across three polymer films (a), PTB-Cl₁₀₀, PTB-Cl₅₀, and PTB-Cl₂₅; positive and negative patterning of PTB-Cl₁₀₀ (b)

The photocrosslinking mechanism of PTB-Cl is believed to be a free radical process. Similar hypotheses have been raised in photocrosslinking studies of conjugated polymers bearing bromine functionalized sidechains.^{405,408} Indeed, chlorofluorocarbon (CFC) is one of the major causes of ozone depletion over Antarctica. The process involves a series of chain reactions that begin with UV-initiated chlorine-free-radical formation.⁴⁷⁸ Homolytic cleavage of the carbon-chlorine bonds have also been utilized in studies of photochemical absorbance of alkyl chloride species.⁴⁷⁹⁻⁴⁸¹ The proposed mechanism is illustrated in Scheme 3.2. Upon UV irradiation, homolysis of the C–Cl bond generates a chlorine radical, leaving a radical species on the end of the side chain. The highly reactive chlorine radical may randomly attack and transfer the unpaired electron onto another alkyl chain by abstracting a hydrogen from the C–H bond. The radical species on the alkyl chains can then terminate, forming new carbon-carbon bonds, which constitute the crosslinking network.



Scheme 3.2 Proposed mechanism of photocrosslinking for PTB-Cl: homolytic photolysis of the C–Cl bond (a); hydrogen abstraction (b); termination of two radical species (c) and (d)

XPS has been performed to verify the hypothesized mechanism. PTB-Cl film samples were surveyed before and after 30 min of UV irradiation in the glovebox. The UV irradiation was performed while the samples were still affixed to the XPS sample holder, and the test positions of the first surveys were saved to ensure the measurements were carried out at the exact same spots before and after UV irradiation. All samples showed a decrease of the chlorine peaks after UV treatment with other peaks almost unchanged (Figure 3.8). The chlorine loss is most prominent in the PTB-Cl₁₀₀ sample, where 20% was

lost after 30 min of UV irradiation. Given the ultra high vacuum of XPS ($< 10^{-9}$ torr), chlorine-containing side products are unlikely to be present in the films. The relatively small reduction of the chlorine signal in a long exposed, fully insolubilized sample suggests that the solid-state photocrosslinking is rather slow but effective because a small portion of the reaction renders the entire film insoluble. A similar observation was made for a thermally crosslinkable polythiophene, where the author found only a 4% reduction of signal in the fully crosslinked samples.⁴⁰⁴ The XPS results demonstrate that the crosslinking process is associated with the disappearance of chlorine. However, the identification of the radical species would involve complex techniques and is beyond the scope of this study.

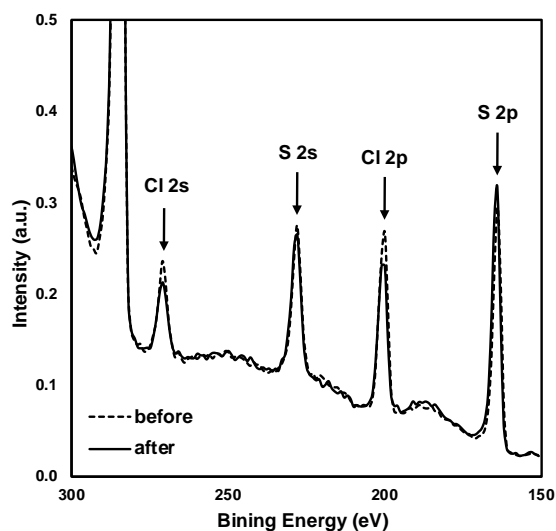


Figure 3.8 XPS spectra of PTB-Cl₁₀₀ before and after UV irradiation

3.3.4. Photovoltaic properties

Bulk heterojunction photovoltaic devices of PTB7 and PTB-Cl_s were fabricated in the conventional ITO/PEDOT:PSS/Polymer:PC₇₁BM/Ca/Al configuration and tested under standard 1 sun AM 1.5G illumination. The active layers were spin-coated from an *o*-dichlorobenzene solution of polymer:PC₇₁BM with a thickness of ~110 nm. J-V curves and EQE curves are presented in Figure 3.9, and PV parameters are tabulated in Table 3.3. All devices showed moderate PCEs of around 4.0–4.5% with similar FF, V_{oc} , and J_{sc} values. This indicates the introduction of photocrosslinkable sidechains on the BDT unit did not alter the PV performance of the polymers. The J_{sc} of the PTB-Cl₁₀₀ device is

noticeably lower than that of the other polymers. Examining the EQE curves, the quantum efficiencies of the PTB-Cl₁₀₀ device in the region of 500–700 nm are inferior to that of other polymers. Since the absorption of all the polymers are similar, this reduction in EQE might be a result of bad charge dissociation between PTB-Cl₁₀₀ and PC₇₁BM, which may be associated with the active layer morphology. A small amount of diiodooctane (DIO) can improve the J_{sc} of PTB/PCBM devices (Section 1.3).^{174,188} J-V and EQE curves of PTB-Cl₁₀₀/PC₇₁CM devices made from CB/DIO (97:3 v/v) are shown in Figure 3.9c. The solvent additive significantly improved the EQE at 500–700 nm for the PTB-Cl₁₀₀ device, providing a 30% increase of J_{sc} . Similar improvements have been reported for multiple PTB polymers in the past, where the authors ascribed the increased photocurrent to the improved morphology.¹⁸⁸ Therefore, the difference in the J_{sc} values observed here is likely an effect of the morphology. However, further morphological studies are required to fully understand the performance characteristics of PTB-Cl devices.

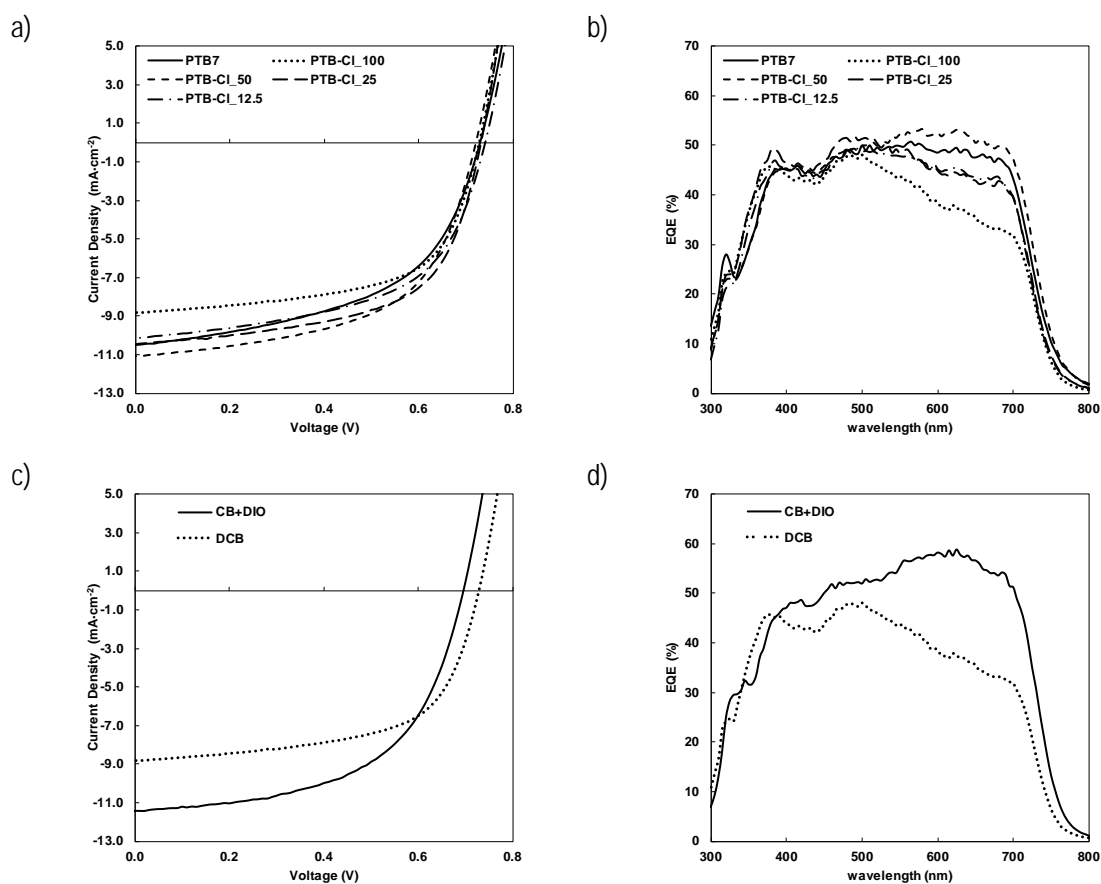


Figure 3.9 Current density–voltage (J-V) curves (a) and external quantum efficiency (EQE) curves (b) of PTB7 and PTB-Cl devices cast from dichlorobenzene (DCB); J-V curves (c) and EQE curves (d) of PTB-Cl₁₀₀ devices made from DCB (dotted) and (solid) CB/DIO (97:3 v/v)

Table 3.3 Photovoltaic characteristics of devices made from PTB7 and various PTB-Cl_s

Polymers	Solvent	J _{sc} (mA·cm ⁻²)	V _{oc} (V)	FF	PCE (%)
PTB7	DCB	10.47	0.73	0.52	4.0
PTB-Cl ₁₀₀	DCB	8.84	0.73	0.61	3.9
PTB-Cl ₅₀	DCB	11.10	0.72	0.57	4.5
PTB-Cl ₂₅	DCB	10.45	0.73	0.60	4.6
PTB-Cl _{12.5}	DCB	10.15	0.74	0.56	4.2
PTB-Cl ₁₀₀	CB+DIO	11.41	0.70	0.57	4.5

The influence of photocrosslinking on the PV performance was investigated. DIO was avoided in this study because of the additional complexity and DIO's detrimental effect on device performance during photocrosslinking.⁴⁰⁵ For all the PTB-Cl polymers, 10 min of UV exposure had a significant impact on the J-V characteristics. Both J_{sc} and V_{oc} values dropped dramatically after UV irradiation (Figure 3.10). This effect is most severe in PTB-Cl₁₀₀ devices, whose photocrosslinking is the strongest. Interestingly, this effect was partially reversed when the devices were thermally annealed following the UV exposure. The same reversible effect has been observed in other photocrosslinkable polymers with bromine-terminated sidechains.^{402,405} Indeed, conjugated polymers can be reversibly p-doped by molecular oxygen, forming a charge-transfer complex (CTC, Section 1.4.3).^{307,308} The formation of the CTC induces trapping sites and causes misalignment of energy levels between the polymer and the fullerene, resulting in losses of J_{sc} and V_{oc}.^{309–311} The formation process is accelerated by illumination while the dissociation process is activated by thermal annealing.^{307,310,312–315} Therefore, along the same line, the partially reversible degradation of performance by crosslinking is attributed to a reversible p-type doping of the polymer by chlorine radicals. However, the irreversible reduction of the PV parameters, especially the J_{sc}, might be caused by another mechanism. To compare, a PTB7 device was also subjected to 10 min of UV irradiation followed by thermal annealing. Unlike the PTB-Cl_s, the UV irradiation mainly affected the photocurrent, causing a loss of J_{sc} that was irreversible upon thermal annealing. Therefore,

the partially reversible deterioration of PV performance of PTB-CI devices was likely a combined effect of the reversible p-doping and certain irreversible effects.

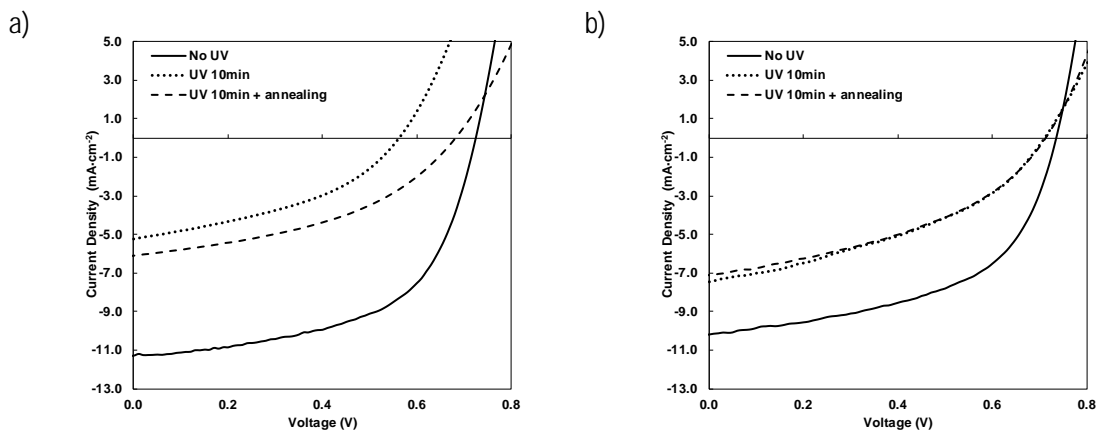


Figure 3.10 J-V curves of PTB-CI₅₀ (a) and PTB7 devices (b): as-cast (solid), after 10-min UV exposure (dotted), and thermally annealed following UV treatment (dashed)

3.3.5. Stability of PV devices

Evaluations of stability were carried out by thermally annealing solar cell devices at 120 °C inside the glovebox and measuring the PV parameters at the end of 1, 3, 5, 10 h of annealing. To find an optimal photocrosslinking condition that introduces sufficient crosslinking to stabilize the cell performance without a negative impact on the PV parameters, UV exposure times less than 10 min (e.g., 30 s, 1 min, 2 min, 5 min) were investigated. PCE profiles plotted against the annealing time are shown in Figure 3.11. Evolutions of J_{sc} , V_{oc} , and FF as functions of the annealing time are presented in Figure 3.12, Figure 3.13, and Figure 3.14, respectively. The PCE of the untreated PTB7 device degraded from 4.01% to 2.13% after 10 h of thermal annealing. In comparison, PTB-CI₁₀₀, PTB-CI₅₀, and PTB-CI₂₅ devices with UV exposure times of 30 s, 1 min, and 2 min exhibited better stabilities. As the UV exposure time increased from 5 min, the negative effect of photocrosslinking became significant, leading to inefficient PV performances. Remarkably, PTB-CI₅₀ devices with short UV irradiation of 30 s, 1 min, and 2 min exhibited the highest stable PCEs among all devices. The kinks on the PCE profiles of PTB-CI₅₀, UV-1min and PTB-CI₅₀, UV-2min devices at 1 h annealing are associated with the reversible doping effect. At this time scale, the effect was fully reversible because no

permanent J_{sc} loss was observed. The high device stability of the briefly UV irradiated samples is a combined result of stable J_{sc} and FF. In contrast, the non-crosslinked PTB-CI films showed poor stabilities, which are mainly caused by rapidly-degrading FF values. The crosslinking effect in the PTB-CI_{12.5} samples did not render the devices more stable than PTB7; however, the samples were more resistant to thermal stress compared to untreated PTB-CI_{12.5} devices.

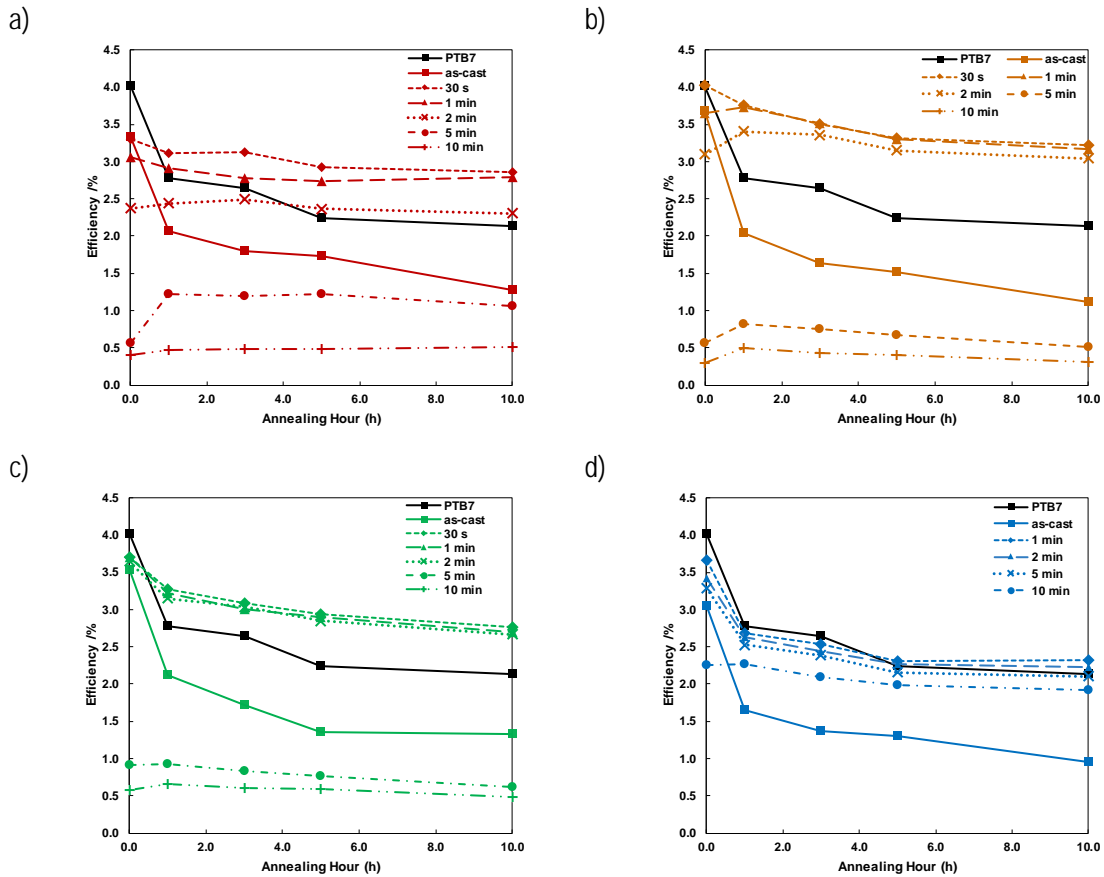


Figure 3.11 PCEs of PTB-CI₁₀₀/PC₇₁BM (a), PTB-CI₅₀/PC₇₁BM (b), PTB-CI₂₅/PC₇₁BM (c), and PTB-CI_{12.5}/PC₇₁BM (d) devices with various UV exposure times as a function of annealing time at 120 °C, compared with PTB7/PC₇₁BM device

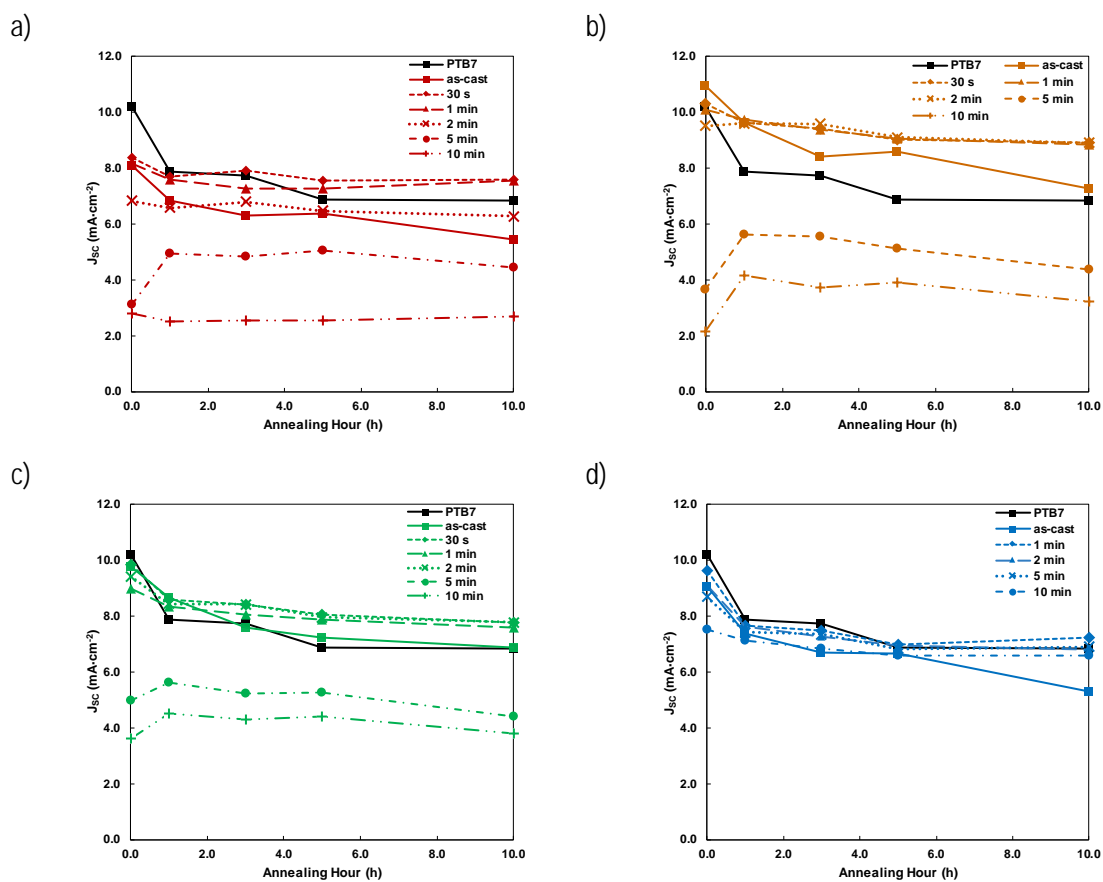
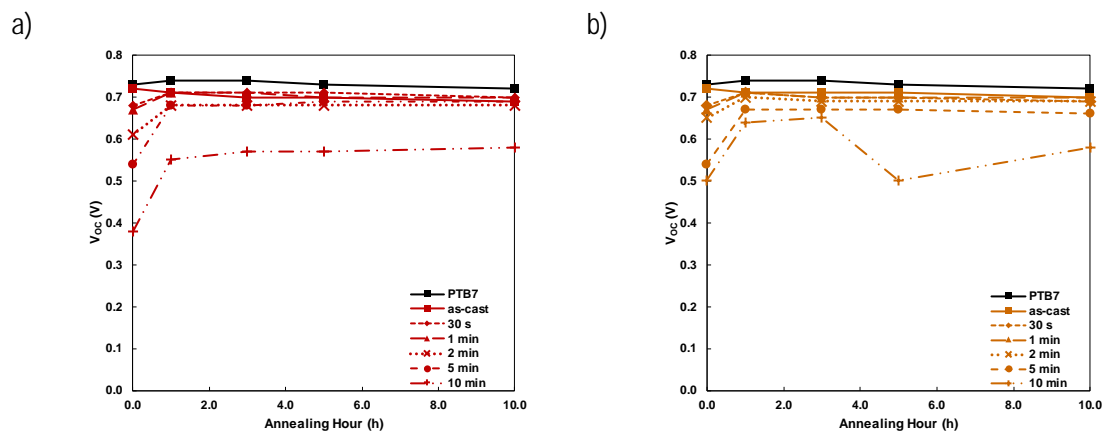


Figure 3.12 J_{sc} of PTB-Cl₁₀₀/PC₇₁BM (a), PTB-Cl₅₀/PC₇₁BM (b), PTB-Cl₂₅/PC₇₁BM (c), and PTB-Cl_{12.5}/PC₇₁BM (d) devices with various UV exposure times as a function of annealing time at 120 °C, compared with PTB7/PC₇₁BM device



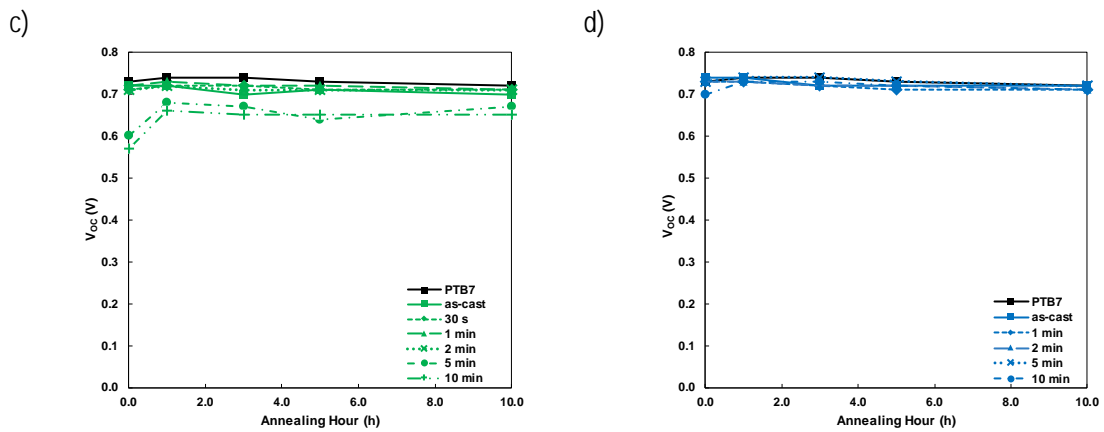


Figure 3.13 V_{oc} of PTB-Cl₁₀₀/PC₇₁BM (a), PTB-Cl₅₀/PC₇₁BM (b), PTB-Cl₂₅/PC₇₁BM (c), and PTB-Cl_{12.5}/PC₇₁BM (d) devices with various UV exposure times as a function of annealing time at 120 °C, compared with PTB7/PC₇₁BM device

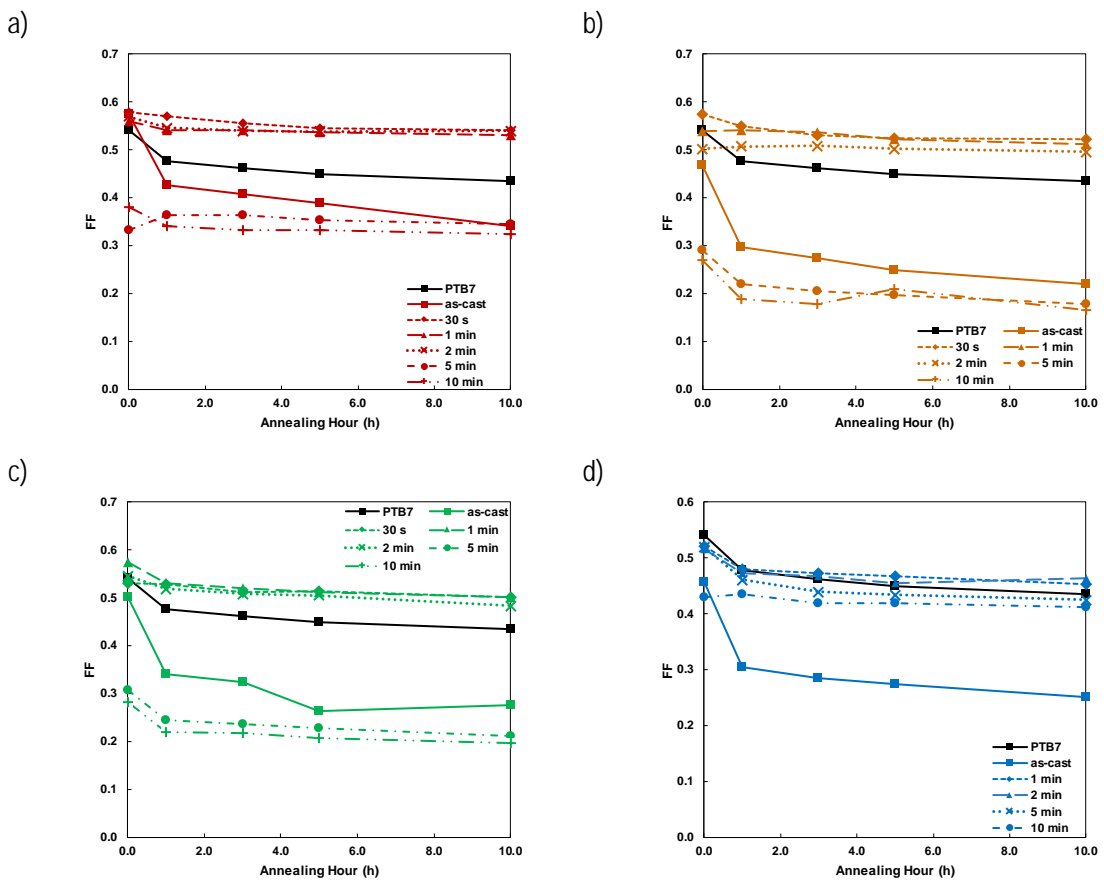


Figure 3.14 FF of PTB-CI₁₀₀/PC₇₁BM (a), PTB-CI₅₀/PC₇₁BM (b), PTB-CI₂₅/PC₇₁BM (c), and PTB-CI_{12.5}/PC₇₁BM (d) devices with various UV exposure times as a function of annealing time at 120 °C, compared with PTB7/PC₇₁BM device

Optical microscopy studies were performed on all devices annealed at 120 °C; however, no PCBM crystallization was observed throughout the 10-h annealing. PC₇₁BM crystallizes at a much slower rate than PC₆₁BM in polymer/PCBM blend films.³³⁷ Consequently, polymer/PC₇₁BM devices are more stable against thermal annealing than the same devices made with PC₆₁BM.⁴⁰² Hence, the degradation of PV parameters observed here is not an effect of large-scale phase segregation caused by PCBM crystallization. However, nanoscale morphologies are also important for device performance.^{238,258} Nanoscale phase segregation that is not in the form of PCBM crystallization has been observed and is responsible for degrading the PV parameters.⁴⁸² Thus, the degradation of non-crosslinked polymer/PCBM devices is probably a result of deterioration of the nanoscale morphology. Photocrosslinking of PTB-CIs, even to a small degree, inhibits the nanoscale morphological degradation and improves the thermal stability of the device. However, prolonged UV irradiation negatively affects the PV performance through the reversible and irreversible mechanisms, and the photocrosslinking should be kept at a moderate level.

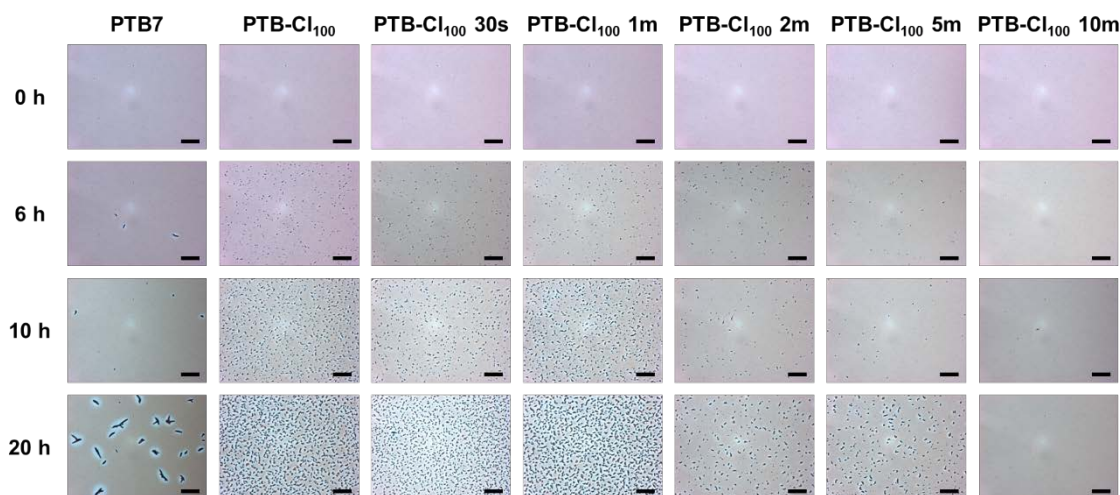


Figure 3.15 Optical microscopic images of PTB-CI₁₀₀/PC₇₁BM films UV treated for different times after 0, 6, 10, 20 h of thermal annealing at 150 °C, compared with PTB7/PC₇₁BM films. Scale bar: 20 μm

Morphological stability was studied at a higher temperature, 150 °C, for up to 20 h to investigate the effect of photocrosslinking on PCBM crystallization within the experimental timeframe. The images were taken on complete PV devices with polymer/PC₇₁BM bulk heterojunctions as the active layers. The results are presented in Figures 3.15, 3.16, 3.17, and 3.18. A clear trend is observed for the PTB-Cl devices. With short UV irradiation or no UV treatment, more PCBM crystals were found after 20 h of thermal annealing when more BDT-Cl unit are present in the structure. In all cases, 10 min of UV exposure was sufficient to secure the active layer morphology against PCBM crystallization. However, at shorter exposure times, the stabilization was less effective as the percentage of the BDT-Cl unit increases. Interestingly, the morphology of PTB7/PC₇₁BM was quite stable during the thermal annealing. Only sporadic crystals were found up to 10 h of annealing. Extending the annealing to 20 h provided large crystalline features with dimensions of 10–20 μm in length. The blue halos surrounding the crystals are regions depleted of PCBM.^{353,358}

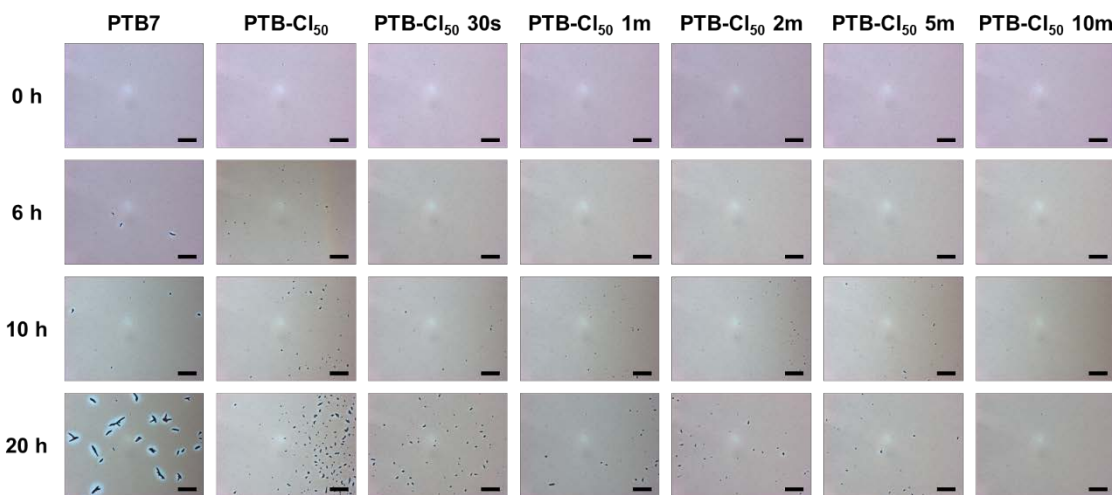


Figure 3.16 Optical microscopic images of PTB-Cl₅₀/PC₇₁BM films UV treated for different times after 0, 6, 10, and 20 h of thermal annealing at 150 °C, compared with PTB7/PC₇₁BM films. Scale bar: 20 μm

The differences in crystal size, number, and onset time are quite noticeable for the PTB7 and PTB-Cl₁₀₀ films. Densely populated, small crystals (~2 μm), which started to appear as early as 6 h into thermal annealing, were found in the final morphology. This observation strongly points to crystallization kinetics with the nucleation rate greater than the growth rate, such that the PCBM molecules tend to emerge from the polymer matrix

and form new nuclei rather than joining existing crystals. In contrast, the PCBM crystallization in the PTB7 film is nucleation limited, i.e., the growth rate is higher than the nucleation rate, resulting in large, sparse crystals. The difference in the PCBM crystallization kinetics of PTB7 and PTB-Cl₁₀₀ films is attributed to the structural dissimilarity of the sidechains on the BDT unit. As also observed in the absorption behaviours, PTB-Cl with linear chlorooctyl sidechains adopts closer π - π stacking than PTB7 with branched 2-ethylhexyl sidechains. Thus, the closely packed PTB-Cl₁₀₀ likely expelled the PCBM from the mixed phase which then became nuclei, whereas the loosely packed PTB7 with branched sidechains hindered this process, leading to contrasting nucleation kinetics.

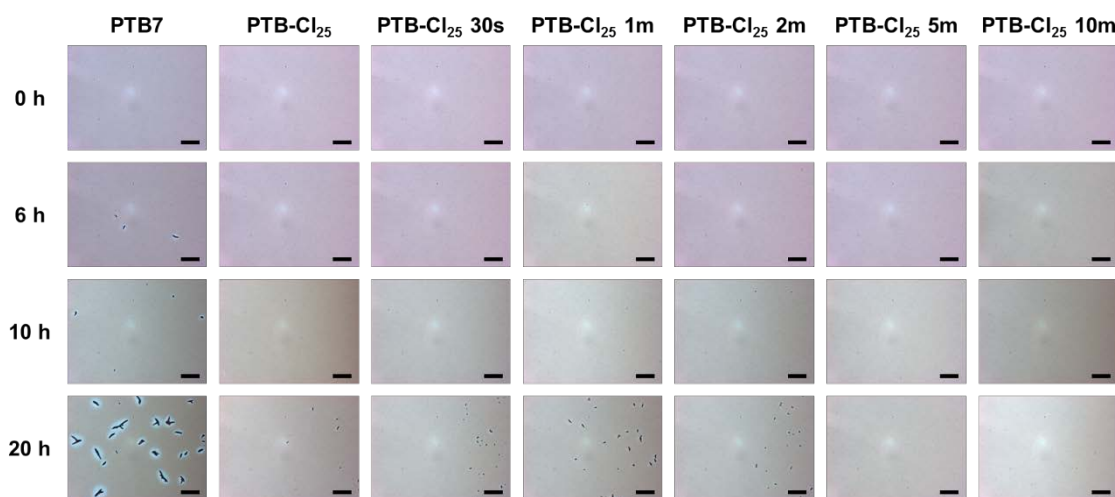


Figure 3.17 Optical microscopic images of PTB-Cl₂₅/PC₇₁BM films UV treated for different times after 0, 6, 10, and 20 h of thermal annealing at 150 °C, compared with PTB7/PC₇₁BM films. Scale bar: 20 μ m

Moderate crosslinking in PTB-Cl_{12.5} can retard nucleation, as evidenced by the lack of PCBM crystals in all samples. However, the low degree of photocrosslinking was not effective to counterbalance the increased nucleation rate caused by the introduction of linear sidechains as the BDT-Cl content increases. As a result, PCBM crystals started to appear in PTB-Cl₂₅ samples after 20 h of thermal annealing. Noticeably, under the optical microscope, no PCBM crystallization was observed near the top electrode for all samples after 20 h of thermal annealing, even for the pristine PTB-Cl₁₀₀ device. The high density of the PCBM crystals on the device appeared hazy on the film to the naked eye; however, a ring of clear film could be seen that surrounds the electrode (Figure 3.19a). Under the

optical microscope, no PCBM crystals could be found in this clear region for all samples. This clear part of the film extends underneath the electrode, where no haziness could be seen from the back of the device, indicating no PCBM crystallization. This finding suggests that the electrode has a strong stabilizing effect on the film morphology, suppressing PCBM crystallization beneath it. This phenomenon, attributed to the confinement effect of the top electrode, has been well documented for other polymer/fullerene BHJ devices.^{356,357}

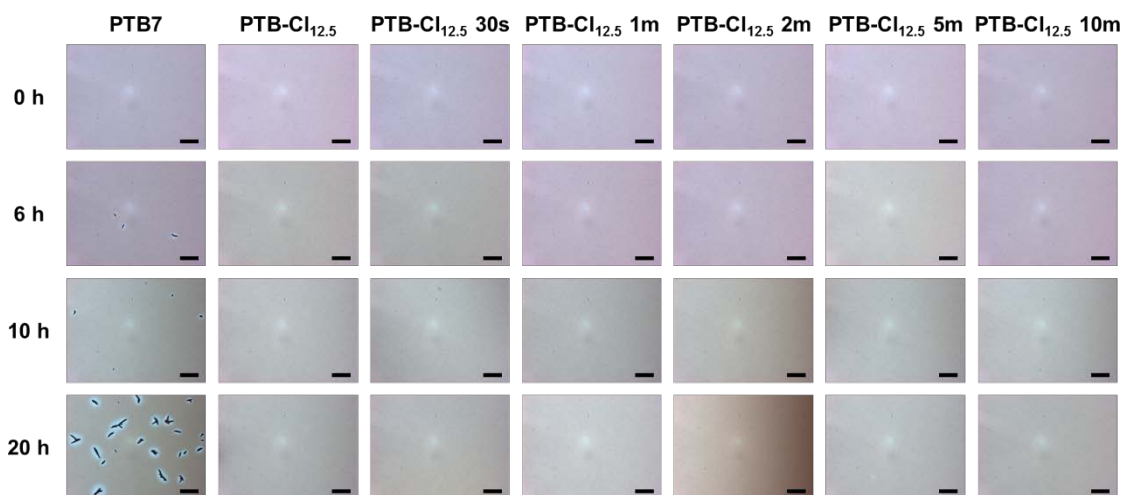


Figure 3.18 Optical microscopic images of PTB-Cl_{12.5}/PC₇₁BM films UV treated for different times after 0, 6, 10, 20 hours of thermal annealing at 150 °C, compared with PTB7/PC₇₁BM films. Scale bar: 20 μm

The photovoltaic stability study at 150 °C annealing was not successful because all the devices readily and dramatically degraded to the same value after only 30 min of thermal annealing, regardless of their initial performance or UV treatment history. Degradation of the metal electrode could be seen after 30 min of thermal annealing, as the electrode lost its mirror-like glossy appearance. Pinholes are seen on the edge of the metal electrode under the optical microscope after prolonged thermal annealing (Figure 3.19b). In addition, no crystallization of PCBM was observed in any part of the devices after 30 min of thermal annealing. Therefore, the dramatic degradation of PCE is not related to the large-scale morphology segregation, but rather a result of deteriorated electrode or organic/metal interface. The degradation of the electrode might be caused by oxygen or moisture absorbed during the transfer of the devices from the glovebox to the vacuum test chamber because the devices were not encapsulated.

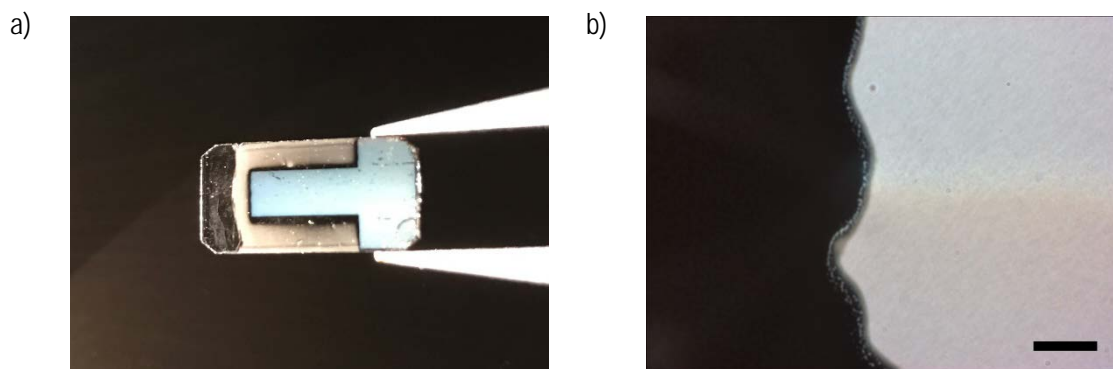


Figure 3.19 The visual appearance of a PTB-Cl₁₀₀/PC₇₁BM device without UV treatment (a), and the optical microscopic image of pinhole formation at the edge of the Ca/Al electrode (scale bar: 20 μm) (b), after 20 h of thermal annealing at 150 °C

3.4. Conclusion

Photocrosslinking with chlorine was demonstrated with a series of low-bandgap, PTB-based polymers containing different percentages of chlorine-terminated n-octyl sidechains. The polymers, named PTB-Cl_s, were synthesized by Stille polycondensation with high molecular weights. Introducing chlorinated sidechains did not significantly alter the opto-electronic properties of PTB-Cl_s compared to those of PTB7. However, PTB-Cl_s with more linear chlorooctyl sidechains (e.g., PTB-Cl₁₀₀) exhibited red-shifted absorption profiles, which are attributed to increased π - π stacking. Photocrosslinking initiated by deep-UV irradiation can effectively insolubilize PTB-Cl thin films, which retained ~90% of the absorption characteristics after solvent immersion. Film patterning was demonstrated using the insolubilization property. The mechanism of the photocrosslinking is probably a radical process, as supported by XPS studies. PSC devices made of PTB-Cl/PC₇₁BM BHJ displayed efficient PCEs that were comparable to that of PTB7/PC₇₁BM devices. However, a partially reversible reduction in both the J_{sc} and V_{oc} values was observed in devices that were UV irradiated for 10 min. This finding was ascribed to a combined effect of reversible p-doping by chlorine radical and irreversible degradations caused by UV irradiation. Low degree photocrosslinking introduced by UV exposure for less than 5 min improved the device stability without damaging the initial performance. However, regarding the large-scale phase segregation in the form of PCBM crystallization, high contents of linear chlorooctyl sidechains increase the nucleation rate, producing a large number of PCBM

crystals, which cannot be prevented by low-degree-photocrosslinking with UV exposure times below 10 min. Only PTB-Cl_{12.5}, the polymer with the fewest linear sidechains, was able to inhibit PCBM crystal formation by mild photocrosslinking. The above findings indicate that substituting linear, chlorooctyl sidechains for the branched 2-ethylhexyl sidechains on the BDT unit introduces three effects associated with PV performance: 1) morphology stabilization induced by photocrosslinking; 2) performance damage inflicted by the reversible polymer doping effect and irreversible photodegradation during prolonged UV exposure; 3) morphology degradation caused by the increased PCBM crystallization as a result of the linearity of the sidechains. The first effect can counterbalance the third effect; however, magnifying the first effect with longer UV exposures inevitably increase the second effect, which is undesirable. Therefore, minimizing the negative effects while utilizing the positive one requires a low content of BDT-Cl and shorter UV exposure. Thus, PTB-Cl_{12.5} with short UV irradiation seems to be the best candidate for PV devices with long-term thermal stability. For future studies, bromine versions of PTB-Cl_s are of great research interest. The less reactive bromine radical may shift the balance of photocrosslinking and UV degradation. A morphological stability strategy with a broader freedom of tuning the chemical structural and crosslinking conditions can be derived from there.

Chapter 4.

Accurate Characterization of Polymer Solar Cells Using a Simple Xenon Arc Lamp in an All-in-one Apparatus

4.1. Introduction

Polymer solar cells have received widespread research attention in the past two decades since the introduction of donor-acceptor bulk heterojunction cell configuration.⁶² Recently, the power conversion efficiencies of single junction polymer solar cells have surpassed 10% using state-of-the-art polymers and advanced fabrication processes.^{31,36,89} The power conversion efficiency, among other parameters, is perceived as the figure of merit of solar cell technologies that justifies the scientific impact of a publication and the worth of an emerging technology for commercialization. This holds true especially for the community of polymer solar cell research, where the advancement on efficiency is extremely difficult, while the highest reported value lies well below other rivaling solar cell technologies.⁴⁸³ Undoubtedly, accurate measurement of efficiency is essential to maintain the credibility and healthy development of this field, particularly when 1% efficiency increase is regarded as a breakthrough these days. In fact, for such purpose, a number of articles have been published addressing the sources of measurement errors and providing corresponding solutions.^{484–491} Despite their efforts, a large fraction of researchers have not been appropriately characterizing their devices following the established standard protocols, which has led to erroneous figures being reported in a great number of literatures.⁴⁹² This problem is partly due to the highly demanding equipment setup, which is emphasized in several papers providing characterization guidelines.^{487–489,491} In practice, an AAA rated solar simulator can be highly costly,⁴⁹³ let alone the accessories and a separate quantum efficiency system needed to complete the whole characterization. For research groups that are not specialized in device characterization, or those with limited funding, getting their newly developed polymers tested in a solar cell device with state-of-the-art instruments can be difficult. A compact, low-cost, but accurate testing station is desired for many polymer solar cell researchers

as they can obtain accurate evaluation of their products in a timely manner and hence make reasonable adjustment to their research. Xenon arc lamps are the most widely used light sources for solar simulation due to the continuous emission spectrum of xenon in the UV-visible region that closely matches the terrestrial solar spectrum.⁴⁹⁴ Using a xenon arc lamp supported by a basic lamp housing seems to be an economic alternative to a solar simulator. However, the light generated in this setup does not meet the quality required by accurate measurement. The lack of spatial uniformity can cause significant errors in efficiency measurements. Some articles have specifically warned against the use of a basic arc lamp as the source of simulated sun light for the same reason.^{488,489} The inaccuracy can be further compounded by the incorrectly assigned device area as well as the wrong choice of calibration devices. In this chapter, possible errors in efficiency measurements of polymer solar cells using a basic xenon arc lamp source will be first presented. Then, improvements of the light quality and the measurement accuracy via simple modifications to the lamp, and by following correct calibration procedures will be demonstrated. The instrument setup in this study can also serve as an example of utilizing a single light source to perform both the current-voltage (I-V) characterization and external quantum efficiency (EQE) measurement while fulfilling the rigorous requirements of accurate testing.

4.2. Experimental Section

4.2.1. Materials and device fabrication

Regioregular P3HT was purchased from Rieke Metals Inc.; PC₆₁BM was purchased from American Dye Sources Inc.; Polyethylenimine, 80% ethoxylated (PEIE) (35-40 wt%) water solution and MoO₃ powder were received from Sigma-Aldrich Co.; ITO glass substrates (15 Ω/□) were purchased from Colorado Concept Coatings LLC., etched and cut in-house. ITO glass slides were sonicated for 15 minutes each in detergent water, 2-propanol, acetone consecutively before UV-ozone treatment for 30 minutes. PEIE is diluted to 4 wt% with methoxyethanol, spin-coated onto ITO at 5000 rpm for 1 minute, and annealed at 100 °C for 10 minutes.⁷² P3HT/PCBM solution (1:1 by weight, 40 mg/mL in chlorobenzene) was stirred overnight at 50 °C on a hotplate inside a nitrogen filled

glovebox. P3HT/PCBM solution was spin-coated onto the PEIE coated ITO glass slides at 1000 rpm for 1 minute inside the glovebox, yielding ~200 nm thick active layers. The devices were further annealed at 160 °C for 10 minutes on a hotplate inside the glovebox before being taken out of the glovebox and placed in a thermal evaporator, where 15 nm MoO₃ and 150 nm Ag were deposited sequentially at $\sim 4 \times 10^{-7}$ torr vacuum.

4.2.2. Photovoltaic measurements

The laboratory setup uses a 300 W xenon arc lamp source (model 66983) and a CS-260 monochromator (model 74100), both supplied by Newport Co. I-V curves are recorded using a Keithley 2400 source-meter controlled by LabVIEW programs. A KG5 filtered silicon diode (Hamamatsu S1133) with a device area of 0.0756 cm², certified at NREL is used to calibrate the light intensity following the aforementioned procedures. The solar cell devices are fixed behind the mask on the cell fixture sealed in a vacuum chamber equipped with a quartz window through which the light passes. The I-V scans are carried out from reverse to forward bias at a scan rate of 0.1 V·s⁻¹. At the NREL, the I-V measurements use an Abet solar simulator calibrated to measure PV performances under AM 1.5G (IEC 60904). The fast scan is carried out from forward to reverse bias and back at 0.09 V/s before and after the slow asymptotic scan. The slow asymptotic scan records around 10 data points around the P_{max} and takes 131–192 seconds.

4.3. Results and Discussion

4.3.1. Instrument setup

In this study, a Newport Cornerstone 260 monochromator connected with a Newport 66983 research arc lamp source was used. A 75/25 beam splitter is installed in the light path to divert 25% of the light onto the direction orthogonal to the original path for I-V measurements. An AM 1.5G filter is placed between the lamp housing and the beam splitter to correct the spectrum of the output light. Additional optics are positioned at the side beam path to improve spatial uniformity (Figure 4.1).

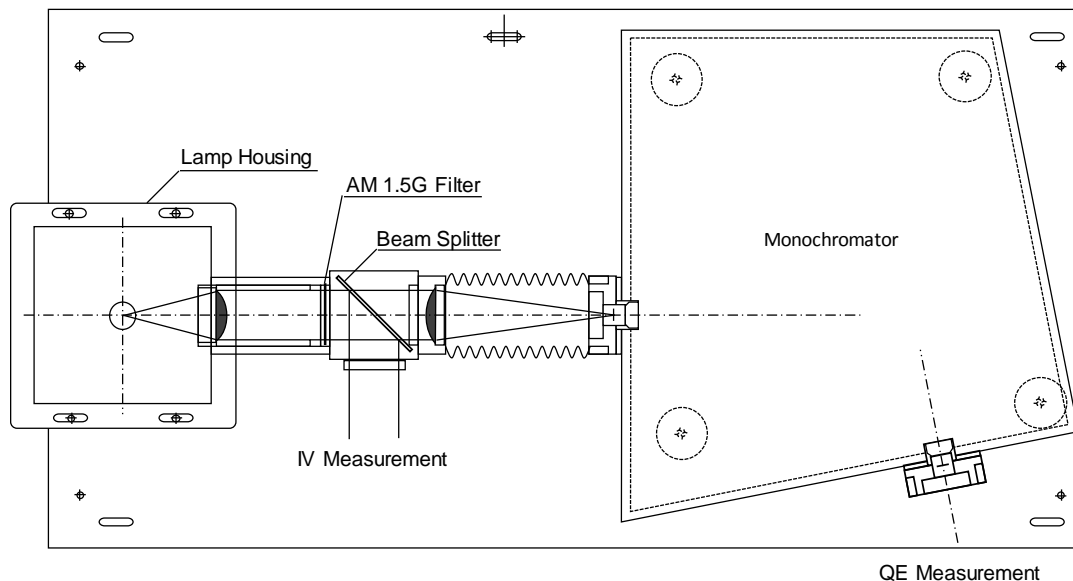


Figure 4.1 The layout of the instrument used in this study. A beam splitter diverts a portion of the light to the side as the source of light for I-V measurement

Basically, this setup uses the light source of an EQE measurement as the simulated sun light. The benefit is the elimination of a stand-alone solar simulator. Also, the monochromator can be used to measure the spectral irradiance of the source light, which is an important piece of information for calibrating the light intensity using the mismatch factor method.^{484,485,488,495}

4.3.2. Device layout and test fixture

The polymer solar cell devices used in this study were fabricated in inverted structures. As shown in Figure 4.2, the device consists of five main layers: the ITO coated glass substrate, PEIE interfacial layer, active layer containing the polymer:PCBM blend, the hole conducting MoO₃ layer, and the silver anode. The effective area of the device is defined as the area where all five layers overlap. The ITO glass substrate used in this work has a dimension of 10 × 20 mm. Each substrate contains only one device with a dimension of 4 × 5 mm² (active area = 0.2 cm²).

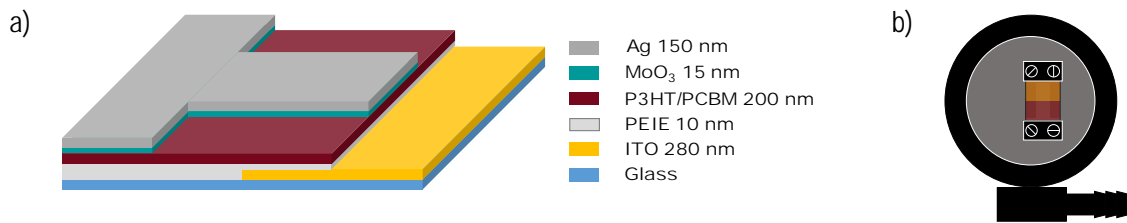


Figure 4.2 PV device layout showing all the layers (a); front view of the device holder (b). The device fixed on the back cover of the vacuum chamber is viewed through the quartz window

The test fixture is fixed on the back cover of a vacuum chamber, which has a quartz window in the front (Figure 4.2b). During a measurement, air is pulled out from the chamber, creating a vacuum for cell operation under light exposure. The vacuum protects the cell from photo-oxidation, as this is a common degradation pathway for polymer solar cells operating in ambient condition.²⁸⁶

4.3.3. Sources of error

The device characterization including the I-V measurement is discussed in Section 1.1.2. During a standard indoor terrestrial solar cell characterization, the solar simulator is adjusted to simulate Air Mass 1.5 Global (AM 1.5 G) irradiance, the total power of which is $1000 \text{ W}\cdot\text{m}^{-2}$.^{162,496,497} Therefore, the value of P_{in} in Equation 1.2b is set to $1000 \text{ W}\cdot\text{m}^{-2}$ (i.e., $100 \text{ mW}\cdot\text{cm}^{-2}$). However, despite a simple calibration with a power meter, the actual power may deviate from $1000 \text{ W}\cdot\text{m}^{-2}$. In theory, the short circuit current is the photocurrent at 0 bias voltage, and scales linearly with illumination intensity.⁴⁹⁸ A greater light intensity results in greater photocurrent and shifts the entire I-V curve towards the fourth quadrant. Besides, V_{oc} increases logarithmically with I_{sc} , while FF is affected by both the I_{sc} and V_{oc} .⁴⁹⁹ If the actual light intensity is higher than $1000 \text{ W}\cdot\text{m}^{-2}$, all three parameters in the numerator of Equation 1.2b will be affected, and an overestimation of PCE is resulted. Another source of error is the inappropriately measured cell area A . Numerous articles have stated that inappropriately estimating the effective cell area, including the absence of a mask, can lead to significant overestimation of the short circuit current density J_{sc} and PCE.^{485,487–489,491,492,500,501} In particular for bulk heterojunction polymer solar cells, this overestimation can be as high as 40%.⁴⁸⁸

4.3.4. Area determination and mask design

Although the device area is defined as the area where all layers overlap, the active layer, which is capable of generating photocurrent, has a greater coverage than the device area. During an I-V measurement, the active layer outside the device area is able to transport photocurrent to the device, as indicated by the blue arrows in Figure 4.4, contributing to an overestimation of current, and hence an overestimation of PCE.

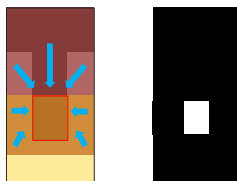


Figure 4.3 A solar cell device viewed from the glass substrate (left), and the configuration of the mask (right). The red rectangle and blue arrows indicate the effective device area and the photocurrent contributed from outside this area, respectively

A mask is constructed following the guideline set out by Krebs et al.⁴⁹⁰ According to the guideline, when the substrate thickness is less than 1 mm, the mask aperture should have dimensions that are ~0.5 mm smaller on each side of the active area to prevent non-collimated light from being absorbed by adjacent materials. The ITO coated glass substrate is 0.7 mm thick, and the dimension of the mask aperture is $2.99 \times 3.74 \text{ mm}^2$ (area = 0.112 cm^2 , NREL certified area = 0.1123 cm^2). The mask is integrated onto the cell fixture, making the fixture light-tight.

Table 4.1 Photovoltaics parameters of P3HT/PCBM devices measured with and without a mask

	J_{sc} ($\text{mA}\cdot\text{cm}^{-2}$)	V_{oc} (V)	FF	PCE (%)
Mask	5.71	0.54	0.57	1.76
No Mask	7.25	0.56	0.55	2.22

To demonstrate how much error could be involved in the absence of a mask, a batch of P3HT/PCBM devices was tested. The J-V curve and PV parameters are presented in Figure 4.5 and Table 4.1, respectively. It is found that without appropriate masking, devices exhibit an overestimation of short circuit current as high as 27%, contributing to the 26% overestimation in PCE. A slight increase in V_{oc} is also found, consistent with the logarithmic correlation of V_{oc} and J_{sc} . Our result highlights again the

importance of using a mask as part of the procedure for accurate measurements of polymer solar cells.

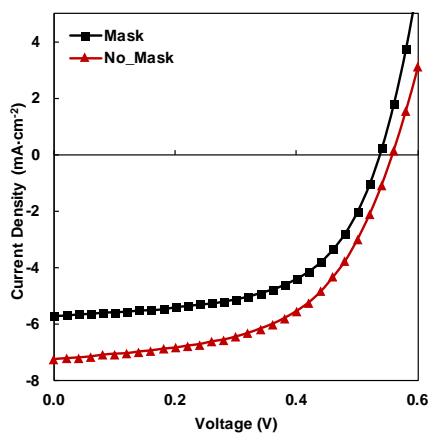


Figure 4.4 I-V curves of P3HT/PCBM solar cells measured with and without a mask

4.3.5. Spectral mismatch

The difficulty in this setup is the use of a simple xenon arc lamp to provide the same quality of light like a solar simulator. According to well-accepted standards, solar simulators are rated on three aspects: spectral match, spatial uniformity, and temporal stability.⁵⁰²⁻⁵⁰⁴ Three classes of performance criteria (A, B, or C) are defined for each of the aspects.⁵⁰²⁻⁵⁰⁴ A solar simulator is then labeled in three letters describing its performances in all three categories. Spectral match is evaluated as follows: the spectrum of the solar simulator is divided into 100 nm wide segments between 400 nm and 1100 nm (except the last segment which spans from 900 nm to 1100 nm), the percentage intensity of each segment with regard to the total intensity of all segments is calculated, and the results are compared to that of the AM 1.5 G spectrum. ASTM standard defines the A rating spectral match to be within $\pm 25\%$ deviation from the AM 1.5 G spectrum, while B rating is $\pm 40\%$, and C rating is -80% to $+100\%$.⁵⁰² In the setup used in this study, an AM 1.5 G filter is placed in front of the beam-splitter holder to correct the output spectrum of the lamp. The spectral match of the xenon arc lamp with the air mass filter is shown in Figure 4.5. The result shows that after the spectral correction with the AM 1.5 G filter, the spectrum match falls within the limit of the B rating. The most useful part of the

spectrum for polymer solar cells (300–800 nm) falls within the A rating limits, except for a slight deviation in the 400–500 segment.

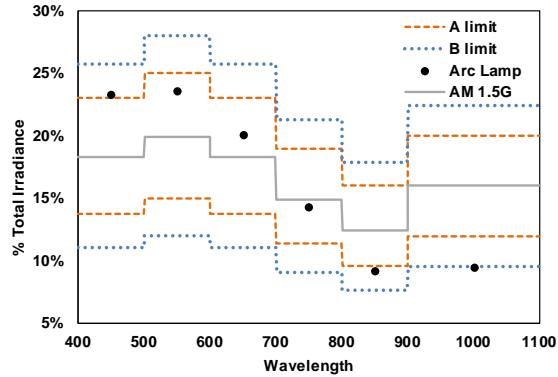


Figure 4.5 The spectral match of the xenon arc lamp source. The orange dashed lines represent $\pm 25\%$ deviation from the AM 1.5 G spectrum (A rating limits). The blue dotted lines represent $\pm 40\%$ deviation from the AM 1.5 G spectrum (B rating limits). The black dots represent the spectrum of the xenon arc lamp corrected by an AM 1.5G filter

4.3.6. Spatial uniformity

The main problem of using a basic xenon arc lamp for I-V measurements is the uneven distribution of the light. Spatial non-uniformity of simulated sunlight is another source of error in I-V measurements. A polymer solar cell device is fabricated and tested to demonstrate how much error may be caused by the spatial non-uniformity. As shown in Figure 4.2, the test fixture is the back cover of the round-shaped vacuum chamber with the cell mounted slightly off-centered to allow space for wiring. When rotating the test fixture, the device encompasses a circle roughly with a diameter of 1 cm. Four tests were performed on the same device when the test fixture is positioned at 0° , 90° , 180° , and 270° while keeping the vacuum chamber at the same position (Figure 4.6). The measured J-V curves and the correlation between PCE and angle of the test fixture are presented in Figure 4.6. The difference between the maximum and minimum measured PCE is 60%. The vast variation of measurement results is a clear indication of the poor spatial uniformity of a basic xenon arc lamp.

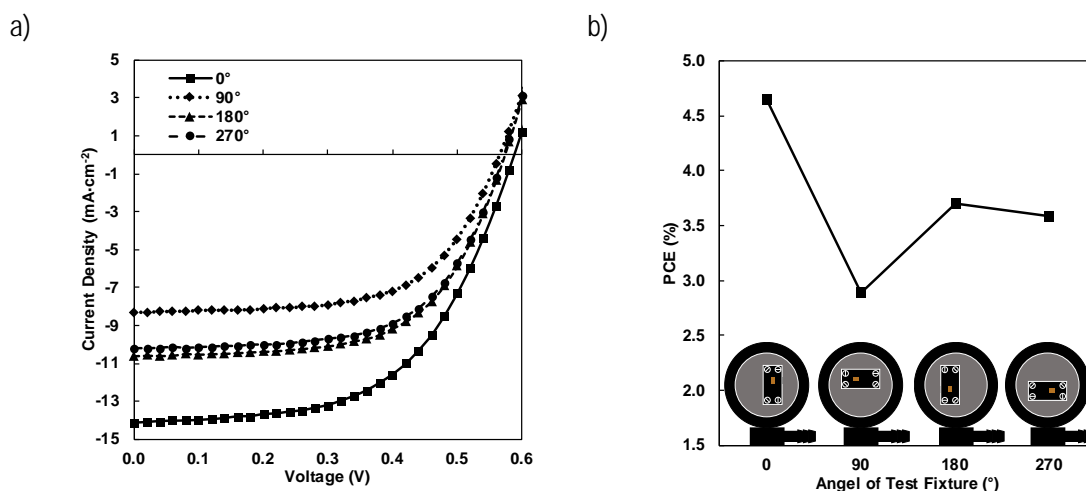


Figure 4.6 I-V curves of a P3HT/PCBM device measured with the test fixture turned at four different angles (a). PCE vs. angle of the test fixture with the orientation of the test fixture illustrated (b)

To further reveal the inhomogeneity of the light distribution, a detailed mapping of the light intensity was carried out. A silicon diode masked with a 2 mm × 2 mm aperture was manually moved by 2 mm increment across a 40 mm × 40 mm square area within the light beam. The light intensity is represented by the magnitude of the recorded short circuit current of the diode. As shown in Figure 4.7, an oval-shaped bright spot resembling the bulb of the lamp is clearly seen on the heat map when no additional optics were used. The center of the bright spot, which is the position of the arc, is nine times more intense than the illuminated area outside the oval. The prominent peak on the topographic map demonstrates the sheer non-uniformity of the light distribution. Since photocurrent is proportional to the incident light intensity,¹⁶¹ significant error may result by only a few millimeters of offset. Errors are also incurred when a reference cell or a power meter with a larger area than the test cell is used. In such case the smaller test cell may sit in a hot spot while the reference cell measures the average intensity across a larger area. The only way to avoid the error caused by spatial non-uniformity is using a reference cell having a similar size and shape as the test cell, and placing the two cells at the exact same position within the light spot.⁴⁸⁸ However, this method becomes non-practical if multi-device substrates are used. Considerable deviation will arise among the cells on the same substrate as they are situated within an area with spatial non-uniformity. Another way of eliminating the error is to correct the spatial non-uniformity with optics. To demonstrate, two homogenizing techniques were applied and compared. The improved light

distributions from the two techniques are presented in Figure 4.7 along with the light distribution of the xenon arc lamp without additional optics.

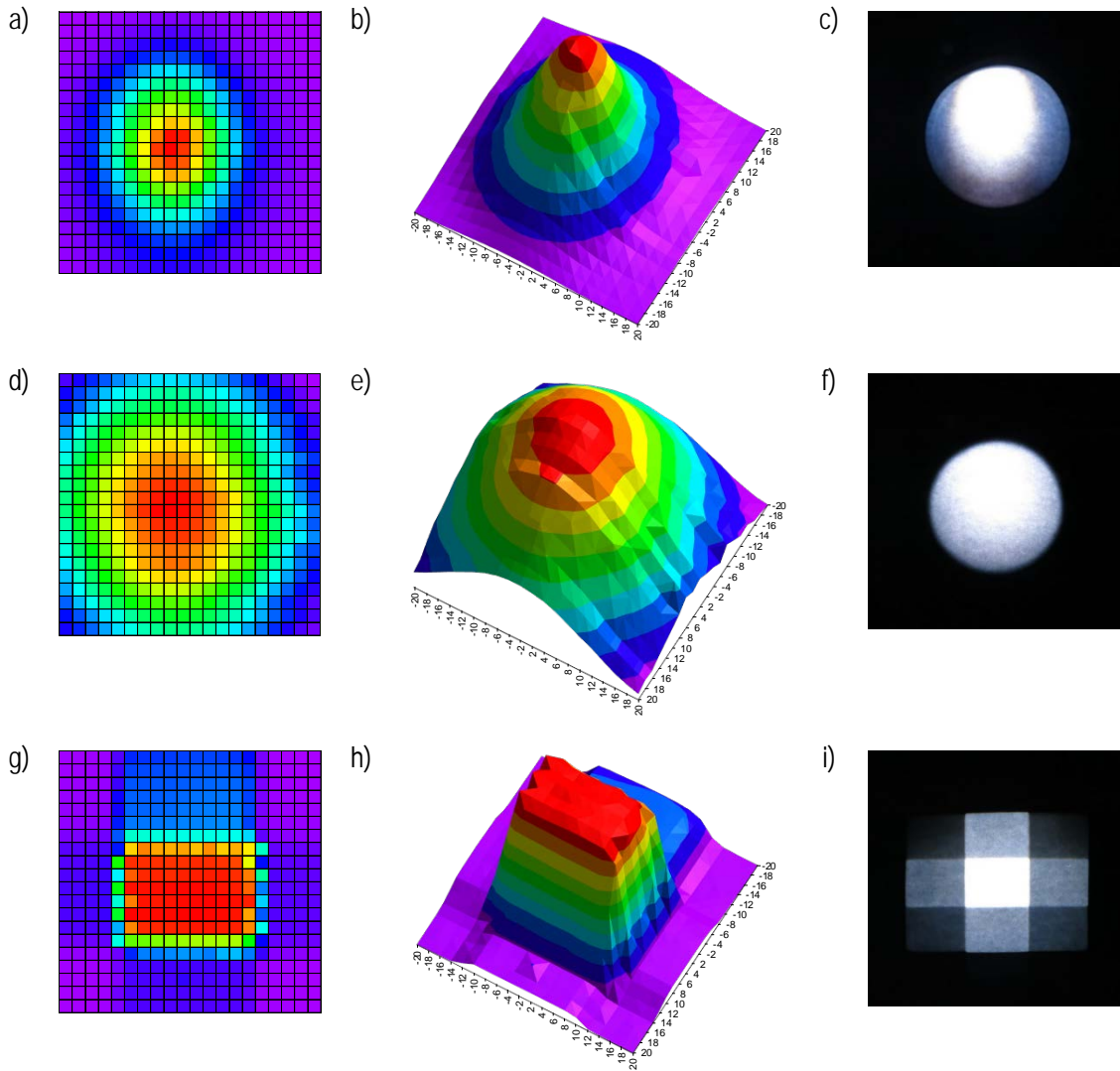


Figure 4.7 Light intensity distribution of the xenon arc lamp using various optics at the test plane, with no optics (a)-(c), with an optical diffuser (d)-(f), with an imaging multi-aperture beam integrator (g)-(i). (a), (d), (g) are heat maps of the test plane, each square in the grids is 2 mm × 2 mm. (b), (e), (h) are topographic maps of the test plane. (c), (f), (i) are the light spot images at the test plane

In the first technique, an optical diffuser was installed in the light path. Optical diffusers have been used to shape laser beams by causing the beam to interfere with itself.⁵⁰⁵ The diffuser spreads the concentrated intense bright spot over the test plane but

does not eliminate it. The slope around the high intensity region is flatter than without a diffuser. The image of the light spot also appears to be more uniform. The second technique uses an imaging multi-aperture beam integrator as the beam homogenizing device. The result shows a square-top profile of light intensity distribution. Most of the light is concentrated and evenly distributed within the center rectangle with clear edges. Quantitatively, the spatial uniformity is calculated based on the minimum and maximum intensity within a certain area. In practice, the test plane with a certain area is divided into equally sized sub-areas, and the intensity of each sub-area is determined.⁵⁰²⁻⁵⁰⁴ The uniformity is evaluated by spatial non-uniformity:

$$\text{Spatial Non - uniformity} = \frac{(MAX_{intensity} - MIN_{intensity})}{(MAX_{intensity} + MIN_{intensity})} \times 100\% \quad (4.3)$$

in which $MAX_{intensity}$ and $MIN_{intensity}$ are the maximum and minimum light intensity of the divided test plane. According to ASTM, the non-uniformity requirements for A, B, and C classes are $< \pm 2\%$, $< \pm 5\%$, and $< \pm 10\%$, respectively.⁵⁰² The test planes in the three scenarios are evaluated using the A, B, and C criteria, and the maximum areas fulfilling each criterion are calculated. The results are tabulated in Table 4.2.

Table 4.2 Sizes of illuminated areas with A, B, or C spatial uniformity ratings using different homogenizing optics (unit: mm²)

Criterion	No Optics	Diffuser	Beam Integrator
A (<±2%)	2×4	6×6	16×10
B (<±5%)	4×6	10×10	16×12
C (<±10%)	6×6	14×14	18×14

Due to the uneven distribution of light, an A rating is only found in a 2×4 mm² area without any optics, which equals two adjacent cells on the heat map. Using a diffuser, the size of the A rating area expands to 6×6 mm², however, no clear boundaries of the area can be identified to assist with positioning the solar cell sample within this area. In contrary, at the test plane of the imaging multi-aperture beam integrator, almost the entirety of the central rectangle, except one row and one column exhibits an A rating uniformity. The size of the A rating area is 16×10 mm² with clear boundaries. Therefore, using this technique, as long as the solar cell sample is placed well within the central rectangle, the measurement error caused by spatial non-uniformity is expected to be less than 2%. In

fact, imaging multi-aperture beam integrators have been applied to shape beam sources with low degree of spatial coherence, and serve as a core component in advanced solar simulators.⁵⁰⁶ The integrator consists of two identical multi-aperture lenslet arrays and a primary condensing lens (Figure 4.8). The object array segments the incoming beam into equally sized channels and focuses them onto the field array, spaced from the object array by its focal length. The field array reimages the apertures of these channels with the primary condensing lens such that they overlap at the illumination plane with a certain magnification. The overlap cancels out the spatial non-uniformity within each sub-aperture and realizes spatial homogenization.⁵⁰⁷

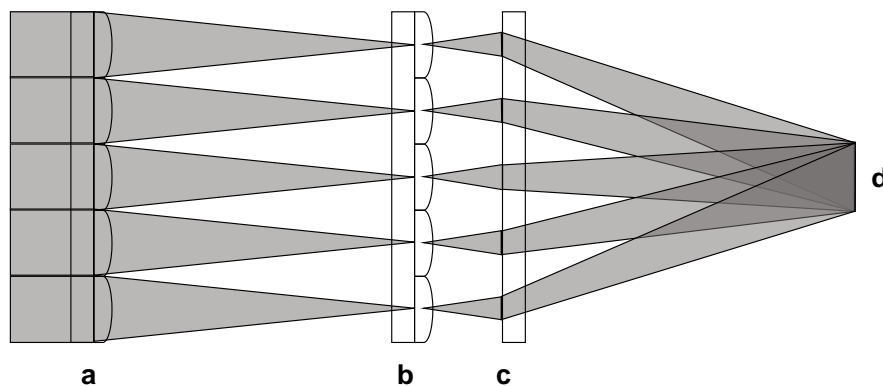


Figure 4.8 Working principle of the imaging multi-aperture beam integrator. object array (a); field array (b); primary condensing lens (c); overlapped image of the sub-aperture at the illumination plane (d)

4.3.7. Mismatch factor and intensity calibration

A common negligence when calibrating the light intensity to one sun is the poor choice of a calibration device. Whether using a power meter or a reference cell, the dimension of the device should be close to the test cells and the mismatch factor should be accounted for. The goal of the light intensity calibration is to achieve the same number of electrons generated by the test cell under the solar simulator as would be generated by the same cell under the AM 1.5G reference light. In other words, the photocurrent of the test cell under the source light equals the photocurrent of the test cell under the AM 1.5G reference light. If the simulator's spectrum matches perfectly the AM 1.5G spectrum, then adjusting the illumination intensity to $1000 \text{ W}\cdot\text{m}^{-2}$ using any reference cell/device would be accurate. However, there is almost always a mismatch between these two spectra, which

can be represented by the short circuit current mismatch of a given PV device under the two different spectra. The mismatch Factor M can be expressed as the ratio of the device's short circuit current measured under the source light J_S to that measured under the reference light J_R (Equation 4.4a). Because the spectral response S of a PV device is measured under the short circuit condition, short circuit current can also be obtained by integrating the device's spectral response over the entire spectrum. Thus, M can be written in the integration form of Equation 4.4b:

$$M = \frac{J_S}{J_R} \quad (4a)$$

$$M = \frac{\int E_S(\lambda)S(\lambda)d\lambda}{\int E_R(\lambda)S(\lambda)d\lambda} \quad (4b)$$

where E_S is the source irradiance, E_R is the AM 1.5G reference irradiance, and S is the spectral responsivity of the device. All three parameters are functions of the wavelength λ . Under the assumption that changing the intensity of the source light will only change the power output at each wavelength by a same factor while keeping the profile of the spectrum intact, i.e.,

$$E'_S(\lambda) = C \cdot E_S(\lambda) \quad (5)$$

where C is a constant, M changes proportionally with E_S . Equation 4.4b is valid for both test cells and reference cells and can be expressed specifically in Equation 4.6a and Equation 4.6b:

$$M_T = \frac{\int E_S(\lambda)S_T(\lambda)d\lambda}{\int E_R(\lambda)S_T(\lambda)d\lambda} \quad (6a)$$

$$M_R = \frac{\int E_S(\lambda)S_R(\lambda)d\lambda}{\int E_R(\lambda)S_R(\lambda)d\lambda} \quad (6b)$$

where M_T and M_R are the mismatch factors of the test cell and the reference cell, respectively, S_T and S_R are the spectral response of the test cell and reference cell, respectively. The ratio of M_T to M_R can be defined as $M_{T,R}$, as expressed by Equation 4.7. Conventionally, $M_{T,R}$ and its integral form are well known as the mismatch factor M .⁴⁸⁵

Because the source irradiance $E_S(\lambda)$ is present in both the denominator and numerator of the equation, $M_{T,R}$ retains the same value under any intensity of the source light given that the source spectrum does not change form with intensity variations.

$$M_{T,R} = \frac{M_T}{M_R} = \frac{\int E_R(\lambda)S_R(\lambda)d\lambda}{\int E_S(\lambda)S_R(\lambda)d\lambda} \cdot \frac{\int E_S(\lambda)S_T(\lambda)d\lambda}{\int E_R(\lambda)S_T(\lambda)d\lambda} \quad (4.7)$$

Under some circumstances, the value of $M_{T,R}$ equals either the mismatch factor of the test cell or the reciprocal of the mismatch factor of the reference cell. When the source light intensity is tuned such that the short circuit current of the reference cell equals its short circuit current under the reference spectrum, in other words,

$$\int E_S^*(\lambda)S_R(\lambda)d\lambda = \int E_R(\lambda)S_R(\lambda)d\lambda \quad (4.8)$$

$M_{T,R}$ equals the mismatch factor of the test cell M_T^* under this source light intensity:

$$M_{T,R} = M_T^* = \frac{\int E_S^*(\lambda)S_T(\lambda)d\lambda}{\int E_R(\lambda)S_T(\lambda)d\lambda} \quad (4.9)$$

where the superscript “*” denotes the values under the specific source light intensity when Equation 4.9 is valid. It should be noted that $M_{T,R}$ is specific to a certain type of test cell and a certain type of reference cell. Therefore, using different reference cells yields different mismatch factors for a certain test cell.

When the source light is being calibrated using the reference cell, the goal is to achieve an intensity where the measured short circuit current of the test cell equals the short circuit current of the test cell under the reference spectrum, i.e.,

$$\int E_S^{**}(\lambda)S_T(\lambda)d\lambda = \int E_R(\lambda)S_T(\lambda)d\lambda \quad (4.10)$$

where the superscript “**” denotes the values under the specific source light intensity when Equation 4.10 is valid. In such case, $M_{T,R}$ takes the reciprocal value of the mismatch factor of the reference cell M_R^{**} under this source intensity (Equation 4.11a). Rearranging Equation 4.11a gives Equation 4.11b and its simplified version, Equation 4.11c:

$$M_{T,R} = \frac{1}{M_R^{**}} = \frac{\int E_R(\lambda)S_R(\lambda)d\lambda}{\int E_S^{**}(\lambda)S_R(\lambda)d\lambda} \quad (4.11a)$$

$$\int E_S^{**}(\lambda)S_R(\lambda)d\lambda = \frac{\int E_R(\lambda)S_R(\lambda)d\lambda}{M_{T,R}} \quad (4.11b)$$

$$J_{S,R}^{**} = \frac{J_{R,R}}{M_{T,R}} \quad (4.11c)$$

where $J_{S,R}$ is the short circuit current of the reference cell under the source light, and $J_{R,R}$ is the short circuit current of the reference cell under the AM 1.5 G reference light. Equation 4.11c should serve as a guidance for calibrating the source light with a reference cell. When $M_{T,R}$ is known, the illumination intensity calibration can be achieved by placing the reference cell under the simulator light, and tuning the intensity of the lamp until the short circuit current reading of the reference cell equals the $1/M_{T,R}$ times of its short circuit current under the AM 1.5G reference light. This method is based on the assumption that the J_{sc} reading under the bias light equals the integration of the spectral response over the light spectrum. However, the two terms have slight deviation but the differences are usually omitted.⁵⁰⁸

In summary, the process of calibrating the illumination intensity for a specific type of test cell is: 1) Measure the spectral response of the test cell, S_T ; 2) Obtain the irradiance of the solar simulator, E_S ; 3) Calculate the mismatch factor ratio of the test cell relative to the reference cell, $M_{T,R}$ (usually called mismatch factor M); 4) Adjust the solar simulator's power such that the short circuit current reading of the reference cell equals $1/M_{T,R}$ times of its short circuit current under AM 1.5 G.

4.3.8. Sample measurements

To showcase how much error can be involved during I-V measurements of polymer solar cells using a basic xenon arc lamp without appropriate intensity calibration, and how much accuracy improvement can be achieved following the simple modification and calibration discussed above, a batch of P3HT/PCBM devices were measured using the setup in our laboratory and subsequently submitted to NREL for verification. Three devices were successfully tested at both locations. For the erroneous test conditions, the light from

the xenon arc lamp was untreated with the intensity calibrated to 1000 W/m^2 using a power meter that has an aperture of 1.13 cm^2 , and the devices were placed under the brightest part of the light for testing. For the improved test conditions, the multi-aperture beam integrator was installed, and the light intensity was calibrated using a KG5 filtered silicon diode that has an aperture of 0.0756 cm^2 and a mismatch factor with P3HT/PCBM of 1.00. Only fast I-V scans were performed in our facility, which is typical for research laboratories. However, only results of slow asymptotic scans (i.e., holding the bias voltage until the current reaches an asymptotic level) are considered valid at NREL because of the slow voltage response of polymer solar cells.⁵⁰⁹ Nevertheless, fast scan data from NREL are also included for comparison. The results of I-V measurements from the two facilities are presented in Figure 4.9 and Table 4.3. The PCEs measured under improved condition in our laboratory deviate from NREL values by as low as 1%, whereas the deviations under erroneous conditions range from 35% to 52%. The 26% deviation of device 667 is due to a low FF at asymptotic state, which is attributed to the device's incapability of maintaining current around P_{max} . However, the low FF is absent in fast scan analysis and the deviation was negligible, proving the accuracy of the methodology. Our results show that characterizing polymer solar cells using a conventional xenon arc lamp without taking proper care can cause great error in the accuracy of the measurement. However, after homogenizing the beam with simple optics and carefully following the appropriate calibration procedure, the results closely match those obtained at NREL facility, considering 15-25% deviation is not uncommon for a single batch of OPV devices.⁴⁸⁹

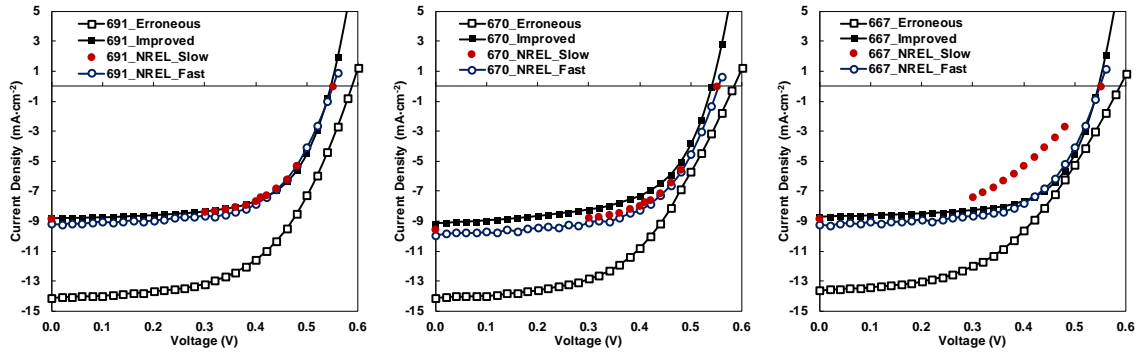


Figure 4.9 J-V curves of P3HT/PCBM devices measured at SFU and NREL: (□) fast scan at SFU under erroneous conditions, (■) fast scan at SFU under improved conditions, (○) fast scan at NREL, (●) slow asymptotic scan at NREL

Table 4.3 Photovoltaic parameters of P3HT/PCBM devices measured at SFU and NREL

Device ID	Test Location	Test Conditions	J_{sc} (mA/cm ²)	V_{oc} (V)	FF	PCE (%)	Difference in PCE (%)*
691	SFU	Erroneous	14.13	0.59	0.56	4.65	52 (49)
		Improved	8.80	0.55	0.64	3.10	1 (2)
	NREL	Slow Scan	8.82	0.55	0.63	3.07	n/a
		Fast Scan	9.19	0.55	0.62	3.13	n/a
670	SFU	Erroneous	14.13	0.58	0.53	4.34	35 (32)
		Improved	9.14	0.54	0.59	2.93	9 (11)
	NREL	Slow Scan	9.54	0.55	0.60	3.21	n/a
		Fast Scan	9.92	0.55	0.60	3.29	n/a
667	SFU	Erroneous	13.63	0.59	0.49	3.91	71 (26)
		Improved	8.71	0.55	0.65	3.10	26 (0)
	NREL	Slow Scan	8.84	0.55	0.47	2.29	n/a
		Fast Scan	9.28	0.55	0.61	3.10	n/a

* differences are compared with NREL slow scan; differences compared with NREL fast scan are shown in parentheses.

4.4. Conclusion

In conclusion, the potential measurement errors associated with I-V measurements using a basic xenon arc lamp are presented, and simple solutions to improve measurement accuracy using basic optics and appropriate calibration procedures are provided. The two major sources of error associated with polymer solar cell measurements are light intensity and device area. By applying a multi-aperture beam integrator, the xenon arc lamp is able to deliver spatially-uniform white light with class A spatial uniformity. Additionally, precise intensity calibration can be realized using a reference cell with similar size to the test cell and taking account of the mismatch factor. The importance of appropriate masking is re-emphasized in this study as a reduction of measurement error as high as 26% is demonstrated. Additionally, when no diffusing optics are used, and the intensity is calibrated by an ordinary power meter with aperture size greater than the test cell, errors as high as 51.5% can be produced. By following appropriate calibration procedures, and applying beam homogenizing optics, this error can be reduced to 1–8.7%. The setup used in this study can serve as an example of simplified instrumentation without significantly compromising on accuracy for PV measurements.

Chapter 5.

General Conclusion and Future Work

Organic photovoltaic devices, particularly polymer solar cells, offer the possibility of high-throughput, roll-to-roll production of photovoltaic modules based on solution deposition techniques and have the potential of lowering the cost of photovoltaic energy to 80–100 USD/MWh. The freedom of finely tuning the energy levels, bandgap, molecular packing, and solubility of conjugated polymers via molecular design and synthesis further broadens the potential of polymer solar cells as a competitive candidate for the next generation of photovoltaic technologies. The power conversion efficiency is crucial for evaluating a solar cell technology, especially for polymer solar cells, which are struggling to achieve comparable efficiencies to those of mature technologies, such as polycrystalline silicon solar cells. Chapter 4 highlights the potential errors associated with the PV measurements of polymer solar cells. Deviations as high as 51.5% from the true efficiency can occur when a basic xenon arc lamp is used without appropriate optics and calibration. Chapter 4 also demonstrates the possibility of achieving accurate measurements using a low-cost, all-in-one setup, combining a solar simulator and monochromator, when appropriate homogenizing optics are installed and appropriate procedures are followed, thus providing a solution to the highly demanding instrumentation involved in polymer solar cell research.

Besides the power conversion efficiency, the lifetime also plays a key role in determining the commercializing potential of a novel photovoltaic technology and the viability of real-life applications. Section 1.4 provides an in-depth review of the degradation mechanisms existing in a polymer solar cell. Conjugated polymers, being excitonic semiconductors, require fullerenes as the electron acceptor for efficient photocurrent generation. The performance of a polymer solar cell largely relies on the interpenetrating network of conjugated polymers and fullerenes in the bulk heterojunction morphology. Thermal stress during module operation drives large-scale phase segregation between the two, which is manifested by fullerene crystallization and deteriorates the efficiencies.

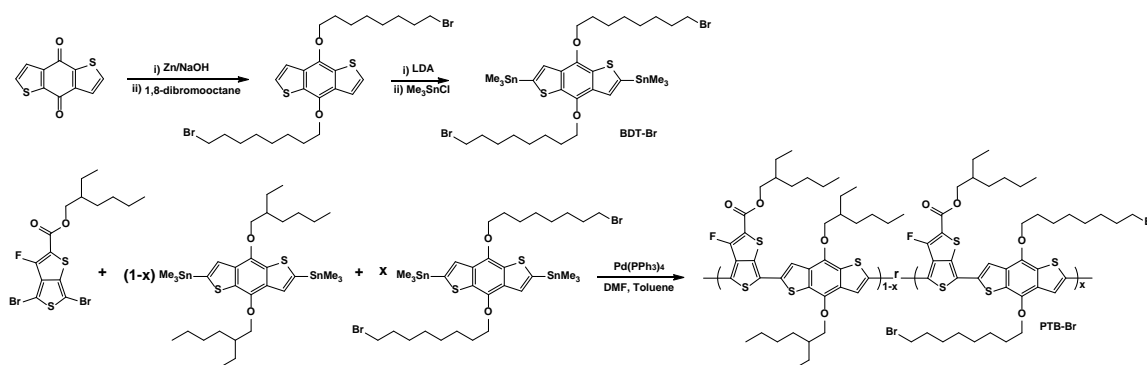
Chapter 2 and Chapter 3 explore two major strategies for morphological and performance stabilization of polymer solar cell devices made from a low-bandgap, highly efficient polymer, PTB, through sidechain modification. In Chapter 2, a PTB polymer with thermally-cleavable sidechains, PTB(THP), is presented. Thermal cleavage shortens the sidechains of PTB(THP), increasing the T_g of the polymer, and potentially forming a hydrogen bonding network through the remaining hydroxyl groups. The experimental results demonstrate that thermal-cleavage of the sidechains stabilizes the morphology against thermal annealing by suppressing fullerene crystallization. As a result, solar cell devices made from PTB(THP) with thermally cleaved sidechains exhibited stable efficiencies throughout the accelerated lifetime test. Chapter 3 demonstrate the performance stabilization through UV-induced crosslinking. PTB polymers with various numbers of photocrosslinkable, chlorine-terminated sidechains were synthesized. The crosslinking can effectively insolubilize the polymer thin films without affecting the absorption behaviours. Patterning through a mask was also realized. Stable PV performances were achieved when low-dosage UV was applied to the devices before depositing the top electrode. Morphological stabilization in terms of suppressing PCBM crystallization could be achieved with low chlorine sidechain content and short UV exposure.

Both techniques have their advantages and shortcomings. Thermally cleaving the sidechain does not involve an additional source of activation. The process can be activated in situ, during device operation. The thermal energy can be provided by the thermal radiation from the sunlight if the rate of the stabilization process is higher than that of degradation. With photocrosslinking, only a small number of crosslinking groups must be present on the polymer for sufficient stabilization. The crosslinking process is fast and compatible with roll-to-roll processing. Patterning with photocrosslinking is also easier than other lithography techniques.

However, both techniques require an external stimulus for activation. The high-temperature thermal annealing and short wavelength UV irradiation are both harmful to the PV performances, as shown in the experimental results. Foreign substances are introduced in both processes. The leaving group, the acid catalyst of the thermal-cleavage route, and the highly reactive radical species of the photocrosslinking route can pose

problems to the device performance. Plus, the thermal-cleavage route requires a high number of thermally-cleavable sidechains for the method to be effective. Both techniques are based on linear sidechains because functionalization of branched sidechains are limited by synthetic difficulties. The substitution of linear sidechains for the original branched sidechain means that the polymers will potentially be less soluble, as demonstrated in Chapter 2 and Chapter 3. Also, the results from these chapters indicate that polymers with linear sidechains can increase the rate of fullerene nucleation, which is a side effect of the close π - π stacking associated with linear sidechains. As a result, the number of chlorinated sidechains must be kept low for long-term stability of the photocrosslinkable polymers.

In the future, improvements to the works presented here may provide a promising path towards stable polymer solar cells by continuing the work that has been achieved so far while mitigating the negative effects. For example, synthesizing the BDT-Br unit with bromine-terminated sidechains may be achievable after carefully tuning the reaction conditions and purification techniques (Scheme 5.1).



Scheme 5.1 Proposed synthetic route for PTB-Brs

The first step of the synthesis of BDT-Br has been accomplished with a yield similar to the chlorine version, BDT-Cl. However, attaching trimethyl tin functionalities has not been successful so far. Replacing the *n*-butyl lithium with lithium diisopropylamide (LDA), a non-nucleophilic, stronger lithiation agent may help with this reaction. In addition, changing the reaction conditions (e.g., temperature, reaction time) and monitoring the reaction process by NMR may provide an appropriate procedure for BDT-Br synthesis.⁵¹⁰ Once the bottleneck of the monomer synthesis is solved, PTB-Br polymers can be synthesized and studied following the experimental procedures set forth in Chapter 3.

Furthermore, the yield of the etherification step may be improved by selecting appropriate bases and solvent systems.^{511,512} Bromine has a lower reactivity than chlorine; therefore, it may be able to withstand longer UV exposures than that used for chlorine before negative effects occur. Furthermore, the inverted structure and encapsulation could be applied to the device to examine its stability at a high annealing temperature to avoid the effect of electrode degradation.^{142,143,376} Alternatively, thermal annealing can be performed before depositing the metal electrode, such that freshly prepared solar cell devices with as-cast and degraded active layers are measured in one batch. This practice has been used before, although it does not reflect certain effects that are present in a complete device, such as the confining effect of the top electrode.^{280,417,418} On a side project, a PTB derivative with the same chemical structure as PTB-Cl₁₀₀ but without chlorine could be synthesized from easily obtained monomers (Figure 5.1, PTB2F). This polymer is named PTB2F because it has the same sidechain pattern as PTB2, except for the fluorine substitution on the TT unit (Figure 1.13). Then, the morphological stability of PTB2F/PC₇₁BM could be studied and compared to those of PTB7/PC₇₁BM and PTB4/PC₇₁BM (Figure 5.1) to gain insight into how the sidechain patterns affect PC₇₁BM crystallization.

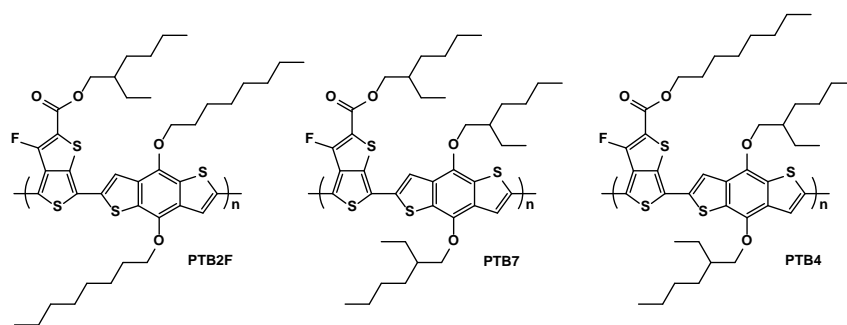


Figure 5.1 Chemical structures of PTB2F, PTB7, and PTB4

Furthermore, a variety of other high-performance polymers as well as alternative thermally-cleavable and photocrosslinkable sidechains could be combined. In the past two years, many articles^{31,33,34,36,73,513} reported single junction polymer solar cells exceeding the 10% efficiency limit that was predicted in 2006.¹¹⁷ These articles all used polythieno[3,4-b]thiophene-benzo[1,2-b:4,5-b']dithiophene with 2-thienyl pendant side chains (PTB7-Th, Figure 5.2) as the donor polymer (Figure 5.2). The great benefit of two thiophenes appended to the BDT unit is that they serve as branching points that allow

more linear chains to be attached, thus simultaneously increasing the solubility and hindering the nucleation of fullerene crystals. Three variations of PTB7-Th are proposed here for future exploration, namely, PTB-Th-Br, PTB-Th-THP, and PTB-Th-ester (Figure 5.2). In the chemical structure of PTB-Th-Br, two n-octyl sidechains are attached to each of the pendent thiophene units: one with a terminated bromine, and one without. Two sidechains on each side are expected to provide high solubility for the polymer, while the bromine is expected to photocrosslink under UV irradiation. Different ratios of the regular BDT-Th unit and photocrosslinkable BDT-Th-Br unit can be applied to tune the photovoltaic and crosslinking properties, as demonstrated in Chapter 3. For the THP version, four 2-((THP-2yl)oxy)ethyl side chains are attached to the pendant thiophenes (Figure 5.2). The additional two THP sidechains on each repeat unit may provide more solubility than that from PTB(THP). After thermal-cleavage, the polymer is expected to form a denser hydrogen bonding network because of the high density of hydroxyl groups. The dihedral angle between the pendant thiophenes and the polymer back bone of PTB7-Th is around 60° .^{514,515} This angle increases from 34° to 61° from furanyl to selenophenyl side groups and is associated with the HOMO level and π - π stacking distance of the polymer. Shortening the side chains of PTB-Th-THP may change the dihedral angle between the aromatic rings, which could be studied to understand the physical property changes caused by thermal-cleavage. The last variation uses ester-protected 2-thienyl side chains (PTB-Th-ester, Figure 5.2). The sidechains could be removed by thermal annealing.⁴³³ The advantage of using an ester sidechain is that a branched alcohol can be attached, eliminating the need for two substitutions. Therefore, the monomer synthesis would be much easier by starting from commercially available 2-thiophene-carboxylic acid. However, the alkyl chains on PTB-Th-ester are attached to secondary alcohols, which may require an unfavorably higher removal temperature. To tackle this problem, trace amounts of catalyzing CSA may be added to reduce the annealing temperature, as reported by Krebs et al.⁴⁴⁰ The ester group with a primary alcohol on the TT unit would remain unaffected because a β -hydrogen is required for sidechain cleavage.^{461,462}

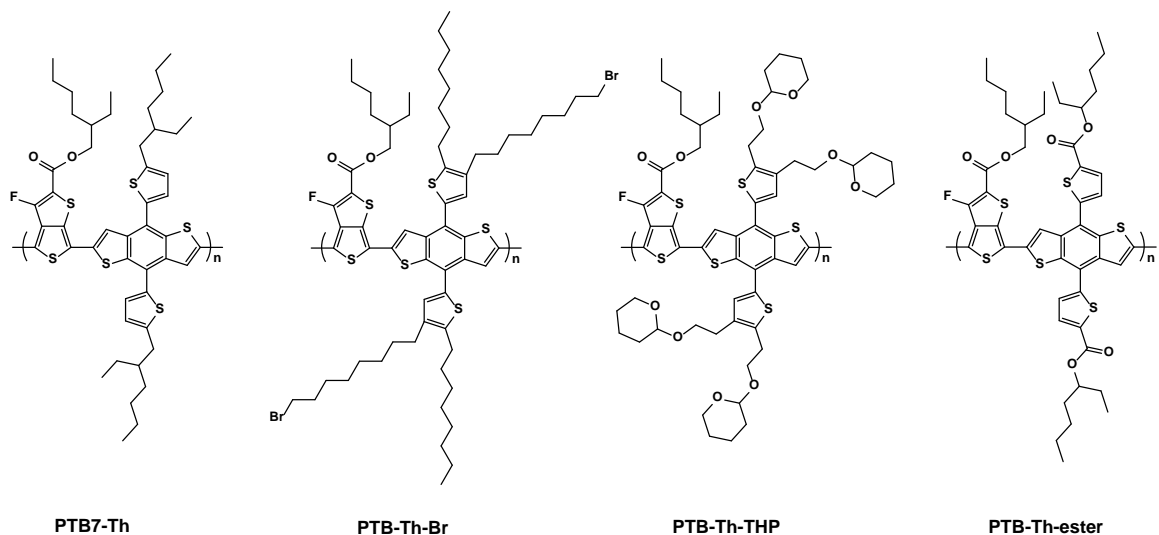
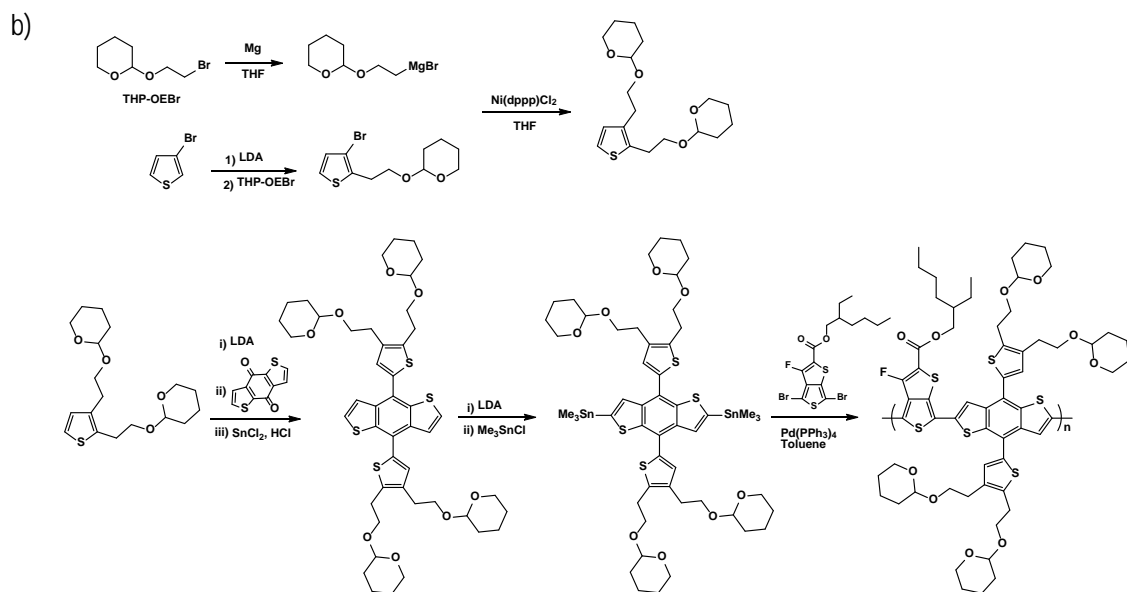
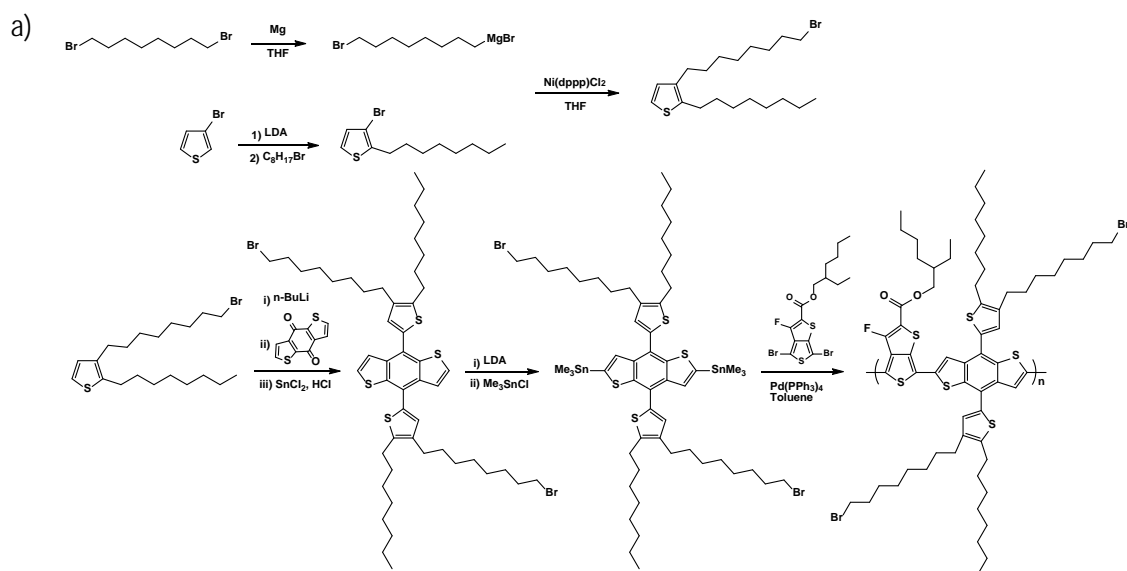
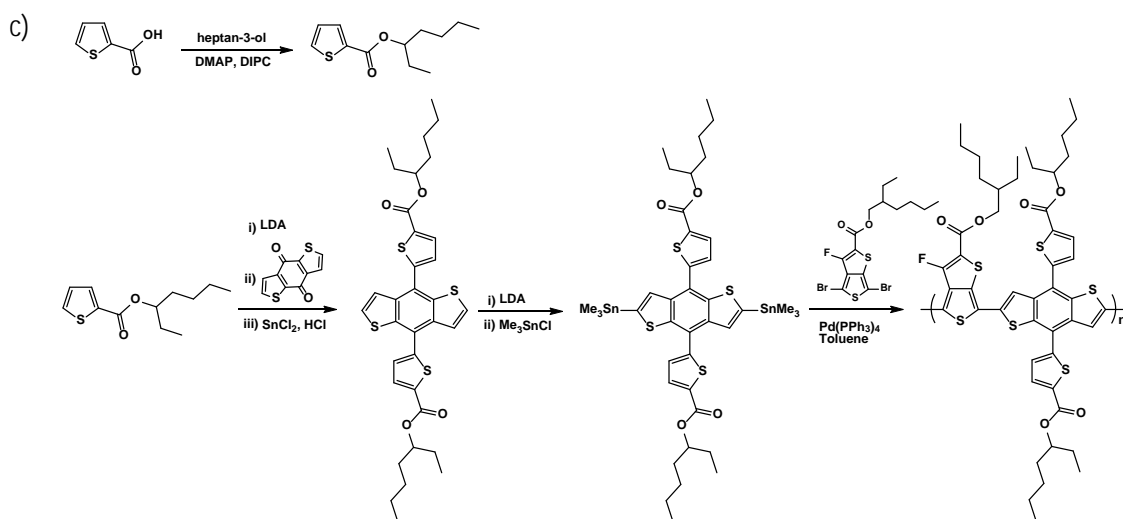


Figure 5.2 Chemical structures of PTB7-Th, PTB-Th-Br, PTB-Th-THP, and PTB-Th-ester

The proposed synthesis routes are listed in Scheme 5.2. For the disubstituted pendent thiophenes, two sidechains are attached through different types of reactions. The first sidechain on the 2-position can be added through a lithiation of 3-bromothiophene.⁵¹⁶ The second sidechain on the 3-position can be attached by a Kumada coupling with a freshly prepared Grignard reagent of the second sidechain.⁵¹⁷ The ester bearing thiophene moieties can be synthesized by a facile ester formation from thiophene-2-carboxylic acid.⁴³⁹ After functionalization, the pendent thiophenes will be incorporated onto the BDT, followed by addition of the trimethyl tin functionalities. The final polymers will be synthesized following a typical Stille polycondensation.^{175,209,210,518}





Scheme 5.2 Proposed synthetic routes for PTB-Th-Br (a), PTB-Th-THP (b), and PTB-Th-ester (c)

The research interest in polymer solar cells has gradually shifted to the development of polymeric or small molecular electron acceptors in recent years.^{121–125} As more and more fullerene replacements are reported, the stability of polymer solar cells using these new types of acceptors should be studied. These non-fullerene acceptors are expected to behave in a completely different manner than the fullerene based acceptors. The dimerization, diffusion, and crystallization of fullerene will no longer be observed in the new devices. Thus, the different behaviours of the acceptors based on polymers and small molecules opens the door for future exploration of the stability of polymer solar cells.

References

- (1) International Energy Agency. *Key Electricity Trends Excerpt from: Electricity Information*; Paris, 2016.
- (2) International Energy Agency. *Key World Energy Trends Excerpt from: World Energy Balances*; Paris, 2016.
- (3) Houghton, J. *Reports Prog. Phys.* **2005**, 68, 1343–1403.
- (4) United Nations Framework Convention on Climate Change (UNFCCC). *Conference of the Parties 21st session*; United Nations: Paris, 2015.
- (5) International Energy Agency. *Energy Technology Perspectives 2014—Harnessing Electricity's Potential*; Paris, 2014.
- (6) International Energy Agency. *World Energy Outlook Special Report: Energy and Air Pollution Executive Summary*, Paris, 2016.
- (7) Morton, O. *Nature* **2006**, 443, 19–22.
- (8) Denholm, P.; Kuss, M.; Margolis, R. M. *J. Power Sources* **2013**, 236, 350–356.
- (9) Krebs, F. C.; Nielsen, T. D.; Fyenbo, J.; Wadstrøm, M.; Pedersen, M. S. *Energy Environ. Sci.* **2010**, 3, 512–525.
- (10) International Energy Agency. *Technology Roadmap: Solar Photovoltaic Energy*, 2014 ed.; Paris, 2014.
- (11) International Energy Agency. *Tracking Clean Energy Progress 2016 Excerpt from: Energy Technology Perspectives 2016*; Paris, 2016.
- (12) Saga, T. *NPG Asia Mater.* **2010**, 2, 96–102.
- (13) Knapp, K.; Jester, T. *Sol. Energy* **2001**, 71, 165–172.
- (14) Shah, A. V.; Schade, H.; Vanecek, M.; Meier, J.; Vallat-Sauvain, E.; Wyrsh, N.; Kroll, U.; Droz, C.; Bailat, J. *Prog. Photovoltaics Res. Appl.* **2004**, 12, 113–142.
- (15) Wu, X. *Sol. Energy* **2004**, 77, 803–814.
- (16) Repins, I.; Contreras, M. A.; Egaas, B.; DeHart, C.; Scharf, J.; Perkins, C. L.; To, B.; Noufi, R. *Prog. Photovoltaics Res. Appl.* **2008**, 16, 235–239.
- (17) Chopra, K. L.; Paulson, P. D.; Dutta, V. *Prog. Photovoltaics Res. Appl.* **2004**, 12,

69–92.

- (18) Söderström, T.; Haug, F.-J.; Terrazzoni-Daudrix, V.; Ballif, C. *J. Appl. Phys.* **2008**, *103*, 114509.
- (19) Kessler, F.; Herrmann, D.; Powalla, M. *Thin Solid Films* **2005**, *480–481*, 491–498.
- (20) Schlatmann, R.; Stannowski, B.; Hamers, E. A. G.; Lenssen, J. M.; Talma, A. G.; Bartl, R.; Jongerden, G. J. *Proceedings of the 21st European Photovoltaic Solar Energy Conference*; Dresden, Germany, Sep. 4, 2006; pp 1587–1589.
- (21) Staebler, D. L.; Wronski, C. R. *Appl. Phys. Lett.* **1977**, *31*, 292–294.
- (22) Ullal, H. S.; Zwelbel, K.; Von Roedern, B. *Conference Record of the 26th IEEE Photovoltaic Specialists Conference*; Anaheim, CA, Sep. 30, 1997; pp 301–305.
- (23) Fthenakis, V. M.; Moskowitz, P. D. *Prog. Photovoltaics Res. Appl.* **1995**, *3*, 295–306.
- (24) Espinosa, N.; Hösel, M.; Angmo, D.; Krebs, F. C. *Energy Environ. Sci.* **2012**, *5*, 5117–5132.
- (25) Krebs, F. *Org. Electron.* **2009**, *10*, 761–768.
- (26) Søndergaard, R.; Hösel, M.; Angmo, D.; Larsen-Olsen, T. T.; Krebs, F. C. *Mater. Today* **2012**, *15*, 36–49.
- (27) O'Connor, T. F.; Zaretski, A. V.; Savagatrup, S.; Printz, A. D.; Wilkes, C. D.; Diaz, M. I.; Sawyer, E. J.; Lipomi, D. J. *Sol. Energy Mater. Sol. Cells* **2016**, *144*, 438–444.
- (28) Po, R.; Bernardi, A.; Calabrese, A.; Carbonera, C.; Corso, G.; Pellegrino, A. *Energy Environ. Sci.* **2014**, *7*, 925–943.
- (29) Brabec, C. J.; Hauch, J. A.; Schilinsky, P.; Waldauf, C.; Borkow, G.; Gabbay, J. *MRS Bull.* **2005**, *30*, 50–52.
- (30) You, J.; Dou, L.; Yoshimura, K.; Kato, T.; Ohya, K.; Moriarty, T.; Emery, K.; Chen, C.-C.; Gao, J.; Li, G.; Yang, Y. *Nat. Commun.* **2013**, *4*, 1446.
- (31) Liao, S.-H.; Jhuo, H.-J.; Yeh, P.-N.; Cheng, Y.-S.; Li, Y.-L.; Lee, Y.-H.; Sharma, S.; Chen, S.-A. *Sci. Rep.* **2015**, *4*, 6813.
- (32) Chen, C.; Chang, W.; Yoshimura, K.; Ohya, K.; You, J.; Gao, J.; Hong, Z.; Yang, Y. *Adv. Mater.* **2014**, *26*, 5670–5677.

- (33) Chen, J.-D.; Cui, C.; Li, Y.-Q.; Zhou, L.; Ou, Q.-D.; Li, C.; Li, Y.; Tang, J.-X. *Adv. Mater.* **2015**, *27*, 1035–1041.
- (34) Zhang, S.; Ye, L.; Zhao, W.; Yang, B.; Wang, Q.; Hou, J. *Sci. China Chem.* **2015**, *58*, 248–256.
- (35) Zhou, H.; Zhang, Y.; Mai, C.-K.; Collins, S. D.; Bazan, G. C.; Nguyen, T.-Q.; Heeger, A. J. *Adv. Mater.* **2015**, *27*, 1767–1773.
- (36) He, Z.; Xiao, B.; Liu, F.; Wu, H.; Yang, Y.; Xiao, S.; Wang, C.; Russell, T. P.; Cao, Y. *Nat. Photon.* **2015**, *9*, 174–179.
- (37) Li, N.; Brabec, C. J. *Energy Environ. Sci.* **2015**, *8*, 2902–2909.
- (38) Yao, H.; Zhao, W.; Zheng, Z.; Cui, Y.; Zhang, J.; Wei, Z.; Hou, J. *J. Mater. Chem. A* **2016**, *4*, 1708–1713.
- (39) Dongaonkar, S.; Loser, S.; Sheets, E. J.; Zaunbrecher, K.; Agrawal, R.; Marks, T. J.; Alam, M. A. *Energy Environ. Sci.* **2013**, *6*, 782–787.
- (40) Gevorgyan, S. A.; Madsen, M. V.; Dam, H. F.; Jørgensen, M.; Fell, C. J.; Anderson, K. F.; Duck, B. C.; Mescheloff, A.; Katz, E. A.; Elschner, A.; Roesch, R.; Hoppe, H.; Hermenau, M.; Riede, M.; Krebs, F. C. *Sol. Energy Mater. Sol. Cells* **2013**, *116*, 187–196.
- (41) Angmo, D.; Krebs, F. C. *Energy Technol.* **2015**, *3*, 774–783.
- (42) Gevorgyan, S. A.; Madsen, M. V.; Roth, B.; Corazza, M.; Hösel, M.; Søndergaard, R. R.; Jørgensen, M.; Krebs, F. C. *Adv. Energy Mater.* **2016**, *6*, 1501208.
- (43) Poghettino, A.; Sella, C. A. *Rend. Accad. Lincei* **1906**, *15*, 355–363.
- (44) Koenigsberger, J.; Schilling, K. *Ann. Phys.* **1910**, *337*, 179–230.
- (45) Volmer, M. *Ann. Phys.* **1913**, *345*, 775–796.
- (46) Einstein, A. *Ann. Phys.* **1905**, *322*, 132–148.
- (47) Chapin, D. M.; Fuller, C. S.; Pearson, G. L. *J. Appl. Phys.* **1954**, *25*, 676–677.
- (48) Kearns, D.; Calvin, M. *J. Chem. Phys.* **1958**, *29*, 950–951.
- (49) Delacote, G. M.; Fillard, J. P.; Marco, F. J. *Solid State Commun.* **1964**, *2*, 373–376.
- (50) Tang, C. W.; Albrecht, A. C. *J. Chem. Phys.* **1975**, *63*, 953–961.

- (51) Tang, C. W.; Albrecht, A. C. *J. Chem. Phys.* **1975**, *62*, 2139–2149.
- (52) Tang, C. W.; Albrecht, A. C. *Nature* **1975**, *254*, 507–509.
- (53) Chiang, C. K.; Fincher, C. R.; Park, Y. W.; Heeger, A. J.; Shirakawa, H.; Louis, E. J.; Gau, S. C. C.; MacDiarmid, A. G. *Phys. Rev. Lett.* **1977**, *39*, 1098–1101.
- (54) Heeger, A. J. *Angew. Chem. Int. Ed.* **2001**, *40*, 2591–2611.
- (55) MacDiarmid, A. G. *Rev. Mod. Phys.* **2001**, *73*, 701–712.
- (56) Shirakawa, H. *Angew. Chem. Int. Ed.* **2001**, *40*, 2574–2580.
- (57) Weinberger, B. R.; Akhtar, M.; Gau, S. C. *Synth. Met.* **1982**, *4*, 187–197.
- (58) Glenis, S.; Tourillon, G.; Garnier, F. *Thin Solid Films* **1986**, *139*, 221–231.
- (59) Tang, C. W. *Appl. Phys. Lett.* **1986**, *48*, 183–185.
- (60) Hiramoto, M.; Fujiwara, H.; Yokoyama, M. *Appl. Phys. Lett.* **1991**, *58*, 1062–1064.
- (61) Knight, B. W.; Wudl, F.; Hummelen, J. C.; Knight, B. W.; LePeq, F.; Wudl, F.; Yao, J.; Wilkins, C. L. *J. Org. Chem.* **1995**, *60*, 532–538.
- (62) Yu, G.; Gao, J.; Hummelen, J. C.; Wudl, F.; Heeger, A. J. *Science* **1995**, *270*, 1789–1791.
- (63) Yi, C.; Hu, X.; Gong, X.; Elzatahry, A. *Mater. Today* **2016**, *19*, 169–177.
- (64) Kraabel, B.; McBranch, D.; Sariciftci, N. S.; Moses, D.; Heeger, A. J. *Phys. Rev. B* **1994**, *50*, 18543–18552.
- (65) Scheblykin, I. G.; Yartsev, A.; Pullerits, T.; Gulbinas, V.; Sundström, V. *J. Phys. Chem. B* **2007**, *111*, 6303–6321.
- (66) Bredas, J.-L.; Norton, J. E.; Cornil, J.; Coropceanu, V. *Acc. Chem. Res.* **2009**, *42*, 1691–1699.
- (67) Grancini, G.; Maiuri, M.; Fazzi, D.; Petrozza, A.; Egelhaaf, H.-J.; Brida, D.; Cerullo, G.; Lanzani, G. *Nat. Mater.* **2012**, *12*, 29–33.
- (68) Bakulin, A. A.; Rao, A.; Pavelyev, V. G.; van Loosdrecht, P. H. M.; Pshenichnikov, M. S.; Niedzialek, D.; Cornil, J.; Beljonne, D.; Friend, R. H.; Pavelyev, G.; Loosdrecht, P.; Pshenichnikov, M. S.; Niedzialek, D.; Cornil, J.; Beljonne, D.; Friend, R. H. *Science* **2012**, *335*, 1340–1344.

- (69) Green, M. A. *Solid. State. Electron.* **1981**, *24*, 788–789.
- (70) He, Z.; Zhong, C.; Huang, X.; Wong, W.-Y.; Wu, H.; Chen, L.; Su, S.; Cao, Y. *Adv. Mater.* **2011**, *23*, 4636–4643.
- (71) He, Z.; Zhong, C.; Su, S.; Xu, M.; Wu, H.; Cao, Y. *Nat. Photon.* **2012**, *6*, 593–597.
- (72) Zhou, Y.; Fuentes-Hernandez, C.; Shim, J.; Meyer, J.; Giordano, A. J.; Li, H.; Winget, P.; Papadopoulos, T.; Cheun, H.; Kim, J.; Fenoll, M.; Dindar, A.; Haske, W.; Najafabadi, E.; Khan, T. M.; Sojoudi, H.; Barlow, S.; Graham, S.; Brédas, J.-L.; Marder, S. R.; Kahn, A.; Kippelen, B. *Science* **2012**, *336*, 327–332.
- (73) Liu, C.; Yi, C.; Wang, K.; Yang, Y.; Bhatta, R. S.; Tsige, M.; Xiao, S.; Gong, X. *ACS Appl. Mater. Interfaces* **2015**, *7*, 4928–4935.
- (74) Ouyang, X.; Peng, R.; Ai, L.; Zhang, X.; Ge, Z. *Nat. Photon.* **2015**, *9*, 520–524.
- (75) Günes, S.; Neugebauer, H.; Sariciftci, N. S. *Chem. Rev.* **2007**, *107*, 1324–1338.
- (76) Salzner, U.; Lagowski, J. B.; Pickup, P. G.; Poirier, R. A. *Synth. Met.* **1998**, *96*, 177–189.
- (77) van Mullekom, H. *Mater. Sci. Eng. R Reports* **2001**, *32*, 1–40.
- (78) Gregg, B. A.; Chen, S.-G. G.; Cormier, R. A. *Chem. Mater.* **2004**, *16*, 4586–4599.
- (79) Gledhill, S. E.; Scott, B.; Gregg, B. A. *J. Mater. Res.* **2005**, *20*, 3167–3179.
- (80) Goh, C.; Scully, S. R.; McGehee, M. D. *J. Appl. Phys.* **2007**, *101*, 114503.
- (81) Shaw, P. E.; Ruseckas, A.; Samuel, I. D. W. *Adv. Mater.* **2008**, *20*, 3516–3520.
- (82) Deibel, C.; Mack, D.; Gorenflot, J.; Schöll, A.; Krause, S.; Reinert, F.; Rauh, D.; Dyakonov, V. *Phys. Rev. B* **2010**, *81*, 85202.
- (83) Gregg, B. A. *J. Phys. Chem. B* **2003**, *107*, 4688–4698.
- (84) Green, M. A. *AIP Adv.* **2013**, *3*, 112104.
- (85) Kasper, E.; Oehme, M.; Bauer, M.; Kittler, M.; Reiche, M.; Nakatsuka, O.; Zaima, S. Group IV Materials. In *Handbook of Silicon Photonics*; Vivien, L., Pavesi, L., Eds.; Series in Optics and Optoelectronics; CRC Press: Boca Raton, FL, 2013; pp 1–54.
- (86) Harrison, M. G.; Grüner, J.; Spencer, G. C. W. *Phys. Rev. B* **1997**, *55*, 7831–7849.
- (87) Mihailetchi, V. D.; Xie, H.; De Boer, B.; Koster, L. J. A.; Blom, P. W. M. *Adv. Funct.*

Mater. **2006**, *16*, 699–708.

- (88) Kim, Y.; Cook, S.; Tuladhar, S. M.; Choulis, S. A.; Nelson, J.; Durrant, J. R.; Bradley, D. D. C.; Giles, M.; McCulloch, I.; Ha, C.-S.; Ree, M. *Nat. Mater.* **2006**, *5*, 197–203.
- (89) Liu, Y.; Zhao, J.; Li, Z.; Mu, C.; Ma, W.; Hu, H.; Jiang, K.; Lin, H.; Ade, H.; Yan, H. *Nat. Commun.* **2014**, *5*, 5293.
- (90) Coakley, K. M.; McGehee, M. D. *Chem. Mater.* **2004**, *16*, 4533–4542.
- (91) Green, M. A.; Keevers, M. J. *Prog. Photovoltaics Res. Appl.* **1995**, *3*, 189–192.
- (92) Kayes, B. M.; Atwater, H. A.; Lewis, N. S. *J. Appl. Phys.* **2005**, *97*, 114302.
- (93) Baeuerle, P.; Segelbacher, U.; Maier, A.; Mehring, M. *J. Am. Chem. Soc.* **1993**, *115*, 10217–10223.
- (94) Onoda, M.; Morita, S.; Iwasa, T.; Nakayama, H.; Yoshino, K. *Jpn. J. Appl. Phys.* **1992**, *31*, 1107–1111.
- (95) Groenendaal, L.; Jonas, F.; Freitag, D.; Pielartzik, H.; Reynolds, J. R. *Adv. Mater.* **2000**, *12*, 481–494.
- (96) Bundgaard, E.; KREBS, F. C. *Sol. Energy Mater. Sol. Cells* **2007**, *91*, 954–985.
- (97) Cheng, Y.-J.; Yang, S.-H.; Hsu, C.-S. *Chem. Rev.* **2009**, *109*, 5868–5923.
- (98) Boudreault, P.-L. T.; Najari, A.; Leclerc, M. *Chem. Mater.* **2011**, *23*, 456–469.
- (99) Bian, L.; Zhu, E.; Tang, J.; Tang, W.; Zhang, F. *Prog. Polym. Sci.* **2012**, *37*, 1292–1331.
- (100) Zaumseil, J.; Sirringhaus, H. *Chem. Rev.* **2007**, *107*, 1296–1323.
- (101) Coropceanu, V.; Cornil, J.; da Silva Filho, D. A.; Olivier, Y.; Silbey, R.; Brédas, J.-L. *Chem. Rev.* **2007**, *107*, 926–952.
- (102) Li, J.; Zhao, Y.; Tan, H. S.; Guo, Y.; Di, C.-A.; Yu, G.; Liu, Y.; Lin, M.; Lim, S. H.; Zhou, Y.; Su, H.; Ong, B. S. *Sci. Rep.* **2012**, *2*, 754.
- (103) Kang, I.; Yun, H.-J.; Chung, D. S.; Kwon, S.-K.; Kim, Y.-H. *J. Am. Chem. Soc.* **2013**, *135*, 14896–14899.
- (104) Tseng, H.-R.; Phan, H.; Luo, C.; Wang, M.; Perez, L. a.; Patel, S. N.; Ying, L.; Kramer, E. J.; Nguyen, T.-Q.; Bazan, G. C.; Heeger, A. J. *Adv. Mater.* **2014**, *26*, 2993–2998.

- (105) Yamashita, Y.; Hinkel, F.; Marszalek, T.; Zajaczkowski, W.; Pisula, W.; Baumgarten, M.; Matsui, H.; Müllen, K.; Takeya, J. *Chem. Mater.* **2016**, *28*, 420–424.
- (106) Sirringhaus, H.; Brown, P. J.; Friend, R. H.; Nielsen, M. M.; Bechgaard, K.; Langeveld-Voss, B. M. W.; Spiering, A. J. H.; Janssen, R. A. J.; Meijer, E. W.; Herwig, P.; de Leeuw, D. M. *Nature* **1999**, *401*, 685–688.
- (107) Noriega, R.; Rivnay, J.; Vandewal, K.; Koch, F. P. V.; Stingelin, N.; Smith, P.; Toney, M. F.; Salleo, A. *Nat. Mater.* **2013**, *12*, 1038–1044.
- (108) Zhang, W.; Smith, J.; Watkins, S. E.; Gysel, R.; McGehee, M.; Salleo, A.; Kirkpatrick, J.; Ashraf, S.; Anthopoulos, T.; Heeney, M.; McCulloch, I. *J. Am. Chem. Soc.* **2010**, *132*, 11437–11439.
- (109) Lee, J. Bin; Kim, K. H.; Hong, C. S.; Choi, D. H. *J. Polym. Sci. A Polym. Chem.* **2012**, *50*, 2809–2818.
- (110) Xie, Q.; Perez-Cordero, E.; Echegoyen, L. *J. Am. Chem. Soc.* **1992**, *114*, 3978–3980.
- (111) Frankevich, E.; Maruyama, Y.; Ogata, H. *Chem. Phys. Lett.* **1993**, *214*, 39–44.
- (112) Haddon, R. C.; Perel, A. S.; Morris, R. C.; Palstra, T. T. M.; Hebard, A. F.; Fleming, R. M. *Appl. Phys. Lett.* **1995**, *67*, 121–123.
- (113) Mihailitchi, V. D.; van Duren, J. K. J.; Blom, P. W. M.; Hummelen, J. C.; Janssen, R. A. J.; Kroon, J. M.; Rispens, M. T.; Verhees, W. J. H.; Wienk, M. M. *Adv. Funct. Mater.* **2003**, *13*, 43–46.
- (114) Guldi, D. M.; Prato, M.; Farmaceutiche, S. *Acc. Chem. Res.* **2000**, *33*, 695–703.
- (115) Wienk, M. M.; Kroon, J. M.; Verhees, W. J. H.; Knol, J.; Hummelen, J. C.; van Hal, P. A.; Janssen, R. A. J. *Angew. Chem. Int. Ed.* **2003**, *42*, 3371–3375.
- (116) He, Y.; Li, Y. *Phys. Chem. Chem. Phys.* **2011**, *13*, 1970–1983.
- (117) Scharber, M. C.; Mühlbacher, D.; Koppe, M.; Denk, P.; Waldauf, C.; Heeger, A. J.; Brabec, C. J. *Adv. Mater.* **2006**, *18*, 789–794.
- (118) Lenes, M.; Wetzelaer, G. J. a H.; Kooistra, F. B.; Veenstra, S. C.; Hummelen, J. C.; Blom, P. W. M. *Adv. Mater.* **2008**, *20*, 2116–2119.
- (119) He, Y.; Chen, H.-Y.; Hou, J.; Li, Y. *J. Am. Chem. Soc.* **2010**, *132*, 1377–1382.
- (120) Zhao, G. J.; He, Y. J.; Li, Y. *Adv. Mater.* **2010**, *22*, 4355–4358.

- (121) Holliday, S.; Ashraf, R. S.; Nielsen, C. B.; Kirkus, M.; Röhr, J. A.; Tan, C.; Collado-Fregoso, E.; Knall, A.; Durrant, J. R.; Nelson, J.; McCulloch, I. *J. Am. Chem. Soc.* **2015**, *137*, 898–904.
- (122) Gao, L.; Zhang, Z.-G.; Xue, L.; Min, J.; Zhang, J.; Wei, Z.; Li, Y. *Adv. Mater.* **2016**, *28*, 1884–1890.
- (123) Zhao, W.; Qian, D.; Zhang, S.; Li, S.; Inganäs, O.; Gao, F.; Hou, J. *Adv. Mater.* **2016**, *28*, 4734–4739.
- (124) Li, S. X.; Liu, W. Q.; Shi, M. M.; Mai, J. Q.; Lau, T. K.; Wan, J. H.; Lu, X. H.; Li, C. Z.; Chen, H. Z. *Energy Environ. Sci.* **2016**, *9*, 604–610.
- (125) Holliday, S.; Ashraf, R. S.; Wadsworth, A.; Baran, D.; Yousaf, S. A.; Nielsen, C. B.; Tan, C.-H.; Dimitrov, S. D.; Shang, Z.; Gasparini, N.; Alamoudi, M.; Laquai, F.; Brabec, C. J.; Salleo, A.; Durrant, J. R.; McCulloch, I. *Nat. Commun.* **2016**, *7*, 11585.
- (126) Chen, L.-M.; Xu, Z.; Hong, Z.; Yang, Y. *J. Mater. Chem.* **2010**, *20*, 2575.
- (127) Lefebvre, M.; Qi, Z.; Rana, D.; Pickup, P. G. *Chem. Mater.* **1999**, *11*, 262–268.
- (128) Kim, Y. H.; Sachse, C.; MacHala, M. L.; May, C.; Müller-Meskamp, L.; Leo, K. *Adv. Funct. Mater.* **2011**, *21*, 1076–1081.
- (129) Djara, V.; Bernède, J. C. *Thin Solid Films* **2005**, *493*, 273–277.
- (130) Kim, J. S.; Friend, R. H.; Cacialli, F. *J. Appl. Phys.* **1999**, *86*, 2774–2778.
- (131) Chen, S.; Manders, J. R.; Tsang, S.; So, F. *J. Mater. Chem.* **2012**, *22*, 24202–24212.
- (132) White, M. S.; Olson, D. C.; Shaheen, S. E.; Kopidakis, N.; Ginley, D. S. *Appl. Phys. Lett.* **2006**, *89*, 143517.
- (133) Hau, S. K.; Yip, H.-L.; Baek, N. S.; Zou, J.; O'Malley, K.; Jen, A. K.-Y. *Appl. Phys. Lett.* **2008**, *92*, 253301.
- (134) Tao, C.; Ruan, S.; Zhang, X.; Xie, G.; Shen, L.; Kong, X.; Dong, W.; Liu, C.; Chen, W. *Appl. Phys. Lett.* **2008**, *93*, 193307.
- (135) Tao, C.; Ruan, S.; Xie, G.; Kong, X.; Shen, L.; Meng, F.; Liu, C.; Zhang, X.; Dong, W.; Chen, W. *Appl. Phys. Lett.* **2009**, *94*, 43311.
- (136) Sun, Y.; Takacs, C. J.; Cowan, S. R.; Seo, J. H.; Gong, X.; Roy, A.; Heeger, A. J. *Adv. Mater.* **2011**, *23*, 2226–2230.

- (137) Brabec, C. J.; Shaheen, S. E.; Winder, C.; Sariciftci, N. S.; Denk, P. *Appl. Phys. Lett.* **2002**, *80*, 1288–1290.
- (138) Paci, B.; Generosi, A.; Albertini, V. R.; Perfetti, P.; de Bettignies, R.; Firon, M.; Leroy, J.; Sentein, C. *Appl. Phys. Lett.* **2005**, *87*, 194110.
- (139) De Bettignies, R.; Leroy, J.; Firon, M.; Sentein, C. *Synth. Met.* **2006**, *156*, 510–513.
- (140) Yan, L.; Song, Y.; Zhou, Y.; Song, B.; Li, Y. *Org. Electron.* **2015**, *17*, 94–101.
- (141) Brabec, C. J.; Cravino, A.; Meissner, D.; Sariciftci, N. S.; Fromherz, T.; Rispens, M. T.; Sanchez, L.; Hummelen, J. C. *Adv. Funct. Mater.* **2001**, *11*, 374–380.
- (142) Lloyd, M. T.; Olson, D. C.; Lu, P.; Fang, E.; Moore, D. L.; White, M. S.; Reese, M. O.; Ginley, D. S.; Hsu, J. W. P. *J. Mater. Chem.* **2009**, *19*, 7638–7642.
- (143) Li, Z.; Chiu, K. H.; Ashraf, R. S.; Fearn, S.; Dattani, R.; Wong, H. C.; Tan, C.-H.; Wu, J.; Cabral, J. T.; Durrant, J. R. *Sci. Rep.* **2015**, *5*, 15149.
- (144) Manificier, J. C. *Thin Solid Films* **1982**, *90*, 297–308.
- (145) Kim, H.; Gilmore, C. M.; Piqué, A.; Horwitz, J. S.; Mattoussi, H.; Murata, H.; Kafafi, Z. H.; Chrisey, D. B. *J. Appl. Phys.* **1999**, *86*, 6451–6461.
- (146) Rakhshani, A. E.; Makdisi, Y.; Ramazaniyan, H. A. *J. Appl. Phys.* **1998**, *83*, 1049–1057.
- (147) Shaheen, S. E.; Brabec, C. J.; Sariciftci, N. S.; Padinger, F.; Fromherz, T.; Hummelen, J. C. *Appl. Phys. Lett.* **2001**, *78*, 841–843.
- (148) Yang, X.; van Duren, J. K. J.; Janssen, R. A. J.; Michels, M. A. J.; Loos, J. *Macromolecules* **2004**, *37*, 2151–2158.
- (149) Kaneto, K.; Yoshino, K.; Inuishi, Y. *Solid State Commun.* **1983**, *46*, 389–391.
- (150) Elsenbaumer, R. L.; Jen, K. Y.; Oboodi, R. *Synth. Met.* **1986**, *15*, 169–174.
- (151) Loewe, R. S.; Khersonsky, S. M.; McCullough, R. D. *Adv. Mater.* **1999**, *11*, 250–253.
- (152) Sirringhaus, H.; Tessler, N.; Friend, R. H. *Science* **1998**, *280*, 1741.
- (153) Wang, G.; Swensen, J.; Moses, D.; Heeger, A. J. *J. Appl. Phys.* **2003**, *93*, 6137–6141.
- (154) Cho, S.; Lee, K.; Yuen, J.; Wang, G.; Moses, D.; Heeger, A. J.; Surin, M.; Lazzaroni,

- R. *J. Appl. Phys.* **2006**, *100*, 114503.
- (155) Padinger, F.; Rittberger, R. S.; Sariciftci, N. S. *Adv. Funct. Mater.* **2003**, *13*, 85–88.
- (156) Ma, W.; Yang, C.; Gong, X.; Lee, K.; Heeger, A. *Adv. Funct. Mater.* **2005**, *15*, 1617–1622.
- (157) Rivaton, A.; Chambon, S.; Manceau, M.; Gardette, J.-L.; Lemaître, N.; Guillerez, S. *Polym. Degrad. Stab.* **2010**, *95*, 278–284.
- (158) Dang, M. T.; Hirsch, L.; Wantz, G. *Adv. Mater.* **2011**, *23*, 3597–3602.
- (159) Dang, M. T.; Hirsch, L.; Wantz, G.; Wuest, J. D. *Chem. Rev.* **2013**, *113*, 3734–3765.
- (160) *Handbook of Oligo- and Polythiophenes*; Fichou, D., Ed.; Wiley-VCH Verlag GmbH: Weinheim, Germany, 1998.
- (161) Koster, L. J. A.; Mihailetschi, V. D.; Xie, H.; Blom, P. W. M. *Appl. Phys. Lett.* **2005**, *87*, 203502.
- (162) *ASTM G173-03(2012) Standard Tables for Reference Solar Spectral Irradiances: Direct Normal and Hemispherical on 37° Tilted Surface*; ASTM International: West Conshohocken, PA, 2012.
- (163) Ooshika, Y. *J. Phys. Soc. Jpn.* **1957**, *12*, 1246–1250.
- (164) Tsuji, M.; Huzinaga, S.; Hasino, T. *Rev. Mod. Phys.* **1960**, *32*, 425–427.
- (165) Brédas, J. L.; Brédas, J. L. *J. Chem. Phys.* **1985**, *82*, 3808.
- (166) Wudl, F.; Kobayashi, M.; Heeger, A. J. *J. Org. Chem.* **1984**, *49*, 3382–3384.
- (167) Brocks, G.; Tol, A. *Synth. Met.* **1996**, *76*, 213–216.
- (168) Zhou, Z.-H.; Maruyama, T.; Kanbara, T.; Ikeda, T.; Ichimura, K.; Yamamoto, T.; Tokuda, K. *J. Chem. Soc. Chem. Commun.* **1991**, *1460*, 1210–1212.
- (169) Son, H. J.; He, F.; Carsten, B.; Yu, L. *J. Mater. Chem.* **2011**, *21*, 18934–18945.
- (170) Xu, T.; Yu, L. *Mater. Today* **2014**, *17*, 11–15.
- (171) Dou, L.; Liu, Y.; Hong, Z.; Li, G.; Yang, Y. *Chem. Rev.* **2015**, *115*, 12633–12665.
- (172) Lu, L.; Zheng, T.; Wu, Q.; Schneider, A. M.; Zhao, D.; Yu, L. *Chem. Rev.* **2015**, *115*, 12666–12731.

- (173) Liu, C.; Wang, K.; Hu, X.; Yang, Y.; Hsu, C.-H.; Zhang, W.; Xiao, S.; Gong, X.; Cao, Y. *ACS Appl. Mater. Interfaces* **2013**, *5*, 12163–12167.
- (174) Liang, Y.; Xu, Z.; Xia, J.; Tsai, S.-T.; Wu, Y.; Li, G.; Ray, C.; Yu, L. *Adv. Mater.* **2010**, *22*, E135–E138.
- (175) Liao, S.-H.; Jhuo, H.-J.; Cheng, Y.-S.; Chen, S.-A. *Adv. Mater.* **2013**, *25*, 4766–4771.
- (176) Piliago, C.; Holcombe, T.; Douglas, J.; Woo, C.; Beaujuge, P.; Fréchet, J. *J. Am. Chem. Soc.* **2010**, *132*, 7595–7597.
- (177) Cabanetos, C.; El Labban, A.; Bartelt, J. A.; Douglas, J. D.; Mateker, W. R.; Fréchet, J. M. J.; McGehee, M. D.; Beaujuge, P. M. *J. Am. Chem. Soc.* **2013**, *135*, 4656–4659.
- (178) Li, W.; Hendriks, K. H.; Roelofs, W. S. C.; Kim, Y.; Wienk, M. M.; Janssen, R. A. J. *Adv. Mater.* **2013**, *25*, 3182–3186.
- (179) Choi, H.; Ko, S.; Kim, T.; Morin, P.-O.; Walker, B.; Lee, B. H.; Leclerc, M.; Kim, J. Y.; Heeger, A. J. *Adv. Mater.* **2015**, *27*, 3318–3324.
- (180) Blouin, N.; Michaud, A.; Gendron, D.; Wakim, S.; Blair, E.; Neagu-Plesu, R.; Belletête, M.; Durocher, G.; Tao, Y.; Leclerc, M. *J. Am. Chem. Soc.* **2008**, *130*, 732–742.
- (181) Zhang, Y.; Zhou, H.; Seiffter, J.; Ying, L.; Mikhailovsky, A.; Heeger, A. J.; Bazan, G. C.; Nguyen, T. Q. *Adv. Mater.* **2013**, *25*, 7038–7044.
- (182) Dou, L.; Chen, C.; Yoshimura, K.; Ohya, K.; Chang, W.; Gao, J.; Liu, Y.; Richard, E.; Yang, Y. *Macromolecules* **2013**, *46*, 3384–3390.
- (183) Brédas, J.-L.; Beljonne, D.; Coropceanu, V.; Cornil, J. *Chem. Rev.* **2004**, *104*, 4971–5004.
- (184) Roncali, J. *Macromol. Rapid Commun.* **2007**, *28*, 1761–1775.
- (185) Liang, Y.; Yu, L. *Acc. Chem. Res.* **2010**, *43*, 1227–1236.
- (186) Liang, Y.; Yu, L. *Polym. Rev.* **2010**, *50*, 454–473.
- (187) Liang, Y.; Wu, Y.; Feng, D.; Tsai, S.-T.; Son, H.-J.; Li, G.; Yu, L. *J. Am. Chem. Soc.* **2009**, *131*, 56–57.
- (188) Liang, Y.; Feng, D.; Wu, Y.; Tsai, S.-T.; Li, G.; Ray, C.; Yu, L. *J. Am. Chem. Soc.* **2009**, *131*, 7792–7799.

- (189) Saadeh, H. A.; Lu, L.; He, F.; Bullock, J. E.; Wang, W.; Carsten, B.; Yu, L. *ACS Macro Lett.* **2012**, *1*, 361–365.
- (190) He, Y.; Zhao, G.; Peng, B.; Li, Y. *Adv. Funct. Mater.* **2010**, *20*, 3383–3389.
- (191) Szarko, J. M.; Guo, J.; Liang, Y.; Lee, B.; Rolczynski, B. S.; Strzalka, J.; Xu, T.; Loser, S.; Marks, T. J.; Yu, L.; Chen, L. X. *Adv. Mater.* **2010**, *22*, 5468–5472.
- (192) Lu, L.; Yu, L. *Adv. Mater.* **2014**, *26*, 4413–4430.
- (193) Wang, Y.; Xin, X.; Lu, Y.; Xiao, T.; Xu, X.; Zhao, N.; Hu, X.; Ong, B. S.; Ng, S. C.; Ong, S.; Ng, S. C. *Macromolecules* **2013**, *46*, 9587–9592.
- (194) Ho, V.; Boudouris, B. W.; Segalman, R. A. *Macromolecules* **2010**, *43*, 7895–7899.
- (195) Jheng, J.-F.; Lai, Y.-Y.; Wu, J.-S.; Chao, Y.-H.; Wang, C.-L.; Hsu, C.-S. *Adv. Mater.* **2013**, *25*, 2445–2451.
- (196) Biniek, L.; Fall, S.; Chochos, C. L.; Anokhin, D. V.; Ivanov, D. A.; Leclerc, N.; Lévêque, P.; Heiser, T. *Macromolecules* **2010**, *43*, 9779–9786.
- (197) Graham, K. R.; Cabanetos, C.; Jahnke, J. P.; Idso, M. N.; El Labban, A.; Ngongang Ndjawa, G. O.; Heumueller, T.; Vandewal, K.; Salleo, A.; Chmelka, B. F.; Amassian, A.; Beaujuge, P. M.; McGehee, M. D. *J. Am. Chem. Soc.* **2014**, *136*, 9608–9618.
- (198) Johansson Seechurn, C. C. C.; Kitching, M. O.; Colacot, T. J.; Snieckus, V. *Angew. Chem. Int. Ed.* **2012**, *51*, 5062–5085.
- (199) Beletskaya, I. P.; Cheprakov, A. V. *Chem. Rev.* **2000**, *100*, 3009–3066.
- (200) Knappe, C. E. I.; von Wangelin, A. J. *Chem. Soc. Rev.* **2011**, *40*, 4948–4962.
- (201) Haas, D.; Hammann, J. M.; Greiner, R.; Knochel, P. *ACS Catal.* **2016**, *6*, 1540–1552.
- (202) Stille, J. K. *Angew. Chem. Int. Ed. Engl.* **1986**, *25*, 508–524.
- (203) Sonogashira, K. *J. Organomet. Chem.* **2002**, *653*, 46–49.
- (204) Kotha, S.; Lahiri, K.; Kashinath, D. *Tetrahedron* **2002**, *58*, 9633–9695.
- (205) Negishi, E. *Angew. Chem. Int. Ed.* **2011**, *50*, 6738–6764.
- (206) Suzuki, A. *Angew. Chem. Int. Ed.* **2011**, *50*, 6722–6737.
- (207) Forster, M.; Annan, K. O.; Scherf, U. *Macromolecules* **1999**, *32*, 3159–3162.

- (208) Jayakannan, M.; van Dongen, J. L. J.; Janssen, R. A. J. *Macromolecules* **2001**, *34*, 5386–5393.
- (209) Huo, L.; Hou, J.; Zhang, S.; Chen, H.-Y.; Yang, Y. *Angew. Chem. Int. Ed.* **2010**, *49*, 1500–1503.
- (210) Huo, L.; Zhang, S.; Guo, X.; Xu, F.; Li, Y.; Hou, J. *Angew. Chem. Int. Ed.* **2011**, *50*, 9697–9702.
- (211) Miyaura, N.; Suzuki, A. *J. Chem. Soc. Chem. Commun.* **1979**, 866–867.
- (212) Amatore, C.; Jutand, A.; Le Duc, G. *Chem. Eur. J.* **2011**, *17*, 2492–2503.
- (213) Frahn, J.; Karakaya, B.; Schäfer, A.; Schlüter, A. D. *Tetrahedron* **1997**, *53*, 15459–15467.
- (214) Ishiyama, T.; Murata, M.; Miyaura, N. *J. Org. Chem.* **1995**, *60*, 7508–7510.
- (215) Schlüter, A. D. *J. Polym. Sci. A Polym. Chem.* **2001**, *39*, 1533–1556.
- (216) Azarian, D.; Dua, S. S.; Eaborn, C.; Walton, D. R. M. *J. Organomet. Chem.* **1976**, *117*, C55–C57.
- (217) Kosugi, M.; Shimizu, Y.; Migita, T. *J. Organomet. Chem.* **1977**, *129*, C36–C38.
- (218) Milstein, D.; Stille, J. K. *J. Am. Chem. Soc.* **1978**, *100*, 3636–3638.
- (219) Lenz, R. W. *Macromolecules* **1990**, *23*, 2417–2418.
- (220) Bao, Z.; Chan, W. K.; Yu, L. *J. Am. Chem. Soc.* **1995**, *117*, 12426–12435.
- (221) Farina, V.; Krishnamurthy, V.; Scott, W. J. The Stille Reaction. In *Organic Reactions*; Denmark, S. E., Abué, J., Berkowitz, D., Busacca, C. A., Cha, J. K., Evans, P. A., Feldman, P., Hall, D., Huryn, Donna, M., Kozlowski, M. C., Molander, G., Montgomery, J., Padwa, A., Weinreb, S. M., Eds.; John Wiley & Sons.: Hoboken, NJ, 1997; Vol. 50.
- (222) Echavarren, A. M.; Stille, J. K. *J. Am. Chem. Soc.* **1987**, *109*, 5478–5486.
- (223) Buck, B.; Mascioni, A.; Que, L.; Veglia, G. *J. Am. Chem. Soc.* **2003**, *125*, 13316–13317.
- (224) Biological Properties of Metal Alkyl Derivatives. In *Metal Ions in Biological Systems*; Sigel, H., Sigel, A., Eds.; Marcel Dekker: New York, 1993; Vol. 29.
- (225) Aldridge, W. N. *Biochem. J.* **1958**, *69*, 367–376.

- (226) Whalen, M. M.; Loganathan, B. G.; Kannan, K. *Environ. Res.* **1999**, *81*, 108–116.
- (227) Gitlitz, M. N.; Moran, M. K. Tin Compounds. In *Kirk-Othmer Encyclopedia of Chemical Technology*, 5th ed.; John Wiley & Sons: Hoboken, NJ, 2004; Vol. 24.
- (228) Wang, M.; Hu, X.; Liu, P.; Li, W.; Gong, X.; Huang, F.; Cao, Y. *J. Am. Chem. Soc.* **2011**, *133*, 9638–9641.
- (229) Li, G.; Shrotriya, V.; Huang, J.; Yao, Y.; Moriarty, T.; Emery, K.; Yang, Y. *Nat. Mater.* **2005**, *4*, 864–868.
- (230) Sanyal, M.; Schmidt-Hansberg, B.; Klein, M. F. G.; Munuera, C.; Vorobiev, A.; Colsmann, A.; Scharfer, P.; Lemmer, U.; Schabel, W.; Dosch, H.; Barrena, E. *Macromolecules* **2011**, *44*, 3795–3800.
- (231) Schmidt-Hansberg, B.; Sanyal, M.; Klein, M. F. G.; Pfaff, M.; Schnabel, N.; Jaiser, S.; Vorobiev, A.; Müller, E.; Colsmann, A.; Scharfer, P.; Gerthsen, D.; Lemmer, U.; Barrena, E.; Schabel, W. *ACS Nano* **2011**, *5*, 8579–8590.
- (232) Kohn, P.; Rong, Z.; Scherer, K. H.; Sepe, A.; Sommer, M.; Müller-Buschbaum, P.; Friend, R. H.; Steiner, U.; Hüttner, S. *Macromolecules* **2013**, *46*, 4002–4013.
- (233) Chou, K. W.; Yan, B.; Li, R.; Li, E. Q.; Zhao, K.; Anjum, D. H.; Alvarez, S.; Gassaway, R.; Biocca, A.; Thoroddsen, S. T.; Hexemer, A.; Amassian, A. *Adv. Mater.* **2013**, *25*, 1923–1929.
- (234) Holdcroft, S. *Adv. Mater.* **2001**, *13*, 1753–1765.
- (235) Na, S.-I.; Kim, S.-S.; Kwon, S.-S.; Jo, J.; Kim, J.; Lee, T.; Kim, D.-Y. *Appl. Phys. Lett.* **2007**, *91*, 173509.
- (236) Han, X.; Chen, X.; Holdcroft, S. *Chem. Mater.* **2009**, *21*, 4631–4637.
- (237) Heeger, A. J. *Adv. Mater.* **2014**, *26*, 10–28.
- (238) Yang, X.; Loos, J.; Veenstra, S. C.; Verhees, W. J. H.; Wienk, M. M.; Kroon, J. M.; Michels, M. A. J.; Janssen, R. *Nano Lett.* **2005**, *5*, 579–583.
- (239) Ruderer, M. A.; Meier, R.; Porcar, L.; Cubitt, R.; Müller-Buschbaum, P. *J. Phys. Chem. Lett.* **2012**, *3*, 683–688.
- (240) Agostinelli, T.; Lilliu, S.; Labram, J. G.; Campoy-Quiles, M.; Hampton, M.; Pires, E.; Rawle, J.; Bikondoa, O.; Bradley, D. D. C.; Anthopoulos, T. D.; Nelson, J.; Macdonald, J. E. *Adv. Funct. Mater.* **2011**, *21*, 1701–1708.
- (241) Kozub, D. R.; Vakhshouri, K.; Orme, L. M.; Wang, C.; Hexemer, A.; Gomez, E. D.

Macromolecules **2011**, *44*, 5722–5726.

- (242) Treat, N. D.; Shuttle, C. G.; Toney, M. F.; Hawker, C. J.; Chabynyc, M. L. *J. Mater. Chem.* **2011**, *21*, 15224–15231.
- (243) Guo, J.; Liang, Y.; Szarko, J.; Lee, B.; Son, H. J.; Rolczynski, B. S.; Yu, L.; Chen, L. X. *J. Phys. Chem. B* **2010**, *114*, 742–748.
- (244) Wang, T.; Pearson, A. J.; Dunbar, A. D. F.; Staniec, P. a.; Watters, D. C.; Yi, H.; Ryan, A. J.; Jones, R. A. L.; Iraqi, A.; Lidzey, D. G. *Adv. Funct. Mater.* **2012**, *22*, 1399–1408.
- (245) Bartelt, J. A.; Beiley, Z. M.; Hoke, E. T.; Mateker, W. R.; Douglas, J. D.; Collins, B. A.; Tumbleston, J. R.; Graham, K. R.; Amassian, A.; Ade, H.; Fréchet, J. M. J.; Toney, M. F.; McGehee, M. D. *Adv. Energy Mater.* **2013**, *3*, 364–374.
- (246) Yao, E.; Tsai, Y.; Hsu, W. *Int. J. Photoenergy* **2014**, *2014*, 952528.
- (247) Liao, H.-C.; Ho, C.-C.; Chang, C.-Y.; Jao, M.-H.; Darling, S. B.; Su, W.-F. *Mater. Today* **2013**, *16*, 326–336.
- (248) Lee, J. K.; Ma, W. L.; Brabec, C. J.; Yuen, J.; Moon, J. S.; Kim, J. Y.; Lee, K.; Bazan, G. C.; Heeger, A. J. *J. Am. Chem. Soc.* **2008**, *130*, 3619–3623.
- (249) Salim, T.; Wong, L. H.; Bräuer, B.; Kukreja, R.; Foo, Y. L.; Bao, Z.; Lam, Y. M. *J. Mater. Chem.* **2011**, *21*, 242–250.
- (250) Clark, J.; Chang, J.-F.; Spano, F. C.; Friend, R. H.; Silva, C. *Appl. Phys. Lett.* **2009**, *94*, 163306.
- (251) van Bavel, S. S.; Sourty, E.; de With, G.; Loos, J. *Nano Lett.* **2009**, *9*, 507–513.
- (252) Kouijzer, S.; Michels, J. J.; van den Berg, M.; Gevaerts, V. S.; Turbiez, M.; Wienk, M. M.; Janssen, R. A. J. *J. Am. Chem. Soc.* **2013**, *135*, 12057–12067.
- (253) Kim, W.; Kim, J. K.; Kim, E.; Ahn, T. K.; Wang, D. H.; Park, J. H. *J. Phys. Chem. C* **2015**, *119*, 5954–5961.
- (254) Su, M.-S.; Kuo, C.-Y.; Yuan, M.-C.; Jeng, U.-S.; Su, C.-J.; Wei, K.-H. *Adv. Mater.* **2011**, *23*, 3315–3319.
- (255) Rogers, J. T.; Schmidt, K.; Toney, M. F.; Bazan, G. C.; Kramer, E. J. *J. Am. Chem. Soc.* **2012**, *134*, 2884–2887.
- (256) Schmidt, K.; Tassone, C. J.; Niskala, J. R.; Yiu, A. T.; Lee, O. P.; Weiss, T. M.; Wang, C.; Fréchet, J. M. J.; Beaujuge, P. M.; Toney, M. F. *Adv. Mater.* **2014**, *26*,

300–305.

- (257) Lou, S. J.; Szarko, J. M.; Xu, T.; Yu, L.; Marks, T. J.; Chen, L. X. *J. Am. Chem. Soc.* **2011**, *133*, 20661–20663.
- (258) Collins, B. A.; Li, Z.; Tumbleston, J. R.; Gann, E.; McNeill, C. R.; Ade, H. *Adv. Energy Mater.* **2013**, *3*, 65–74.
- (259) Cheng, P.; Zhan, X. *Chem. Soc. Rev.* **2016**, *45*, 2544–2582.
- (260) Jørgensen, M.; Norrman, K.; Krebs, F. C. *Sol. Energy Mater. Sol. Cells* **2008**, *92*, 686–714.
- (261) Jørgensen, M.; Norrman, K.; Gevorgyan, S. A.; Tromholt, T.; Andreasen, B.; Krebs, F. C. *Adv. Mater.* **2012**, *24*, 580–612.
- (262) Grossiord, N.; Kroon, J. M.; Andriessen, R.; Blom, P. W. M. *Org. Electron.* **2012**, *13*, 432–456.
- (263) Fraga Domínguez, I.; Distler, A.; Lüer, L. *Adv. Energy Mater.* **2017**, *7*, 1601320.
- (264) Norrman, K.; Larsen, N. B.; Krebs, F. C. *Sol. Energy Mater. Sol. Cells* **2006**, *90*, 2793–2814.
- (265) Norrman, K.; Alstrup, J.; Jørgensen, M.; Lira-Cantu, M.; Larsen, N. B.; Krebs, F. C. *Proceedings of SPIE*; Kafafi, Z. H., Lane, P. A., Eds.; San Diego, CA, Aug. 13, 2006; Vol. 6334, p 63340O.
- (266) Krebs, F. C.; Norrman, K. *Prog. Photovoltaics Res. Appl.* **2007**, *15*, 697–712.
- (267) Norrman, K.; Gevorgyan, S. A.; Krebs, F. C. *ACS Appl. Mater. Interfaces* **2009**, *1*, 102–112.
- (268) Klumbies, H.; Karl, M.; Hermenau, M.; Rösch, R.; Seeland, M.; Hoppe, H.; Müller-Meskamp, L.; Leo, K. *Sol. Energy Mater. Sol. Cells* **2014**, *120*, 685–690.
- (269) Glen, T. S.; Scarratt, N. W.; Yi, H.; Iraqi, A.; Wang, T.; Kingsley, J.; Buckley, A. R.; Lidzey, D. G.; Donald, A. M. *Sol. Energy Mater. Sol. Cells* **2015**, *140*, 25–32.
- (270) Hermenau, M.; Riede, M.; Leo, K.; Gevorgyan, S. A.; Krebs, F. C.; Norrman, K. *Sol. Energy Mater. Sol. Cells* **2011**, *95*, 1268–1277.
- (271) Glen, T. S.; Scarratt, N. W.; Yi, H.; Iraqi, A.; Wang, T.; Kingsley, J.; Buckley, A. R.; Lidzey, D. G.; Donald, A. M. *J. Polym. Sci. B Polym. Phys.* **2015**, *54*, 216–224.
- (272) Glatthaar, M.; Riede, M.; Keegan, N.; Sylvester-Hvid, K.; Zimmermann, B.;

- Niggemann, M.; Hinsch, A.; Gombert, A. *Sol. Energy Mater. Sol. Cells* **2007**, *91*, 390–393.
- (273) Wagenpfahl, A.; Rauh, D.; Binder, M.; Deibel, C.; Dyakonov, V. *Phys. Rev. B* **2010**, *82*, 115306.
- (274) Cros, S.; Firon, M.; Lenfant, S.; Trouslard, P.; Beck, L. *Nucl. Instr. Meth. Phys. Res. B* **2006**, *251*, 257–260.
- (275) Lögdlund, M.; Brédas, J. L. *J. Chem. Phys.* **1994**, *101*, 4357–4364.
- (276) Krebs, F. C.; Carlé, J. E.; Cruys-Bagger, N.; Andersen, M.; Lilliedal, M. R.; Hammond, M. A.; Hvidt, S. *Sol. Energy Mater. Sol. Cells* **2005**, *86*, 499–516.
- (277) Kawano, K.; Pacios, R.; Poplavskyy, D.; Nelson, J.; Bradley, D. D. C.; Durrant, J. R. *Sol. Energy Mater. Sol. Cells* **2006**, *90*, 3520–3530.
- (278) Voroshazi, E.; Verreet, B.; Buri, A.; Müller, R.; Di Nuzzo, D.; Heremans, P. *Org. Electron.* **2011**, *12*, 736–744.
- (279) Ecker, B.; Nolasco, J. C.; Pallarés, J.; Marsal, L. F.; Posdorfer, J.; Parisi, J.; Von Hauff, E. *Adv. Funct. Mater.* **2011**, *21*, 2705–2711.
- (280) Manceau, M.; Rivaton, A.; Gardette, J.-L.; Guillerez, S.; Lemaître, N. *Sol. Energy Mater. Sol. Cells* **2011**, *95*, 1315–1325.
- (281) Norrman, K.; Madsen, M. V.; Gevorgyan, S. A.; Krebs, F. C. *J. Am. Chem. Soc.* **2010**, *132*, 16883–16892.
- (282) Cowan, S. R.; Schulz, P.; Giordano, A. J.; Garcia, A.; MacLeod, B. A.; Marder, S. R.; Kahn, A.; Ginley, D. S.; Ratcliff, E. L.; Olson, D. C. *Adv. Funct. Mater.* **2014**, *24*, 4671–4680.
- (283) Venkatesan, S.; Ngo, E.; Khatiwada, D.; Zhang, C.; Qiao, Q. *ACS Appl. Mater. Interfaces* **2015**, *7*, 16093–16100.
- (284) de Jong, M. P.; van IJzendoorn, L. J.; de Voigt, M. J. A. *Appl. Phys. Lett.* **2000**, *77*, 2255–2257.
- (285) Bulle-Lieuwma, C. W. T.; van Gennip, W. J. H.; van Duren, J. K. J.; Jonkheijm, P.; Janssen, R. A. J.; Niemantsverdriet, J. W. *Appl. Surf. Sci.* **2003**, *203–204*, 547–550.
- (286) Rivaton, A.; Tournebize, A.; Gaume, J.; Bussière, P.-O.; Gardette, J.-L.; Therias, S. *Polym. Int.* **2014**, *63*, 1335–1345.

- (287) Abdou, M. S. A.; Holdcroft, S. *Macromolecules* **1993**, *26*, 2954–2962.
- (288) Abdou, M. S. A.; Holdcroft, S. *Can. J. Chem.* **1995**, *73*, 1893–1901.
- (289) Chambon, S.; Rivaton, A.; Gardette, J.-L.; Firon, M.; Lutsen, L. *J. Polym. Sci. A Polym. Chem.* **2007**, *45*, 317–331.
- (290) Manceau, M.; Rivaton, A.; Gardette, J.-L.; Guillerez, S.; Lemaître, N. *Polym. Degrad. Stab.* **2009**, *94*, 898–907.
- (291) Manceau, M.; Gaume, J.; Rivaton, A.; Gardette, J.-L.; Monier, G.; Bideux, L. *Thin Solid Films* **2010**, *518*, 7113–7118.
- (292) Hintz, H.; Egelhaaf, H.-J.; Peisert, H.; Chassé, T. *Polym. Degrad. Stab.* **2010**, *95*, 818–825.
- (293) Tournebize, A.; Bussière, P.-O.; Wong-Wah-Chung, P.; Thérias, S.; Rivaton, A.; Gardette, J.-L.; Beaupré, S.; Leclerc, M. *Adv. Energy Mater.* **2013**, *3*, 478–487.
- (294) Bussière, P.-O.; Rivaton, A. A.; Thérias, S.; Gardette, J.-L. *J. Phys. Chem. B* **2012**, *116*, 802–812.
- (295) Holdcroft, S. *Macromolecules* **1991**, *24*, 2119–2121.
- (296) Holdcroft, S. *Macromolecules* **1991**, *24*, 4834–4838.
- (297) Foote, C. S.; Clennan, E. L. Properties and Reactions of Singlet Dioxygen. In *Active Oxygen in Chemistry*; Foote, C. S., Valentine, J. S., Greenberg, A., Liebman, J. F., Eds.; Structure Energetics and Reactivity in Chemistry Series; Springer: Dordrecht, the Netherlands, 1995; Vol. 2, pp 105–140.
- (298) Soon, Y. W.; Cho, H.; Low, J.; Bronstein, H.; McCulloch, I.; Durrant, J. R. *Chem. Commun.* **2013**, *49*, 1291.
- (299) Alem, S.; Wakim, S.; Lu, J.; Robertson, G.; Ding, J.; Tao, Y. *ACS Appl. Mater. Interfaces* **2012**, *4*, 2993–2998.
- (300) Wasserman, H. H.; Scheffer, J. R.; Cooper, J. L. *J. Am. Chem. Soc.* **1972**, *94*, 4991–4996.
- (301) Dam, N.; Scurlock, R. D.; Wang, B.; Ma, L.; Sundahl, M.; Ogilby, P. R. *Chem. Mater.* **1999**, *11*, 1302–1305.
- (302) Ma, L.; Wang, X.; Wang, B.; Chen, J.; Wang, J.; Huang, K.; Zhang, B.; Cao, Y.; Han, Z.; Qian, S.; Yao, S. *Chem. Phys.* **2002**, *285*, 85–94.

- (303) Hoke, E. T.; Sachs-Quintana, I. T.; Lloyd, M. T.; Kauvar, I.; Mateker, W. R.; Nardes, A. M.; Peters, C. H.; Kopidakis, N.; McGehee, M. D. *Adv. Energy Mater.* **2012**, *2*, 1351–1357.
- (304) Silva, H. S.; Tournebize, A.; Bégué, D.; Peisert, H.; Chassé, T.; Gardette, J.-L.; Therias, S.; Rivaton, A.; Hiorns, R. C. *RSC Adv.* **2014**, *4*, 54919–54923.
- (305) Mateker, W. R.; Heumueller, T.; Cheacharoen, R.; Sachs-Quintana, I. T.; McGehee, M. D.; Warnan, J.; Beaujuge, P. M.; Liu, X.; Bazan, G. C. *Chem. Mater.* **2015**, *27*, 6345–6353.
- (306) Manceau, M.; Bundgaard, E.; Carlé, J. E.; Hagemann, O.; Helgesen, M.; Søndergaard, R.; Jørgensen, M.; Krebs, F. C. *J. Mater. Chem.* **2011**, *21*, 4132–4141.
- (307) Abdou, M. S. A.; Orfino, F. P.; Son, Y.; Holdcroft, S. *J. Am. Chem. Soc.* **1997**, *119*, 4518–4524.
- (308) Desiraju, G.; Steiner, T. *The Weak Hydrogen Bond: In Structural Chemistry and Biology*; Oxford University Press: Oxford, England, 2001.
- (309) Schafferhans, J.; Baumann, A.; Deibel, C.; Dyakonov, V. *Appl. Phys. Lett.* **2008**, *93*, 93303.
- (310) Seemann, A.; Sauermann, T.; Lungenschmied, C.; Armbruster, O.; Bauer, S.; Egelhaaf, H.-J.; Hauch, J. *Sol. Energy* **2011**, *85*, 1238–1249.
- (311) Aygu, U.; Hintz, H.; Egelhaaf, H.-J.; Distler, A.; Abb, S.; Peisert, H.; Chassé, T. *J. Phys. Chem. C* **2013**, *117*, 4992–4998.
- (312) Liao, H.-H.; Yang, C.-M.; Liu, C.-C.; Horng, S.-F.; Meng, H.-F.; Shy, J.-T. *J. Appl. Phys.* **2008**, *103*, 104506.
- (313) Lüer, L.; Egelhaaf, H.-J.; Oelkrug, D.; Cerullo, G.; Lanzani, G.; Huisman, B.-H.; de Leeuw, D. M. *Org. Electron.* **2004**, *5*, 83–89.
- (314) Seemann, A.; Egelhaaf, H.-J.; Brabec, C. J.; Hauch, J. A. *Org. Electron.* **2009**, *10*, 1424–1428.
- (315) Aguirre, A.; Meskers, S. C. J.; Janssen, R. A. J.; Egelhaaf, H.-J. *Org. Electron.* **2011**, *12*, 1657–1662.
- (316) Chambon, S.; Rivaton, A.; Gardette, J.-L.; Firon, M. *Sol. Energy Mater. Sol. Cells* **2008**, *92*, 785–792.
- (317) Manceau, M.; Chambon, S.; Rivaton, A.; Gardette, J.-L.; Guillerez, S.; Lemaître, N.

Sol. Energy Mater. Sol. Cells **2010**, *94*, 1572–1577.

- (318) Susarova, D. K.; Piven, N. P.; Akkuratov, A. V.; Frolova, L. A.; Polinskaya, M. S.; Ponomarenko, S. A.; Babenko, S. D.; Troshin, P. A. *Chem. Commun.* **2015**, *51*, 2239–2241.
- (319) Wohlers, M.; Werner, H.; Herein, D.; Schedel-Niedrig, T.; Bauer, A.; Schlögl, R. *Synth. Met.* **1996**, *77*, 299–302.
- (320) Kroll, G. H.; Benning, P. J.; Chen, Y.; Ohno, T. R.; Weaver, J. H.; Chibante, L. P. F.; Smalley, R. E. *Chem. Phys. Lett.* **1991**, *181*, 112–116.
- (321) Creegan, K. M.; Robbins, J. L.; Robbins, W. K.; Millar, J. M.; Sherwood, R. D.; Tindall, P. J.; Cox, D. M.; McCauley, J. P.; Jones, D. R. *J. Am. Chem. Soc.* **1992**, *114*, 1103–1105.
- (322) Tapponnier, A.; Biaggio, I.; Günter, P. *Appl. Phys. Lett.* **2005**, *86*, 112114.
- (323) Bastos, J. P.; Voroshazi, E.; Fron, E.; Brammertz, G.; Vangerven, T.; Van der Auweraer, M.; Poortmans, J.; Cheyns, D. *ACS Appl. Mater. Interfaces* **2016**, *8*, 9798–9805.
- (324) Hamed, A.; Sun, Y. Y.; Tao, Y. K.; Meng, R. L.; Hor, P. H. *Phys. Rev. B* **1993**, *47*, 10873–10880.
- (325) Rao, A. M.; Zhou, P.; Wang, K.-A.; Hager, G. T.; Holden, J. M.; Wang, Y.; Lee, W.-T.; Bi, X.-X.; Eklund, P. C.; Cornett, D. S.; Duncan, M. A.; Amster, I. J. *Science* **1993**, *259*, 955–957.
- (326) Rao, A. M.; Menon, M.; Wang, K.-A.; Eklund, P. C.; Subbaswamy, K. R.; Cornett, D. S.; Duncan, M. A.; Amster, I. J. *Chem. Phys. Lett.* **1994**, *224*, 106–112.
- (327) Segura, J. L.; Martín, N. *Chem. Soc. Rev.* **2000**, *29*, 13–25.
- (328) Zhou, P.; Dong, Z.-H.; Rao, A. M.; Eklund, P. C. *Chem. Phys. Lett.* **1993**, *211*, 337–340.
- (329) Adams, G. B.; Page, J. B.; Sankey, O. F.; O’Keeffe, M. *Phys. Rev. B* **1994**, *50*, 17471–17479.
- (330) Knol, J.; Hummelen, J. C. *J. Am. Chem. Soc.* **2000**, *122*, 3226–3227.
- (331) Wang, Y.; Holden, J. M.; Dong, Z.-H.; Bi, X.-X.; Eklund, P. C. *Chem. Phys. Lett.* **1993**, *211*, 341–345.
- (332) Eklund, P. C.; Wang, Y.; Holden, J. M.; Rao, A. M.; Zhou, P.; Wang, Y.; Holden, J.

M. *Thin Solid Films* **1995**, 257, 185–203.

- (333) Wang, J.; Enevold, J.; Edman, L. *Adv. Funct. Mater.* **2013**, 23, 3220–3225.
- (334) Wang, Y.; Holden, J. M.; Bi, X.; Eklund, P. C. *Chem. Phys. Lett.* **1994**, 217, 413–417.
- (335) Distler, A.; Sauermann, T.; Egelhaaf, H.-J.; Rodman, S.; Waller, D.; Cheon, K.-S.; Lee, M.; Guldi, D. M. *Adv. Energy Mater.* **2014**, 4, 1300693.
- (336) Piersimoni, F.; Degutis, G.; Bertho, S.; Vandewal, K.; Spoltore, D.; Vangerven, T.; Drijkoningen, J.; Van Bael, M. K.; Hardy, A.; D’Haen, J.; Maes, W.; Vanderzande, D.; Nesladek, M.; Manca, J. *J. Polym. Sci. B Polym. Phys.* **2013**, 51, 1209–1214.
- (337) Wong, H. C.; Li, Z.; Tan, C. H.; Zhong, H.; Huang, Z.; Bronstein, H.; McCulloch, I.; Cabral, J. T.; Durrant, J. R. *ACS Nano* **2014**, 8, 1297–1308.
- (338) Heumueller, T.; Mateker, W. R.; Distler, A.; Fritze, U. F.; Cheacharoen, R.; Nguyen, W. H.; Biele, M.; Salvador, M.; von Delius, M.; Egelhaaf, H.-J.; McGehee, M. D.; Brabec, C. J. *Energy Environ. Sci.* **2015**, 9, 247–256.
- (339) Dzwilewski, A.; Wågberg, T.; Edman, L. *J. Am. Chem. Soc.* **2009**, 131, 4006–4011.
- (340) Wang, J.; Larsen, C.; Wågberg, T.; Edman, L. *Adv. Funct. Mater.* **2011**, 21, 3723–3728.
- (341) Neugebauer, H.; Brabec, C. J.; Hummelen, J. C.; Sariciftci, N. S. *Sol. Energy Mater. Sol. Cells* **2000**, 61, 35–42.
- (342) Reese, M. O.; Nardes, A. M.; Rupert, B. L.; Larsen, R. E.; Olson, D. C.; Lloyd, M. T.; Shaheen, S. E.; Ginley, D. S.; Rumbles, G.; Kopidakis, N. *Adv. Funct. Mater.* **2010**, 20, 3476–3483.
- (343) Sengupta, E.; Domanski, A. L.; Weber, S. A. L.; Untch, M. B.; Butt, H.-J.; Sauermann, T.; Egelhaaf, H.-J.; Berger, R. *J. Phys. Chem. C* **2011**, 115, 19994–20001.
- (344) Tournebize, A.; Bussière, P.-O.; Rivaton, A.; Gardette, J.-L.; Medlej, H.; Hiorns, R. C.; Dagrón-Lartigau, C.; Krebs, F. C.; Norrman, K. *Chem. Mater.* **2013**, 25, 4522–4528.
- (345) Chen, Y.; Lin, K. *J. Polym. Sci. A Polym. Chem.* **1999**, 37, 2969–2975.
- (346) Morton, J. R.; Negri, F.; Preston, K. F. *Acc. Chem. Res.* **1998**, 31, 63–69.
- (347) Morton, J. R.; Preston, K. F.; Krusic, P. J.; Hill, S. A.; Wasserman, E. *J. Phys. Chem.*

1992, 96, 3576–3578.

- (348) Cremonini, M. A.; Lunazzi, L.; Placucci, G.; Krusic, P. J. *J. Org. Chem.* **1993**, *58*, 4735–4738.
- (349) Prat, F.; Stackow, R.; Bernstein, R.; Qian, W.; Rubin, Y.; Foote, C. S. *J. Phys. Chem. A* **1999**, *103*, 7230–7235.
- (350) Distler, A.; Kutka, P.; Sauermann, T.; Egelhaaf, H.-J.; Guldi, D. M.; Di Nuzzo, D.; Meskers, S. C. J.; Janssen, R. A. J. *Chem. Mater.* **2012**, *24*, 4397–4405.
- (351) Treat, N. D.; Chabinyk, M. L. *Annu. Rev. Phys. Chem.* **2014**, *65*, 59–81.
- (352) Cardinaletti, I.; Kesters, J.; Bertho, S.; Conings, B.; Piersimoni, F.; D'Haen, J.; Lutsen, L.; Nesladek, M.; Van Mele, B.; Van Assche, G.; Vandewal, K.; Salleo, A.; Vanderzande, D.; Maes, W.; Manca, J. V. *J. Photonics Energy* **2014**, *4*, 40997.
- (353) Zhong, H.; Yang, X.; deWith, B.; Loos, J. *Macromolecules* **2006**, *39*, 218–223.
- (354) Conings, B.; Bertho, S.; Vandewal, K.; Senes, A.; D'Haen, J.; Manca, J.; Janssen, R. A. J. *Appl. Phys. Lett.* **2010**, *96*, 163301.
- (355) Lindqvist, C.; Sanz-Velasco, A.; Wang, E.; Bäcke, O.; Gustafsson, S.; Olsson, E.; Andersson, M. R.; Müller, C. *J. Mater. Chem. A* **2013**, *1*, 7174.
- (356) Yang, X.; Alexeev, A.; Michels, M. A. J.; Loos, J. *Macromolecules* **2005**, *38*, 4289–4295.
- (357) Watts, B.; Belcher, W. J.; Thomsen, L.; Ade, H.; Dastoor, P. C. *Macromolecules* **2009**, *42*, 8392–8397.
- (358) He, C.; Germack, D. S.; Joseph Kline, R.; Delongchamp, D. M.; Fischer, D. A.; Snyder, C. R.; Toney, M. F.; Kushmerick, J. G.; Richter, L. J. *Sol. Energy Mater. Sol. Cells* **2011**, *95*, 1375–1381.
- (359) Müller, C. *Chem. Mater.* **2015**, *27*, 2740–2754.
- (360) Bertho, S.; Janssen, G.; Cleij, T. J.; Conings, B.; Moons, W.; Gadisa, A.; D'Haen, J.; Goovaerts, E.; Lutsen, L.; Manca, J.; Vanderzande, D. *Sol. Energy Mater. Sol. Cells* **2008**, *92*, 753–760.
- (361) Swinnen, A.; Haeldermans, I.; vande Ven, M.; D'Haen, J.; Vanhoyland, G.; Aresu, S.; D'Olieslaeger, M.; Manca, J. *Adv. Funct. Mater.* **2006**, *16*, 760–765.
- (362) Pearson, A. J.; Wang, T.; Jones, R. A. L.; Lidzey, D. G.; Staniec, P. A.; Hopkinson, P. E.; Donald, A. M. *Macromolecules* **2012**, *45*, 1499–1508.

- (363) Müller, C.; Bergqvist, J.; Vandewal, K.; Tvingstedt, K.; Anselmo, A. S.; Magnusson, R.; Alonso, M. I.; Moons, E.; Arwin, H.; Campoy-Quiles, M.; Inganäs, O. *J. Mater. Chem.* **2011**, *21*, 10676.
- (364) Bergqvist, J.; Lindqvist, C.; Bäcke, O.; Ma, Z.; Tang, Z.; Tress, W.; Gustafsson, S.; Wang, E.; Olsson, E.; Andersson, M. R.; Inganäs, O.; Müller, C. *J. Mater. Chem. A* **2014**, *2*, 6146–6152.
- (365) Strobl, G. *The Physics of Polymers*; Springer: Berlin, Heidelberg, 2007.
- (366) Li, Z.; Wong, H. C.; Huang, Z.; Zhong, H.; Tan, C. H.; Tsoi, W. C.; Kim, J. S.; Durrant, J. R.; Cabral, J. T. *Nat. Commun.* **2013**, *4*, 2227.
- (367) Tipnis, R.; Bernkopf, J.; Jia, S.; Krieg, J.; Li, S.; Storch, M.; Laird, D. *Sol. Energy Mater. Sol. Cells* **2009**, *93*, 442–446.
- (368) Peters, C. H.; Sachs-Quintana, I. T.; Kastrop, J. P.; Beaupré, S.; Leclerc, M.; McGehee, M. D. *Adv. Energy Mater.* **2011**, *1*, 491–494.
- (369) Roesch, R.; Eberhardt, K.-R.; Engmann, S.; Gobsch, G.; Hoppe, H. *Sol. Energy Mater. Sol. Cells* **2013**, *117*, 59–66.
- (370) Reese, M. O.; Gevorgyan, S. A.; Jørgensen, M.; Bundgaard, E.; Kurtz, S. R.; Ginley, D. S.; Olson, D. C.; Lloyd, M. T.; Morvillo, P.; Katz, E. A.; Elschner, A.; Haillant, O.; Currier, T. R.; Shrotriya, V.; Hermenau, M.; Riede, M.; R. Kirov, K.; Trimmel, G.; Rath, T.; Inganäs, O.; Zhang, F.; Andersson, M.; Tvingstedt, K.; Lira-Cantu, M.; Laird, D.; McGuinness, C.; Gowrisanker, S.; Pannone, M.; Xiao, M.; Hauch, J.; Steim, R.; DeLongchamp, D. M.; Rösch, R.; Hoppe, H.; Espinosa, N.; Urbina, A.; Yaman-Uzunoglu, G.; Bonekamp, J.-B.; van Breemen, A. J. J. M.; Giroto, C.; Voroshazi, E.; Krebs, F. C. *Sol. Energy Mater. Sol. Cells* **2011**, *95*, 1253–1267.
- (371) Schuller, S.; Schilinsky, P.; Hauch, J.; Brabec, C. J. *Appl. Phys. A* **2004**, *79*, 37–40.
- (372) Gevorgyan, S. A.; Jørgensen, M.; Krebs, F. C. *Sol. Energy Mater. Sol. Cells* **2008**, *92*, 736–745.
- (373) Pickett, J. E.; Sargent, J. R. *Polym. Degrad. Stab.* **2009**, *94*, 189–195.
- (374) Haillant, O.; Dumbleton, D.; Zielnik, A. *Sol. Energy Mater. Sol. Cells* **2011**, *95*, 1889–1895.
- (375) Ahmad, J.; Bazaka, K.; Anderson, L. J.; White, R. D.; Jacob, M. V. *Renew. Sustain. Energy Rev.* **2013**, *27*, 104–117.
- (376) Sachs-Quintana, I. T.; Heumüller, T.; Mateker, W. R.; Orozco, D. E.; Cheacharoen, R.; Sweetnam, S.; Brabec, C. J.; McGehee, M. D. *Adv. Funct. Mater.* **2014**, *24*,

3978–3985.

- (377) Hamley, I. W. *The Physics of Block Copolymers*; Oxford University Press: Oxford, England, 1998.
- (378) Bates, F. S.; Fredrickson, G. H. *Annu. Rev. Phys. Chem.* **1990**, *41*, 525–557.
- (379) Matsen, M. W.; Bates, F. S. *Macromolecules* **1996**, *29*, 1091–1098.
- (380) Sommer, M.; Huettner, S.; Thelakkat, M. *J. Mater. Chem.* **2010**, *20*, 10788–10797.
- (381) Topham, P.; Parnell, A.; Hiorns, R. *J. Polym. Sci. B Polym. Phys.* **2011**, *49*, 1131–1156.
- (382) Liu, C.-L.; Lin, C.-H.; Kuo, C.-C.; Lin, S.-T.; Chen, W.-C. *Prog. Polym. Sci.* **2011**, *36*, 603–637.
- (383) Stalmach, U.; de Boer, B.; Post, A. D.; van Hutten, P. F.; Hadziioannou, G. *Angew. Chem. Int. Ed.* **2001**, *40*, 428–430.
- (384) Sary, N.; Mezzenga, R.; Brochon, C.; Hadziioannou, G.; Ruokolainen, J. *Macromolecules* **2007**, *40*, 3277–3286.
- (385) Sary, N.; Richard, F.; Brochon, C.; Leclerc, N.; Lévêque, P.; Audinot, J.-N.; Berson, S.; Heiser, T.; Hadziioannou, G.; Mezzenga, R. *Adv. Mater.* **2010**, *22*, 763–768.
- (386) Miyanishi, S.; Zhang, Y.; Tajima, K.; Hashimoto, K. *Chem. Commun.* **2010**, *46*, 6723–6725.
- (387) Sivula, K.; Ball, Z. T.; Watanabe, N.; Fréchet, J. M. J. *Adv. Mater.* **2006**, *18*, 206–210.
- (388) Olsen, B. D.; Segalman, R. A. *Mater. Sci. Eng. R Reports* **2008**, *62*, 37–66.
- (389) de Cuendias, A.; Hiorns, R. C.; Cloutet, E.; Vignau, L.; Cramail, H. *Polym. Int.* **2010**, *59*, 1452–1476.
- (390) Barrau, S.; Heiser, T.; Richard, F.; Brochon, C.; Ngov, C.; van de Wetering, K.; Hadziioannou, G.; Anokhin, D. V.; Ivanov, D. A. *Macromolecules* **2008**, *41*, 2701–2710.
- (391) Gholamkhash, B.; Peckham, T. J.; Holdcroft, S. *Polym. Chem.* **2010**, *1*, 708–719.
- (392) Gholamkhash, B.; Holdcroft, S. *Chem. Mater.* **2010**, *22*, 5371–5376.
- (393) Lin, Y.; Lim, J. A.; Wei, Q.; Mannsfeld, S. C. B.; Briseno, A. L.; Watkins, J. J. *Chem.*

Mater. **2012**, *24*, 622–632.

- (394) Lai, Y.-C.; Ohshimizu, K.; Takahashi, A.; Hsu, J.-C.; Higashihara, T.; Ueda, M.; Chen, W.-C. *J. Polym. Sci. A Polym. Chem.* **2011**, *49*, 2577–2587.
- (395) Yang, C.; Lee, J. K.; Heeger, A. J.; Wudl, F. *J. Mater. Chem.* **2009**, *19*, 5416–5423.
- (396) Chan, S.-H.; Lai, C.-S.; Chen, H.-L.; Ting, C.; Chen, C.-P. *Macromolecules* **2011**, *44*, 8886–8891.
- (397) Heuken, M.; Komber, H.; Erdmann, T.; Senkovskyy, V.; Kiriya, A.; Voit, B. *Macromolecules* **2012**, *45*, 4101–4114.
- (398) Yun, M. H.; Kim, J.; Yang, C.; Kim, J. Y. *Sol. Energy Mater. Sol. Cells* **2012**, *104*, 7–12.
- (399) Zappia, S.; Mendichi, R.; Battiato, S.; Scavia, G.; Mastria, R.; Samperi, F.; Destri, S. *Polymer* **2015**, *80*, 245–258.
- (400) Wantz, G.; Derue, L.; Dautel, O.; Rivaton, A.; Hudhomme, P.; Dagron-Lartigau, C. *Polym. Int.* **2014**, *63*, 1346–1361.
- (401) Rumer, J. W.; McCulloch, I. *Mater. Today* **2015**, *18*, 425–435.
- (402) Griffini, G.; Douglas, J. D.; Piliago, C.; Holcombe, T. W.; Turri, S.; Fréchet, J. M. J.; Mynar, J. L. *Adv. Mater.* **2011**, *23*, 1660–1664.
- (403) Kim, H. J.; Han, A.-R.; Cho, C.-H.; Kang, H.; Cho, H.-H.; Lee, M. Y.; Fréchet, J. M. J.; Oh, J. H.; Kim, B. J. *Chem. Mater.* **2012**, *24*, 215–221.
- (404) Miyanishi, S.; Tajima, K.; Hashimoto, K. *Macromolecules* **2009**, *42*, 1610–1618.
- (405) Yau, C. P.; Wang, S.; Treat, N. D.; Fei, Z.; Tremolet de Villers, B. J.; Chabinec, M. L.; Heeney, M. *Adv. Energy Mater.* **2015**, *5*, 1401228.
- (406) Diacon, A.; Derue, L.; Lecourtier, C.; Dautel, O.; Wantz, G.; Hudhomme, P. *J. Mater. Chem. C* **2014**, *2*, 7163–7167.
- (407) Cheng, P.; Yan, C.; Lau, T.-K.; Mai, J.; Lu, X.; Zhan, X. *Adv. Mater.* **2016**, *28*, 5822–5829.
- (408) Kim, B. J.; Miyamoto, Y.; Ma, B.; Fréchet, J. M. J. *Adv. Funct. Mater.* **2009**, *19*, 2273–2281.
- (409) Carlé, J. E.; Andreasen, B.; Tromholt, T.; Madsen, M. V.; Norrman, K.; Jørgensen, M.; Krebs, F. C. *J. Mater. Chem.* **2012**, *22*, 24417–24423.

- (410) Qian, D.; Xu, Q.; Hou, X.; Wang, F.; Hou, J.; Tan, Z. *J. Polym. Sci. A Polym. Chem.* **2013**, *51*, 3123–3131.
- (411) Chen, X.; Chen, L.; Chen, Y. *J. Polym. Sci. A Polym. Chem.* **2013**, *51*, 4156–4166.
- (412) Gougousi, T.; Samartzis, P. C.; Kitsopoulos, T. N. *J. Chem. Phys.* **1998**, *108*, 5742–5746.
- (413) Lee, Y.; Chen, C.; Lin, S. *J. Chem. Phys.* **2003**, *118*, 10494–10501.
- (414) Zhu, R.; Tang, B.; Ji, L.; Tang, Y.; Zhang, S.; Zhang, B. *Opt. Commun.* **2004**, *235*, 325–331.
- (415) Jo, J.; Kim, S.-S.; Na, S.-I.; Yu, B.-K.; Kim, D.-Y. *Adv. Funct. Mater.* **2009**, *19*, 866–874.
- (416) Nam, C.; Qin, Y.; Park, Y. S.; Hlaing, H.; Lu, X.; Ocko, B. M.; Black, C. T.; Grubbs, R. B. *Macromolecules* **2012**, *45*, 2338–2347.
- (417) Derue, L.; Dautel, O.; Tournebize, A.; Drees, M.; Pan, H.; Berthumeyrie, S.; Pavageau, B.; Cloutet, E.; Chambon, S.; Hirsch, L.; Rivaton, A.; Hudhomme, P.; Facchetti, A.; Wantz, G. *Adv. Mater.* **2014**, *26*, 5831–5838.
- (418) Derue, L.; Lecourtier, C.; Gorisse, T.; Hirsch, L.; Dautel, O.; Wantz, G. *RSC Adv.* **2015**, *5*, 3840–3843.
- (419) Rumer, J. W.; Ashraf, R. S.; Eisenmenger, N. D.; Huang, Z.; Meager, I.; Nielsen, C. B.; Schroeder, B. C.; Chabinyk, M. L.; McCulloch, I. *Adv. Energy Mater.* **2015**, *5*, 1401426.
- (420) Murray, K. A.; Holmes, A. B.; Moratti, S. C.; Friend, R. H. *Synth. Met.* **1996**, *76*, 161–163.
- (421) Klima, R. F.; Gudmundsdóttir, A. D. *J. Photochem. Photobiol. A Chem.* **2004**, *162*, 239–247.
- (422) Png, R.-Q.; Chia, P.; Tang, J.; Liu, B.; Sivaramakrishnan, S.; Zhou, M.; Khong, S.-H.; Chan, H. S. O.; Burroughes, J. H.; Chua, L.-L.; Friend, R. H.; Ho, P. K. H. *Nat. Mater.* **2010**, *9*, 152–158.
- (423) Prato, M.; Li, Q. C.; Wudl, F.; Lucchini, V. *J. Am. Chem. Soc.* **1993**, *115*, 1148–1150.
- (424) Lowe, J.; Holdcroft, S. *Macromolecules* **1995**, *28*, 4608–4616.
- (425) Feser, S.; Meerholz, K. *Chem. Mater.* **2011**, *23*, 5001–5005.

- (426) Xu, Q.; Wang, F. Z.; Qian, D. P.; Tan, Z. A.; Li, L. J.; Li, S. S.; Tu, X. H.; Sun, G.; Hou, X. L.; Hou, J. H.; Li, Y. F. *ACS Appl. Mater. Interfaces* **2013**, *5*, 6591–6597.
- (427) Chen, C.-P.; Huang, C.-Y.; Chuang, S.-C. *Adv. Funct. Mater.* **2015**, *25*, 207–213.
- (428) Bundgaard, E.; Helgesen, M.; Carlé, J. E.; Krebs, F. C.; Jørgensen, M. *Macromol. Chem. Phys.* **2013**, *214*, 1546–1558.
- (429) Liu, J.; Kadnikova, E. N.; Liu, Y.; McGehee, M. D.; Fréchet, J. M. J. *J. Am. Chem. Soc.* **2004**, *126*, 9486–9487.
- (430) Krebs, F. C.; Spanggaard, H. *Chem. Mater.* **2005**, *17*, 5235–5237.
- (431) Krebs, F. C. *Proceedings of SPIE*; Kafafi, Z. H., Lane, P. A., Eds.; San Diego, CA, Jul. 31, 2005; Vol. 5938, p 59380Y.
- (432) Edder, C.; Armstrong, P. B.; Prado, K. B.; Fréchet, J. M. J. *Chem. Commun.* **2006**, 1965–1967.
- (433) Bjerring, M.; Nielsen, J. S.; Nielsen, N. C.; Krebs, F. C. *Macromolecules* **2007**, *40*, 6012–6013.
- (434) Gevorgyan, S. A.; Krebs, F. C. *Chem. Mater.* **2008**, *20*, 4386–4390.
- (435) Krebs, F. C. *Sol. Energy Mater. Sol. Cells* **2008**, *92*, 715–726.
- (436) Krebs, F. C.; Thomann, Y.; Thomann, R.; Andreasen, J. W. *Nanotechnology* **2008**, *19*, 424013.
- (437) Bjerring, M.; Nielsen, J. S.; Siu, A.; Nielsen, N. C.; Krebs, F. C. *Sol. Energy Mater. Sol. Cells* **2008**, *92*, 772–784.
- (438) Helgesen, M.; Gevorgyan, S. A.; Krebs, F. C.; Janssen, R. A. J. *Chem. Mater.* **2009**, *21*, 4669–4675.
- (439) Helgesen, M.; Bjerring, M.; Nielsen, N. C.; Krebs, F. C. *Chem. Mater.* **2010**, *22*, 5617–5624.
- (440) Søndergaard, R. R.; Norrman, K.; Krebs, F. C. *J. Polym. Sci. A Polym. Chem.* **2012**, *50*, 1127–1132.
- (441) Yang, K.; He, T.; Chen, X.; Cheng, S. Z. D.; Zhu, Y. *Macromolecules* **2014**, *47*, 8479–8486.
- (442) Liu, C. C.; Dong, S.; Cai, P.; Liu, P.; Liu, S.; Chen, J.; Liu, F.; Ying, L.; Russell, T. P.; Huang, F.; Cao, Y. *ACS Appl. Mater. Interfaces* **2015**, *7*, 9038–9051.

- (443) Yang, L.; Yu, Y.; Gong, Y.; Li, J.; Ge, F.; Jiang, L.; Gao, F.; Dan, Y. *Polym. Chem.* **2015**, *6*, 7005–7014.
- (444) Yu, J.; Abley, M.; Yang, C.; Holdcroft, S. *Chem. Commun.* **1998**, 1503–1504.
- (445) Yu, J.; Holdcroft, S. *Macromolecules* **2000**, *33*, 5073–5079.
- (446) Han, X.; Chen, X.; Vamvounis, G.; Holdcroft, S. *Macromolecules* **2005**, *38*, 1114–1122.
- (447) Gordon, T. J.; Yu, J.; Yang, C.; Holdcroft, S. *Chem. Mater.* **2007**, *19*, 2155–2161.
- (448) Han, X.; Chen, X.; Holdcroft, S. *Adv. Mater.* **2007**, *19*, 1697–1702.
- (449) Gordon, T. J.; Vamvounis, G.; Holdcroft, S. *Adv. Mater.* **2008**, *20*, 2486–2490.
- (450) Han, X.; Chen, X.; Gordon, T.; Holdcroft, S. *Macromol. Rapid Commun.* **2009**, *30*, 2089–2095.
- (451) Brusso, J. L.; Lilliedal, M. R.; Holdcroft, S. *Polym. Chem.* **2011**, *2*, 175–180.
- (452) Schelkle, K. M.; Becht, S.; Faraji, S.; Petzoldt, M.; Müllen, K.; Buckup, T.; Dreuw, A.; Motzkus, M.; Hamburger, M. *Macromol. Rapid Commun.* **2015**, *36*, 31–37.
- (453) Kuhn, M.; Ludwig, J.; Marszalek, T.; Adermann, T.; Pisula, W.; Müllen, K.; Colsmann, A.; Hamburger, M. *Chem. Mater.* **2015**, *27*, 2678–2686.
- (454) Jakob, S.; Moreno, A.; Zhang, X.; Bertschi, L.; Smith, P.; Schlüter, A. D.; Sakamoto, J. *Macromolecules* **2010**, *43*, 7916–7918.
- (455) Bundgaard, E.; Hagemann, O.; Bjerring, M.; Nielsen, N. C.; Andreasen, J. W.; Andreasen, B.; Krebs, F. C. *Macromolecules* **2012**, *45*, 3644–3646.
- (456) Kasegaonkar, A. S.; Barqawi, H.; Binder, W. H. *J. Polym. Sci. A Polym. Chem.* **2015**, *53*, 642–649.
- (457) Smith, Z. C.; Meyer, D. M.; Simon, M. G.; Staii, C.; Shukla, D.; Thomas, S. W. *Macromolecules* **2015**, *48*, 959–966.
- (458) S. W. Thomas III. *Macromol. Chem. Phys.* **2012**, *213*, 2443–2449.
- (459) Smith, Z. C.; Pawle, R. H.; Thomas, S. W. *ACS Macro Lett.* **2012**, *1*, 825–829.
- (460) Sun, B.; Hong, W.; Aziz, H.; Li, Y. *J. Mater. Chem.* **2012**, *22*, 18950–18955.
- (461) Hurd, C. D.; Blunck, F. H. *J. Am. Chem. Soc.* **1938**, *60*, 2419–2425.

- (462) Taylor, R. Pyrolysis of acids and their derivatives. In *Acid Derivatives*; Patai, S., Ed.; PATAI'S Chemistry of Functional Groups; John Wiley & Sons: Chichester, UK, 1979; Vol. 2, pp 859–914.
- (463) Gala, D.; Steinman, M.; Jaret, R. S. *J. Org. Chem.* **1986**, *51*, 4488–4490.
- (464) Casa, C. D.; Bizzarri, P. C.; Salatelli, E.; Bertinelli, F. *Adv. Mater.* **1995**, *7*, 1005–1009.
- (465) Bolognesi, A.; Mendichi, R.; Schieroni, A.; Villa, D.; Ahumada, O. *Macromol. Chem. Phys.* **1997**, *198*, 3277–3284.
- (466) Toušek, J.; Toušková, J.; Remeš, Z.; Kousal, J.; Gevorgyan, S. A.; Krebs, F. C. *Synth. Met.* **2012**, *161*, 2727–2731.
- (467) Hagemann, O.; Bjerring, M.; Nielsen, N. C.; Krebs, F. C. *Sol. Energy Mater. Sol. Cells* **2008**, *92*, 1327–1335.
- (468) Liu, C.; Xu, W.; Guan, X.; Yip, H.-L.; Gong, X.; Huang, F.; Cao, Y. *Macromolecules* **2014**.
- (469) Hammond, M. R.; Kline, R. J.; Herzing, A. A.; Richter, L. J.; Germack, D. S.; Ro, H.-W.; Soles, C. L.; Fischer, D. A.; Xu, T.; Yu, L.; Toney, M. F.; DeLongchamp, D. M. *ACS Nano* **2011**, *5*, 8248–8257.
- (470) Pommerehne, J.; Vestweber, H.; Guss, W.; Mahrt, R. F.; Bäessler, H.; Porsch, M.; Daub, J. *Adv. Mater.* **1995**, *7*, 551–554.
- (471) Son, H. J.; Wang, W.; Xu, T.; Liang, Y.; Wu, Y.; Li, G.; Yu, L. *J. Am. Chem. Soc.* **2011**, *133*, 1885–1894.
- (472) Tedder, J. M. *Angew. Chem. Int. Ed. Engl.* **1982**, *21*, 401–410.
- (473) Leclerc, M.; Najari, A.; Zou, Y. Novel Photoactive Polymers. WO 2011/063534 A1, June 9, 2011.
- (474) Ashby, E. C.; Pham, T. N. *J. Org. Chem.* **1987**, *52*, 1291–1300.
- (475) Li, Y. N.; Sonar, P.; Murphy, L.; Hong, W. *Energy Environ. Sci.* **2013**, *6*, 1684–1710.
- (476) Wright, A. G.; Holdcroft, S. *ACS Macro Lett.* **2014**, *3*, 444–447.
- (477) Razzell-Hollis, J.; Wade, J.; Tsoi, W. C.; Soon, Y.; Durrant, J.; Kim, J.-S. *J. Mater. Chem. A* **2014**, *2*, 20189–20195.
- (478) MacKenzie, A. R. Chemistry and Pollution of the Stratosphere. In *Pollution: Causes,*

Effects and Control, 4th ed.; Harrison, R. M., Ed.; Royal Society of Chemistry: Cambridge, UK, 2001; pp 220–245.

- (479) Zhou, X.-L.; White, J. M. *Chem. Phys. Lett.* **1990**, *167*, 205–208.
- (480) Solymosi, F.; Kiss, J.; Révész, K. *J. Chem. Phys.* **1991**, *94*, 8510–8519.
- (481) Kokh, D. B.; Liebermann, H.; Buenker, R. J. *J. Chem. Phys.* **2010**, *132*, 074707.
- (482) Schaffer, C. J.; Palumbiny, C. M.; Niedermeier, M. A.; Jendrzewski, C.; Santoro, G.; Roth, S. V.; Müller-Buschbaum, P. *Adv. Mater.* **2013**, *25*, 6760–6764.
- (483) NREL. Best Research-Cell Efficiencies (Accessed Jan/2016) http://www.nrel.gov/ncpv/images/efficiency_chart.jpg.
- (484) Kroon, J. M.; Wienk, M. M.; Verhees, W. J. H.; Hummelen, J. C. *Thin Solid Films* **2002**, *403–404*, 223–228.
- (485) Shrotriya, V.; Li, G.; Yao, Y.; Moriarty, T.; Emery, K.; Yang, Y. *Adv. Funct. Mater.* **2006**, *16*, 2016–2023.
- (486) Dennler, G. *Mater. Today* **2007**, *10*, 56.
- (487) Smestad, G. P.; Krebs, F. C.; Lampert, C. M.; Granqvist, C. G.; Chopra, K. L.; Mathew, X.; Takakura, H. *Sol. Energy Mater. Sol. Cells* **2008**, *92*, 371–373.
- (488) Snaith, H. J. *Energy Environ. Sci.* **2012**, *5*, 6513–6520.
- (489) Snaith, H. J. *Nat. Photon.* **2012**, *6*, 337–340.
- (490) Gevorgyan, S. A.; Eggert Carlé, J.; Søndergaard, R.; Larsen-Olsen, T. T.; Jørgensen, M.; Krebs, F. C. *Sol. Energy Mater. Sol. Cells* **2013**, *110*, 24–35.
- (491) Gordon, I.; Krebs, F. C.; Mathew, X.; Lampert, C. M.; Rougier, A.; Smestad, G. P.; Subrahmanyam, A. *Sol. Energy Mater. Sol. Cells* **2015**, *133*, A1–A6.
- (492) Zimmermann, E.; Ehrenreich, P.; Pfadler, T.; Dorman, J. A.; Weickert, J.; Schmidt-Mende, L. *Nat. Photon.* **2014**, *8*, 669–672.
- (493) Newport Co. Class AAA Solar Simulators (accessed Jan/2016) <http://www.newport.com/Class-AAA-Solar-Simulators/842468/1033/info.aspx>.
- (494) Matson, R. J.; Emery, K. A.; Bird, R. E. *Sol. Cells* **1984**, *11*, 105–145.
- (495) Ye, L.; Zhou, C.; Meng, H.; Wu, H.-H.; Lin, C.-C.; Liao, H.-H.; Zhang, S.; Hou, J. *J. Mater. Chem. C* **2015**, *3*, 564–569.

- (496) *IEC Standard 60904-3 Measurement Principles for Terrestrial Photovoltaic Solar Devices with Reference Spectral Irradiance Data, 2.0.*; International Electrochemical Commission: Geneva, Switzerland, 2008.
- (497) *ASTM E948-15 Standard Test Method for Electrical Performance of Photovoltaic Cells Using Reference Cells Under Simulated Sunlight*; ASTM International: West Conshohocken, PA, 2015.
- (498) Tress, W. Photovoltaic Energy Conversion. In *Organic Solar Cells: Theory, Experiment, and Device Simulation*; Springer Series in Materials Science; Springer: Cham, Switzerland, 2014; Vol. 208, pp 15–66.
- (499) Lindholm, F. A.; Fossum, J. G.; Burgess, E. L. *IEEE Trans. Electron Dev.* **1979**, *26*, 165–171.
- (500) Cravino, A.; Schilinsky, P.; Brabec, C. J. *Adv. Funct. Mater.* **2007**, *17*, 3906–3910.
- (501) *Nat. Photon.* **2014**, *8*, 665.
- (502) *ASTM E927-10(2015) Standard Specification for Solar Simulation for Terrestrial Photovoltaic Testing*; ASTM International: West Conshohocken, PA, 2015.
- (503) *IEC 60904-9:2007 Photovoltaic devices-Part 9: Solar simulator performance requirements, 2.0.*; International Electrochemical Commission: Geneva, Switzerland, 2007.
- (504) *JIS C 8912:1998 Solar simulators for crystalline solar cells and modules*; Japanese Industrial Standards Committee: Tokyo, Japan, 1998.
- (505) Brown, J. D.; Brown, D. R. Beam Shaping with Diffractive Diffusers. In *Laser Beam Shaping Theory and Techniques*, 2nd ed.; Dickey, F. M., Ed.; CRC Press: Boca Raton, FL, 2014; pp 333–365.
- (506) Henning, T. F. E.; Unnebrink, L.; Scholl, M. *Proceedings of SPIE*; Dubowski, J. J., Mazumder, J., Migliore, L. R., Roychoudhuri, C., Schaeffer, R. D., Eds.; San Jose, CA, Jan. 27, 1996; Vol. 2703, p 62.
- (507) Brown, D. M.; Dickey, F. M.; Weichman, L. S. Multi-aperture Beam Integration Systems. In *Laser Beam Shaping Theory and Techniques*, 2nd ed.; Dickey, F. M., Ed.; CRC Press: Boca Raton, FL, 2014; pp 405–439.
- (508) Wehenkel, D. J.; Hendriks, K. H.; Wienk, M. M.; Janssen, R. A. J. *J. Org. Electron.* **2012**, *13*, 3284–3290.
- (509) Emery, K.; Moriarty, T. *Proceedings of SPIE*; Kafafi, Z. H., Lane, P. A., Eds.; San Diego, CA, Aug. 10, 2008; Vol. 7052, p 70520D.

- (510) Lohwasser, R. H.; Thelakkat, M. *Macromolecules* **2011**, *44*, 3388–3397.
- (511) Liu, P.; Huang, L.; Faul, M. M. *Tetrahedron Lett.* **2007**, *48*, 7380–7382.
- (512) Pandey, J.; Mishra, M.; Bisht, S. S.; Sharma, A.; Tripathi, R. P. *Tetrahedron Lett.* **2008**, *49*, 695–698.
- (513) Jagadamma, L. K.; Al-Senani, M.; El-Labban, A.; Gereige, I.; Ngongang Ndjawa, G. O.; Faria, J. C. D.; Kim, T.; Zhao, K.; Cruciani, F.; Anjum, D. H.; McLachlan, M. A.; Beaujuge, P. M.; Amassian, A. *Adv. Energy Mater.* **2015**, *5*, 1500204.
- (514) Jiang, J.-M.; Lin, H.-K.; Lin, Y.-C.; Chen, H.-C.; Lan, S.-C.; Chang, C.-K.; Wei, K.-H. *Macromolecules* **2014**, *47*, 70–78.
- (515) Zhang, S.; Ye, L.; Zhao, W.; Liu, D.; Yao, H.; Hou, J. *Macromolecules* **2014**, *47*, 4653–4659.
- (516) Yao, H.; Zhang, H.; Ye, L.; Zhao, W.; Zhang, S.; Hou, J. *ACS Appl. Mater. Interfaces* **2016**, *8*, 3575–3583.
- (517) Nakanishi, T.; Shirai, Y.; Han, L. *J. Mater. Chem. A* **2015**, *3*, 4229–4238.
- (518) Yu, J.; Zhao, B.; Nie, X.; Zhou, B.; Li, Y.; Hai, J.; Zhu, E.; Bian, L.; Wu, H.; Tang, W. *New J. Chem.* **2015**, *39*, 2248–2255.